AN ANALYTICAL AND QUANTITATIVE ANALYSIS OF THE LASER-INDUCED INCANDESCENCE OF SOOT

A Thesis Presented to the
Academic Faculty

By

Richard T. Wainner

In Partial Fulfillment of the
Requirements for the Degree
Doctor of Philosophy in Aerospace Engineering

Georgia Institute of Technology
August 1999

AN ANALYTICAL AND QUANTITATIVE ANALYSIS OF THE LASER-INDUCED INCANDESCENCE OF SOOT

Approved:

____

Jerry M. Seitzman, Chairman

____

Jechiel I. Jagoda

____

Lawrence M. Matta

____

Ben T. Zinn

____

Sheldon M. Jeter

Date Approved:_____________

ACKNOWLEDGEMENTS

Most sincere thanks are offered to the National Science Foundation, and the DoD (through a small business initiative (SBIR) subcontracted from Metrolaser, Inc.) for their financial support of this research.

I would like to thank Ping Yang for his patience and persistence in learning the ropes of this research and to thank Brian Ritchie, Brian Scully, and Mael Disseau for their "advice and assistance" in the lab. Similar thanks go to those fellows whose job it is to make "lab life" bearable: Bob Daniel, Larry Matta, and David Scarborough.

For their invaluable help on particular aspects of this research, I wish to thank Bernd Mewes (programming the initial LII model), Shengquan Liang (PDPA droplet size measurements), Raghavanasari Jeenu (SEM particle size measurements), Dr. Stefan Martin of Metrolaser, Inc.(initial soot generator and polarization ratio measurements), and Dr. Roy Howard of Princeton Instruments, Inc.(dual-camera measurements).

The late Dr. Warren Strahle is remembered fondly for his warm heart and encouragement at the beginning of the author's graduate studies.

Also, I could not have come this far without the love, support and education provided by my parents, my sisters, my friends, and my dear, incredible wife Kellee Middlebrooks.

During some crucial times, my interim and constant second advisor, Dr. Jeff Jagoda, was always willing to help and lend advice or encouragement.

Last, but certainly not least, I must gratefully thank Dr. Jerry Seitzman for his limitless help and knowledge. The patience of this person and his dedication to "eschewing obfuscation" are much appreciated. I'm not sure mentors get better than this. Thanks.

TABLE OF CONTENTS

NOMENCLATURE

A. Physical Constants

Symbol	Name	Value	Source
α	thermal accommodation factor	0.9	[1]
c	Speed of light (in air)	3.00×10^{8} m/s	[2]
c_s	heat capacity of soot	2079 J/kg-K	[3]
G	geometry factor for spherical particles	6.29 (flame) or 7.04	[1]
h	Planck's constant	6.63×10^{-34} J-s	[2]
η_0	dyn. viscosity of local gas (1 atm., 0 °C)	1.7116×10^{-5} kg/m-s	[4]
k	Boltzmann constant	1.3805×10^{-23} J/K	[2]
k_0	thermal conductivity at 1 atm., 0°C	0.0241 W/m-K	[4]
γ	ratio of specific heats	1.27 (flame) or 1.4	[2]
p^*	reference vaporization pressure	101325 Pa	[3]
ρ_s	density of solid soot	2100 kg/m^3	[3]
R	specific gas constant (air)	287 J/kg-K	[2]
$\Re$	universal gas constant	8.314 J/mol-K	[2]
S_k	Sutherland const. for thermal conductivity	194 K	[4]
S_η	Sutherland constant for dynamic viscosity	111 K	[4]

T^*	soot vaporization temperature (at p^*)	3915 K	[3]
T_{k0}	thermal conductivity reference temperature	273 K	[4]
$T_{\eta 0}$	dynamic viscosity reference temperature	273 K	[4]
W_s	molecular weight of solid carbon	0.012 kg/mol	[3]
W_v	molecular weight of soot vapor (C_3)	0.036 kg/mol	[3]

B. Physical Variables

Symbol	**Name**	**Units**
$\alpha_{\lambda,p}$	primary soot particle absorptivity	(none)
d_p	primary soot particle diameter	(nm)
e_λ	spectral radiant exitance	(W/m^2-nm)
$e_{\lambda,b}$	blackbody spectral radiant exitance	(W/m^2-nm)
$\varepsilon_{\lambda,p}$	primary soot particle emissitivity	(none)
G_λ	detector/optics response function	(none)
η	dynamic viscosity of surrounding gas	(kg/m-s)
H_v	latent heat of vaporization for soot	(J/mol)
I	laser irradiance	(W/m^2)
k_∞	thermal conductivity of surrounding gas	(W/m-K)
λ	wavelength of light	(nm)

λ_{det}	nominal wavelength of detected light	(nm)
λ_{mfp}	mean free path of surrounding gas	(m)
m	refractive index of material	(none)
m_p	mass of primary soot particle	(kg)
S	Signal detected from a single particle	(J)
S_λ	spectral signal ratio (long/short wavelengths)	(none)
t	time	(sec)
T_{p}	primary soot particle temperature	(K)
T_∞	temperature of surrounding gas	(K)
Ω	solid angle of detection	(srad)

SUMMARY

The focus of this research was on the development of a diagnostic method called Laser-Induced Incandescence (LII) for the measurement of different parameters of combustion-generated carbon particulate, or soot. This non-intrusive technique involves the heating of soot particles in-situ with a pulsed laser source and detecting the subsequent visible emission from the particles. In this research, LII signals were acquired in both a well-documented diffusion flame and a simulated exhaust flow for the purpose of making concentration and particle size measurements. For both types of measurements, the effect on the LII signal of experimental paameters such as gas temperature, particle size, soot composition and morphology, laser fluence, laser wavelength, detection wavelength and timing are analyzed. Two particle sizing methods were considered, one based on the post-laser-heating signal decay rate (conductive cooling rate) and the other by measuring the peak temperatures attained (pyrometry).

A dependence of the LII signal per soot volume on particle size was found, with larger particles emitting more signal. This is in agreement with the numerical predictions of a modeled simulation of the LII process. Positive results are obtained for sizing measurements with each of the proposed techniques. However, limitations for both are also noted. Both model and experimental results indicate that nonuniform particle size distributions will make such size measurements more difficult. For an effective 1-D Gaussian laser distribution, the detected (integrated) LII signal magnitude, spectral signal profile (observed temperature, ±200 K), and signal decay rate are insensitive to changes in laser fluence above a certain threshold (0.3 to 0.5 J/cm^2, depending on laser wavelength). At higher fluences with visible wavelength illumination, significant emission from laser-produced C_2 is also noted. In general, this additional signal scales similarly to LII, with soot concentration. However, it behaves differently with changing laser fluence and in the soot formation regions of the diffusion flame. In these regions, the C_2 signal actually scales more like the commonly-used extinction technique than does LII. The LII signal was also detected at time intervals delayed from the laser illumination. Little difference (<10%) from ‘promptly’ detected signals was noted up to delays of 100 ns.

The LII signal also showed some sensitivity to the laser beam shape, to strong soot concentration gradients through the illuminated zone, and at higher intensities, to small nonmonotonicities in the laser beam ‘wings’. In the high soot concentration zones of the flame, trapping of the signal by soot in the detection path also becomes an issue to be avoided or corrected for. The LII model predicts the behavior of promptly detected LII signals fairly well with respect to varying particle size and laser fluence. However, the predicted signal decay rates are faster than experimental observations by at least a factor of 4, suggesting the model needs improvement in its conductive cooling mechanism. In conclusion, the implications of these LII signal characteristics for applications in real-world combustion and exhaust environments are discussed.

CHAPTER I

INTRODUCTION

1.1 Motivation

1.1.1 Environmental Inplications

From many standpoints, the byproducts of fossil fuel combustion (particulates, unburned hydrocarbons, SO_x and NO_x,), which tend to be highly concentrated in urban areas, are the focus of great concern. Specifically, particulate carbon (coke, char, ash, soot) is receiving much attention for its health, environmental, and engineering implications. Soot (or smoke), the product of gas-phase chemical reactions, is the most common form. It is generated in, if not emitted from, almost all hydrocarbon flames, and is present at highly varying concentrations at different locations in our atmosphere. Thus, its sources and effects have drawn much scrutiny.

Most soot released into the environment is from the incomplete combustion of fossil fuels and other organic matter. Natural sources, such as forest fires, account for a significant fraction[5] of the soot particles present in the lower atmosphere. However, the contribution to airborne soot and organic carbon particles from man-made (anthropogenic) sources can be quite large.[5] This is especially true in developed industrial countries, particularly in cities with high concentrations of mobile oil-burning engines, and most specifically diesel engines.[5-10] For ground-based sources, the probability of the emissions being transported and dispersed by air currents can be low, and locally high concentrations of gaseous hydrocarbon species and soot particles can lead to severe smog. Solar scattering from particulates in the lower atmosphere contributes to the white haze of smoggy days, but the effect soot particulates have on O_3 production (produced by reaction of NO_x and hydrocarbons with UV radiation) is uncertain. Some evidence suggests that soot may contribute to the production of NO_x in the atmosphere, while on the other hand soot and water droplets formed by condensation on soot will absorb UV light, and thus may reduce the UV radiation that reaches the city-level atmosphere.[11] When introduced at higher altitudes, the soot particles can again act as condensation sites for other molecules, such as water. This can lead to increased cloud formation, which could effect global environmental changes. Soot can contain or condense sulfuric and nitric acids, also, which can produce acidic rain. Many studies have linked exposure to high levels of soot to increased occurrences of various types of cancer.[5,12] The degree to which adsorbed hydrocarbons or sulfur play a role, and the degree to which humans are at a risk from cancer from typical soot pollution levels are debated issues. At any rate, even low levels of particulate pollution, to which soot contributes, may lead to chronic cardiopulmonary problems or mortalities, especially for those with preexisting conditions.[13,14] Fine particles (less than a μm) appear to be of primary importance for their ability to penetrate not only into indoor areas but to the depths of the respiratory system.[13] Recognition of these problems motivated the EPA to set new national ambient air quality standards (NAAQS) for particulate matter in July of 1997. The levels cited were $< 50\ \mu g/m^3$ "annual mean" and $< 150\ \mu g/m^3$ "maximum 24 hour period" for the PM10 ($\leq 10\ \mu m$) category and $< 15\ \mu g/m^3$ and $< 65\ \mu g/m^3$, respectively, for the PM2.5 category ($\leq 2.5\ \mu m$). Therefore, there is increasing interest in measurement of soot concentrations as they tend to be in the fine particle size class. Naturally, there is also interest in discerning the size distribution of ambient or exhausted smokes.

1.1.2 Engineering Issues

A number of sectors in the engineering field are also concerned with the ability to measure soot concentrations and particle size. In the semiconductor industry, for example, detection and quantification of particulate contaminants on semiconductor surfaces is important. The 1997 National Technology Roadmap for Semiconductors calls for the ability to resolve 50 nm particles in-situ by 2012 and to automatically quantify defects of this size by 2006.[15] Particles in this size range tend to be sulfates, acids, metal salts, and carbon.[13] A technique that could isolate one of these (e.g., soot) or some fraction of these while also having the ability to measure particle size would be useful for the quantification of these defects. Similarly, a diagnostic technique for discriminating amorphous carbon (like that which comprises soot) from its diamond form would be beneficial in the chemical vapor deposition of diamond. Also, the carbon black industry strives to produce soots with very defined particle size and agglomeration parameters. Currently, they rely on an ex-situ analysis to quantify the particles. A real-time, in-situ technique would speed the refined control of manufactured carbon black particles.

In the field of energy conversion, soot formed in hydrocarbon combustors can influence flame temperatures and produce enhanced radiation to combustor walls. The designs of many boilers attempt to maximize this effect, then eliminate the residual soot downstream.[16] Gas turbine engine designers, on the other hand, aim to transfer the energy of combustion to the product gases, and thus the turbine, rather than decrease the lifetime of combustor liners through radiative heating. Soot is also an indicator of incomplete combustion, and soot measurements have been used for active control strategies.[17,18] Considering these above issues, there may be as great a demand for monitoring soot production in the reaction zones of engines and furnaces as there is for monitoring the final exhaust of combustion devices for environmental reasons.

1.1.3 Soot Diagnostics

The motivations for soot measurements just listed are also joined by a fundamental scientific desire to understand the processes of hydrocarbon combustion, including the mechanisms of soot production and oxidation. This scientific curiosity has been one of the oldest running motivations for combustion research and has led to the development of many techniques along the way for the measurement and analysis of soot.

The experimental methods for measurement of combustion generated soot can be divided into two categories, intrusive and non-intrusive. Intrusive techniques introduce a foreign device into the flow of interest, generally to divert or 'grab' particles for subsequent analysis by secondary instrumentation. This yields unknown effects on the very flow one is attempting to quantify. These effects have to either be assumed as negligible or data correction methods must be attempted. Considering the hostile environments of most practical combustion systems, making soot measurements away from the source is often preferred and commonly done. Exhaust flows can be diverted and passed through soot-measuring devices directly. Particle number densities can be measured by a Condensation Nucleus Counter.[19-23] Particle sizes have been measured with Particle Mobility Analyzers[6,22-24] or Impactors,[5,6,8,13,19,25] which identify particle sizes or size ranges for particles by inertia-differentiating means. Exhaust soot concentrations are most simply and most often measured by measuring the mass collected in a timed period on paper filters (this is often the output medium for impactors).[5,6,13] Similarly, this can be done with a more durable collecting device in the combustion zone itself. This is usually referred to as 'sampling'. For example, this method is employed for subsequent analysis of the size and structure of the collected soot by electron microscopy.[10,26-41]

The problem with the above techniques, though they can provide a wealth of information, is that they are tedious and exhibit poor time and space resolution. This may suffice for environmental monitoring in certain cases, but is not desirable for engineering research. Intrusive, but in-situ methods for monitoring soot concentrations also exist. Since these do not require sampling, they provide better time resolution.. For example, soot ionization and subsequent ion detection by probes has been performed in a few cases.[42-44] Still, the presence of intrusive probes can lead to unknown disturbances on the soot field of interest. Non-intrusive techniques, which measure in-situ, are preferred and many have been developed. Most of these involve some means of optical illumination and light detection.

1.1.4 Laser Techniques

The majority of optical soot diagnostic procedures have employed laser illumination and the detection of elastic laser scattering and/or laser beam extinction (attenuation).[26,44-62] Laser light scattering is a technique with good spatial and temporal resolution, thus making it especially useful for fluctuating or turbulent flows. The spatial resolution comes as a result of its being an imaging technique. One can spread the laser beam into a sheet and, with an imaging detector (camera), record a two-dimensional signal distribution, with maximum resolution usually defined by the limits of the detector. Because it uses elastically scattered light, however, laser scattering is susceptible to large background interferences from walls, windows and other particles, such as liquid droplets, in the region of interest. Also, direct observation of elastic scattering is not particularly useful for concentration measurements where a range of particle sizes is present. This is due to the fact that the strength of the scattering signal is very sensitive to the effective optical diameter of the soot particles. A region with a range of particle sizes will introduce a strong bias on the scattering signal toward the larger particles.

Extinction measurements for small absorbing soot particles, on the other hand, are proportional to the mass, or effectively volume, of material the light beam encounters. Since extinction measures the decrease on a large, possibly fluctuating background signal, very small changes associated with low soot concentrations are difficult to measure. Also, longer pathlengths can make beam steering a problem. Furthermore, extinction is a line-of-sight or path integrating technique with poor spatial resolution. It requires approaches such as tomographic inversion to recover soot profile information.[52,62-66]

Attempts have also been made to deduce particle size information from the above two methods. Varied success has been seen in efforts at quantifying soot shape and size with a combination of scattering and extinction,[45,49-52,54,55,60] angular scattering disymmetry,[46,53] and spectral broadening of scattered light.[48]

An alternative laser diagnostic for soot measurements that has recently received attention is laser-induced incandescence (LII). It combines the best properties of the two laser approaches above. LII is an imaging technique with a strong signal that is also proportional to the amount of soot the laser beam encounters. Also, the spectrally broadband nature of the LII signal allows one to avoid possible interfering signals with careful choice of illumination and detection wavelengths.

1.2 Background / Previous LII Research

1.2.1 Laser-Induced Incandescence

The earliest evidence of this technique was an observation of the different temporal emission profiles of different sized particles in laser-irradiated carbon black and alumina aerosols by Weeks and Duley in 1974[67]. This laser-induced optical signal was first observed in the realm of combustion as an interference in Raman measurements in a flame in 1977. [68] The observations and analyses (modeling) by Eckbreth[68] in that research are the starting point and first thorough resource for most LII investigations today. Since these early measurements, the physical process behind this signal has been employed and tested for making simple, nonintrusive measurements of combustion-generated soot.

Laser-induced incandescence of soot occurs when soot particles absorb laser illumination. If the laser absorption rate is sufficiently high, i.e., the intensity is high enough (pulsed lasers are typically required), the particle's temperature will rise to a level where the soot particles will glow (incandesce) noticeably stronger than the background emission, e.g., from non-illuminated particles heated to the flame temperature. If the temperature is high enough, e.g., 3915 K for bulk graphite, significant vaporization may occur simultaneously. The emitted incandescence is spectrally broadband and is a strong function of the particle temperature. Also, the overall cooling rate is slow enough that a detectable signal may survive longer than a microsecond, though the laser excitation may typically last only a few nanoseconds.

1.2.2 LII Soot Diagnostics

The first attempt at optimizing the technique for measurements of soot concentration, was made by Melton[69] in 1984. Melton used a model of the LII physics and was the first to suggest that the LII signal may have a dependence on particle size and that the degree of this dependence may depend on the wavelength (or wavelength range) used for detection. He concluded that long wavelengths should minimize the size effect. Simultaneously, Dasch[47] experimentally and numerically examined the particle vaporization induced by high intensity laser pulses. Dasch concluded that vaporization, when present, will occur at the surface and the particle size will shrink inwards. Simultaneously, some investigations[44,70] were interested in a byproduct of soot vaporization, namely C_2, and the laser-induced fluorescence (LIF) of that radical, for marking the presence of soot and/or other hydrocarbons and analyzing the relative contribution of these two sources.

LII then received little attention until the early 1990's, when a few application-oriented investigations were performed. Zur Loye *et al.*,[71,72] then Pinson *et al.*,[73] employed a laser sheet in an optically accessible cylinder of a diesel engine for in-situ, qualitative images of soot concentration. Here, short wavelength detection was advised for the rejection of background luminostiy. Hofeldt[74] calculated optimal excitation and detection parameters and detection limits for measuring soot concentrations in diesel engine exhausts. He made a detailed analysis of the expected size-dependence of the LII signal on excitation and detection wavelengths and suggested this dependence might be used for determining particle size information if the local soot concentration could be determined by other means. Cignoli *et al.* used LII for qualitative images of soot concentration in a diffusion flame.[75] They were the first to employ delayed detection for the rejection of interfering signals. Laser-induced fluorescence of C_2 was again investigated for monitoring soot concentration[76-78] and was compared to LII by Bengtsson and Aldén.[78]

1.2.3 Quantitative Soot Concentration Measurements

Quantitative measurements of soot concentration in flames were performed by Santoro *et al.* in 1994-95. They calibrated the LII signal in flames to soot concentrations measured by laser extinction in coflow jet diffusion flames.[79,80] These and earlier measurements also established this particular diffusion flame[49] as a well-defined standard and grounds for inter-lab comparison that other researchers have continued to use.[33,39,49,51,52,55,56,59,62,63,79-81] Vander Wal *et al.* also made calibrations for LII signals, using both extinction[82,83] and sampling[64] directly from the flame via a sampling tube, with the concentration determined gravimetrically[84]. These two groups employed LII for measurements in laminar and turbulent flames, premixed and diffusion flames, in microgravity combustion, and around burning droplets.[83] Transmission electron microscopy (TEM)[30-32,35-38] images were also obtained from sampled soot by Vander Wal *et al.* and it was noted that some significant changes were observable in laser-heated soot compared with unilluminated soot.[30,38,40] Shaddix and Smyth also made measurements in the diffusion flame designed by Santoro.[63] and calibrated their LII signals to extinction data. In addition,, they applied corrections for signal extinction within the flame (by soot between the region of interest and the detector) and for the effect of the varying focused width of the laser beam (in the beam propagation direction) for imaging measurements.

1.3 Concurrent Research

In late 1995, Santoro *et al.* observed different temporal decay rates for the LII signal at different points in a flame, suggesting this was due to variations in soot particle size.[80] They suggested gating the signal detector early, during the laser pulse, to avoid such a sensitivity for soot concentration measurements. At the same time, Will *et al*[85]. proposed sizing soot particles by the variations in these LII decay rates, similar to the approach used in the first LII experiments in 1972. Some time later, Mewes and Seitzman[86] calculated that this approach could have a significant sensitivity to local gas temperatures and proposed an alternative means for particle sizing based on different-sized particles reaching and maintaining higher average temperatures.

Currently, aside from this doctoral research, several groups are doing LII studies. Most of these are concerned with verifying and modeling the above particle size effects for both soot concentration and particle size measurements. Some work has also been done on further analyzing the effects of high laser fluence on the structure and other properties of irradiated soot particles. Several good efforts along these tracks have been published in the last few years,[34-38,65,66,81,86-94] including a few in the last few months.[38,66,93]

1.4 Research Objectives

Improved understanding of LII will allow this laser diagnostic technique to be more confidently employed in a range of combustion environments. Therefore, the aim of this research is to improve the understanding and applicability of the LII process, through comparisons of modeling and experimental results. under varying ambient and experimental parameters. To date, comparisons between model and experimental results are few, and current models may need enhancement or modification of the physical processes and rates involved.

The detailed objectives of this research included the following. The model described previously predicts that the LII signal will have a dependence on primary particle size. Essentially, larger particles, due to their smaller surface area to volume ratio, will reach higher temperatures and, therefore, emit more signal per unit volume (mass). Soon after the laser pulse ends, this effect is even more pronounced and a sensitivity to the local gas temperature should be enhanced. Therefore, an environment with a range of particle sizes and gas temperatures will likely be susceptible to errors in volume fraction measurements. Experiments that investigate the LII signal behavior are used to test the model. Accurately capturing these signal trends under various conditions (e.g. over a range of laser intensities) requires that the model correctly represent the various heating and cooling processes involved. At the same time, an attempt is made to exploit the expected particle size dependence for simultaneous measurement of soot particle size with concentration. The particle sizing effort includes the approach based on the relative maximum temperatures reached by different sized particles, as well as a technique that exploits their different conductive cooling rates. With particle size known, this latter method might also be employed for measuring local gas temperature. It is also yet to be proven whether a delayed signal will provide a good quantitative measure of soot concentration, given the lower temperatures at delayed times and, therefore, increased sensitivity of the signal to gas temperature and particle size.

At higher excitation intensities, where interference from C_2 may be significant, the best excitation and detection strategies for reducing this contribution are determined. The physical mechanism for the C_2 emission is also uncertain. In particular, the question is whether the C_2 emission is simply an artifact of the vaporization of carbon molecules from the soot, or whether at commonly used LII excitation wavelengths, there is an additional contribution from direct, laser-induced fluorescence. The applicability of LII to engine exhausts is also investigated. Low soot concentrations, characteristic of many important combustion exhausts, are studied in order to determine the detection limits of the LII technique.

Again, LII is a candidate for soot measurements both in combustors and exhausts flows. Therefore, two environments are be analyzed in this study.

Measurements in a reacting flow focus on a sooty diffusion flame, while a heated, carbon-bearing gas flow is used to simulate engine exhaust conditions. Again, the goal is to bring the technique to a level where LII may be employed for measurements from combustors to exhausts in as versatile and easy a manner as current, established optical diagnostics.

1.5 Organization of the Thesis

The following chapter begins with a detailed description of the current understanding of the LII process. This is followed by a report of how this process is modeled in this work for the numerical simulations, including the simplifications and assumptions made, the determined sensitivities to various parameters, and some predictions for the experimental results. Chapter 2 also includes a brief review of the outstanding questions that are to be investigated and the predictions from the LII model. The experimental facilities are illustrated in Chapter 3, including the soot source, excitation, and detection hardware and parameters, and some calibrations.

The results of this research are divided into the next two chapters. Chapter 4 covers results for a coflowing, ethylene-air laminar diffusion flame. The discussion includes an analysis of the challenges presented by the physics of the process itself, including the presence of interfering signals and the behavior with varying laser fluence. An accounting follows with the results of efforts at measuring soot concentration and particle size. Comparisons to model predictions are made throughout, as well as a running discussion of important issues and problems encountered where they are most appropriate to the dissertation. The results of the diffusion flame measurements are summarized and the lessons learned are carried into the next chapter. Chapter 5 presents a similar recounting of interferences, fluence effects, concentration and particle size measurements in the very different environment of the soot generator. This simplified environment for LII measurements is intended to simplify comparisons to the model, and also to investigate conditions similar to an exhaust flow. As this source is far less documented than the diffusion flame, some initial analysis and discussion is presented to try to quantify the produced soot aerosol. This includes electron microscope images of collected soot particles. The more important findings drawn from the experimental results are listed in Chapter 6 and recommendations for future investigations and modifications to the existing techniques are proffered.

CHAPTER II

LASER-INDUCED INCANDESCENCE AND MODELING

2.1 Laser-Induced Incandescence

The soot particles produced by hydrocarbon combustion processes are comprised of branchy aggregates of nominally spherical primary particles on the order of a few tens of nanometers (see Figure 1). This morphology of carbon is often referred to as 'aciniform' carbon and the carbon molecules in these particles are arranged in a ‘turbostratic’ arrangement, segments of graphitic crystallite layers. These ‘cells’ are arranged in a randomly oriented manner, except near the particle surface where they are oriented more parallel to the surface (see Figure 2).

In general, when a soot particle absorbs energy from a laser beam, its temperature increases. For small particles ($\pi d_p/\lambda \ll 1$, where d_p is the particle diameter and λ is the wavelength of the incident or emitted radiation) with a refractive index m not far from 1, much more of the incident radiation is absorbed than is scattered.[95] Though many values for the refractive index of flame soot have been quoted[96-101], a commonly used value for absorption calculations employ a refractive index of soot of $m = 1.57 - 0.56i$.[102]

With a sufficiently high energy absorption rate (i.e, high laser intensity), the temperature will rise to levels where significant incandescence can occur. This incandescence is essentially blackbody emission, modified by the spectral emissivity of the material, and is thus approximately dependent on temperature to the fourth power. When the particle reaches a certain temperature (e.g., 3915 K is the nominal vaporization temperature for graphite), rapid vaporization begins to take place, presumably at the particle surface. As the temperature of the particle increases, so does the vaporization rate until a balance is attained and the particle temperature levels out. The vaporization rate is dependent on the heat of vaporization at the particle temperature ($H_v(T_p)$) and the vapor pressure of the vapor species ($p_v(T_v=T_p)$), where the vapor temperature is assumed to be in equilibrium with the particle surface temperature. As the laser pulse ends, the temperature drops and the vaporization rate falls with it. The cooling due to conduction is of the same magnitude as that due to vaporization around 3500 K. Thus, during this interval, the dominant cooling mode transitions from vaporization to conductive cooling by the surrounding gas. Also, since the incandescence is a strong function of temperature, the signal emitted in this last region decays quickly, and is much lower than during the laser pulse. However, measurements with short delays from the laser pulse or with sufficiently long gating after the laser can produce a measurable signal for delayed detection. Though the light emitted by the particle is the signal of interest, radiation plays a much smaller role in cooling the particle than do the above two mechanisms.

As mentioned above, the emitted light from the soot particle surface (e_λ (W/m^2-nm)) is adjusted from an ideal blackbody by its spectral emissivity ($\varepsilon_{\lambda,p}$).[103]

$$e_\lambda = \varepsilon_{\lambda,p} e_{\lambda,b} = \varepsilon \frac{2\pi hc}{\lambda^5}\left(\frac{1}{e^{hc/\lambda kT_p}-1}\right) \tag{1}$$

According to Kirchoff's Law,[103] this value for emissivity is equivalent to the absorptivity ($\alpha_{\lambda,p}$). This value is not only dependent on the material (refractive index), but on the wavelength of the incident/emitted light, and the size of the particle. The small characteristic sizes of soot particles typical of engine exhausts and hydrocarbon flames are categorized as being in the 'Rayleigh limit', i.e. they are much smaller than the laser excitation wavelength ($\pi d_p/\lambda << 1$). In this extreme, the particles should absorb and emit closely proportional to their volume (or mass). Since the standard radiation equations are written for absorption and emission from surfaces, the absorption/emission coefficient for small particles is close to proportional to the size of the particle ($d^2 \cdot d = d^3$). On the other hand, the primary energy loss mechanisms of conduction and evaporation are expected to scale closer to d^2. Thus, it is predicted that primary particle size and gas temperature would affect the volumetric nature of the LII signal through these cooling mechanisms.

Another interesting characteristic of the LII signal is that it becomes less sensitive to energy input beyond a certain intensity. This 'threshold' fluence has been determined to be on the order of 0.2 to 0.5 J/cm^2 (20 to 50 MW/cm^2) for nanosecond scale, visible to near visible wavelength lasers, and for soot particle sizes typical of those in sooty flames. Therefore, for higher laser fluences, it is thought that average soot temperatures and signals begin to level out as most of the additional energy goes into vaporization. The actual signal behavior above threshold depends on the spatial profile of the laser beam or sheet. [80,104] For typical Gaussian distributions, falling signals due to vaporization at the center of the beam may be countered by increasing signals in the 'wings'. It has also been suggested that increasing maximum signals (from higher maximum temperatures) are offset by the sharper signal decays that result from increasing vaporization.[37]

For ultraviolet (UV) excitation, soot indices of refraction start to become a strong function of the optical wavelength, and thus absorption and scattering coefficients are affected (mostly dependent on *k*).[95] Also, the Rayleigh limit may no longer be valid, as $\pi d_p/\lambda$ is not small for small λ. In addition, excitation of fluorescence from larger hydrocarbons, including polycyclic aromatic hydrocarbons (PAH) and of laser-generated C_2 can occur.[76,105] Thus, UV excitation of LII is usually disadvantageous. While molecular fluorescence is not typically an interference for longer wavelength excitation, strong laser excitation in the visible regime has been shown to produce significant emission in the Swan bands of C_2.[70,76,106] Vander Wal *et al.*[31,32,36,82] suggested the use of infrared excitation for weakening spectral interferences from general photochemical effects, but did not note the presence of laser-generated C_2 emission from visible excitation. Their data showed notable interferences from OH and O near 300 nm and 850 nm with 532 nm excitation (0.2 J/cm^2) and the presence of small C_2 emission with somewhat stronger excitation (0.5 J/cm^2) at 1064 nm. One might conclude that interferences in the visible spectrum are not significant for visible excitation of moderate intensity. Other research has shown that radiative emissions from C_2 begin to appear, not surprisingly, at excitation intensities that are sufficient to begin vaporizing the soot.[70,78] These interferences are one of several problems that need to be addressed when making LII measurements. Errors in LII measurements may also be produced by signal trapping from soot between the region of interest and the detector. To date, tomographic reconstruction for a steady environment is the only method for correcting for this.[52,62-66,] The soot concentrations in flames, especially turbulent ones, can be just such a troublesome environment.

2.2 Model

Typical models of the LII process most often entail an energy and mass balance for the absorption of energy from the laser with soot energy loss mechanisms. Generally, the temperature and particle size history is calculated for an individual, homogeneous, spherical primary soot particle with no relative motion compared to the surrounding atmosphere and constant physical properties. The computational model used in this research to numerically simulate the LII process also followed these guidelines.[107] Most current models, including this one, are still based on the physical analyses performed by Eckbreth[68] and Melton,[69] and simulate the energy and mass balances on a single primary soot particle. This model balances the absorption of energy from the laser with the internal energy increase of the particle and the loss mechanisms of radiation, vaporization, and conduction. The vaporization of the particle is also related to its size change, which in turn influences the energy terms.

These energy and mass balances are:

(2) $$m_p c_s \frac{dT_p}{dt} = \alpha_{\lambda,p} I \frac{\pi}{4} d_p^2$$ (change in particle stored energy = absorbed...)

$$-\frac{\Delta \ H_v(T_p)}{W_v}\frac{\pi}{2}\rho_s d_p^2\left(-\frac{d}{dt}\left(d_p\right)\right)$$ (- vaporization...)

$$- \ \pi d_p^2 \frac{k_\infty\left(T_\infty\right)}{\left(1+G\frac{\lambda_{mfp}}{d_p}\right)}\frac{\left(T_p-T_\infty\right)}{\frac{d_p}{2}}$$ (- conduction...)

$$-\pi d_p^2 \int_0^\infty \alpha_{\lambda,p}\left[M_{\lambda,b}\left(T_p\right)-\varepsilon_{\lambda,p} M_{\lambda,b}\left(T_p\right)\right] d\lambda$$ (- radiation...)

(3) $$\frac{d}{dt}\left(d_p\right) = -\frac{1}{\rho_s}\left(\frac{2W_v}{RT_p}\right)^{\frac{1}{2}} p^* e^{\frac{\left(\Delta H_v\left(T_p\right)\right)\left(T_p-T^*\right)}{\Re T_p T^*}}$$ (size change =mass loss)

where some of the above physical properties are obtained from:

(4) $$k_\infty(T) = k_0\left(\frac{T}{T_{k0}}\right)^{\frac{3}{2}}\frac{T_{k0}+S_k}{T+S_k}$$ (thermal conductivity)

(5) $$\lambda_{mfp}(T_\infty, p_\infty) = \frac{2\eta(T_\infty)\sqrt{RT_\infty}}{p_\infty}$$ (local mean free path)

(6) $$\eta(T) = \eta_0 \left(\frac{T}{T_{\eta 0}} \right)^{\frac{3}{2}} \frac{T_{\eta 0} + S_\eta}{T + S_\eta}$$ (dynamic viscosity)

(7) $$G = \frac{2(9\gamma - 5)}{\alpha\,(\gamma + 1)}$$ (geometry factor)

Note that the conduction equation employs a factor (1/(1+G•Kn)) which transitions the cooling rate between the continuum limit (Kn small) and free molecular flow (Kn large), where

(8) $$q_{cond.K} = \frac{\alpha}{2} p c_v (\gamma + 1) \Delta T \sqrt{2\pi m k T}$$ (Knudsen regime conduction)

The conduction rates are reported to be accurate for all Knudsen numbers to within 5% [3].

For a given laser intensity, including temporal profile, and ambient conditions, a simultaneous solution of the two first-order differential equations above yields a time history for both the temperature and size of a given primary particle. With these calculated histories, a simulation of the detected signal *S* from that particle can be obtained with the following integration over an arbitrary time interval (gate) of t_1 to t_2, and spectral interval, $\lambda^-_{\det}$ to $\lambda^+_{\det}$, nominally centered at $\lambda_{\det}$.

$$S(t_1,t_2,T_{p,0},d_{p,0},I_t,\lambda_{det}) = \frac{\Omega}{4\pi}\int_{t_1}^{t_2} \pi d_p^2 \int_{\lambda_{det}^-}^{\lambda_{det}^+} G_\lambda \varepsilon_{\lambda,p} e_{\lambda,b}\, d\lambda\, dt \tag{9}$$

Here, $T_{p,0}$ and $d_{p,0}$ are the initial temperature and size of the particle (previous to the laser pulse), G_λ is the response function of the detector and detection optics at a given wavelength, and Ω is the solid angle of light collected by the detection optics. Since the soot particles are typically smaller than 50 nm, the laser intensity, I_t, can be assumed constant across the spatial dimension of the particle. This signal from a single particle is useful for computationally inexpensive comparisons of the different signals generated by different excitation energies and wavelengths, or for particles of different sizes. Again, the numerical simulation calculates the temperature and particle size history of a particle exposed to a laser source having an arbitrary temporal pulse shape. In the data presented below, measured laser pulse shapes were used.

For a more realistic representation of the actual signal generated by a large number of soot particles distributed across a nonuniform laser beam or sheet, one must integrate over the observed, illuminated volume with the excitation intensity varying from point to point through this volume. To this end, the program utilized in this research, developed by Mewes,[107] was modified with the spatially-integrating routine listed in Appendix E. In agreement with the experimental strategy employed in this work, the situation corresponds to a laser intensity that is (nearly) uniform in two directions (transverse to the detection optical path) and Gaussian in the depth-of-field direction (along the detection optical path).

The index of refraction used in this and other calculations varied with the wavelength of light as described by D'Alessio *et al*. (200-500 nm)[98] and Lee and Tien (> 500 nm).[101] These values of the index of refraction yield a dependence (Bohren and Huffman[108]) of the absorptivity/emissivity on the wavelength of light as well as the primary particle diameter. This behavior and the index of refraction data are shown in Figure 3. The enthalpy of vaporization employed is a function of the particle temperature as described by Leider *et al.*[3] (see Figure 4).

Other inputs to the model include: laser energy, detection wavelength, detection bandwidth, detection integration time or gate, initial particle size and temperature, specific heat ratio (γ), and gas pressure and temperature. The detection parameters in the simulation were matched to those used in the experiment.

Beyond these known input parameters, a number of assumptions are made. In most cases, the (primary) particle size distribution is assumed to be monodisperse (again, with spherically modeled geometry). This is at least likely to be true for flames, where the distribution of particle sizes is narrow for a given spatial location.[52] The initial particle temperature is assumed to be equal to the local gas temperature. The particle properties (including the index of refraction) are assumed to remain constant from before to after laser illumination, as are the properties of the local surrounding gas, and the thermal conduction time scale inside the particle is predicted to be much smaller than the rates of heat transfer away from the particle, so the particle is always in spatial thermal equilibrium.[109] The thermal accommodation coefficient, a factor which accounts for radiation reflection off the particle surface, is fixed at 0.9 as has commonly been done in other models. The major species (> 75%, and modeled as the only species) produced by particle surface evaporation is predicted to be $C_{3,}$[3] and the vapor species are assumed to be in thermal equilibrium with the particle surface (T_v=T_p). These molecules are also assumed to react or disperse, and thus not form new particles or recombine with existing particles. Particles are assumed not to interact with each other, including radiatively. Finally, while it is known that soot particles form aggregates of primary particles, the structure of the particles is determined to be sufficiently open and chainlike that a significant deviation from the heating and cooling rates of the primary particles alone, a function of the surface area to volume ratio, is not attained. This at least appears to be valid for the absorption of incident light.[110]

The following section provides results from numerical simulations of the LII process for various conditions, some of which are important for comparison to experimental results presented later.

2.3 Model Predictions

2.3.1 Typical Model Results

The first half of the LII numerical routine produces the time histories of the particle size and temperature. The second half provides the radiated signal from a single particle at the requested wavelength(s). Examples of these LII model outputs are shown in Figure 5 for excitation with a nanosecond scale Nd:YAG (1064 nm) laser and for two spatial laser profiles: uniform (Figure 5a,b) and one-dimensionally Gaussian (Figure 5c,d). Two laser fluences levels are presented for each profile. The uniform illuminating fluences are 0.2 and 2.7 J/cm^2. For the 1-d Gaussian, they are 0.6 J/cm^2 and 6.0 J/cm^2. The illuminating fluence in this nonuniform case is defined as the total beam energy divided by the beam height (uniform direction) and beam width at the full-width half-maximum (FWHM) points (this definition is followed throughout the rest of this dissertation). The detection wavelength is 650 nm with a bandwidth of 10 nm FWHM (unless otherwise noted, this is the bandwidth used on all calculations).

Considering the uniform intensity cases (a,b), one can see that peak temperatures increases with increasing incident laser fluence. This also results in an increase in the emitted incandescence. The higher energy pulse, though, exceeds the particle's vaporization temperature (set to 3915 K in the model). The significant mass loss in this case is apparent. The dramatically smaller particle cools off rapidly from both vaporization during the high temperature period and from conduction at the later times. Thus, the signal, while very strong for a short time, dies quickly. For increasing laser fluence, a signal that is averaged over, say, 50 ns will eventually see a decrease in the total signal as the particle is vaporized very quickly. The important result is that the signal behavior versus laser fluence is nonmonotonic, increasing to a maximum value, then dropping quickly back down. For a 50 ns integration, the high fluence shown (b) is actually beyond the 'optimum' value.

To perform the Gaussian calculation, the beam is divided into 16 (equally wide) zones between the peak and 'edge' of the 'wings', defined here to be at 1.5×FWHM (at this point the Gaussian fluence profile has dropped to 0.2% of its peak value). The corresponding intensity levels are used to compute the particle response for each zone, and the reported signals are summations over the zones (and then doubled to include both halves of the symmetric beam, with a total width of 3×FWHM). The reported temperatures and particle sizes are averaged results over the complete profile, with each zone given equal weighting, i.e., they are not weighted by the relative signal produced by particles in each zone. In general, the behavior of the various parameters (Figure 5c-d) is similar to the uniform cases. An obvious difference is the lower average particle temperatures for the Gaussian profile, associated with the cold particles in the wings. More importantly, the change in signal between the two fluence levels (a factor of ten for both profiles) is much less for the Gaussian beam.

2.3.2 LII Threshold

This effect is more clearly seen in Figure 6, which show 50 ns integrated signals versus incident laser fluence for both the fundamental (1064 nm) and frequency-doubled (532 nm) outputs of a YAG laser. For low fluences, there is almost no signal, since the particles cooling exceeds the laser heating. Then near 0.1 J/cm^2, the signal rapidly increases. This rise slows, and the signals peak at ~0.9 and 1.5 J/cm^2 for the visible and infrared (IR) wavelengths, respectively. The observed displacement of the two curves from each other is the result of the difference in the absorption coefficients for soot at the two wavelengths, with the green wavelength absoprtion approximately 1.7 times that for the infrared wavelength. For the next decade of laser intensity change (and beyond), the signal decreases very slowly. This matches the results shown in Figure 5c-d, if one considers the nearly equal areas under the two signal curves for the first 50 ns. Thus beyond a certain laser fluence level, the LII ‘threshold’, the total signal is nearly constant. This holds, in general, for signal integration that is performed over any significant time gate.

The threshold behavior of the integrated LII signal is primarily associated with the nonuniform beam profile. Calculations for different parts of the beam are shown in Figure 7 for the fundamental wavelength. The Gaussian curve is also shown, which, again, is a result of summing the signals from each of the 16 beam segments. The reason for the weaker dependence on laser fluence for the Gaussian beam is associated with the range of fluences seen by the particles in the beam. Particles at any given discrete point in the beam see essentially a uniform illumination. As the overall laser intensity increases, the higher intensities in the middle of the beam induce particle vaporization first. The region of strongest signals shifts from the center to the wings as particles are rapidly vaporized by the stronger intensities. However, the total signal is integrated over the entire beam width. At lower intensities, very little signal can come from the wings, which are hardly heated. At high intensities, less signal is contributed by the middle of the beam, where particles are almost totally vaporized. The effects of increasing vaporization (reduced mass and faster signal decay) and an increasing volume of particles that reach vaporization temperatures (strong emission) are offsetting.

2.3.3 Temperature and Particle Size Sensitivity

The 50 ns detection gate was not chosen randomly. The particle temperatures, and therefore the generated signal (per soot mass) can be sensitive to the initial particle size and to the local gas temperature. For measurements of local soot concentrations (or volume fraction f_v), it is desirable that this sensitivity to the particle size and local gas temperature be minimized. This can be achieved by keeping the detection gate prompt and relatively short, during the high temperature period of the heated particle's history.

The rationale behind this is illustrated in Figure 8, which shows examples of the instantaneous error in f_v incurred at different times due to a variation in particle size or gas temperature. The error is the fractional change between the instantaneous LII signal per volume fraction of soot at the nominal conditions (20 nm particle, 1700 K gas) and the LII signal at the other conditions. For both parameter changes, the relative errors increase for detection delays after the laser pulse and result from changes in particle cooling rates. The effect that the local gas temperature has on the conductive cooling rate to the local gas is obvious. During portions of the signal that are dominated by conductive cooling, the heat transfer rate to the gas is set by the difference between the particle and gas temperature.

The reason for the particle size effect may be less apparent. The major cooling mechanisms of vaporization and conduction (in the continuum limit) are expected to be surface effects and are, thus, modeled as dependent on the instantaneous surface area. The cooling rate for the whole particle thus depends on the surface area to volume (mass) ratio of the particle, or $\sim 1/d = d^2/d^3$. Thus, the model indicates that particles of different sizes will reach different maximum temperatures and cool down at different rates. Larger particles reach higher temperatures and cool down more slowly. This, of course, yields larger integrated signals as well. This effect is seen in the model results shown in Figure 9, which displays the 50 ns integrated signals per unit soot volume for two visible detection wavelengths against particle size for an IR YAG pulse of 1.6 J/cm^2. Due to the blackbody-like nature of the emitted signals (discussed below), the shorter wavelengths are more sensitive to this effect.

This behavior with particle size is in agreement with the analytical calculations of Melton,[69] which showed that in the limit of negligible conduction and radiative losses, for a nearly constant particle temperature (near the vaporization temperature), and for low mass loss, the LII signal would scale as d^n with $n=3+0.154/\lambda_{\text{detection}}$. This expression has usually been interpreted as indicating that longer detection wavelengths are preferable for accurate volume fraction ($\propto d^3$) measurements. This would also imply that the LII signal would underpredict f_v for small particles if the detection system were calibrated in a flame or region with large soot particles.

2.3.4 Primary Particle Size Measurements

The prediction that larger particles should cool down more slowly than smaller ones has been investigated for making measurements of (primary) particle size.[38,85,87,91] The signal emitted during the post-vaporization period is a function of the size and temperature of the particle just after the vaporization period, the surrounding gas temperature, and the overall conductive cooling rate. These particle conditions after the laser pulse are, in turn, a function of the original particle diameter. An example of the simulated signals from different sizes of particles for a given laser fluence and surrounding gas temperature is plotted in Figure 10. The slower signal decay rate of the larger particles is apparent. Note that signals are normalized at a time soon after the laser pulse to isolate the dependence of the decay rate on the mechanism of conductive cooling. However, the lower particle temperatures at longer times will yield much weaker signals and the cooling should be more sensitive to changes in local gas temperature. Theoretically, the accuracy of particle size measurements by this technique would be limited only by the resolution of the detector and the uncertainty in the local gas temperature.

Alternatively, it has been suggested[86] that primary particle size could be monitored by a pyrometric technique, more specifically by determining the maximum temperatures reached by particles of different sizes in terms of the relative strength of signals at two different wavelengths. Again, the higher heating to cooling rate ratio ($\sim d^3/\sim d^2 = \sim d$) of the larger particles should yield higher temperatures. This is also essentially the mechanism behind the larger than volumetric scaling of the LII signal predicted by Melton.[69] In terms of blackbody radiation, the larger particles would not only emit more strongly than the smaller particles, but would have their radiation shifted toward the blue (shorter wavelengths).

This blackbody behavior is illustrated in Figure 11, which also shows how a ratio of signals at a long and short wavelength (defined here as S_λ) would respond with the blackbody temperature. Ratio curves are depicted for several of the detection wavelengths used in this research (long/short wavelengths). In all cases, S_λ monotonically decreases as temperature increases. Similar to the blackbody curves, the red/blue ratio (e.g., $S_{650/400}$) of integrated signals at two wavelengths from the LII simulation also yields a monotonically decreasing behavior with increasing particle size, as the larger particles are calculated to reach higher temperatures. This is predicted to occur for most all experimental parameters. Recall from the previous Section that the model actually calculates the emission from a blackbody and modifies the signal by the spectral emissivity of the soot particle at the given wavelength.

Figure 12 displays a calculation of the ratios of signals detected at 650 and 400 nm that would be generated by an unfocused 200 mJ (1.6 J/cm^2) IR pulse in a 300 K environment (exhaust). Figure 13 shows those, which would be generated by a focused 10 mJ (1.2 J/cm^2) pulse in a 1700 K environment (flame). Both of these are experimental conditions that are used in this research. Along with this information are plotted the blackbody temperatures (see Figure 11) that these ratios represent. This is not, in effect, the average temperature across the span of the laser beam. The signals, and therefore the signal ratios, are weighted toward the hotter particles in the laser energy distribution. For the particle size range of interest, the monotonically decreasing behavior of the signal ratio is evident in both examples. The results also indicate that the higher energy pulse generates higher average particle temperatures (~4300-5000 K), while the other case reaches perhaps 4600 K. Around 100 nm, it is also apparent that the curve begins to flatten out. This is due to the particle size beginning to exceed the Rayleigh limit for the emitting wavelength of 400 nm before 650 nm.

Eventually, for even larger sizes, the efficiency of absorbing the illuminating wavelength of 1064 nm should also decline and the particles will not attain temperatures as great as the smaller ones (at least on a volume-average basis; Larger particles will progress toward surface absorption).

For an excitation energy of 0.4 J/cm^2 at 532 nm (or 0.8 J/cm^2 at 1064 nm), a 30% change in the signal ratio is demonstrated for a particle diameter change from 10 to 40 nm. For this same laser fluence, Mewes and Seitzman[86] obtained the same numbers and calculated that primary particle diameters typical of those found in flames could be determined by the pyrometric technique above to an accuracy better than ±2 nm. Also, while they calculated the optimum excitation energy for spectral ratio measurements to be on the order of 0.4 J/cm^2, calculations made here with the same model show that the optimum (yielding ~30% change in signal ratio) is independent of fluence above threshold. Figure 14 shows the behavior of the spectral signal ratio at fluences near and above threshold. For a wide range of fluences, the relative magnitude for different sizes of particles remains essentially the same. Note also that a variation of 2 in fluence represents a change in interpreted particle size of about 5 nm.

The independence of the relative S_λ magnitudes can be explained by the effects of an insensitivity of S_λ to temperature at high temperatures (recall Figure 11) and the sensitivity of vaporization to particle size at high fluences (temperatures), as follows. All particles will heat up at nominally the same rate. The different specific surface areas of the particles will cause larger particles to reach higher temperatures and vaporize more quickly than smaller ones. A greater rate of energy input will increase this discrepancy. The relative change in diameter from vaporization is also greater for the larger particles. While the temperature difference between large and small particles increases for higher fluence, vaporization causes the particle sizes to get closer to each other in size. Also, at higher temperatures, the spectral signal ratio becomes less sensitive to changes in temperature (i.e., different particle sizes).

For increasing delay of the detection gate, however, the sensitivity to particle size is increased. This is because the spectral signal ratio is more sensitive at the lower temperatures and because the superior cooling of the smaller particles has increased the temperature difference from the large particles. However, the improved sensitivity at longer delays is coupled with an unwanted increased sensitivity to local gas temperature variations. The model indicates an error of ~10% for a 20 nm particle and temperature variations of ± 200 K.

CHAPTER III

EXPERIMENTAL PROCEDURE

This Chapter describes the various experimental conditions and apparatus used in this research. It includes complete descriptions of two flows containing carbonaceous aerosols. It also describes the laser and optical arrangements that were used to radiatively heat the carbonaceous (soot) particles. Finally, the various detectors and detection optics and arrangements are detailed.

3.1 Soot Flowfields

In order to characterize the LII technique, two dissimilar sooty environments are investigated. The first environment is a reacting flow in which soot was formed via physiochemical processes. The second flow involves no chemical reactions; rather, the carbonaceous aerosol is produced by artificial means. From a practical point of view, the reacting flow is more like a combustor environment, while the nonreacting flow more closely resembles an engine exhaust flow.

3.1.1 Diffusion Flame

The reacting flow is a well-calibrated combustion environment; a simple, laminar, axisymmetric diffusion flame that has been used extensively in a number of soot studies (see Section 1.2.3). Figure 15 shows the design of the burner that generates this flame. Ethylene (C_2H_4) was chosen as the fuel for its high sooting tendency. The fuel flows through a central tube of 11.1 mm i.d., surrounded by a concentric flow of air contained in a 101.6 mm i.d. honeycombed outer tube. The central tube is 12 inches in length, sufficiently long to produce a fully-developed laminar pipe flow for lower fuel flowrates. Preceding the flow-straightening honeycomb section, uniform distribution of the air flow (which enters the burner through two ports) is achieved by directing the flow through a compartment bounded by wire mesh and filled with 3 mm glass beads. The supply air is also dried and filtered before reaching the burner. The burner itself is mounted on a heavy milling machine base with three-dimensional positioning with an accuracy of 0.001 inches.

One modification to the original burner design[49] is the omission of the optically accessible chimney. In most cases, the flame is open except for the co-flow of air and a 15 cm dia. vent located 30 cm above the flame tip. Some data were acquired with a small (11 cm high) chimney, which can provide better flame stability. The chimney is made from thin steel shim stock, with a diameter that matches the outer diameter of the burner. Holes were cut in the chimney just sufficiently large to allow passage of the laser and signal collection from the full collection angle defined by the first lens of the detection setup (see Section 3.3.1). In both cases, the exhaust vent, a flexible aluminum tube, is present. When the chimney is used, however, the flame position and stability show sensitivity to both the alignment of the vent with the chimney and the separation distance between the two. For measurements at different heights in the flame, this shim cylinder had to slide up or down the burner as the burner was moved to maintain the relative position of the ports in the chimney to the laser and detector. Thus, the height of this chimney with respect to the burner varied. To avoid this, another chimney was constructed with vertical slits as tall as the flame, rather than circular holes. The stability of the flame was impaired by the large nonuniform draft this created, so thin glass windows were added. Some laser reflection issues were discovered with these in place, though, and they could not withstand much energy in the focused laser beam. Thus, in general, the addition of the chimney was not advantageous and was usually omitted.

The flowrates for fuel and air through the burner were 3.85 cm^3/s and 713 cm^3/s, respectively. The two flowrates were measured by calibrated rotameters (see Appendix A for details on the calibrations). These flowrates were chosen to match conditions from previous research.[51] This provides a nonsmoking, bright yellow flame that matches previous measurements of observable luminescence to 88 mm in height. Figure 16 displays an LII image of the flame produced by a 0.7 J/cm^2 (532 nm) laser sheet that is about 10 cm tall. The signal is detected at 430 nm and integrated over a time interval of 30 ns. Cross-sectional intensity profiles are also provided for three heights in the flame At the burner exit, the velocities of the air flow and fuel flow are quite different, so one might expect vortices to form. However, this is a reacting flow and, before any notable shear effects can occur, buoyancy dominates, accelerating the flow in the center. Figure

17 displays the axial and radial velocity profiles as measured by Santoro *et al.*[51] via laser velocimetry.

The darker regions of Figure 16 show the areas of higher soot concentration and the region of maximum soot concentration inside the flamefront is clearly evident. All the pointwise flame measurements that are presented in the rest of this thesis are from along this region of maximum soot concentration. Two-dimensional signals are also produced, but even these are processed to yield the information at these peak signal (peak soot concentration zones). Figure 18 shows the spatial location of this 'path' of maximum soot volume fraction (f_v) This data is generated by finding the positions of maximum LII signal, but is identical to the maximum soot locations determined by the extinction measurements of Santoro, *et al.*[51] These data (contour format) are displayed in Figure 19. The exact extinction measurements from this work along the path of maximum soot f_v are recorded by Quay *et al*[79] (but originate in earlier work[49,51]) and are shown along with the (image) extinction measurements of Greenberg and Ku[62] in Figure 20. This data provides the basis for comparison of concentration measurements made by LII and extinction in the diffusion flame.

It will be noted here that the extinction measurements which are used as the reference in this work,[79] were acquired with a spatial resolution of 200 μm from a focused, continuous, chopped beam. This might cause concern over the fairness of a comparison to signals obtained with 100 μm resolution (most common camera resolution presented below). The deviations of the LII signals from the extinction data could simply be due to better resolving of the sharp peaks of the soot concentration profiles at the heights with the most soot (sharpest peaks). However, the full-field extinction measurements of Greenberg and Ku[62] were acquired with 100 μm resolution and agree with those from the other reference. LII data are acquired with both the camera and PMT at different spatial resolutions. Significant deviations were not noted for resolutions up to 500 μm.

A number of other flame variables have also been measured by previous researchers. For example, local gas temperatures as a function of height and radial location have been measured by a rapid insertion technique with a type S thermocouple of 200 μm bead diameter.[51] This data is displayed in Figure 21. A few investigations which also studied this flame made direct measurements of the particle sizes and structure through the flame via either optical techniques or sampling and electron microscopy. Some of these focused on profiles across the flame or up the centerline[29,33,49] Others, with information more pertinent to this investigation, provided the variation of primary particle size, primary particle number density, and aggregate particle number density along the path of maximum soot volume fraction, just inside the flamefront.. Primary particle size measurements along this path are shown in Figure 22 as a function of height above the burner. These data[39] were acquired from thermophoretic sampling and TEM observations, and thus may exhibit systematic errors associated with intrusive sampling in the flame. Still, the overall trend in particle size is as expected. Specifically, there is primary particle growth early in the flame and it is followed by a size decrease as the soot is oxidized. Primary and aggregate particle number densities and the (resultant) primary particles per aggregate are shown in Figure 23. These data, from Puri *et al.*[55] and earlier supporting work,[39,51,52] are obtained from measurements of the scattering cross-section (Q_{vv}) and the extinction coefficient (k_{ext}) at the various points (e.g., $N_a \propto k_{ext}/(D_{30})^3 \propto k_{ext}/(D_{63})^3 \propto (k_{ext})^2/Q_{vv}$).

3.1.2 Soot Generator

The second flowfield employed provides the combination of a controlled carbon aerosol field and simulation of an engine exhaust environment. The flow is attained with the use of a soot generator, which provides an aerosol of carbon black particles (see Figure 24). The flow at the output of the generator is nonreacting, has no potential interferences associated with the presence of larger hydrocarbons, and is dilute enough to avoid signal trapping. It is also designed to be nearly uniform in temperature, concentration, and (as far as possible) particle size.

The aerosol is obtained in the following manner. A dispersion of carbon black in distilled water (5.6 g C / L H_2O) is prepared with 1 mL gum arabic added per liter of water as an emulsifier. This solution is atomized with the use of an aspirator/impingement type nebulizer (Inspiron), providing a carbon/water fog which is then diluted by a secondary air flow. The design of this venturi-style aspirator is depicted in Figure 25. Phase-Doppler particle analyzer (Aerometrics, model RCV-2216) measurements of the nebulizer droplet diameter yielded an average value for D_{10}, D_{20}, and D_{30} (diameter-, area-, and volume-weighted average) of 4.3, 4.8, and 5.4 μm, respectively, with a 2 μm FWHM for the measured size distribution (see Figure 26). The solution is aspirated with air at a constant flow rate of 9.2 L/min, yielding a solution flow rate of 0.34 mL/min. The meters regulating the two air flows are detailed in Appendix A.

The carbon black material (Cabot 800) is composed of approximately 20 nm particles with fairly simple aggregate structure (aggregate diameter about 3 to 3.5 times the primary particle diameter).[113] This material is essentially soot generated in a carefully controlled pyrolytic combustion process by subjecting a fuel like lamp oil or heavy residual oil feedstock (the actual fuel is proprietary) to extremely high temperatures. These carbon black particles are similar, though not identical, to the soot encountered in the combustion region of a gaseous hydrocarbon flame such as the diffusion flame described above. Measurements comparing the properties of carbon blacks and soot produced from common combustion processes have generally found the morphology (shape and geometry) and microstructure to be the same.[27,28] Typical combustion-generated soot may have a higher content of adsorbed organic hydrocarbons than do carbon blacks, which have almost none. However, in the very hot zone of maximum soot f_v in the flame, one might expect very little hydrocarbon content in the soot particles.

The aerosol-containing flow and the secondary air flow are separately directed into an aluminum drying cylinder, 3 in. diameter and 24 in. long, held vertically. To evaporate the water droplets, the cylinder's temperature is raised with heating tape to a nominal value of 100 ºC. The resulting aerosol of dry carbon particles, air, and water vapor exits the top of the drying cylinder out a 12 inch long, 5/8 inch diameter aluminum tube. This produces a soot-laden jet, approximately 15 mm in diameter. The gas temperature at the exhaust is monitored by a type K thermocouple (1 mm bead). The exhaust temperature was generally maintained between 70 and 130 ºC. The exit temperature of the jet could also be varied by preheating the secondary air flow, diverting some fraction of it through a coiled-filament heater (Sylvania - Process Heat). The maximum exit temperature obtained in this arrangement was 300 ºC. All of the measurements in the soot generator, unless otherwise indicated, are made approximately 15 mm above the jet exit.

Small variations in the carbon aerosol concentration are obtained by changing the secondary air flow rate, for a given concentration of the liquid carbon/water dispersion. This flow rate varied from 315 to 1110 cm^3/s, which produces a variation in the overall aerosol concentration of roughly 3 times. Greater variations in the carbon aerosol concentration are achieved by diluting the liquid carbon/water dispersion. This, however, also changes the size of the carbon particles produced. The size changes because the amount of carbon per water droplet varies with the concentration of the liquid dispersion (while the number of droplets remains constant). As each carbon-laden water droplet evaporates, it is hypothesized that surface tension and electrostatic forces tend to cause all the small (20 -60 nm) carbon black particles to bunch and form a single, nominally spherical, particle by the time the water is evaporated (see Figure 27).[*] Thus the particle size at the generator exit will theoretically vary with the cube root of the concentration of the carbon solution. The greatest dilution of the nominal carbon/water solution was 6400. Thus, the aerosol concentrations employed in this work ranged from 2 parts per

---

[*] See Chapter 5 for experimental validation.

trillion (ppt) (4 $\mu g/m^3$) to 30 parts per billion (ppb) (70 mg/m^3). The calculated mean particle size ($d_{p,10}$) thus varied from 32 to 590 nm as shown in Figure 28.

3.2 Laser Excitation

A few different pulsed laser beams were used to characterize the LII signal, and provided variations in the laser pulse length and laser wavelength. Most of the LII signals analyzed in this research are produced by the fundamental (1064 nm) or frequency-doubled (532 nm) output of a Nd:YAG laser, though some information was obtained with the use of a tunable dye laser.

3.2.1 Dye Laser

The earliest measurements in this research were produced by the output from a linear flashlamp-pumped dye laser (590 nm, Rhodamine 590 dye) of about 1.6 μs duration (FWHM). The 1 cm diameter laser beam was focused into the flame through a 50.8 mm diameter, 200 mm focal length, spherical lens to a waist of about 1.2 mm diameter (~0.5 mm FWHM) 0.8 mm^2 (≈ 1 mm dia.). Laser energies varied from 10 to 80 mJ (5 to 40 J/cm^2) throughout all the experiments due to dye lifetime, but typically varied by less than 5% over the course of any given experiment (4000-10,000 shots). A tuner consisting of three prisms spectrally filtered the output beam to a bandwidth of approximately 5 nm FWHM and allowed for spectral tuning of the laser wavelength.

The dye laser results were instrumental in deducing some of the points visited in Appendix D, but are otherwise not reported here. One of the motivations for using a long-pulse laser, rather than the more commonly employed nanosecond scale lasers, is the signal strength. The model predicts that for an optimal fluence for each laser, the longer laser pulse will yield a larger signal (see Figure 29). This holds if both signals are integrated over their respective pulse durations, or if both are integrated over the duration of the 200 times longer, dye laser, pulse. The superiority of the longer pulse follows from the fact that the LII signal is limited by the amount of time that the particle exists at high temperatures, assuming both lasers raise the particle (near) to its vaporization temperature. For the short-duration laser pulse, the particle does not stay at elevated temperatures as long. It is not fair to compare the signals generated by similar pulse energies or fluences. While the short pulse laser will have a higher intensity for a given pulse energy (same energy in less time), the energy above the threshold value primarily succeeds in vaporizing more of the particle mass and reducing the signal. Thus, for a fixed spatial resolution, the longer pulse laser can achieve a higher signal-to-noise ratio. Some evidence also suggests that the dye laser may produce less interference from C_2. This would also be a characteristic worth taking advantage of. Future research may be warranted for investigating this predicted advantage.

3.2.2 Nd:YAG Laser

The vast majority of this research employed the 8 ns, high power ND:YAG laser and the results presented are from those experiments. The Nd:YAG laser (Continuum

Surelite I-10) was operated at 10 Hz, with maximum pulse energies of 450 mJ and 200 mJ for the infrared (IR) (1064 nm) and visible (green) (532 nm) wavelengths, respectively. For measurements in the flame, the 8 mm diameter beam (measured by a burn mark method and Rayleigh scattering) was focused by a 90 mm diameter, 500 mm focal length fused-silica cylindrical lens to a waist of about 0.2 mm (FWHM). Regions larger than the beam height can be illuminated by adding a second cylindrical lens (f=5mm) in the beam path with a focal direction perpendicular to the first. Measurements in the soot generator generally employed an unfocused beam.

The spatial distributions of the laser energy, as determined by monitoring the pulse energy while moving a knife-edge across the beam, are described in Appendix B for the various illuminating conditions. The full-width half-maximum (FWHM) measurement of the beam size is 2.45 and 3.0 mm for the unfocused green and infrared cases, respectively, and 190 µm and 210 µm for the focused cases. This definition of the beam width is used for obtaining the average intensity across the beam as it is the most commonly used definition of beam width. The spectral linewidth of the output light is 1 cm^{-1} (~0.1 nm) at the fundamental YAG wavelength and the duration of the fundamental laser pulse is 8 ns FWHM. The temporal profile of the pulse is also shown in Appendix B.

Laser intensity is varied by employing the combination of a polarizing beam splitter preceded by a half waveplate. This has very little effect on the beam shape. Rotating the waveplate rotates the beam polarization. With the prism remaining fixed, the fraction of transmitted and reflected energies is varied. The energy is measured in a time-averaged manner, i.e., in Watts at the 10-Hz rate, by a pyroelectric joulemeter/powermeter (see Appendix B) (energy/shot = average power × repetition rate). Most results reported here are for average energy fluences above threshold, or greater than 0.1 J/cm^2, though LII signals for the full range of intensities are analyzed. The repeatability of pulse-to-pulse laser energy and temporal profile were generally good, with a worse case variation of ± 7%.

The move to the YAG laser was made early in the research for a number of reasons. The higher power and improved coherence of the YAG laser were estimated to be more than sufficient to attain fluence values well above threshold, even for a significantly expanded beam. The improved focus of the YAG laser also increases the spatial resolution of the measurements. The YAG laser also provides a more Gaussian spatial profile and a more temporally stable (shot-to-shot repeatable) output intensity. For particle sizing and interpretation of the LII signal, the fast decay of the nanosecond scale laser pulse permits observation of the LII signal decay rates based solely on conductive cooling, which occurs on a much longer time scale. The YAG laser output is in the infrared (IR) at 1064 nm, but can easily be frequency-doubled into the visible region (532 nm). As suggested by Vander Wal,[82] employing the infrared pulse of the Nd:YAG may be preferable for the total rejection of elastic scattering. Also, the visible (or near-IR) LII signal can be detected by commonly used detectors that do not respond to the elastically scattered IR radiation.

3.3 Signal Detection

The signal of interest is the emission generated by laser-heated soot particles. Thus, the laser beam and the focal point of the employed detector are aligned to intersect at the soot-containing region of interest. The objective is to observe the soot particles not only at a defined spatial location, but under known illuminating conditions and at the precise time of interest. Depending on the requirements for spatial resolution and illuminating intensity, the laser beam size (height and width) is modified with the lenses mentioned above.

The signal is recorded in one of two ways. In the first mode, a light detector with one (relatively) large light collecting and integrating surface is employed, in this case a photomultiplier tube (PMT). The light from the signal-emitting volume is imaged on this surface (not necessarily in focus). If the imaged volume is made small enough (say, to the desired spatial resolution of the soot field), this can be called ‘point’ detection. In the second method, a two dimensional array of smaller light detectors (in this research, an intensified charge-coupled device (ICCD) camera) has the radiated light imaged (in focus) onto the array. This is designated as ‘image’ detection as the detector produces a two-dimensional picture of point signals. The size of the array is the effective image aperture. The size of the individual detectors (‘pixels’) is the effective point aperture, or smallest resolvable area. Where parameters in a flow have strong spatial gradients, as in the flame, it is important to have good spatial resolution and to know what region of space is being observed.

3.3.1 Point Detection

Achieving the spatial resolution required by the flame is realized in two procedures. First, the 500 mm focal length cylindrical lens is employed to focus the beam into the region of interest. Second, a rectangular aperture (adjustable in both the vertical and horizontal directions) is placed in the optical path of the imaged light. This aperture limits the height of the observed region to only the middle ~2 mm or less (vertically) of the laser sheet. Only this much of the beam is included in the collection volume in order to keep both the soot concentration and the laser intensity nearly constant across the imaged region. Similarly, the imaged dimension in the horizontal direction is limited to between 0.2 and 4.0 mm. Soot concentrations in the flame change more rapidly in this direction (recall Figures 14 and 17). These aperture measurements were more easily set by placing the aperture at an image location of 2x magnification.

Pointwise LII signals are recorded at a right angle to the laser beam by a photomultiplier tube (PMT) (Hamamatsu R928B) behind the collection optics of 150 mm and 50 mm spherical lenses (50.8 mm dia.), optical filters, and the rectangular aperture (see Figure 30) The pointwise signals were recorded in one of two ways. For spectrally broadband detection, the detector is positioned directly behind the collection optics. Finer spectral resolution is achieved by recording signals at the output slit of a half-meter Jarrell Ash monochromator. Signals detected in this manner have the input and output slits fully open, providing a bandpass of 3.7 nm FWHM and an image width of 0.4 mm or with the output slit at a smaller setting which provides a bandpass of 0.7 nm (see Appendix C). The first lens (f = 150 mm) of the collection optics is positioned 22.5 cm from the region of interest, providing a magnification of 2 at the rectangular aperture and thus a relative aperture or f-number (*f*#) of 4.4, or a 0.11 numerical aperture (N.A.). Both *f*# and N.A. are measures of collection solid angle, with $N.A._{max}=1$ for transmission through air.[112] Employing the monochromator, however, limits the amount of light reaching the detector to an *f*# of 12. To prevent extra room light from reaching the PMT, the detection optics were covered by a light tight box from the first lens to the PMT or monochromator input (see Appendix D, Figure D3).

The employed optical filters include neutral density filters to keep the PMT in its linear operating range. Also, the wavelength selectivity of the monochromator was enhanced with spectral filters to prevent interference from signals at other wavelengths, in particular, elastic scattering. These filters included Schott colored glass filters (mostly high-pass edge filters: RG630 (3 mm), OG570 (3 mm), OG550 (2 mm), BG-18 (1mm), and BG3 (1 mm)), bandpass filters (650, 550, and 430 nm (10 nm FWHM), 514.5 nm (8 nm FWHM) and 460 nm (3 nm FWHM)), a holographic notch filter at 532 nm, and a fused-silica dichroic laser mirror (532 nm, 45°). Calibrations for the spectral transmissivities of these filters are described in Appendix C. In a similar manner, the spectral response of the monochromator and PMT combination were determined and is also detailed in Appendix C.

The output signal (current) from the PMT was collected with a digital oscilloscope (Tektronix TDS350) or a boxcar averager (SRS SR250). Both devices have the capability of averaging the signal on a shot-to-shot basis and integrating the signal at a defined time and over a defined time interval (gate). The scope has the further capability of recording the time history of the signal. Typically, data were collected in a ‘prompt’ manner during the laser pulse (with a 30-50 ns gate), though other detection timing was also investigated. Background signals of the flame luminescence and room scattering (no flame) were also recorded.

The movement of the flame is somewhat unpredictable. Environmental conditions and the position of the exhaust inlet can even cause the flame to bend one way or the other. Employing the chimney is possible for measurements made with the PMT and monochromator. This can improve the stability of the flame, but small movements (leaning side to side) as large as the region of interest are unavoidable. Most measurements were acquired with the boxcar averager (triggered by the laser) and recorded to computer. The 10 Hz rate of the laser and the slight movements of the flame yielded a signal trace with a number of peak values that attained the same nominal magnitude. The LII data points represent averages over 10 to 20 of these peaks. The signals are detected at different wavelengths are acquired by tuning the monochromator to those wavelengths. Appropriate supplemental spectral filters are also employed for visible excitation. Signals produced by the infrared (IR) pulse employed only the monochromator for spectral selection.

For quantitative measurements, it is important to know when the magnitude of the PMT signal is linearly proportional to the amount of light reaching it. This range of linearity is determined by having the detector observe a light source and then varying the amount of light reaching the detector in a known fashion. This is achieved by adding neutral density (ND) filters, singly or in combination, into the optical path. The linearity of the PMT is shown in Figure 31 for a Nd:YAG-induced LII signal. The top plot shows that the linearity of the PMT output (when operated at 900 V) versus the incident signal is similar for both signals acquired at the peak of the LII pulse, and for signals averaged over the first 50 ns of the signal. In both cases, the voltages were recorded on the oscilloscope and averaged over 512 laser pulses.[*] The linear range of the PMT can be extended by varying the supply voltage to the PMT, as seen in the bottom plot of Figure 31. A lower operating voltage (700 V) yields a greater linear dynamic range of input signals at the expense of gain/sensitivity (slope).

Measurements in the exhaust of the soot generator were, of course, not troubled by background flame radiation. However, the optical setup for these low concentrations was made as sensitive as possible so background room light had to be minimized. The sensitivity for this setup was enhanced by a few modifications to the arrangement above. As the 'exhaust' flow was essentially uniform, the beam was left unfocused to increase the size of the illuminated region. The detected volume was increased not only by the larger beam width, but by increasing the aperture width to image an 4 mm wide area of the flow. The image height was 2 mm. An even greater signal increase was obtained by increasing the detected spectral bandwidth. The region of interest was imaged directly onto the PMT with filters providing the spectral selection. Long wavelengths were acquired with only the OG570 filter present, or with the OG550 added. This provided a

---

[*] Care should be taken when using the averaging function of the oscilloscope. While the average signal may be within the scope's measurement range (slightly greater than screen display), instantaneous signals may be clipped, producing a lower than true average, and can lead to the determination of a lower saturation point.

bandwidth of ~140 nm centered on 650 nm. Short wavelengths were detected through the combination of the BG3 and BG18 filters, which provided a bandwidth of ~100 nm centered on 400 nm.

3.3.2 Image Detection

Data were also collected with similar temporal and spatial gates using a cooled, intensified CCD camera (Princeton Instruments ICCD-576-S / RB-E, 576 × 384 pixels). With a 55 mm camera lens (Nikon Micro-Nikkor *f*2.8) positioned about 21 cm from the region of interest, pixel spatial resolution was 98 × 98 μm. Images were collected both at a right angle to the laser beam (as shown in Figure 30) or at a ~50° angle (camera closer to laser). Though the images acquired at an angle were slightly narrower and the image could be expected to be not uniformly in focus left-to-right, this was not really an issue.

Most data were acquired with the beam height maintained at its original diameter and data were collected in an essentially pointwise fashion. The beam was normally focused in the direction of the optical detection path. As the flame is traversed through the beam, the intensity remains fixed at the points in space that the camera is observing. Thus, on finding the maximum signal in the middle of the beam, the camera is employed essentially as a point detector, like the PMT. Nonetheless, the images are very useful for easily pinpointing the desired region of interest (maximum soot zone) and as a constant monitor on alignment and beam shape. This method is preferable to monitoring the local laser intensity across a large sheet which illuminates the full flame.

For comparison to the extinction data above, the region of interest remained along the path of maximum soot, usually at the side of the flame nearest the laser, as was true with the PMT. Figure 32 shows typical images generated by passing the focused beam through the middle of the flame at heights of 10, 25, 40, and 55 mm HAB. As was done in the point measurement setup, the signals were averaged (integrated) over the middle of the beam for a number of pixels equivalent to 2 mm or less (≤ 20). In the horizontal direction, the signals were either integrated over 0.5 mm or so (~5 pixels) or the peak signal was recorded. The camera is appreciated for its ability to instantaneously identify the position of the flame and the region of interest. However, sufficient rejection of scattered light, for prompt detection and visible illumination, can be challenging to achieve. The spectral filters above were again utilized to isolate signals at certain wavelengths. The holographic notch filter was generally employed for 532 nm illumination. Some imaging of the full flame was performed. This required spreading the beam into a sheet of at least 90 mm height. This was achieved by adding the second cylindrical lens (*f*=5mm) with a focal direction perpendicular to the first.

Some images were acquired with a second ICCD camera , provided on a temporary basis by Princeton Instruments. This camera will be referred to as camera 2, while the previous one is camera 1.This imager produced less noise than the one used for most of this research. Though the spectral response curve of this second camera is not known, it was used for some of the measurements presented here, including instantaneous LII imaging at two detection wavelengths (one per camera).

The linearity of the ICCD camera was checked in a similar manner as was the PMT, but with an image of fluorescing acetone vapor, induced by a pulsed KrF laser (~80 ns), as the source. The integration time was 100 ns. For a particular gain setting, the camera has a fairly strong sensitivity and a dynamic range of about 10. From a gain of 1.5 to 9.5, the camera yields a dynamic range of over 200, with good linearity for all settings (see Figure 33). Again, background signals of the flame luminescence and room scattering (no flame) were recorded. Few attempts were made to measure signals from the soot generator with the ICCD camera due to its lower sensitivity and the low soot concentrations presented by this flow.

3.3.3 Temperatures from Signal Ratios

As detailed in Section 2.3, the shape of the spectral emittance curve, and thus the ratios of the signals detected at two different wavelengths, reveals information concerning the temperature of the observed soot particles. The absolute magnitude of the individual signals does not need to be calibrated. As long as the relative responses of the detector and filters are known for the two detection bands, the spectral ratio can be 'absolutely' measured. Then that ratio can be converted to an equivalent blackbody spectral ratio by dividing by the ratio of the emissivities of the (soot) particle at the two detection wavelengths. This ratio provides a measure of the nominal temperature (averaged over all particles that emit, but weighted by their relative luminosity) as predicted by Figure 11. This procedure is equivalent to comparing the measured signal ratios that have not been corrected for spectral emissivites to the ratio of blackbody signals that have been corrected for soot spectral emissivities, what might be called an equivalent ‘soot’ body. Both methods yield the same particle temperature.

As a method of validating this procedure for converting observed signal ratios to particle temperatures, measurements were made of the steady, luminosity from the diffusion flame. Figure 34 shows the ratio of signals detected at 650 nm and 460 nm along the path of maximum soot concentration. The data are corrected for the spectral response functions of the filter(s) and monochromator/PMT, and calculated soot emissivities[108]. These values are compared to the spectral ratios (650nm/460nm) that would be produced by a blackbody at the local gas temperature as it varies either: 1) along the maximum soot pathline or 2) along the maximum temperature pathline. These temperatures are obtained from the thermocouple measurements of Santoro *et al.*[51] (see Figure 21). Note that if the present measurements were made at the center of the flame, the signal would be integrated across the entire flame and thus, the observed temperature would be lower than the temperature of the soot near the reaction zone. However the measured signal ratios are determined at the edge of the flame, so the detector should see only the particles in the dense soot region. It is not known how much the particle temperature varies through the detection volume (which is a very small region), but the local gas temperature is not expected to vary much, so the expectation is the same for the particles. Again, as described in Chapter II, due to the strong sensitivity of the emitted signal to particle temperature, the observed temperature should be weighted toward the hottest particles.

The measured signal ratios (or particle temperatures) are in reasonable agreement with those predicted from the thermocouple measurements. The luminosity measurements indicate that temperatures are about 1650 K through the lower flame and decrease from there very slightly to near 1550 K at 55 mm HAB. At higher points in the flame, a discrepancy on the order of 100 K exists between the thermocouple measurements and the luminous emission measurements. This is fairly close considering the 10% uncertainty in the luminous signal ratio measurements. For a 650 nm / 430 nm ratio, this translates to an uncertainty in temperature of ± 100 K to ±400 K from 3000 K to 6000 K signals. The thermocouple measurements are also somewhat uncertain, as mentioned in the reference, due to a number of possible error sources such as conduction along the thermocouple wire.

As mentioned earlier, most of the flame data were recorded from the region of maximum soot volume fraction (f_v), and therefore strongest signals, just inside the flamefront. Detection at the edge of the flame nearest the laser assures minimal laser absorption by soot between the laser and the region of interest and that the full beam width encounters the soot peak. Detection at the edge of the flame nearest the detector assures minimal signal trapping by soot between this region and the detector. Data were recorded with each of these arrangements.

CHAPTER IV

DIFFUSION FLAME MEASUREMENTS

The results presented here are from measurements performed in the laminar, ethylene diffusion flame. Measurements were acquired with both pointwise detection using the monochromator and PMT and via images captured by the ICCD camera. Excitation of LII was achieved using both the fundamental (1064 nm) and doubled (532 nm) output of the Nd:YAG laser. Again, most measurements were concerned with the annular region of maximum soot volume fraction, though the ICCD images yield LII signals across the entire flame.

In addition to the experimental description presented in Chapter III, a number of issues regarding the optical detection systems employed here are presented in Appendix D, specifically methods employed to remove potential sources of systematic error in the LII measurements. The lessons learned here may be beneficial to future laser diagnostic students.

4.1 Fluence Effects

As outlined in Chapter II, the LII model predicts that increasing laser fluences (energy per unit area) will increase the LII signal up to some point, often referred to as the LII 'threshold'. Beyond this threshold fluence, the LII signal level decreases with further increase of the laser intensity. Experimental evidence of such behavior has been shown,[74,104] but other types of behavior have also been observed. For example, some researchers report signal levels that decrease much more rapidly after the threshold,[35,37,74,80,82] or are nearly the same (constant), or are even increasing beyond the threshold fluence (though at a lower rate than below threshold).[63,79] In addition, there is significant variation in the reported threshold fluence levels. This issue of LII threshold behavior is important, since there can often be sufficient extinction of laser light across a soot-laden flow that the laser energy decreases substantially. If the signal level is effectively independent of laser fluence beyond the threshold, then the interpretation of LII results is greatly simplified, requiring no laser intensity corrections. Therefore, some effort was expended in this research to try to clarify the effects of varying laser fluence for the current experimental setup.

4.1.1 Threshold Curves

Experimental results for Nd:YAG laser excitation are shown in Figure 35. LII signals, integrated over 50 ns, are plotted against laser fluence for both infrared (IR, 1064 nm) and visible (green, 532 nm) excitation using both 'prompt' detection (where the integration starts at the onset of the signal) and, in one case, detection delayed 80 ns from the signal onset. Signals are recorded with the PMT/monochromator for wavelength bands centered at 650 nm and at 430 nm. The data of Figure 35 are recorded at a height of 25 mm in the flame and at the side of the flame nearest the detector (see position 1, Figure 36). The imaged region lies at the radial point of maximum soot volume fraction for this height, nominally 7 ppm. A region representing only the middle 1.5 mm of the 8 mm beam (vertically) and 300 μm horizontally (along the beam propagation path) is imaged into the monochromator.

As expected, the results show a region of relative insensitivity of the LII signal to changing laser fluence beyond some threshold, with some variations for the different excitation/detection methods. The threshold fluences for green and IR excitation, respectively, are about 0.3 and 0.5 J/cm^2. To understand the fluence dependence of the signal, we can examine the LII model. The model predicts that for increasing fluence above the threshold value, the maximum particle temperature increases, but the particle size decreases (by vaporization). This might seem sufficient to produce a ‘leveling off’ of the LII signal. In fact, some researchers have suggested this as the driving mechanism for the LII plateau behavior.[37] However, as shown in Chapter II, the model indicates that for a *uniform* laser intensity across the soot region, the mass loss induced by higher intensities will overwhelm the increased particle temperature, thus lowering the LII signal (see Figure 5a,b). This is at least true for a detection gate of any significant duration (e.g., >20 ns). Thus, the tradeoff between peak temperature and lost mass is not the primary cause of the nearly constant LII signal ('plateau') often found for fluences beyond the threshold.

The model does predict a relatively constant signal beyond the threshold for the case of *nonuniform intensity profiles*, e.g., Gaussian intensity distributions. This is in fact the case in the current arrangement. Since we only record LII produced by a small part of the laser sheet in the vertical direction and horizontal directions, the distribution of the laser intensity through the observed region should be nearly constant in those directions. In the direction parallel to the detection axis, however, the beam profile is nearly Gaussian (a 1-D Gaussian distribution is used in the model results of Figure 6). These results also agree with experimental results for other Gaussian arrangements. [74,81,104]

The threshold behavior of LII can be exploited to remove the need to make laser energy corrections. In many diagnostic techniques where imaging is performed using a laser sheet, great care is often taken to ensure that the illuminating intensity is either uniform or well-defined, so that data corrections can be made. This need is essentially removed for laser fluences above threshold, due to the 'saturation' behavior of the LII signal. Figure 37 illustrates this effect. A laser sheet is formed by passing a beam (532 nm) through a rod of relatively poor quality glass. The resultant sheet, which is quite streaky and nonuniform, illuminates the diffusion flame. The middle 4.2 cm of the flame, centered on 30 mm HAB, is pictured in the figure for both an average illuminating fluence of 0.35 J/cm^2 and 0.65 J/cm^2.

The effects of a streaky beam are quite evident for the image with the fluence level closer to threshold. A clearer illustration of this is present in the included graph, which shows the signal levels along the left (side near laser) path of maximum soot concentration. These plots are averages of the path of maximum signal from 10 images. The smoothness of the higher intensity curve attests to its reaching threshold everywhere, except perhaps at 40 mm, where the biggest ‘hole’ in the intensity of the beam is evident from a comparison to the data at lower intensity. Without any corrections, the ‘saturated’ data provides a larger amount of quantitatively useful data.

As noted above, there are some differences between the different excitation/detection combinations shown in Figure 35. For example, the ‘plateau’ with red detection (650 nm) is less flat for the IR case than for green excitation. An even more noticeable difference between the IR and green excitation occurs for the case of signals detected at 430 nm (blue). For the green laser, these signals seem to be steadily increasing with higher laser intensity. For comparison, there is virtually no difference between blue and red detection with IR excitation. This increasing LII signal beyond threshold excitation is similar to the results of Shaddix and Smyth[63] who also used visible (560 nm) excitation and blue detection (420±30 nm).

The fluence curves become even more interesting for high laser fluences. These results are displayed in Figure 38 for red, blue and green (516 nm) detection. Though the trend begins at different fluences and to different degrees, all signals increase at the highest laser fluences. The maximum dynamic range of the plateau region is perhaps 10. The most notable response occurs for 516 nm detection. This wavelength, as it turns out, corresponds to the band head of a spectral region of C_2 emission. The increasing signal becomes notable by 1 J/cm^2. One might conclude that all channels may have some significant interference due to C_2 by the highest fluences. However, the similarity of the delayed to the prompt signal behavior suggests that at least part of such an interference must be relatively long-lived, which is not expected of C_2. Also, no significant excitation of C_2 is expected from infrared illumination. There must be another mechanism involved in the observed signal behavior. The relative contributions from C_2 fluorescence at different energies and excitation wavelengths is investigated in the following Section, while the other mechanism is described in Section 4.1.3.

4.1.2 LII Spectra

As part of the soot vaporization process, some of the incident laser energy ends up producing high energy (hot), molecular carbon species (e.g., C_2, C_3). Though the major vapor constituent is predicted to be C_3,[3] and C_3 does emit at certain wavelengths, no emissions from this molecule were identified here, nor are they reported in the literature for laser-irradiated soot. The visible emissions from C_2, however, can be quite strong for high intensity excitation Notable emissions have been observed from C_2 in the Swan spectral bands for visible (532-570 nm) and UV (266 and 355 nm) illumination, and for both resonant wavelengths and high-intensity wavelengths away from a C_2 resonant line.[70,76,106] Some research has attempted to make use of the strength of this interference signal itself for soot measurements[70,76,78] and some proof exists that the C_2 signal scales linearly with soot concentration, like LII.[78] However, for resonantly tuned C_2 LIF, it has been shown that the C_2 signal does not behave in a similar manner as LII with changing laser fluence, and it has been noted that this emission can be produced by soot precursor molecules and smaller hydrocarbons.[76,78] Since this behavior may have an influence in practical situations (e.g., nonuniform laser sheets, soot forming zones of flames), and since a goal of this work is to test the accuracy of standard LII models, it is preferred that the LII signal be isolated from any possible interference.

Initial spectral information was acquired at a height of 25 mm above the burner at the radial point of maximum soot volume fraction at position 1. Signals are integrated over the first 30 ns from the onset of the laser. Figure 39 shows the spectral profile of the laser-induced signal with 532 nm excitation. Results are displayed for signals generated with an excitation intensity near threshold (0.6 J/cm^2) and prompt detection, as well as a high intensity pulse (12 J/cm^2) with both prompt and 30 ns delayed detection. Bands of C_2 emission from the Swan system (438.3, 473.7, 516.5, 563.6, and 619.1 nm)[113] are clearly present in the high intensity case and just on the verge of detectability for the delayed and low intensity cases. The strong anti-Stokes shifted (lower wavelength) vibrational bands evident in the spectra indicate the excited nature of the C_2 vaporized from the soot particle. While we would expect the strongest interference at $\Delta\upsilon=0$, this region (485-540 nm) was not recorded because of insufficient rejection of the elastic laser scattering. The relative interference is much less for the low intensity case. Thus, the C_2 emission exhibits a stronger scaling with laser intensity than does the LII signal which, as shown above, “saturates” beyond a certain fluence. Also worth noting is the fact that the small interferences on the delayed signals show that the lifetime of the C_2 emission is not much longer than 30 ns.

Improved measurements were acquired with the addition of the holographic notch filter (Appendix C) for narrowband rejection (> 4 O.D) of the 532 nm light. These spectrally resolved LII signals were also acquired for more laser fluences to study the behavior of the different Swan lines with excitation energy. The prompt (30 ns) LII emission spectra across the visible wavelengths are displayed in Figure 40 for both 532 and 1064 nm excitation, and for laser fluences near and above the threshold values. Emission from the C_2 Swan bands is again evident at very high laser fluences, with the emission at $\Delta\upsilon=0$ (516 nm) now apparent. In these scans, the signal-to-noise ratio (averaging) was sacrificed for a faster scan speed. ND filters were also employed, as was the OG570 filter for wavelengths above 600 nm. These data were acquired at position 3, and are corrected for the response of the detection system (see Appendix C) and for the spectral emissivity of the soot particles.

Note that some Swan band structure is present in the IR-excited signals at high fluence. These emissions likely come from thermally excited C_2 leaving the soot. An alternative mechanism, besides thermal emission, to explain the IR produced C_2 signal, would be two-photon LIF. It is not readily apparent due to the log scaling, but all the signals of Figure 38 increase linearly at the highest fluences. For illustration, these data are replotted on a linear scale in Figure 41. The linear scaling of the signals at 516 nm for IR illumination suggests that two-photon events are not the controlling process in this case (since two-photon LIF is a nonlinear process with a signal that scales like I^2). Therefore, it seems likely that ‘hot’ C_2 is produced linearly with increasing laser fluence. For green excitation, the scaling is also linear, but to a stronger degree.

Comparing the signals generated by the fundamental and doubled YAG beams, one can see that the relative C_2 interference is much larger for the visible excitation, roughly six times larger at 516 nm. The increase in C_2 could be caused by higher vaporization rates for 532 nm excitation, since the soot is more absorbing there then at 1064 nm (~1.7 times higher absorption coefficient). However, the increase is much more than this (this can be seen by scaling both fluence curves by the threshold fluence, and observing that the green excitation still produces more C_2 signal). Therefore the green excitation would somehow have to favor C_2 production in the vaporization process for some other reason (e.g., breaking of C_3?) if the cause is simply increased vaporization. Therefore, it is suspected that LIF can be a significant contributor to C_2 interference with 532 nm excitation. There is evidence to support this theory, as the extent of the Swan bands is quite large. If the C_2 produced by vaporization is vibrationally hot (and note that the nominal temperature of the particle from which the carbon is vaporized is ~4000 K or greater), the laser may excite hot bands that lie between the ($\Delta\upsilon$=-1) bandhead at 563.6 nm and the ($\Delta\upsilon$=0) bandhead at 516.5 nm. The high laser photon density used here, might also explain the linear scaling of the 516 nm signal for 532 excitation. It is likely that such high power densities would saturate the LIF process, and that signal would scale simply as the vaporization rate (which appears to scale linearly with laser fluence/intensity).These sensitivity issues aside, the difference between using 532 nm and 1064 nm excitation is a drastic reduction in C_2 interference. This interference varies dramatically depending on the chosen detection wavelength.

From the spectral scans, it is now clear that molecular interference certainly causes some of the behavior observed in the fluence curves (Figures 32 and 35) with 532 nm illumination. The rapid rise of the signals detected at 516 nm for both excitation wavelengths is most certainly due to the presence of C_2 emission. This was confirmed by acquiring signals using green illumination with detection at 650 and 430 nm and with the camera gated during only the first 10 ns of the laser pulse. This biases the measurement more towards the short-lived C_2 fluorescence. The results showed an increase in the rate at which the blue signals with green excitation increased with the highest fluences, indicating that there is indeed some measure of C_2 interference within the bandpass of the 430 nm signals. The red signals were unaffected. This is significant since a number of LII measurements reported in the literature employ detection near 430 nm.*

Interference from C_2, however, does not explain the increase in signal seen at very high intensities for both lasers. As seen in the spectral scans, the signal is spectrally quite broad, and delayed detection indicates that it is long lived. These are characteristic traits of LII, not molecular fluorescence. In addition, the shape of the spectral emission does not change significantly at high fluence compared to threshold fluence. Thus it is unlikely the added signal is associated with any significant increase in the signal per particle due to an increase in particle temperature. If the signal is due to soot LII, and the soot is not giving more signal more particle, it appears that the amount of soot contributing to the signal is somehow increasing. Widening of the beam as it passed through the flame, for

---

* The usual reason given is to reduce *possible* background due to flame luminosity that is expected to be more prevalent at longer wavelengths. In addition, possible interference from PAH LIF is more likely to be red-shifted than blue-shifted from the laser wavelength.

example by some laser-induced refractive process, was ruled out by farfield beam size measurements. The beam size determined at a point well beyond the flame did not vary with laser power. The most likely cause involves the spatial wings of the laser. This is examined in the following Section.

4.1.3 Spatial Effects

In order to examine effects associated with the wings of the laser, fluence curves measured at two locations on the circumference of the flame are compared. Measurements were recorded at the side of the flame nearest the laser (position 1 in Figure 36) with the camera (650nm/10nm FWHM and 514.5nm/8nm FWHM bandpass filters were employed). The recorded data are averages of the peak signals from 10 images (integrated over 1 mm height in the middle of the laser beam), and the resolution is 100 μm. In Figure 42 these results are compared to data from Figure 35, acquired at position 3 (closest to the detector) with the PMT/monochromator. For the camera data (position 1), the gradients in the flame are essentially zero (uniform) in the direction parallel to the beam width (with its nominally Gaussian profile). For position 3, the gradients in the flame conditions (e.g., soot concentration and temperature) are now considerable in that direction. The FWHM of the soot volume fraction profile is ~0.8 mm, which is somewhat broader than the 0.2 mm FWHM laser.

The first thing to note from the data of Figure 42 is the agreement for the two positions up to a certain fluence. Then, the signals from position 1 (camera) begin their upward climb at a lower fluence than observed for position 3 (PMT). If some feature in the wings of the beam profile is responsible for the signal increase, we would expect position 3 to produce a smaller increase, since the soot levels are lower in the wings for this condition. This is consistent with the results shown in Figure 42.

In detail, the idea is that as the laser intensity increases, soot particles in the wings of the laser beam begin to contribute to the signal. Initially, the laser fluence in the wings is too low to produce an LII signal, since the fluence is well below the threshold value there. At higher intensities, the local fluence can exceed the threshold level. Also, vaporization of the particles in the beam center becomes likely at the higher intensities. A small region of slightly increased laser intensity in the wings can contribute to the integrated signal faster than the loss of signal from the vaporizing particles at the center.

A numerical simulation with the LII model is employed to illustrate this, and its results are shown in Figure 43. Small nodes of increased intensity are added to the wings of the standard Gaussian profile. The added intensity at the peaks of the nodes is 2.5% of the intensity at the beam center. Such a small deviation from a Gaussian profile would be extremely difficult to detect, especially with the method used here (Appendix B) for measuring the beam width.[*] The resultant upward trend in the LII signal is even stronger than that observed in the experimental data. Therefore, only a very small nonmonotonicity in the intensity profile at the wings is required to produce a significant change in the behavior of the LII signal with laser fluence. Such an effect may help explain the difference in fluence curves reported by various researchers, since the beam

---

[*] Indeed, bumps were not noticeable in the beam profile measured with the razor blade technique.

profiles of various lasers can easily differ by such small amounts. This may also explain the difference in the high fluence regions for the green and IR lasers employed here. Even though both beams are produced by the same laser cavity, the profile for the green beam is changed as it passes through the (nonlinear) frequency-doubling crystal. Note, these wing effects, i.e., small bumps in the beam profile, only contribute at relatively high fluences. Therefore, most measurements employed in this work for quantitative concentration or particle size measurements are performed at fluences below this level.

Another issue for image measurements should be mentioned in regard to the focusing of the beam. If there is interest in measuring signals along the direction of beam propagation, concern may arise that there will be a beam focusing effect on the signal. Again, due to the threshold effect, the change in light intensity as the beam focuses and diverges should present no problem. However, if the depth of the illuminated region that the camera sees changes across the image, then an effect would be expected on the signal magnitude. For a uniform soot field across the beam width, more signal should arise from the wider (deeper) parts of the beam that are away from the focal point. Minimizing the change in beam width was one of the motivating factors for using a long focal length (500 mm), cylindrical (1-D) lens. Shaddix and Smyth[63] noted a 5% increase in signal 5mm away from the focus of their beam and a 20% increase at 10 mm. However, their lens had a shorter focal length (300 mm) and was spherical. Thus, their beam width changes faster and the intensity changes along the beam at a rate greater than the square of the rate that occurs in these experiments.

4.1.4 Spectral Signal Ratios

As was just mentioned, the shape of the spectral emittance curve, and thus the ratios of the signals detected at two different wavelengths, reveals information concerning the temperature of the observed soot particles. Figure 44 displays LII spectral signal ratios for both the green and IR illumination versus incident laser fluence. The signals have been corrected for the detection system response parameters to represent the equivalent soot particle temperature. The ratios generated by the green laser (650 nm/450 nm) would suggest that particle temperatures increase throughout the entire range of laser fluences, minus one ‘kink’, up to temperatures of near 4800 K. What is actually occurring is that the C_2 signals are adding to the LII signals at higher fluences (above threshold). The interference is most likely for the data with blue detection, since the spectral scans showed the signals near 650 nm to be fairly free of any C_2 structure.

This data does, however, seem to flatten out between threshold and ~ 1 J/cm^2. This is more apparent in the IR data. As seen in the spectral plots, the IR-produced LII signals have essentially no C_2 interference for either red or blue detection. Above the threshold, the ratio exhibits a slight downward trend for both ratios: 650 nm/515 nm and 650 nm/430 nm. Interference from C_2 at 515 nm is probably occurring above 10 J/cm^2. The range of S_λ for this ratio would indicate 4100 K temperatures in the ‘plateau’ and that the hottest particles were attaining temperatures near 5200 K. This is rather hot, especially when considering the signals are averaged over 50 ns (though, again, biased to the hottest times). The 650 nm/430 nm ratio yields temperatures above threshold that range between 4000 and 4400 K (±150 K uncertainty). This compares well to the model predictions for particles of this size (30 nm) that range from 4100-4600 K. This suggests the model reasonably captures the physics of the vaporization-dominated period. Further experimental information and model comparison are required to test the model's accuracy.

In summary, it should be noted that higher excitation energies can produce effects beyond simple LII which require consideration. At shorter wavelengths, C_2 emission can be quite strong for visible excitation. Red detection or delayed detection are viable alternatives for avoiding this influence. The influence is essentially removed with IR illumination. Approximating a 1-D Gaussian beam appears to be the optimal arrangement for achieving the 'plateau' effect with changing laser fluence. Very high fluences should be avoided, however, as the majority of the integrated signal will come from the wings of the laser beam, which are generally not as well constructed as the middle.

4.2 Concentration Measurements

Perhaps the most important goal of this research was to determine the accuracy of using LII for making soot concentration measurements and to determine the sensitivity of the technique to several experimental parameters. Though point measurements with the PMT and monochromator were explored first, issues with uncertainties engendered by flame motions and spatial and temporal averaging motivated a change to the ICCD camera. Agreement, though, between the two detectors is illustrated and data are presented here from each in an order most conducive to illustrating the points to be made. The measurements are generally acquired from position 1 (Figure 36), since the soot profile is essentially uniform in the depth direction and small movements of the flame normal to the laser will not change the signal.

4.2.1 Signal Trapping

Significant extinction of the signal (trapping) by soot located between the emitting locations and the detector can occur in sooty diffusion flames such as the one used in this study. The loss in signal is potentially a significant error source for soot concentration measurements. Estimates for signal trapping in this flame were obtained by observing LII signals at different points (through different soot pathlengths) in the flame. The process is described in Appendix D. For a 90° observation angle, signal trapping (fraction of signal lost) from the location of maximum soot at 40 mm HAB was calculated to be near 30% and 45% for red and blue signals, respectively. The calculated trappings at 15 mm HAB, where there is less soot, are 8% and 13%, respectively. The blue signal experiences more loss since the soot absorption coefficient is greater there.

To reduce the trapping, it was decided to move to an observation angle of 50°, which gives a shorter soot path from the measurement volume to the detector (Figure 45). The effective volume of soot between the detector and the measurement volume was calculated to decrease by a factor of 5, which reduces the trapping to 6% and 9% at 40 mm, and to 2% and 3% at 15 mm (again for red and blue signals, respectively). These small values at 50° represent a small error in relative soot concentration measurements versus flame height (~4% effect for red detection, ~6% for blue detection). From these numbers, the calculated difference in the dynamic range of signals low to high in the flame for the two detection angles of 26%.

Reducing the trapping by moving to the angled position does produce a tradeoff in the effective resolution of the measurement, as the detection volume is effectively lengthened. In addition, the soot profile in the depth-of-field direction for a given pixel is not as uniform as for right-angle imaging. Based on the known soot profiles, however, these effects will have a minor influence on relative concentration measurements between low and high points in the flame and is far outweighed by the improvement in the soot trapping. Figure 45 illustrates the change in the observed volume and detection path for a single pixel with the camera at 50° (white strip) and 90° (black strip). To be conservative, the beam width at 3× FWHM (~0.6 mm) is illustrated. Considering this width to be the signal-generating width of the beam, the 100 μm resolution turns into 500 μm resolution. This resolution width is still narrow enough to sit on top of the crest of the soot profile without integrating much of the lower concentration region nearby. The width of the soot 'spike' is at all heights at least 800 μm FWHM.

Figure 46 presents a comparison of signals acquired with the camera positioned at a right angle to the laser beam and at 50°. Signals are generated with a 1.2 J/cm^2 IR pulse and are the average of the maximum signals from 10 images, again integrated over 1 mm vertically. Signals are integrated for 50 ns from the onset of the signal. The average standard deviation among the integrated signals was 5%. The fractional difference between the two measurements (90º vs. 50º) as a function of height in the flame is very close to the predicted amount based on trapping

A few point measurements (Figure 47) were also made at the side of the flame nearest the detector (position 3), where we expect minimal trapping (the path of soot between the laser and the detector is very small). The data are a little noisier due to the challenge of measuring up the curved surface of the flame and directing the laser into the appropriate point tangential to the flame sheet. Also great care had to be taken to ensure that the flame was stable and did not wander in the direction normal to the laser. Still, the comparison to the 50° data of Figure 46 (shown again in Figure 47) is good, with 7-8% deviation at 40 mm for the two signals normalized at 10 mm. This is close to the expected error (4-5%) due to trapping at position 1. For all these reasons, it is concluded that the 50º data from position 1 are sufficient for a quantitative examination of the linearity of the LII signal with soot concentration.

4.2.2 Comparison to Extinction Data

The LII signals are compared to the extinction measurements of Quay *et al*[79] for two detection wavelengths in Figure 48. For the comparison, the data are normalized at the peak volume fraction measurement, a common approach in other reported work. In general, the LII signals agree relatively well with the extinction data. Close inspection of the smallest signals (low in the flame), however, shows significant discrepancies. These sorts of discrepancies have also been noted in other research.[63,74,78,79] The possibility that all these deviations from the extinction data were the result of changing particle sizes through the flame was one of the motivations for this research. Recall that the model predicts that LII signals calibrated (normalized) to soot concentration at a signal generated by larger particles will underpredict the concentration where smaller particles are present. A renormalization of the signals at the lowest data point better illustrates the different scaling of the two diagnostic techniques with height in the flame (see Figure 49). The data appear to show the expected increase in LII signal with particle size that is predicted by the model.

The particle size effect can be better analyzed by defining a calibration constant, C, as the LII signal normalized by the local soot volume (mass). For the experimental data, the C values are calculated by dividing the LII signals by the concentrations provided by the extinction measurements. In Figure 50, these values are compared to the C values predicted by the model for conditions that match the experimental conditions, especially primary particle size variations with height (Figure 20). Between 25 and 55 mm HAB, the primary particle size changes very little, even though the volume fraction is varying. Since the measured C is nearly constant in this region, it can be seen that LII scales very well with f_v, *at least in the absence of changes in primary particle size*.

Where the primary particle size is growing significantly (up to ~22 mm HAB), both the model and experimental data show C increasing. However, the measured C values exceed the particle size effect that is predicted by the model. It might be suggested that the changes at low height in the flame are not due to particle size, but rather caused by the fact that the soot there may be significantly ‘younger’. In other words, its structure/composition may be different, for instance, the material might be more hydrogenated. TEM results do show that the optical properties of the growing soot particles change as the soot precursor particles transform into turbostratic soot. However soot has been shown to ‘age’ into its turbostratic form as one moves from the axis of the flame to the flame sheet, just as it does vertically through the flame. There is no experimental evidence in the literature to determine whether the soot in the lower *annular regions* is noticeably ‘younger’ or not. If the soot low in the flame *is* somewhat different, this could explain the additional change over that predicted for the particle size effect alone. Alternatively, there could be perhaps precursors or large macromolecules (which we will not call soot for the sake of this argument) that exist in parallel with the soot low in the flame. They could contribute to the extinction (absorption/scattering) across the flame, without contributing to the LII signal. Thus, the extinction results would overpredict the soot concentration and produce the discrepancy of Figure 50. This issue is addressed further in the Section 4.2.3.

As a note, the precision and the signal/noise ratio of the acquired LII images are improved by averaging. Finding the average of the maximum signals in a set of single-shot data is preferred over the maximum signal in a (multiple shot) averaged image, due to flame movement. Figure 51 presents an example of the typical errors introduced in acquiring data in such a manner. Experimental conditions are the same as in Figure 50. While the results appear to agree better with the extinction results, it is caused by increased flame movement. Even though the flame appears stable to the eye, small motions can be detected that result in effective spatial averaging in the image (and thus a drop in the maximum signal equivalent to a spatial average of >0.5 mm for a 100 image average). The increased flame movement at higher points in the flame causes the data to appear to agree with the extinction values, masking the size effect. Also, the effect is not consistent, as the amount of flame movement for each accumulated image is unknown.

The repeatability and versatility of the LII measurements are demonstrated in Figure 52 shows data acquired on different days, with different cameras, and different spectral bandwidths at nominally 650 nm detection and 1.2 J/cm^2 IR excitation. All data are averages of maximum values from 10 images, vertically integrated over 1 mm. The point-wise 650 nm data at 50° (from Figure 46) are compared in Figure 53 to the signals generated with the expanded laser sheet. In a testament to the robustness of the technique, good agreement between the data sets is observed everywhere except perhaps at the peak, where the intensity of the large sheet has probably not reached threshold. Even here, though, they agree within a small error. The two experiments not only employed different laser sheets, but also different illuminating wavelengths, and different bandwidths of filters (10 and 130 nm centered on 650 nm).

In summary, the LII soot volume fraction measurements above indicate that consistent results can be obtained for a range of different illumination and detection parameters. In the end, though, the LII measurements show deviation from those made by extinction, at least low in the flame. This may be partly attributable to the variation in the LII signal (or C) with particle size. This is explored further in the soot generator experiments.

4.2.3 Measurements with C_2 Interference

Visible excitation and prompt detection at fluences beyond the threshold value presents a new issue which is, not surprisingly, related to C_2 interference. In Figure 54, signals generated at a fluence a little above threshold (0.6 J/cm^2, 532 nm) are compared to signals at much higher fluence for both 1064 and 532 nm illumination. The detection is gated for only 30 ns in order to enhance any short-lived molecular interference. Good agreement between the low and high fluence results is observed for most signals detected at 650 nm. However, the high fluence signals at 430 nm show a different behavior. These signals *appear* to scale like the extinction data. Note, however, the data are subject to signal trapping because of the right-angle detection scheme used (Section 4.2.1). Corrected for this, they would yield a 30% greater scaling with HAB than does the extinction data.

As shown in Section 4.1.2, the blue channel has a significant contribution from C_2 emission for green illumination. Signals from laser-generated C_2 have been shown to scale like LII in sooty regions,[78] and thus might be expected to have little influence on the signal behavior with varying soot concentration. The indication here, though, is that as this interference becomes large (at higher fluences or at detection near the emitting bands), the trend of the overall signal with HAB, and thus the known concentration, is changed. Thus, the C_2 emission appears to scale differently than LII.

Figure 54 also indicates that the same process occurs, to a lesser extent, for very high fluence at 1064 nm. At even higher energies, similar behavior may begin for red detection and 532 nm illumination. While no C_2 is structure is evident at 650 nm in the spectral scans (Section 4.1.2), the detection gate there is considerably longer than the C_2 lifetime and some contribution may be present at the $\Delta\upsilon$=-3 band.

The important point here is that the creation and excitation of C_2 has *also* been attributed to laser interaction with soot precursors, or macromolecules such as PAH.[76] While some PAH may be present in the *annular region* at low heights, the presence of soot precursor particles, such as those shown in Figure 1 from samples along the *flame axis*, seem more likely. If so, it is probable that they do not behave like the older, developed soot particles. If they are absorbing, laser energy they receive from pulses of lower fluence may simply go to a different process than internal heating, such as dehydrogenation. Or it may simply be the fact that their optical properties are quite different. In Figure 1, they are more transparent to the electron beam than the bigger soot particles. They may contribute little to the signal until the laser energy is sufficiently high to break them down into fragments that include C_2. If this is the case, the visibly excited signals detected in the blue may actually be a better representation of the combined soot+precursor concentration, which could be of interest as they together account for carbon that is destined to be soot.

Since it was determined that this process can occur with larger hydrocarbons and visible excitation, it might be assumed that this illumination and detection combination is not a good idea for general combustion environments, unless one wishes to identify both PAH and soot simultaneously. This conclusion may be in error, though. In this and other[63] research, no signal contribution is detected from PAH either at very low intensities (where LII has not yet 'turned on') or in the high PAH zones in the interior of the flame for any intensity. At lower heights in the flame, this zone should show up as a second annular region of signal significantly closer to the centerline than the soot zone. These always appear with UV excitation.[31,32] This would suggest that neither PAH LIF nor PAH-sourced C_2 emission is a contributor.

4.2.4 Delayed Detection

Delayed detection was first suggested by Cignoli *et al*[75] to avoid signal contributions from short-lived molecular emissions and elastic scattering. Most LII research has avoided detection at any significant delay, possibly based on the prediction that particle size and gas temperature variations will induce relative errors on the LII signals (see Figure 8). Delayed detection[74,75] and extended gate lengths[63,82] have been explored for biasing the signal against these interferences and increasing the overall signal. However, conclusive results have not been offered to suggest how accurate the measurements are or, rather, at what delays do the particle size and temperature sensitivities become significant.

To this end, LII signals were acquired in the flame for different delays of the detection gate. Figure 55 shows these measurements, which were acquired up the front of the flame with 650 nm detection. The IR wavelength was employed at 0.36 J/cm^2 and detection gates were 20 ns long. These delayed signals are, of course, much smaller in magnitude than the prompt results, but once again the data have been normalized to the extinction data at their lowest points. Signals with increased delays showed agree reasonably well with prompt signals until ~100 ns, with deviations less than 10% from the prompt results until then.

This indicates that short detection delays (up to ~100 ns) provide as good a measure of soot concentration as promptly detected signals (at least at flame temperatures). The prompt and delayed detection gates are dominated by the cooling mechanisms of vaporization and conduction, respectively. The agreement suggests that the particle size dependence of the signal on the two mechanisms scales the same for each, or that a small amount of conductive cooling occurs in the first 100 ns. Another positive result is that good agreement is seen for signals at short delays up to the highest laser fluences, with both green and IR excitation. Figure 56 shows signals detected with the camera for a 30 ns delay and 20 J/cm^2 excitation at 532 nm. They agree well with prompt results that also use right-angle detection, e.g., low intensity, red detection results in Figure 54.

Thus, if molecular interferences or elastic scattering are potential interferences for a particular excitation/detection scheme, delayed detection can be employed without cost to alleviate the problem. Again, to isolate the LII signal, red or delayed detection can be utilized, or IR illumination can be employed to remove the issue altogether. However, the C_2 signal seems to scale more like the extinction signal, and thus deserves attention as an alternative technique to extinction. The combination of LII and C_2 emission may possibly provide an avenue for discriminating soot precursors and other absorbing carbon species from fully grown "blackbody"-emitting soot particles.

4.3 Particle Sizing

While it has been predicted that the accuracy of the LII technique for soot volume fraction measurements may depend on primary soot particle size, it has also been proposed that this dependency may provide the means for monitoring particle sizes themselves. In order to test this, LII signal behavior from different points in the diffusion flame were compared against previous particle size measurements at those positions (Section 3.1.1). An attempt was made to capture the predicted particle size effect based on the maximum temperature attained by the particles and also via the expected different signal decay (particle cooling) rates of different sized particles.

4.3.1 Spectral Ratio Method

The first proposed method in this research was to capture the predicted particle size effect by monitoring the average temperature observed over the integrated LII signal. This is achieved by recording the ratio of the signals at two different wavelengths (S_λ). This pyrometric technique has been employed before for monitoring flame temperatures.[114-116] For LII, larger particles were expected to reach higher temperatures and give smaller S_λ.

If, as suggested above (Section 4.2.2), the LII signal is sensitive to particle size as it changes low in the flame, then lower signals there should be a result of lower average particle temperatures. Again, a measure for the particle temperature is the spectral signal ratio, S_λ. Figure 57 shows the ratio of prompt signals detected with the camera at 650 and

430 nm for the two detection angles (50° and 90°). As before, the 90° data is expected to suffer from signal trapping. The 90° ratios show an increase with flame height, a 15% increase in S_λ from the lowest to highest location. On the other hand, the ratio is essentially constant for 50° detection. The difference in the two cases is due to signal trapping. Recall, the amount of trapping is different for the two detection wavelengths (Figure 43), with the blue wavelengths more strongly absorbed. Thus the ratio of the two signals is expected to change as trapping is increased, in this case by 15%.

For fluences above threshold, S_λ shows little change for both the IR and visible excitation. In effect, the trend of S_λ is for all intensive purposes flat, roughly 2 for the 650nm/430nm ratio. This indicates an average temperature of ~4150 K for particles at all observed points along the path of maximum soot. This is important considering the fact that the particles lower in the flame seem to be producing less signal (lower C). The model predicts a variation between 4000 and 4300 K for 10 to 35 nm particles. In terms of signal ratio, the model predicts a dynamic range of about 1.2 to 1.4 for the tested fluence range, 0.6-20 J/cm^2. Also worth noting is that as the uncertainty in the signals is on the order of 5%, the uncertainty in the signal ratios is on the order of 10%. This makes a relative rise or fall of S_λ rather imperceptible through the scatter of the data. Finally any residual signal trapping will tend to increase S_λ with flame height, as seen in the 90° results. Thus measuring a small decrease in S_λ in the flame is difficult.

Prompt gating, of course, was originally determined to be the optimal gating for particle size insensitivity of concentration measurements. A detectable change on the spectral ratio was still expected, though, for prompt 50 ns gates. For increased sensitivity, signal ratios at longer delays were investigated. The deviations at long delays (Figure 52) occur because smaller particles cool faster. When displayed for various gate delays and heights in the flame, it can be seen that the greatest sensitivity to detection delay for S_λ occurs low in the flame, where particle size is changing the fastest. This is illustrated in Figure 58 for four heights in the flame, IR illumination at 1.2 J/cm^2, and 20 ns gates for 650/430nm detection. The signal ratio has not been corrected for filter or detector responses. Here, finally, the predicted particle size effect is seen.

Considering these results, measurement of the particle size in the flame by the pyrometric method appears impractical. It appears that several factors combine to make the technique fairly insensitive. In the only region where particle size variations are significant, it seems the thermal or optical behavior of the soot is affected by other mechanisms or property variations. The environment is too unknown and complex to draw a strong decision about the controlling factors. While the concentration measurements seem to indicate a size dependence of the LII signal, this conclusion can not be verified by the spectral ratio results. Further analysis of this technique is performed with the soot generator and is resolved in Chapter V.

4.3.2 Signal Decay Method

While the observed peak soot temperatures proved to be insensitive to primary particle size, the primary particle size was also expected to have an effect on the cooling rate of the soot particles to the local gas. Thus, the other suggested LII-based method for particle sizing that was investigated was concerned with the decay rate (cooling rate) of the LII signal. Though concern over the sensitivity of the LII signal decay rate method to local gas temperature does exist, this technique has the positive characteristic of being insensitive to the effects of signal trapping. The shape of the temporal signal should be the same no matter what fraction of the signal reaches the detector. It should be mentioned here, though, that unlike the pyrometric method, the magnitude of these decaying signals are a function of particle number density and detection setup. Thus, some form of normalization is generally required.

It would not be surprising that this technique should prove to be more sensitive to particle size than the pyrometric method. The signal decay rate (slope) should at least be more sensitive to the chosen detection delay time than the integrated signal (which is essentially the area under a segment of this slope). The concern turns to whether variations in local gas temperature will induce too much change in the detected signal decay rates to obtain reasonable particle size information. The pyrometric method was designed to acquire signals when the particles are hottest and, thus, less sensitive to such local temperature variations.

4.3.2.1 Sizing Results

Recall that the signals with significantly delayed detection above showed noticeably different cooling rates depending on the position in the flame. It could be assumed that this is a strong sensitivity to the soot particle size and the surface-area dependence of conductive cooling ($\propto d_p^2 \Delta T$). A longer time delay for detection allows smaller particles, which may have peaked at similar temperatures as the larger ones (consider the spectral ratio data), to be observed at relatively smaller temperatures, i.e., the temperature difference between large and small particles becomes greater over time

($[T_\infty - T_1]/[T_\infty - T_2]$), at least until all particles begin to approach the local gas temperature. In fact, this is where the pyrometric technique could be employed. Unlike the prompt data, the delayed signals above show signs of a decreasing red/blue signal ratio, especially below 20 mm HAB (see Figure 58).

Alternatively, we may be seeing more of a dependence on local gas temperature ($[T_{\infty,1} - T]/[T_{\infty,2} - T]$). This would imply that a significant temperature difference (increase) exists between the surrounding gas at 10 mm and at 40 mm HAB. Such a temperature difference, though, between 10 and 40 mm HAB is not seen in either the pyrometric or thermocouple data of Figure 34 or in temperature profiles of Figure 19. Thus, the assumption is made that the observed effects in Figure 58 are mostly due to particle size variation.

Time-resolved measurements were performed with the PMT and monochromator. The following data were generated with a 2 mJ, 532 nm focused beam (0.3 J/cm^2). The holographic notch filter ($>10^6$ scattering rejection, see Appendix C) was employed to spectrally filter visible scattering before the monochromator. Measurements were made at 5 heights in the flame for 450 and 650 nm detection. Signals were recorded on an oscilloscope with a running average of 128 signal traces and these average traces were recorded and saved to computer. Examples of such records are shown in Figure 59. The curves are normalized at 60 ns after the onset of the signal to isolate the signal behavior during the conduction-dominated period. This data illustrates the blackbody behavior of the incandescing soot. The decay rates for detection at 430 nm are larger than for signals detected at 650 nm. This follows from the higher temperature sensitivity of blackbody emission in the blue (shorter wavelength) part of the spectrum compared to red (longer) wavelengths.

Results for the LII signal decay rates at different heights in the ethylene flame are shown in Figure 60. Signals are again normalized at 60 ns after the signal onset. Observations in this flame are over a limited range of primary particle diameters (14 to 33 nm), but a dependence on particle size is apparent for the signal decay. The signals from the regions with larger primary particle size decay more slowly than the signals associated with smaller particles.

The LII model (result is shown for 14 nm particle (10 mm HAB)), on the other hand, somewhat overpredicts the signal decay rate. This essentially means one of two things. Either the conductive cooling equations in the model are incorrect, or the soot particle conditions, e.g., temperature and size, at the end of the vaporization period are incorrectly predicted by the model. The latter would mean the physics during the vaporization-dominated period are incorrectly modeled. The incident fluence was purposely chosen to be toward the low side of threshold to produce little vaporization. Considering the indicated temperature from the spectral ratio, though, at least some particles are hitting vaporization temperatures. The model seems to be peaking at somewhat higher temperatures, so, if anything, the model underpredicts the vaporization. The model shows the decay rate to be essentially independent of the incident laser fluence, and thus the amount of vaporized soot. An experimental investigation of the effects of laser fluence is presented below.

4.3.2.2 Fluence Effects

It was considered above, for concentration measurements, that both particle size and physical changes in the soot through the flame may have an effect on C (signal/volume). As laser fluence may have an influence on both of these, one should also consider the possibility that laser fluence might also have an effect on C. In Section 4.1.1, though, it was shown that, for laser fluences above threshold, varying the fluence has little effect on the total integrated signal. Given this and the fact that the average particle temperatures were also relatively insensitive (Section 4.1.4), one might infer that signal decay rates would have to change very little with varying laser fluence. This would be beneficial for particle size measurements in the same way that the 'saturation' effect is beneficial to concentration measurements. Two-dimensional images of particle size could be acquired with an expanded laser sheet, without corrections for beam intensity wherever the intensity is above threshold.

Figure 61 shows LII signals generated with various laser intensities from 0.06 to 33 J/cm^2 and predicted signal decay from the model for a 0.15 J/cm^2 pulse (i.e., near threshold). Signals are recorded at the fixed height of 40 mm HAB. The graph reveals the signal decay rate to be independent of laser intensity beyond the threshold fluence. Again, the model also predicts such an insensitivity in the decay rate. Though the actual decay rates are off, the model seems to represent the effects of the Gaussian beam fairly well.

One may consider for a moment the possibility that the model is indeed overestimating the true conductive cooling rate. As an artifice to adjust the cooling rate, the thermal conductivity of the surrounding gas could be adjusted. The conductivity would have to decrease by a factor of nearly 5 to achieve decay rates that would nominally match the experimental data.

The above information *does* show, however, that the signal decay rate method for particle sizing will be a useful tool for such measurements. Much like the signal ‘plateau’ versus laser fluence that was observed for concentration measurements, the signal decay for a 1-D Gaussian beam is also not sensitive to changing laser fluence above a threshold value. The value of the pyrometric technique in this flame environment is less optimistic. This technique is more sensitive to short-lived interferences, varying optical properties (as might be present low in the flame), and signal trapping from the high soot concentrations typical near flamefronts.

4.4 Diffusion Flame Environment

Through these experiments it was learned that the diffusion flame, though simple in nature and geometry, is a difficult environment in which to attempt to analyze and calibrate the LII technique. It is difficult to control all the parameters simultaneously. The region of interest has steep gradients in soot concentration. Simultaneously, the flame will not sit perfectly still unless some very drastic modifications are made to the experimental setup and environment (like an isolation chamber). The dense soot loadings in this flame also present a challenge in the form of signal trapping. The presence of soot precursor particles and precursor molecules (such as PAH) present an unknown influence in terms of their laser absorption characteristics (e.g., extinction measurements), broadband fluorescence, and ability to produce excited C_2 under high laser fluence. Lastly, other parameters than soot concentration and primary particle size are changing through the flame and along the path of interest. The degree of soot agglomeration certainly varies and the local chemistry may do so as well. The soot particles themselves may even undergo a transformation of physical or optical properties during their lifetime through the flame and along the path of maximum soot volume fraction.

The following chapter presents an investigation of the use of LII in an environment that has been designed to try to alleviate most of the challenges just listed.

CHAPTER V

SOOT GENERATOR MEASUREMENTS

As shown in Chapter IV, there are many difficulties in characterizing specific LII attributes in even a relatively simple environment as the laminar diffusion flame. Identifying the importance of a single variable is hampered by the fact that a number of parameters change from one location to another, some in an uncontrolled and unknown way. Also the change in some parameters, such as particle size, is too small in much of the flame to accurately test model predictions. A controlled soot environment with fewer unknown parameters is required. Therefore, an investigation was performed in a much simpler environment, the soot aerosol flow produced by the soot generator.

5.1 Soot Aerosol Characterization

Employing the soot generator for LII measurements should alleviate some of the problems encountered in the flame measurements. The uniformity of the flow neutralizes the problem of accurately targeting the zone of interest for detection. The diluteness of the flow remedies the effects of signal trapping that were observed in the flame.

Simultaneously, control over the average soot particle size and aerosol concentration allows a controlled test of the lower detection limit for concentration measurements, a determination of the effect of the soot particle size on the LII signal, and an independent calibration for measured soot volume fractions. Purposely, and as a result of the above properties of the soot generator, conditions typical of a jet engine exhaust flow are investigated.

However, given the possible differences between the carbon-black aerosol and soot, it is important to know whether the results obtained from the soot generator can be transposed to soot found directly in real combustion environments, i.e., flames and exhausts. Previous research has generally found carbon black "soot" (produced usually in oxygen-lean, pyrolytic reactors) and combustion-generated soot to have similar internal structure (see Section 3.1.2). Some differences exist, however. More specifically, differences exist between flame soot and the carbon aerosol generated by the soot generator. Their influence on the LII signals observed in the following experiments was unknown. To this end, the size, structure, and LII behavior of the generator-produced soot aerosol were characterized. This included measuring the LII signal behavior with varying laser fluence, and characterizing the aerosol particles with a scanning electron microscope (SEM).

5.1.1 Laser Fluence Effects

As a check on the material properties of the carbon black employed in the soot generator, the behavior of the aerosol LII was obtained as a function of laser fluence.

This includes integrated signals (spectrally and temporally) and spectrally-resolved records of the laser-induced emission versus laser fluence.

5.1.1.1 Signal Threshold

Figure 62 depicts signals generated in the exhaust of the soot generator for varying fluence levels with IR illumination and broadband red detection (OG570 filter, 650 nm center wavelength). These signals are compared to the data of the flame from Figure 42. While most of the data from the soot generator were obtained with an unfocused beam in order to achieve larger collection volumes, and thus larger signal levels, the higher fluences needed here required the beam to be focused. The reduced signal-generating volume necessitates that one of the higher soot loadings be employed. Thus the solution concentration is 0.035 g/L, producing an aerosol concentration of 0.4 mg/m^3 (0.2 ppb). The imaged area is 4 mm wide by 2 mm high and is imaged directly onto the PMT. Very similar behavior is observed for the exhaust signals and the signals generated in the flame at the side of the flame near the laser. The fact that these two data sets match best is not surprising considering that these two conditions have the most uniform soot fields in the direction of the detection path. This agreement lends strong support to the idea that the optical and physical properties of the soot in the two cases are the same.

5.1.1.2 LII Spectra

Further evaluation of the “soot” produced in this flow is achieved by examination of the spectrally-resolved LII signals at high intensities. Figure 63 reveals the spectral signature of the LII signal using a full-power, unfocused, 532 nm beam (1.9 J/cm^2) and also the spectra generated with very high fluence (12 J/cm^2), for both green and IR excitation, at 17 mg/m^3 (8 ppb) aerosol concentration. Note that the reduced spectral bandwidth (3.7 nm) imposed by the monochromator requires even higher soot concentrations than the previous experiment. A few differences from the flame spectra are quickly noted. A few large spikes are present near 600 nm which are not seen in the flame data. These structures are very likely the emissions of O_2 and O_2^+,[113] representing the beginning of laser-induced breakdown of the surrounding gases which was not apparent by eye or ear. This difference from the flame spectra is not surprising considering that the soot in the diffusion flames is in an oxygen-starved environment until very high in the flame.

The second difference from the flame spectra is that the soot from the soot generator appears to more readily yield C_2 emission with IR excitation. If the IR-generated C_2 emission is, in fact, due to thermally excited C_2 leaving the soot (or a fast dissociation product of some larger carbon molecule, e.g., C_3), this could suggest that the thermal properties of the soot in the two environments are somewhat different. The difference, though, may be the result of a few very large particles present in the distribution that are beyond the Rayleigh limit for light absorption and thus heat up at their surface (recall, the nebulizer produces a range of droplet sizes, and thus should produce a range of particle sizes). This would likely produce much more ‘hot’ C_2 than a distribution of particles that are all within the Rayeligh limit. The C_2 signal in such a nonuniform distribution would thus not very well represent the soot concentration of the detected region. The remainder, and majority of the particles produce LII. This would explain the good agreement for the 650 nm data above for the integrated signals at the highest fluences.

5.1.2 SEM Measurements

The SEM analysis was performed to characterize the shape of the carbon black aerosol, and the size of the particles, including the size distribution. Recall that it was expected that in the process of evaporating, the water droplets, containing suspended carbon black particles, would produce spherical carbon aggregates, with a size determined by the number of primary particles in the droplet. Based on the measured size distribution (Figure 24) of the water droplets produced by the nebulizer, it was expected that the soot generator would produce a range of soot particle sizes for a given liquid concentration.

Particle sampling was performed by exposing a 10 mm gold-coated (vacuum sputtered) sapphire disk, with its surface normal to the flow direction, to the center of the soot generator aerosol jet at a height of ~10 mm above the exit. Exposure times varied, but the results presented here are for exposure times of 3 minutes. The collected samples were subsequently coated with gold and imaged in a scanning electron microscope, with a resolution at maximum magnification of roughly 50 nm. The in-house SEM (located in the AE solid-propellant combustion laboratory) does not have the resolution of a transmission electron microscope (TEM), but it was sufficient for the current investigation. The SEM (polaroid) photographs were digitized for this investigation.

Three carbon/water solutions were analyzed: 2.8, 0.7, and 0.007 g/L. These corresponded to calculated concentrations of 34, 8.5, and 0.085 mg/m^3 (16, 4.0, and 0.004 ppb) and mean particle sizes (based on the mean droplet diameter) of 430, 270, and 60 nm. Figure 64 shows SEM pictures of portions of the collection surface after exposure to the 34 and 0.085 mg/m^3 concentrations. The first thing to note is that the generator does indeed produce fairly round (spherical) particles. This is more clearly evident in the close-up of Figure 65. Since the soot generator does produce nearly spherical particles, it permits meaningful comparisons to the LII model, which is based on spherical particles.

A standard image analysis package is used for the determination of particle size. Particles in the SEM images are identified, counted, measured, and binned in a size group. Figure 66 shows the distribution of particle sizes for the three cases. The average particle sizes for the three distributions were 340, 270, and 160 nm. A volume-weighted average yields sizes of 745, 415, and 180 nm, respectively. As predicted, the particle size does increase with liquid concentration. The comparison of the predicted and measured mean particle sizes is reasonable for the higher concentrations, but off by almost a factor of three for the smallest value.

The measured particle sizes, especially for small particles, are prone to a number of errors. First, the sampling technique biases against collection of small particles. Bigger particles, with higher inertia, are more likely to impact (and stick to) the sample surface, while smaller particles can follow the flow around it. It is also difficult to identify particles below the resolution limit of the SEM, again biasing the measured size distributions toward larger particles. There is some evidence of these problems. Samples were acquired for even smaller liquid concentrations, but it was difficult to identify a sufficient number of particles in the SEM to perform the analysis. As the number density of particles is held constant by the flow rate of the carbon/water solution, this suggests the inability to sample and size the smaller particles. Alternatively, there is likely to be some lower bound on the aggregate particle size that can be produced, given the initial 20 nm primary particle size. These particles stick together before being placed in the solution, and there may be a limit of how finely they can be 'broken up' with mechanical stirring. There could also be some amount of agglomeration that occurs during the evaporation process. Given the potential limitations in the SEM measurements, the agreement between the measured and predicted particle sizes is sufficient to state that the soot generator is behaving as expected.

5.1.3 Cross-Calibration with Flame

In an effort to compare the soot calibration in the two environments, flame and soot generator, measurements were made in both soot fields with the detection setup held constant (focused IR beam, 1.2 J/cm^2, broadband Schott glass filters (Appendix C), PMT without monochromator). Again, a high soot loading in the soot generator was employed, due to the reduced image width and depth. Therefore, comparable particle sizes for the soot generator and flame could not be analyzed. The lowest detectable concentration employed was 4.6 mg/m^3 (2.2 ppb). This corresponds to a predicted (mean) particle size of ~300 nm, rather than the nearly 30 nm primary particles found in the flame.

In Figure 67, LII signals (50 ns gate) from the two environments are compared to the soot concentrations calculated from the flow rates of the soot generator and from the extinction measurements in the flame. The lines on the plot represent a linear dependence between the signal and soot concentration. The comparison revealed the flame to have a C value (signal/soot volume) ~2 times greater than that of the soot generator data. This comparison is made for the smallest particles from the soot generator and the higher points in the flame, where C is constant. According to the model, correcting for the difference in local gas temperatures in the two environments reduces the difference by ~30% ($C_{gen}/C_{flame}=1.7$). However, the model also predicts that the larger particles of the soot generator exhaust should reach higher temperatures and should thus emit up to 2 times more signal per unit mass than the flame soot. It should be noted that significant uncertainty is created by the additional ND filtering (~2 orders of magnitude) employed in the flame to compensate for its much higher soot concentration, and thus higher signal. The optical density values for these filters are known to within about 3%, which results in a relative signal magnitude uncertainty of ~15%. Since there is a discrepancy between the measured and predicted relationship between C in the flame and C in the generator exhaust, it is possible that the difference could be symptomatic of soot particles with notably different properties. Further discussion of this subject is deferred until later in this chapter.

It is also useful to note that the red/blue signal ratio (50 ns gate) was roughly the same for the flame and soot generator data. This would suggest the particles were reaching similar temperatures, which may appear surprising since particles of different size are expected to reach different temperatures. One of the reasons may be that the very large particle sizes in the soot generator aerosol are exceeding the Rayleigh limit for emission (further discussed in Section 5.2.2).

5.2 Concentration Measurements

Measurements were performed to determine the detection limit of LII for exhaust like flows, and to investigate its linearity. Based on the previous results and advantages associated with scattering rejection and particle size dependence, infrared excitation at a moderate intensity (1.6 J/cm^2) was chosen for making soot concentration measurements in the soot generator. Broadband detection in the red was chosen to provide large signals and to reduce particle size effects.

5.2.1 Detection Limits

Figure 68 displays LII signals against soot concentration for concentrations ranging over 4 orders of magnitude from about 0.008 to 70 mg/m^3 (4 ppt to 30 ppb). Four different air dilutions were applied, without preheating the dilution air, and six different liquid dilutions were employed. The initial carbon solution was reduced, by adding distilled water, to 2, 8, 32, 320, and 3200 times lower concentration. The temperature at the measurement volume for this case is 70 ºC. Concentrations are corrected for the air density (volume flow rate) change due to heating in the dryer. In the figure, each liquid dilution is represented by a unique symbol.

At the smallest concentration, an ND=1 filter was still employed. Thus, the detection limit for this *f*4.4 system with broadband detection and 8mm^2 image area is better than 1 ppt.

Another consideration for detection limits is interference from other particulates. The air supplied to the soot generator was filtered to remove ambient particulate matter. Air flowing through an engine will contain such particles. Most of this matter, as it turns out, like silica[10] is essentially nonabsorbing, and thus will give no LII signal. Metals and metal oxides, however, are absorbing. Whether they will give rise to an LII interference depends on the temperature to which they can be heated. The fact that typical melting temperatures of metals are well below 4000 K suggests that they may not contribute significantly to the LII signal unless they are present in large concentrations. Ambient carbonaceous particles may be present as well, but they would likely be oxidized in the combustor. The interior of the combustion laboratory where these experiments were performed certainly does have ambient soot. It is interesting to note that the signal level generated by the ambient concentration of particles in the lab is equivalent to a soot volume fraction on the order of 10 ppt.

A few LII images were also acquired in the soot generator with the IR laser. The detection was broadband (unfiltered) and signals were integrated for 200 ns. An example image with the beam focused and spread vertically to about 5 cm is shown in Figure 69. An unfocused beam yielded an image detection limit (*f* 2.8) of ~0.2 ppb, while the focused beam resulted in a sensitivity perhaps 15 times less (3 ppb), still rather sensitive.

5.2.2 Linearity and Size Dependence

Considering the very large range of carbon concentrations, the LII signal is nearly proportional to soot loading. However, it deviates from a completely linear dependence (slope=1) and is best fit by a slope of 1.07, i.e., a signal that scales with concentration to the 1.07 power. The best fit line was produced using only measurements with a single air dilution (the maximum). Thus, with particle number density held constant (assuming one particle per water droplet as previously described), this line represents the behavior of the LII signal as a function of particle size (concentration $\propto Nd^3$). Converting to a size dependence, we find the LII signals scales like $d^{3.21}$. For comparison, an approximation from Melton[69] yields $d^{3.24}$ at a detection wavelength of 650 nm (an approximate average for broad bandwidth). The LII model, based on the parameters of the experiment, has a $d^{3.40}$ dependence for particles below ~200 nm diameter.

Based on the droplet size measurements by the PDPA and the soot concentration per droplet, the mean soot particle sizes range from 40 nm for the most dilute solution to 600 nm for the full strength solution. The effect of particle size is shown more clearly in Figure 70. The experimental calibration constant, C (signal normalized by carbon concentration as defined in Chapter IV), is plotted at different liquid dilutions, for the highest air dilution. This air dilution is chosen for its low soot density and short dryer residence time to avoid any possible influence of particle agglomeration. Alongside the experimental data, the results of the numerical LII model are also shown. Though the spectral bandpass extends from around 570 to 700 nm, the model result is reported for a constant detector responsivity over a small range (645-655 nm) where we expect the combination of detector response and LII emission to peak. Calculations near 550 and 750 nm change the result only slightly, moving the peak by about 50 nm in particle diameter in their respective directions.

The model and experiments both indicate a nonmonotonic size dependence. The calibration constant increases for small particle sizes, then reaches a peak before falling at larger sizes. The nonmonotonic response can be explained as follows. For particle sizes below the Rayleigh limit ($d_p \approx \lambda/\pi$), based on the *laser* wavelength, larger particles reach higher temperatures and emit more signal per unit volume (larger C) as described in Chapter II (laser absorption heating scales like volume but the dominant cooling mechanisms scale closer to surface area). For 1064 nm excitation, the limit is ~300 nm. Another Rayleigh limit can be defined, based on the *detection* wavelength (e.g., 200 nm for 650 nm detection). For particles above this size, nonvolumetric emission begins to reduce the signal per soot volume, i.e., the rise in C decreases. For particles larger than the excitation based Rayleigh limit, nonvolumetric absorption (proportional to surface area for very large particles) yields lower particle temperatures, which also tends to reduce the emission per soot volume. Together, these effects cause C to drop for particles larger than ~300 nm. This explains the different powers for size dependence previously noted for the experimental ($d^{3.21}$) and model ($d^{3.4}$) results. Including particles beyond the peak in the experimental fit, but not in the model prediction, produces a lower power than the model. For the smaller particles alone, both model and experiment scale like $d^{3.4}$

Looking back at Figure 68, it is difficult to determine whether the individual data sets for a given liquid dilution (particle size) scale linearly with soot volume fraction on their own. There is, in fact, some variation in C for each of these sets, though the deviation is on average only 10%. In addition, this variation is random, showing no correlation with air dilution across the different data sets.

5.2.3 Exhaust Temperature Dependence

Temperatures of common combustion exhausts can certainly vary. To test the temperature dependence of the LII signals, further measurements were made with the secondary air preheated before it was mixed with the carbon-loaded flow. LII signals for jet exit temperatures elevated to 300 ºC, and the earlier data at 70 ºC (which have been normalized by the average C's from this data set), are presented in Figure 71 against carbon concentration. Three liquid dilutions were employed (1, 1/20, and 1/400 strength) with a single air dilution of 770 cm^3/s. The plotted carbon concentrations were again corrected for the exit velocity variations from the elevated temperatures. This data agrees fairly well with the earlier data at 70 ºC. If a difference in local gas temperature has a significant effect on the rate of conductive cooling, one would expect the particles to have higher average temperatures in the hotter flow. Such an effect is not obvious in this data, which was, again, with 50 ns integration of the beginning of the signal. Again, for prompt detection, the model also predicts relatively little sensitivity in the peak particle temperatures to local gas temperature for a given particle size.

In summary, LII shows the ability to measure soot concentration over a wide range of concentrations and local temperatures. The particle size effect *is* present and seems to match the behavior predicted by the LII model. If particle size can be monitored separately or simultaneously, corrections can be made to concentration measurements where particle sizes are varying. The proposed methods for particle sizing are further explored in the soot generator in the following Section.

5.3 Particle Sizing

The spectral variation and temporal decay of the LII signal were measured to determine if either of the two particle sizing methods exhibited a sensitivity to the changing particle size. Further measurements employed both broadband detection in the red (OG570 filter) and the blue (BG3 & BG18 filters). Numerous carbon/water dilutions and fluences (IR) between 0.16 and 2.0 J/cm^2 were employed.

5.3.1 Spectral Ratio Method

For fluences below threshold, no variation in the red/blue signal ratio was observed for changing concentrations/particle size. In fact, C was also invariant for fluences below threshold. This would indicate that the size effect is vaporization limited.

The model indicates that vaporization cooling does dominate, at least, when it is present. If the conductive cooling mechanism is turned off in the model for fluences where significant vaporization occurs, much greater temperatures are, of course, observed over a 50 ns gate. This is due to the essentially nonexistant cooling over the latter half of the detection gate. However, the relative behavior of C and the spectral ratio with varying particle size remain essentially unchanged from results which include conduction. The variation in particle temperatures at early times is primarily induced by the different degrees of superheating attained during the vaporization period.

At higher fluences, where the nonmonotonic behavior of C is evident, a variation in the spectral signal ratio also occurs. Figure 72 displays signal ratios acquired with an unfocused IR pulse of 1.6 J/cm^2. Aerosol concentrations from 0.02 to 65 mg/m^3 are employed. Signal ratios are corrected to the best known absolute value by employing an integrated, average transmissivity for the broad filters, and correcting for the manufacturer-supplied spectral response of the PMT. In addition, the ratios are converted to equivalent blackbody values by correcting for the emissivity of the carbon particles.[*]

A decreasing trend in the signal ratio is apparent for increasing particle sizes. Then, the curve seems to increase again beyond 400 nm particles. This is quite different from the model, which says the minimum for the ratio occurs near 100 nm, even before the peak in C occurs near 200 nm. Peak temperatures are also about 500 K hotter than predicted. If the Rayleigh limit for the two detection wavelengths were in error, say the

---

[*] Caution should be applied in interpreting the temperature results, since the PMT degrades with time and may deviate from the original, manufacturer supplied spectral responsivity.

limiting size for the two were closer to each other, then a curve more like the experimental data might be attained. In general, though, the model and experiment agree in terms of the trend of the particle size effect.

For a number of exhaust concentrations, ranging from 0.01 to 4 ppm, signal ratios were acquired as a function of laser fluence. This data is shown in Figure 73. The measurements employed the unfocused IR beam from low to maximum energy, producing a maximum fluence of almost 3 J/cm^2. Once again, signal ratios (particle temperatures) can be seen to level out a little before the signal threshold fluence value. For these measurements, signals in the red were acquired with a long-pass filter (RG630) of slightly longer wavelength ‘cut-on’ value. Again, the signal ratios are corrected by a response factor that results from a calculated integration over the broadband response of the filter and the response of the PMT. This response curve fairly well falls on the 850 nm/450 nm curve of Figure 11. Calculated temperatures in the plateau region range from about 3800 K for the smallest particles to 4500 K for the largest, with an uncertainty of ±100 K.

5.3.2 Signal Decay Method

Given the promising results of the pyrometric method, an attempt was made to detect particle size variations by the expected differences in the LII signal decay rates. First, to satisfy a curiosity, a comparison is made between signals from the generator exhaust and the flame. Figure 74 shows LII temporal signal records for the smallest particle size (~40 nm) and concentration employed in the soot generator and at a height of 25 mm (30 nm particle) in the flame. A focused and an unfocused beam are used for the flame and exhaust, respectively, while the intensity is maintained at about 1 J/cm^2. Signals were recorded on the oscilloscope and are an instantaneous capture of a running average of 128 shots. The signal from the soot generator decays much more quickly. Higher temperatures can produce a quicker signal decay due to the ~T^4 behavior of blackbody radiation. However, a comparison of the instantaneous signal ratios at 60 ns suggests the particles in the flame are a few hundred degrees hotter. The influence of the very different local gas temperatures is clear; the particles in the colder exhaust cool much faster than the particles in the hot flame.

Further measurements were made with various aerosol concentrations and laser intensities. Figure 75 depicts an example of LII signals at an illuminating intensity of 1.0 J/cm^2. A running average of 128 shots on the oscilloscope is again employed. Data are displayed for the signals normalized both at the signal peak and at a 60 ns delay from the onset of the signal. For the data normalized at the peak signal, a change in signal decay is very hard to discriminate for particle sizes beyond the smallest three or four cases. Normalizing the data at a 60 ns delay results in no discernable difference in signal decay rate. This is significant, since these longer times correspond to the conduction-dominated period of the LII decay. These results occur in all cases, both above and below the threshold intensity.

Possible, but unlikely reasons, for this behavior include the following. One might believe that the higher temperatures reached by the larger particles, which would produce a faster signal decay, might be balanced by the slower conductive cooling of the larger particles. This would be an unfortunate coincidence for particle size measurements by this method. However, the model predicts similar variations in maximum particle temperatures as are experimentally detected, while predicting very discernable differences in the signal decay rates. This is also counter to the results from the flame showing the ability to discriminate different-sized (though smaller) particles. Another possibility might be that the spheroid agglomerates of carbon black that the generator produces blow apart (from internal vapor pockets, for instance) some time after the laser heating. If all the particles broke down into their constituent parts (~20 nm carbon black particles), the signal decay rates might be very similar. However, the fact that different particle temperatures are being attained suggests that if this happens, it does not happen quickly and it seems less likely that the particles would break apart at later times. Also, the signal decays do not exhibit some abrupt change that would coincide with such an event.

A more likely reason relates to the relative change in cooling with size for large particles, i.e., the larger particles all cool at similar rates. This is predicted by the model for very large particle sizes (> 200 nm), where the surface area to volume ratio is becoming very small. The four smallest particle sizes of Figure 75 are below 200 nm and thus should be detectable. However, these are number weighted average particle sizes. Recall that the aerosol has a range of particle sizes (Figure 64). More soot mass is accounted for by a larger particle than a smaller one. Therefore, the LII behavior would be weighted toward the larger particle sizes present. The effects of such particle size *distributions,* which are likely present in many practical systems, may cause errors for LII measurements in such environments. These are addressed in the next Section.

5.4 Distribution Effects

As an exercise for determining the influence of a nonuniform particle size distributions on the observed LII signal, a theoretical distribution is proposed. This is shown at the top of Figure 76. For simplicity, this distribution is comprised of particles from 3 nm up to 100 nm in diameter, therefore all particles are within the Rayleigh limit and absorb and emit volumetrically. The distribution is given a high population in a narrow region and a tail toward larger particle sizes, resulting in an average size of about 22 nm. This shape is similar to the nebulizer droplet distribution of Figure 24.

A numerical simulation is run for each particle size for IR illumination at 0.6 J/cm^2. The resulting value for the calibration parameter, C, for each size is shown at the bottom of Figure 76 for 650 nm detection. Then, the total signal for the distribution is calculated and divided by the total soot volume. This effective C for the distribution is also plotted where it falls on the existing curve, near 50 nm. This position corresponds to the volume-weighted diameter, $d_{43} = \int P(d_p) d_p^4 \, d d_p \Big/ \int P(d_p) d_p^3 \, d d_p$, of the distribution $P(d_p)$. The average C for the distribution ($\equiv \int C(d_p) P(d_p) d_p^3 \, d d_p \Big/ \int P(d_p) d_p^3 \, d d_p$) corresponds to $C(d_p = d_{43})$ because $C(d_p)$ is nearly a linear function of d_p (see Figure 76).

Much like the predicted sensitivity of the LII signal to particle size, this result suggests that where size distributions are present the LII signal will be sensitive to changes in this distribution. However, the sensitivity will be weighted more towards changes in the number density of the larger particles. In exhausts, premixed flames, and turbulent flows, where particle size distributions exist and change, it will be difficult to maintain a single calibration for concentration measurements. The change in C may not be unreasonable; for example for a d_{43} change from 15 nm to 40 nm, Figure 76 predicts only a 30-35% change in C for the modeled conditions. For environments where a nominally uniform distribution changed with position (e.g., the diffusion flame), it was proposed that particle size measurements could be simultaneously monitored with LII and used to correct concentration data. This also becomes more difficult with nonuniform distributions.

While the effective particle size of the emitting distribution in terms of signal magnitude is volume-weighted, the particle size as measured by the two proposed methods will vary depending on the detection timing. In Figure 77, results for both techniques are shown for discrete particle sizes and also for the given distribution. The pyrometric method (650 nm/400 nm, 50 ns gates) yields a diameter somewhat smaller than d_{43}, near 40 nm. This is due to the fact that while signals are volume-dependent, temperature differences between particles are dependent on specific surface areas. The signal decay method yields a similar number for early times, but at later times the decay is more like that of the largest particles. In this method, the decay is measured typically over quite long durations (>500 ns) to achieve good sensitivity to particle size.[91] If long times are employed, it will be difficult to calibrate this technique to a uniform distribution, whether one looks at a ratio of signals at two times or curve fits the whole decay. Without information on the actual distribution, the discrepancy between the measured particle size and the effective emitting size will be unknown.

Things may get a little more complicated for distributions, such as those from the soot generator, which include particle sizes that exceed the Rayleigh limit. In determining an effective C and particle size, one will integrate over a nonmonotonic function (for discrete particle sizes). The resulting function, which averages values at a discrete particle size with neighboring sizes, will not produce as sharp a peak in the nonmonotonic curve. This was seen in the data of Figure 70 which are shown again in the upper graph of Figure 78. This data utilized mean particle sizes as calculated from the droplet size distribution. The effective particle size should be somewhat larger. As the exact distributions are not known, the data are best fit to the model curve with a scaling factor on the calculated mean diameters. In the lower graph of Figure 78, the data have been replotted with the diameters scaled by 1.25, to larger sizes. The data do fit the model prediction better with the weighting toward larger particles.

On the whole, either particle size technique may remain valid for primary particle size measurements for real environments. However, varying particle size distributions and very large particle sizes will not be conducive to simple size measurements or modeling.

CHAPTER VI

CONCLUSIONS AND RECOMMENDATIONS

6.1 Concluding Remarks

Concentration Measurements

Measurements of the laser-induced incandescence (LII) of soot were made in a reacting flow (diffusion flame) where soot concentrations, particle sizes and a number of other parameters are well-known. LII was also applied to a non-reacting, exhaust-like flow (soot generator) where soot concentration is also known, particle sizes are controllable and at least qualitatively known, and other parameters are mostly unimportant due to their spatial uniformity. Good agreement (linearity) is shown between the LII signals and the known soot concentrations. The results indicate that consistent and accurate measurement of soot volume fraction (f_v) can be obtained with a variety of excitation and detection strategies for exhausts and combustion flow.

In fact, the broadband LII signal employed in the soot generator was shown to provide a reasonable measurement of the volume fraction of soot in air over a range of 4 orders of magnitude. Also, a soot detection limit for LII with this optical setup (*f* 4.4) better than 1 part per trillion (ppt) was observed. This sensitivity is well below the ability of extinction measurements and much preferred to the long sampling times and intrusive effects of sampling.

In the flame, where particle sizes were spatially varying (at low heights), the variation in C (40%) exceeded that predicted by the model (25%). Based on the soot generator results, it is likely that part of the change in C in the flame is due to particle size effects, and the remainder is the result of changes in soot composition/morphology, or perhaps more likely, the presence of soot precursors. The two soot concentration diagnostic methods (LII and extinction) would likely have different sensitivity to these effects. While both are absorption based, extinction and LII respond to different particle parameters (e.g., particle emission versus scattering). The complexities of this environment were one of the motivating factors for moving to the soot generator, where the behavior of LII with certain parameters, like particle size, could be better isolated.

Strong gradients in soot concentration will be a challenge for LII concentration measurements where the signal 'saturation' effect is desired. Through the 'plateau' range of fluences, the signal-emitting region shifts from the middle of the beam to the wings. Differing LII signal versus laser fluence curves were obtained for detection at position 1 (and in the uniform soot generator aerosol) and position 3. In the direction of the detection path, Position 1 has a near uniform profile, while position 3 does not. The different responses are believed to be different weightings of a small beam irregularity by the two concentration profiles. Thus, the LII signal is sensitive to the soot concentration, particle size or property distribution in the detection path direction.

Particle Sizing

Two LII-based particle sizing methods were also proposed. Under the right conditions, each should be capable of making useful particle size measurements. The first was essentially a measure (S_λ) of the temperatures attained by different-sized particles. The sensitivity of this method to local gas temperature is very low. The predicted trend in the signal ratio with particle size was found for the soot generator data. Ratios decreased with increasing particle size, then increased again at very large sizes (~400 nm). This is quantitatively in some disagreement with the model, which predicted a peak in the curve at ~100 nm and a peak temperature nearly 500 K greater.

This technique was also used to measure particle temperatures with changing laser fluence. In the flame, the particle temperature (50 ns integration, 30 nm particle) was found to vary from 4000 to 4400 K (±150 K) from threshold to more than 100 times threshold. This is not a big change considering the large change in input laser energy. This is also very close to the model prediction, which indicates a temperature range of 4100 to 4600 K. In the soot generator, temperatures were measured against fluence only to about 5 times threshold. These were fairly constant over this range, yielding particle temperatures of 3800 to 4500 K for mean particle sizes from 40 to 300 nm.

The other proposed sizing method examined the decay rates of the LIII signals from different sized particles. This method has the positive aspect of being insensitive to signal trapping, which was certainly a factor in the flame. These differing decay rates were easily discernable in the flame and repeated particle sizes fell on nearly the same curve. In the soot generator, only the two smallest particle sizes were resolvable. The model shows that decay rates do become hard to distinguish at about 200 nm. This indicated that the effective particle size for the soot aerosol was probably greater than the mean value calculated from the droplet size distribution.

Soot Generator

The soot generator performed to expectation. An analysis of samples of the exhausted aerosol by scanning electron microscope (SEM) indicated that, as intended, the device was producing nominally spherical particles and that the average particle size was indeed increasing with the concentration of the carbon black/water solution. The results of the particle size distribution analysis of the SEM pictures indicate distributions which are similar in shape to the measured droplet distribution form the nebulizer. However, small particles are expected to evade capture in the sampling process and agglomeration effects in the liquid solution or downstream are unknown. Therefore, the size distribution measurements are considered merely qualitative.

Other analysis was performed on the character of this exhausted aerosol. Spectral emission scans and LII signal measurements with changing laser fluence were performed. These experiments copied those made previously in the flame in order to compare the LII/thermal behavior of the two carbon particulates. While definite differences exist in the size and structure of the soot in the diffusion flame and the aerosol produced by the soot generator, agreement was shown for the spectral character of the emitted LII signal and the response to varying laser fluence. This is in agreement with other research that concluded the internal structure of combustion-generated soot and pyrolysis-generated carbon black to be the same. Also, given the differences in the two soot fields and some sizeable uncertainties in the calibration, the measured factor of 1.7 agreement in C between the flame and soot generator is reasonable.

LII measurements were made in this exhaust over a temperature range of 70 to 300 °C. Though a few hundred degrees can have a significant effect on the local gas density, this does not appear to have a serious effect on the particle temperatures during and near the laser pulse (e.g. the first 50 ns).

LII Model

A numerical model of the LII process was also employed in a predictive manner and in simulation of some of the exact experimental parameters employed in this research. The model predicted that the LII signal would have a dependence on the size of the soot particles. Thus, the linearity of LII measurements with concentration where particle sizes were changing along with soot concentration would also be dependent. Illumination and detection conditions were arranged to minimize this effect. However, a notable effect was still expected. This was, in fact, experimentally demonstrated in the soot generator. Bigger particle sizes were shown to reach higher temperatures and thus emit stronger signals due to their surface area/volume ratio (cooling rate/heating rate ratio). Beyond a certain particle size, the model predicted this signal strength per soot volume (C) to decline again due to exceeding the Rayleigh particle size limit for volumetric emission and, perhaps, absorption. This nonmonotonic behavior was also demonstrated experimentally.

Good agreement was shown for temperature measurements (via S_λ) in the flame and temperatures were not grossly off in the soot generator. This builds confidence in the ability of the model to reproduce the physics of the vaporization process. Measured signal decay rates, however, are significantly off the model prediction in both the soot generator and the flame. Thus, a flaw in the conductive cooling model may be indicated.

Laser/Fluence Issues

With varying laser fluence, both soot fields exhibited the 'threshold' effect expected of a 1-D Gaussian illuminating beam profile. The usefulness of this quality for LII imaging was demonstrated with the production of a relatively smooth signal from a streaky laser sheet. In analyzing the LII signals in the flame against laser fluence, the trend of the LII signal above threshold was determined to be sensitive to a number of parameters. This includes a strong sensitivity to small beam shape defects, concentration gradients in the soot field on the order of the beam size, and, for visible excitation, the emission from laser-produced C_2 molecules. This helps explain the wide variety of results to be found in the literature on the response of LII to changing laser fluence.

For lower intensities, the insensitivity of the LII signal to laser fluence will depend on the general shape of the beam. As the intensity is increased, the signal-generating region moves to the wings of the laser. The signal will become more dependent on any small inhomogeneities in the edge of the beam.

For 532 nm illumination, the presence of C_2 emission is quite pronounced for fluences above threshold. However, there does appear to be a small range of fluences above threshold where C_2 emission may not be significant for blue detection (at least for soot concentration measurements, but not perhaps for temperature measurements). For red detection, there seems to be no problem for any fluence level. Images acquired in this research are in agreement with the findings of Shaddix and Smyth[63] that fluorescence from PAH is not detectable with the visible source. Therefore, if visible excitation were preferred for some reason (ease of alignment, simultaneous scattering measurements, etc.), accurate LII concentration measurements should be achievable.

The C_2 emission itself may be a contender for soot concentration measurements. Blue signals at high intensity (much C_2 interference) showed a better agreement with the extinction measurements than signals without interference. The C_2 signal seems to be sensitive to the same species low in the flame (e.g., soot precursors) that extinction is. Of course, this would not be advisable in a range of high soot concentration, where the laser is significantly attenuated. Recall, the C_2 signal has a strong dependence on the laser intensity. Also, other sources for the creation of C_2 exist in the form of PAH molecules. Thus, this approach may be isolated to nonreacting flows such as exhausts.

The infrared source would be the preferred source for consistent LII measurements, since it does not exhibit significant C_2 interferences over a large range of fluences. At high fluences, only detection near 516 nm and 474 nm are significantly effected. Thus, either red or blue (e.g., 430 nm) detection can be used. Signals are nearly as strong as with visible excitation, and can be increased further by increasing the bandwidth of the spectral filtering. Also, laser beam trapping in dense environments will be limited to particles and the largest molecules. In addition, for measurements made in the presence of PAH, the infrared source should have difficulties exciting fluorescence from these molecules or being absorbed to break them down into C_2.

The C_2 emission that *is* produced by the IR beam (e.g., at 516 nm) at very high energies increases in a linear manner with laser fluence. It is assumed that this production is proportional to the amount of C_2 vapor produced, i.e., that the IR illumination does not couple into the vapor (in a two-photon process) and induce fluorescence. Assuming the thermal behavior of the soot particle is the same for green or IR illumination, then C_2 is produced in proportion to laser fluence for the green laser, also. As the C_2 contribution at 516 nm with green illumination increases at a very high rate, yet is still linear, it is concluded that laser-induced fluorescence of the species is occurring and that the process is saturated.

C_2 interference can also be avoided with the use of delayed detection. Signals gated within 100 ns from the signal onset showed good agreement with prompt LII data. Note that these delayed signals are somewhat smaller in magnitude. Longer detection gates will increase the signal, but is uncertain how this might affect the scaling with concentration. The lower particle temperatures at increasing delays, when conductive heat transfer is the dominant mode, are expected to make the signal more sensitive to local gas temperatures and particle size. The greatest sensitivity to detection delay in the flame was seen at the lowest heights. C decreased faster here and the spectral ratio (S_λ) increased faster here, both indicative of faster cooling. As flame temperatures are not significantly cooler here, this is assumed to be the result of a higher cooling rate for smaller particles.

Application Issues

The maximum trapping in the flame (at 40 mm HAB and a 90° detection angle) was measured to be 30% and 45% for red and blue detection, respectively. Measurements at a detection angle of 50° reduced the amount of trapping by a factor of about 4, yielding a good compromise between minimizing the trapping and trying to maintain a detection angle somewhat normal to the laser beam. Trapping levels from this angle were ~10% at 40 mm HAB and ~5% at 15 mm HAB.

Some analysis was made of the effect of a nonuniform particle size distribution on making accurate soot concentration and particle size measurements. The idea that the effective particle size is larger than the calculated mean is supported by the fact that the C's for the different aerosol concentrations/particle sizes match the model better when scaled to slightly greater particle sizes. Also, the measured nonmonotonic curve (C vs d) was somewhat flatter than the model result. This is also expected to occur for a distribution of particle sizes with a significant range. The behavior of a distribution of particles will be weighted toward the larger particles. Without some prior knowledge of the distribution, accurate particle size measurements will be difficult for either of the proposed techniques. The calibration for concentration measurements will also be susceptible to error in regions where the nonuniform distribution is changing.

Finally, a side application for LII was instigated in the exhaust of the soot generator, and then continued in the flame. This was a type of flow tagging that was developed for velocity measurements in particle-laden flows. It involved employing a high-intensity laser pulse to vaporize a region of soot and subsequent interrogation by imaging the surrounding region (and empty zone) with either LII or elastic laser scattering. This technique was termed Particle Vaporization Velocimetry or PVV. Simultaneous mass concentration (from the LII signal of the marking pulse) and velocity measurements can be made that would permit determination of local soot mass flux. The long lifetime of the tagged regions (>2 ms) allows velocity measurements over a wide range of velocities. Recent results have been summarized in a submitted journal paper, reference .

6.2 Recommendations

General

Several recommendations are offered for future work. In general, the infrared laser source is suggested for most LII measurements as it is less problematic. Most detectors are rather blind to this wavelength, the beam shape is unmodified by any frequency-doubling device, and photons of this energy will have a difficult time exciting emission from nascent PAH or C_2 or from vaporization-generated C_2. Detection at any visible wavelength should produce similar results. Red signals last longer, but detectors are generally more sensitive to shorter wavelengths.

Attention should be payed to the shape of the laser beam, and to the comparative dimensions of the beam depth (direction of detection) and soot concentration gradients in the region of interest. If possible, the beam depth should be made small compared to such soot (or other property) gradients. For imaging, long focal length lenses should be used for laser focusing. A laser intensity distribution close to uniform in two dimensions and Gaussian in the other appears optimal for producing the LII signal 'plateau' behavior. Highest laser energies should be avoided to prevent all the signal from originating in the wings of the beam.

The long-pulse dye laser remains open for investigation as a potential visible LII excitation source. The lower power density may be less susceptible to generating C_2 emission and higher overall signal strengths may be achievable.

If a method can be found to produce a carbon black aerosol with a narrow particle size distribution, such an aerosol could be used for seeding flows without particulates. Such seeding could yield local gas temperatures from the signal decay method and flow tagging velocities with long lifetimes from LVV.

The double pulse capability of the current laser setup could also be taken advantage of for LII measurements. A second LII-generating pulse could probe the conditions of particles shortly after heating by a first pulse. One such investigation has already been performed in other research.[37]

Flames

Hydrocarbon flames often contain high concentrations of soot. The trapping of LII signals in such an environment is difficult to avoid. Measurement of the LII signal from different detection angles should at least provide the ability to determine qualitatively whether trapping is a significant issue for a given combustion zone. A more adventurous idea would be to remove the soot from between the region of interest and the detector. This could done with another laser beam focused into this area, perhaps limited to only a stripe vaporized by a laser sheet transverse to the imaging sheet.

For regions where the particle size does not change very much, the spectral signal ratio could perhaps also be used as an indicator of how much soot was blocking the signal. This would require a reference ratio at a region where trapping is very small. Signals affected by trapping could be corrected for the interfering effect of the determined volume of soot.

Visible excitation may provide alternative information. LII and C_2 signals seem to sensitive to different materials. Initial indications suggest that C_2 signals are generated by anything that will absorb visible light and produce C_2 on breaking down. LII meanwhile (red detection preferred), is sensitive to carbon particulate. Visible excitation, with two spectrally separated detectors, could provide an instantaneous map of the regions where these different species are concentrated.

Exhausts

Most combustion devices utilize ambient air as the oxidizer. This gas contains nascent soot as well as particulates of other species. It would be useful to find out how other particulate matter, like metal oxides e.g., might interfere with soot LII. Alternatively, LII might be applied to these particulates in other chemical processes or for 'cleanroom' particle sensing and quantification.

Very large particles, outside the Rayleigh regime, should be avoided. Surface heating will cause an increase in particle surface temperatures, resulting in higher vaporization rates and 'thermal' C_2 emission. However, the volume-specific absorption and photon emission are decreased. Thus, so is the volume-specific signal (C). The model and experiments disagree somewhat on the effect for the observed particle temperature, except that the initial trend with increasing particle size is toward higher temperatures. The exact effects are dependent on the particle size distribution, which is generally not known. For particle sizes in typical combustion flows, this condition is generally not a problem.

Soot Generator

Particles of this magnitude (>~200 nm) do exist in the present soot generator and the lower limit is at the high end of typical combustion situations. It would be worthwhile to research the possibility of soot generator design that could produce smaller particle sizes. A *uniform* size distribution or *control* over the size distribution or *measurement* of the size distribution would aid in further research to understand and model the particle size effect on the LII signal.

Aside from these motivations, the current soot generator has a flaw that is inherent to the design of the atomization process. Due to the venturi design, a small pressure differential creates the spray. As a result, the nozzle is subject to a slow or instantaneous clogging and/or unclogging. Avoiding the highest solution concentrations helps. Likewise, the highest concentrations also show some signs of particle settling, necessitating constant stirring. Design of a new generator with a more stable output is suggested. If liquid atomization is kept in the design, a greater pressure differential should do the forcing.

LII Model

The model has shown reasonable agreement with experiments for the vaporization-dominated period. Signal decays suggest the conductive cooling model may be significantly off. It has been suggested[89] that the thermal accomodation coefficient may be way off (factor of 4.5, in fact). This detail, and the overall model, could use some investigation.

It has also been suggested, from TEM analysis, that the soot particles, when heated, undergo a 'melt' which allows their structure to proceed to a denser and more energy-conservative crystallite arrangement. Some pictures show radiated soot particles with the graphitic crystallites rearranged tightly in parallel at the outside of the soot particle with a void in the middle. The timing or reality of this process are not known for certain, but model adjustments could be made to explore the effects of accounting for a process such as this or, for example, for the energy that goes into 'hot' C_2.

FIGURES

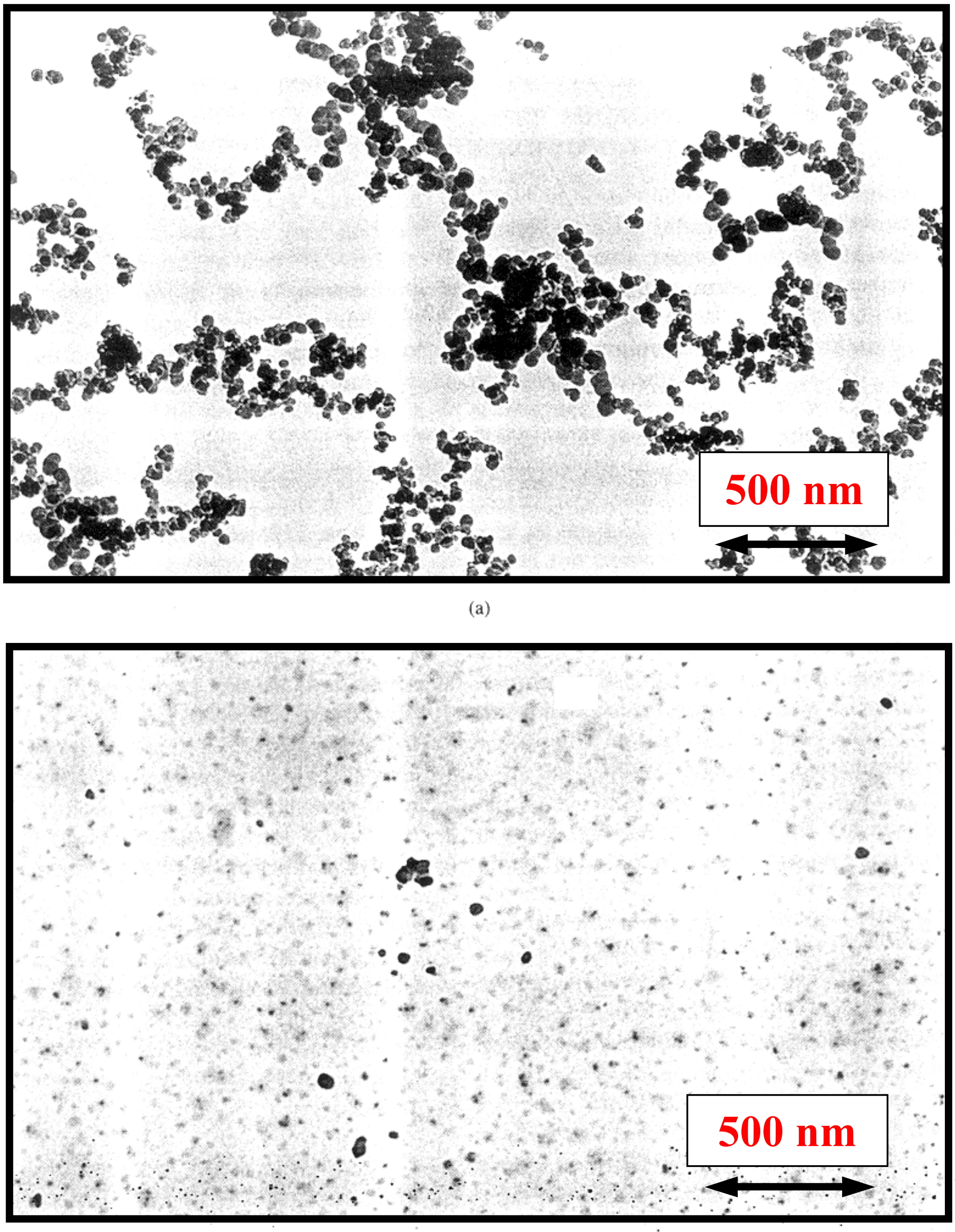

Figure 1. Transmission electron microscopy (TEM) image of particles sampled from 50 mm (above) and 12.7 mm (below) height at the axis of an ethylene flame identical to the one used in this research.[29]

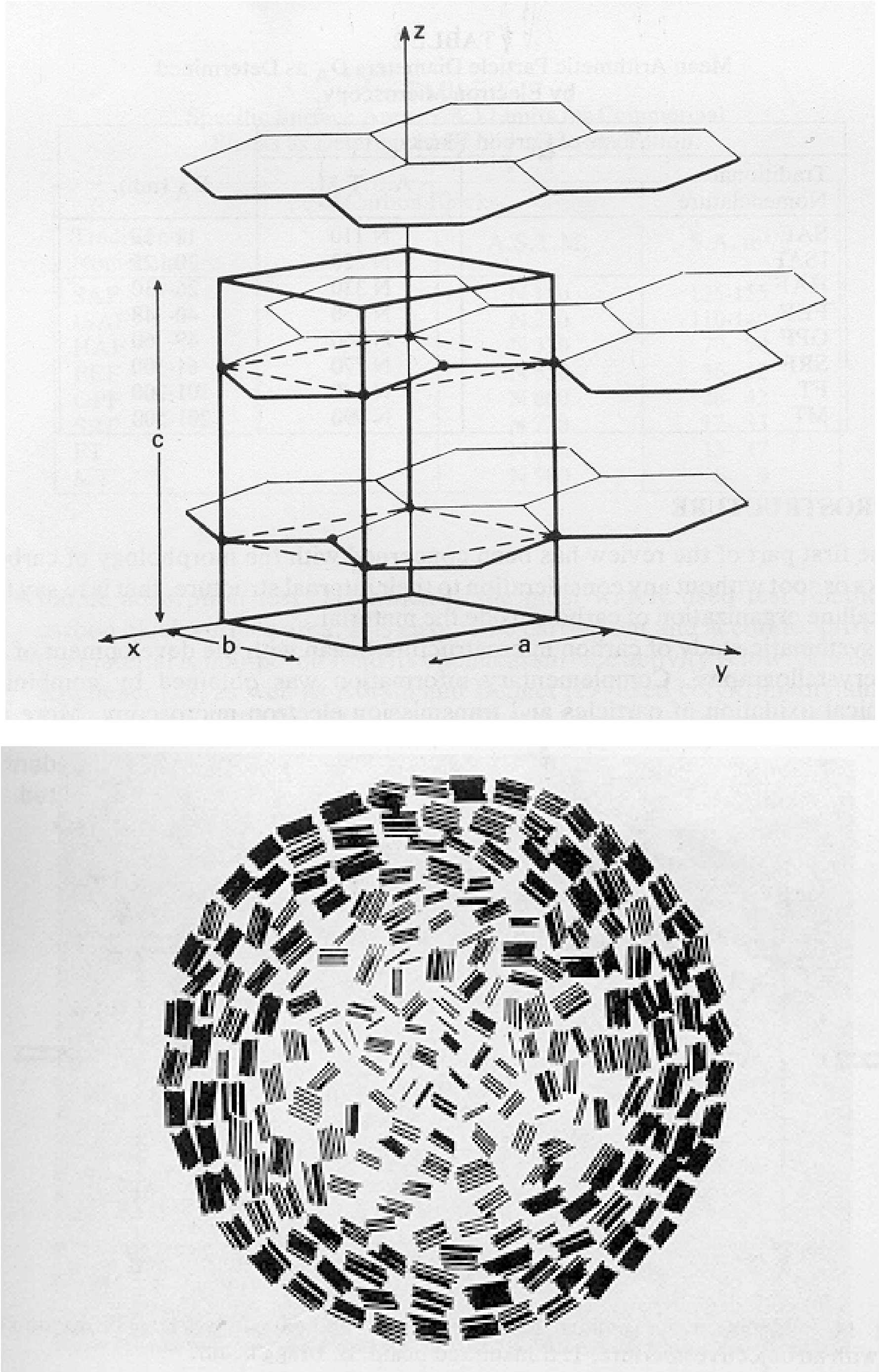

Figure 2. The internal structure of soot. Above: Molecular structure of graphite (symmetrical hexagon, a = b = 0.2461 nm, c = 0.6708 nm).[27] Below: Schematic of Heckman and Harling's 1966 model of carbon black microstructure.[27]

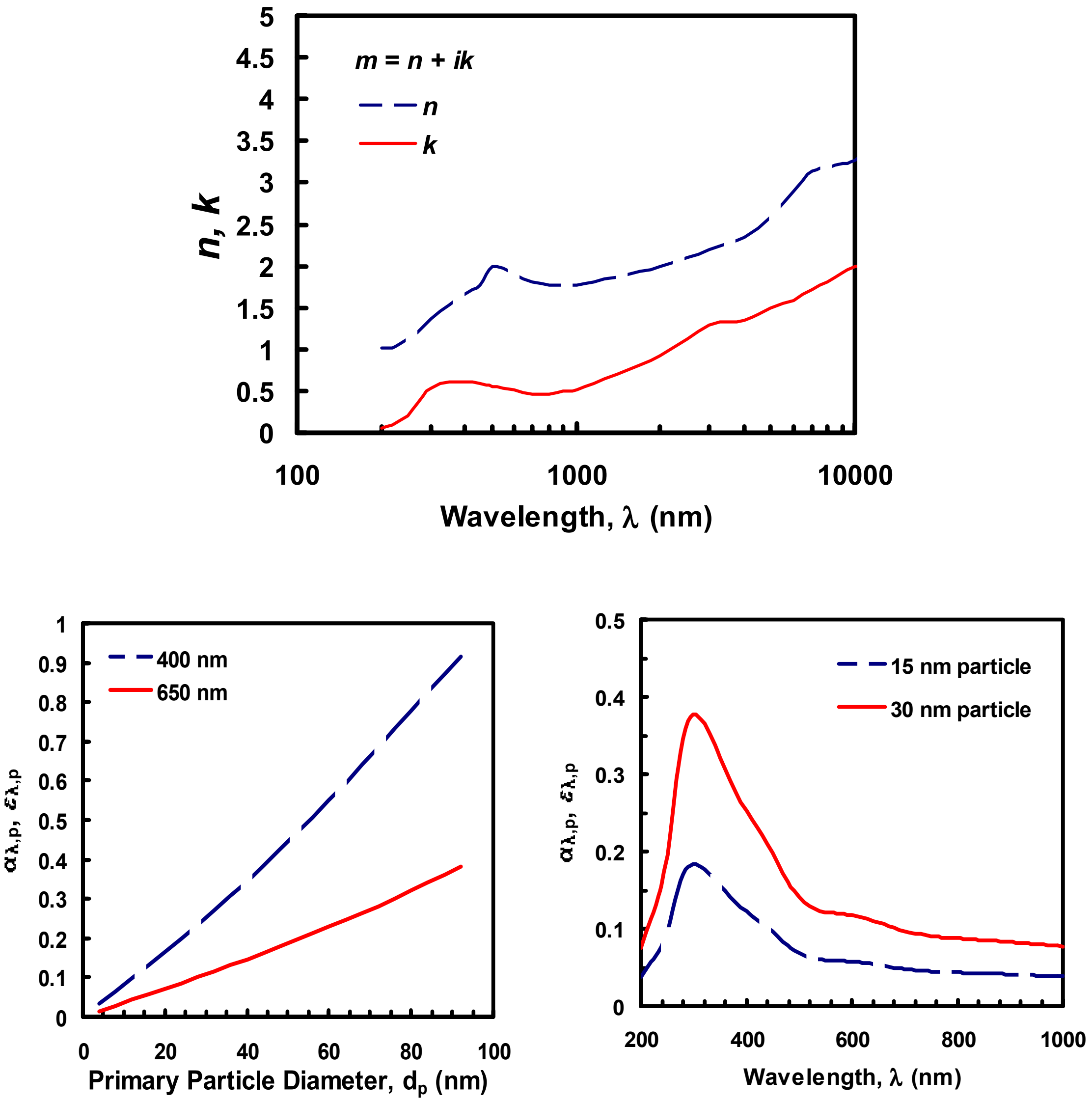

Figure 3. The optical properties of soot. Above: Real (*n*) and imaginary (*k*) parts of the complex index of refraction of soot.[98,101] Below: Spectral absorptivity/emissivity of primary soot particle versus particle size (for two wavelengths) and versus wavelength of light (for two particle diameters)[108]

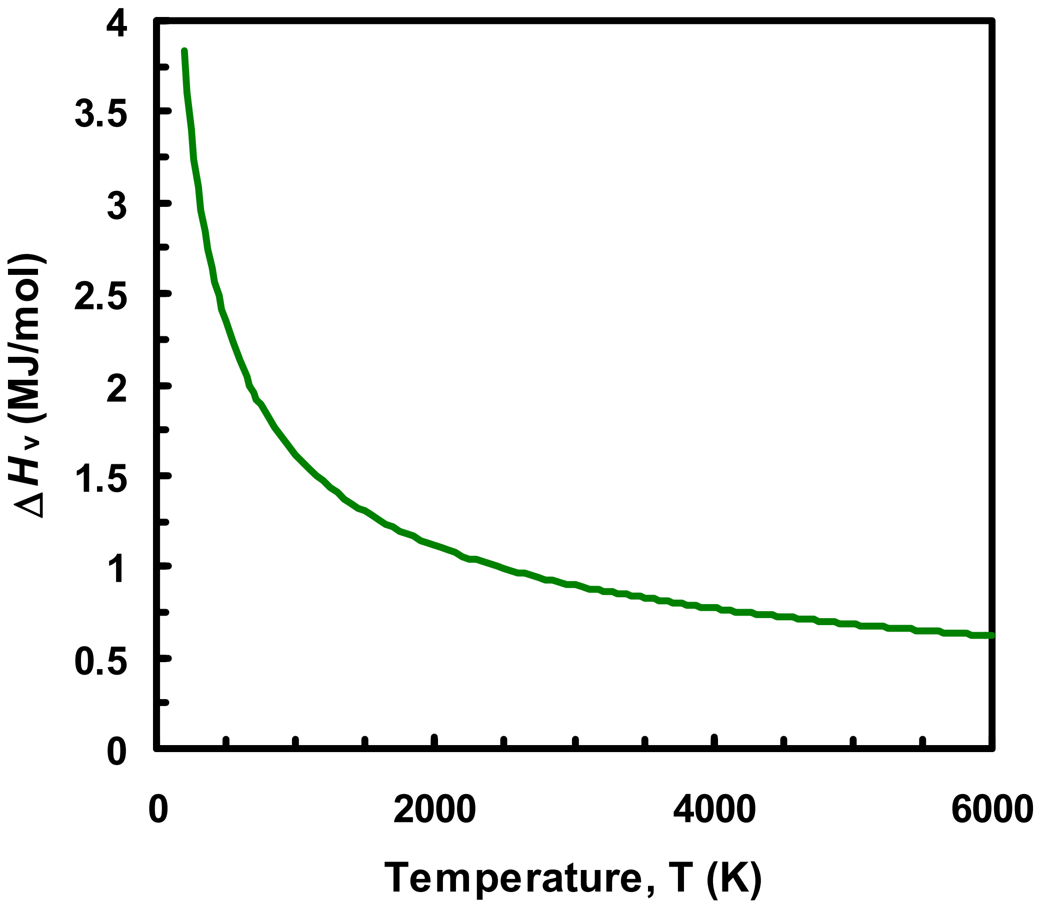

Figure 4. The enthalpy of vaporization of carbon as a function of particle temperature. The graph is a curve fit ($\Delta H_v = 6.58 \times T^{-0.536}$) to the data of Leider *et al.*[3]

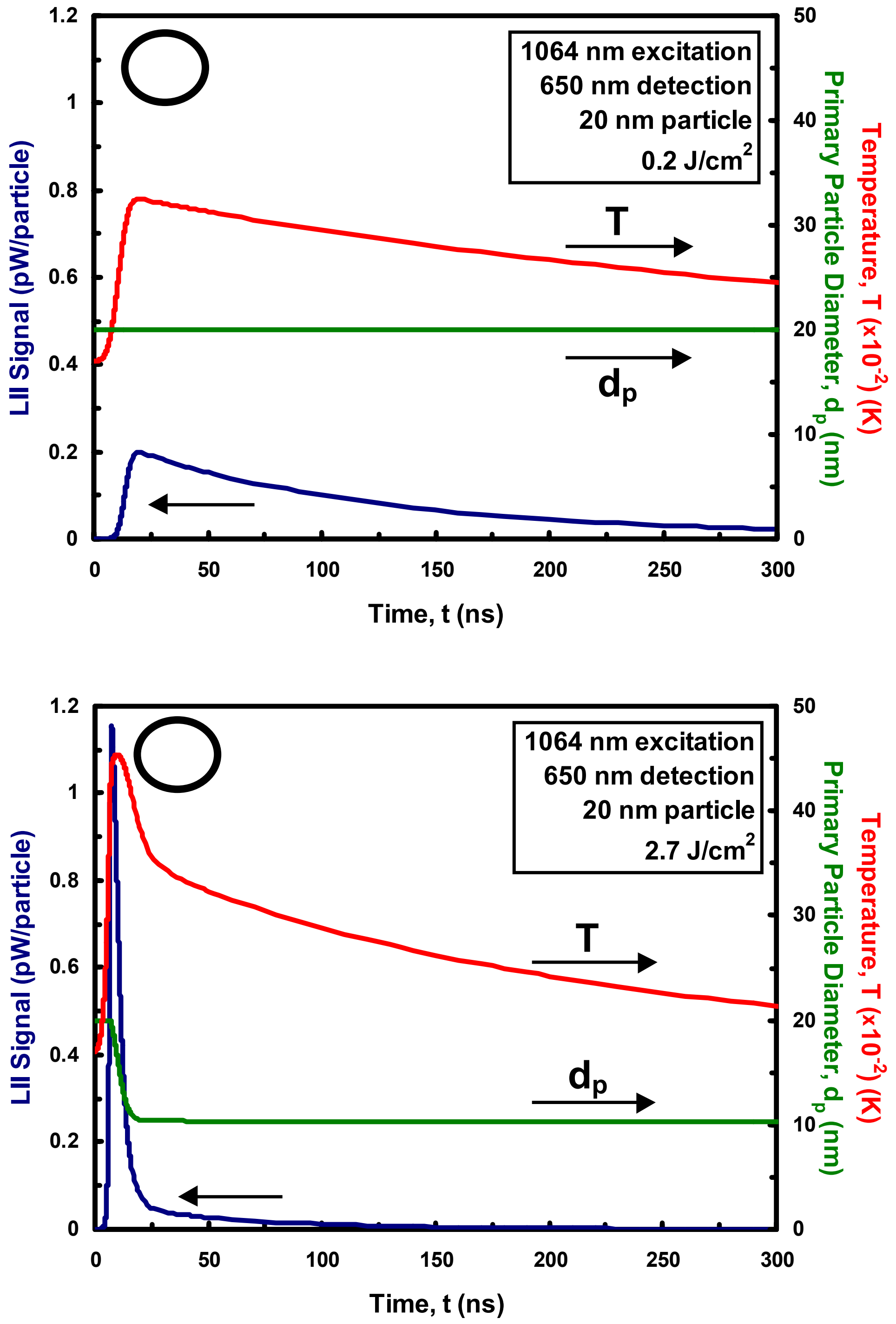

Figure 5. Uniform laser profile: Temperature, size, and signal (650 nm) time histories for a 20 nm particle illuminated by a 8 ns FWHM Nd:YAG pulse (1064 nm) of 0.2 (A) and 2.7 (B) J/cm^2.

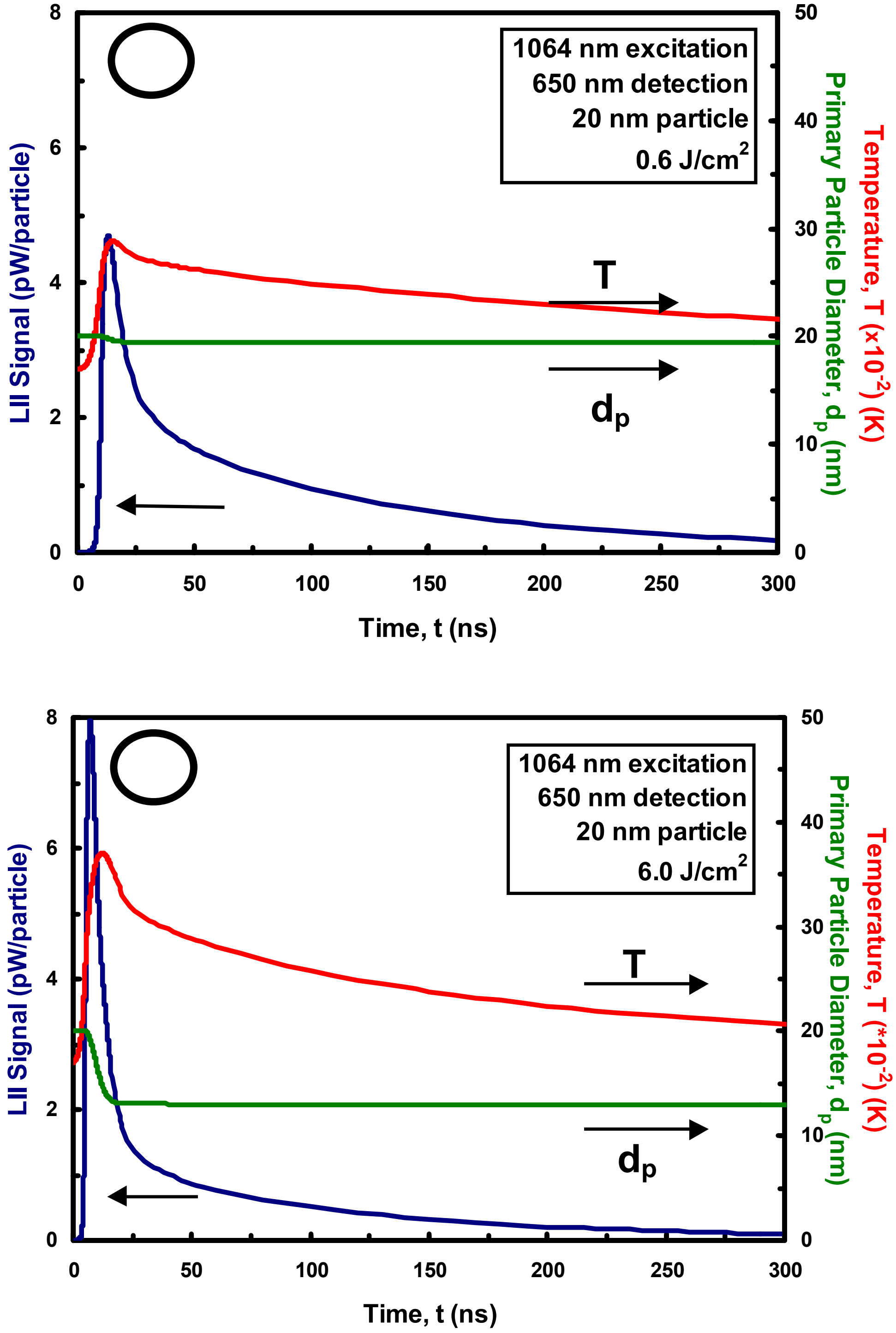

Figure 5. Gaussian laser profile: Temperature, size, and signal (650 nm) time histories for a 20 nm particle illuminated by a 8 ns FWHM Nd:YAG pulse (1064 nm) of 0.6 (C) and 6.0 (D) J/cm^2.

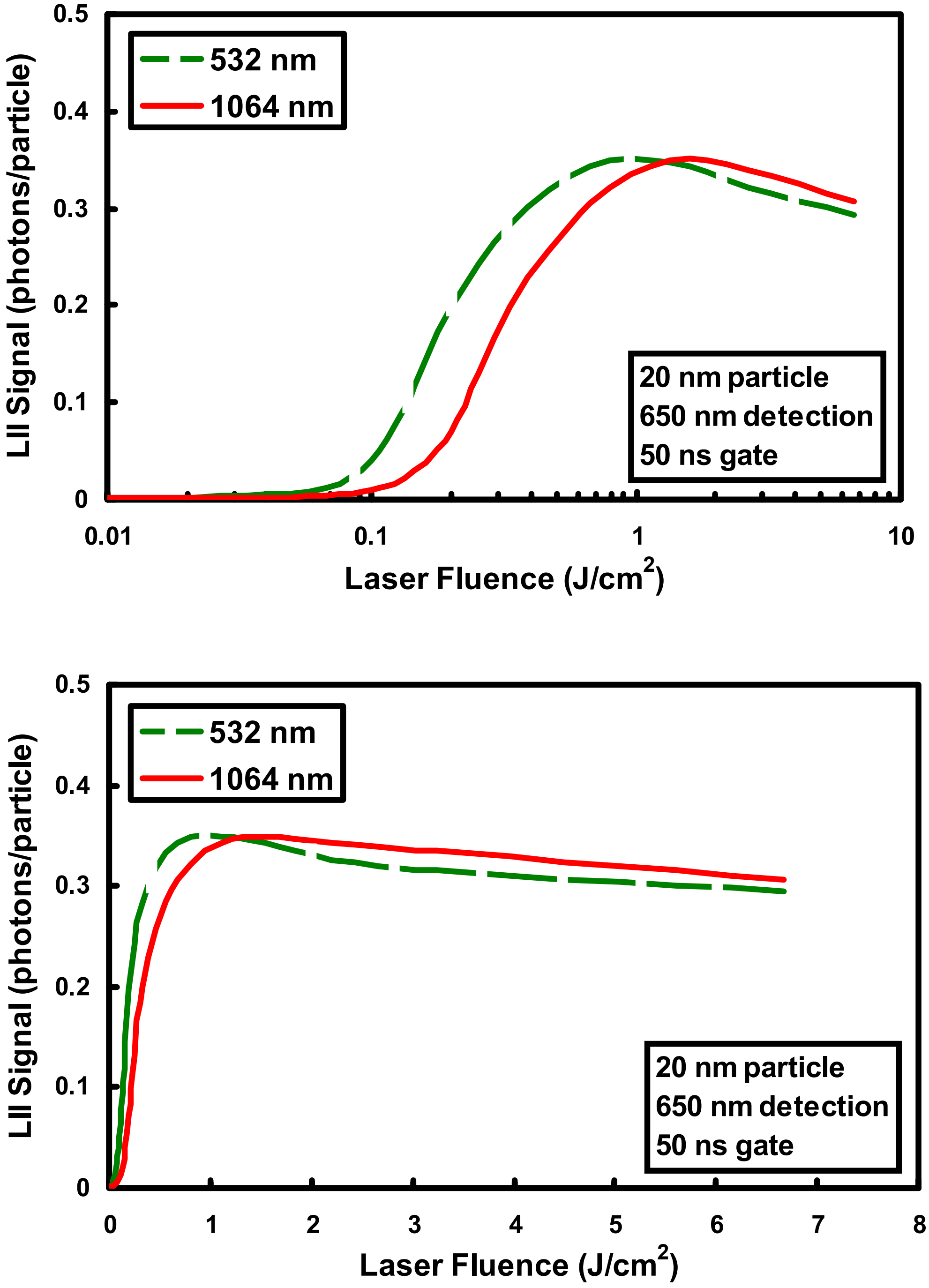

Figure 6. Time-integrated (50 ns prompt gate) LII signal for a 20 nm particle versus nominal beam-integrated (FWHM) laser fluence for 1-D Gaussian illumination at 532 and 1064 nm. Local gas temperature is 1700 K and detection is at 650 nm, 10 nm bandwidth.

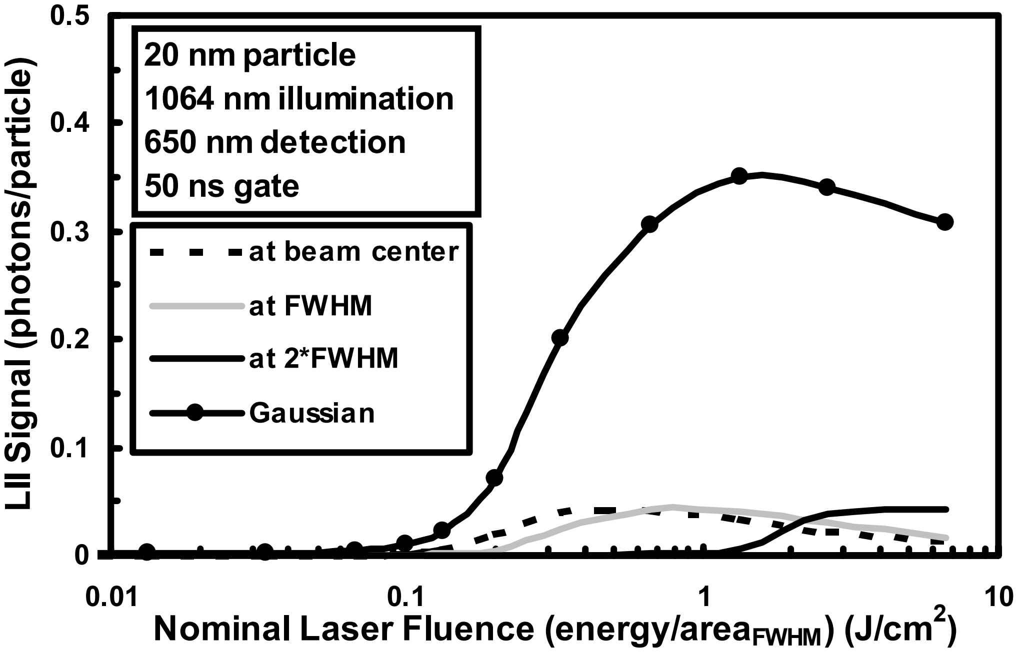

Figure 7. Time-integrated (50 ns prompt gate) LII signal for a 20 nm particle and time-integrated contribution from three discrete locations in the beam versus nominal beam-integrated (FWHM) laser fluence. Local gas temperature is 1700 K, laser excitation is at 1064 nm, and detection is at 650 nm.

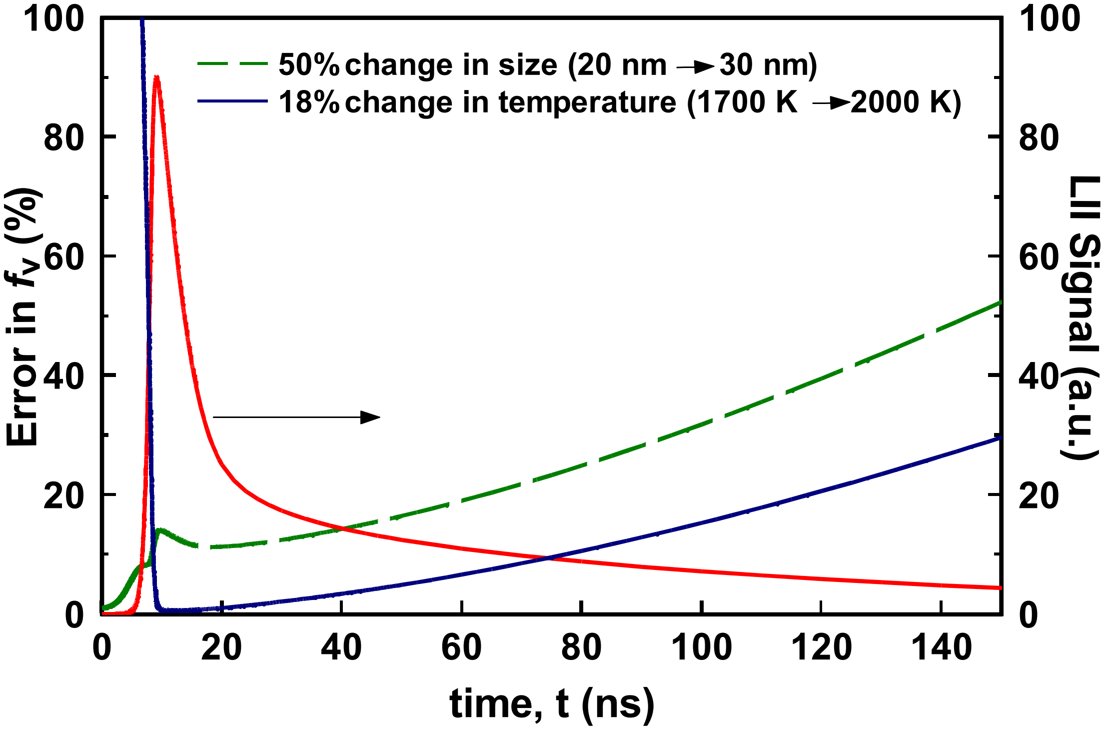

Figure 8. Error incurred in LII measurement of soot volume fraction for a 50% variation in particle size or a 18% variation in local gas temperature, at the nominal conditions of a 20 nm particle in a 1700 K environment. Laser excitation is by a 0.5 J/cm^2 pulse at 532 nm. Signal detection is at 650 nm.

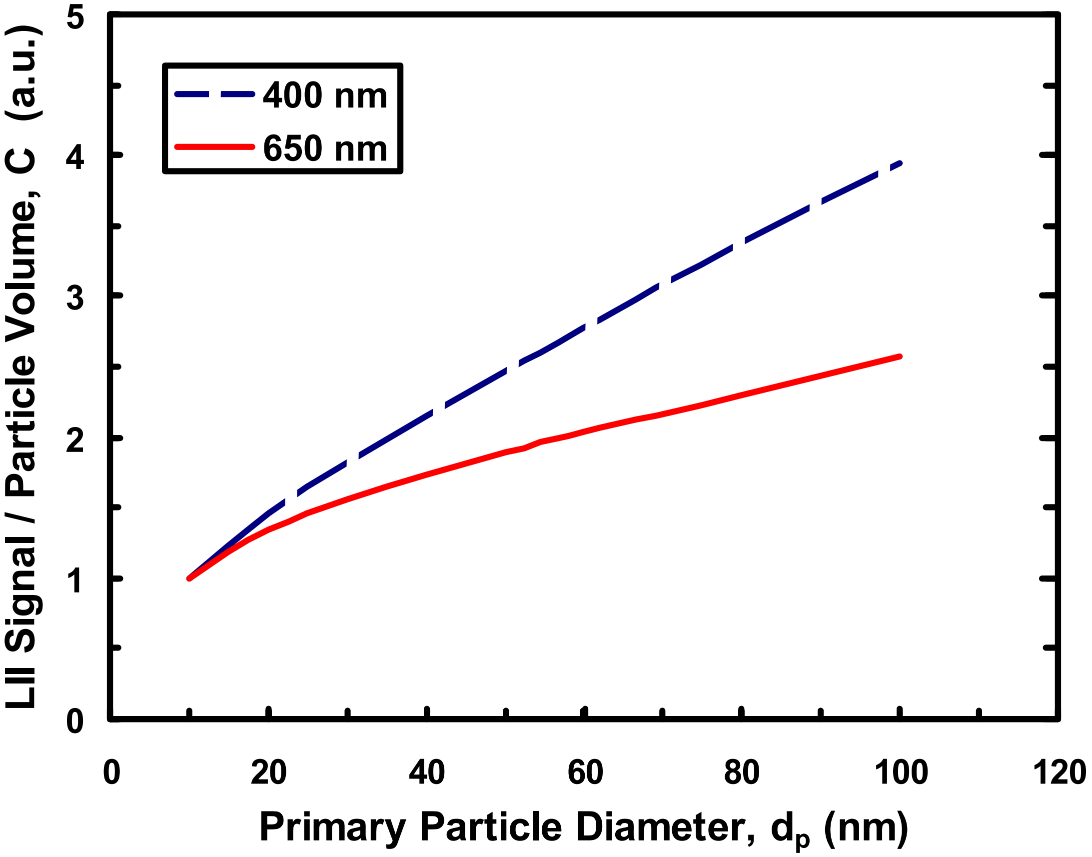

Figure 9. Time-integrated (50 ns prompt gate) signal per unit soot volume (mass) versus particle diameter for 650 and 400 nm detection. Local gas temperature is 300 K and the laser excitation is by a 1.6 J/cm^2 pulse at 1064 nm.

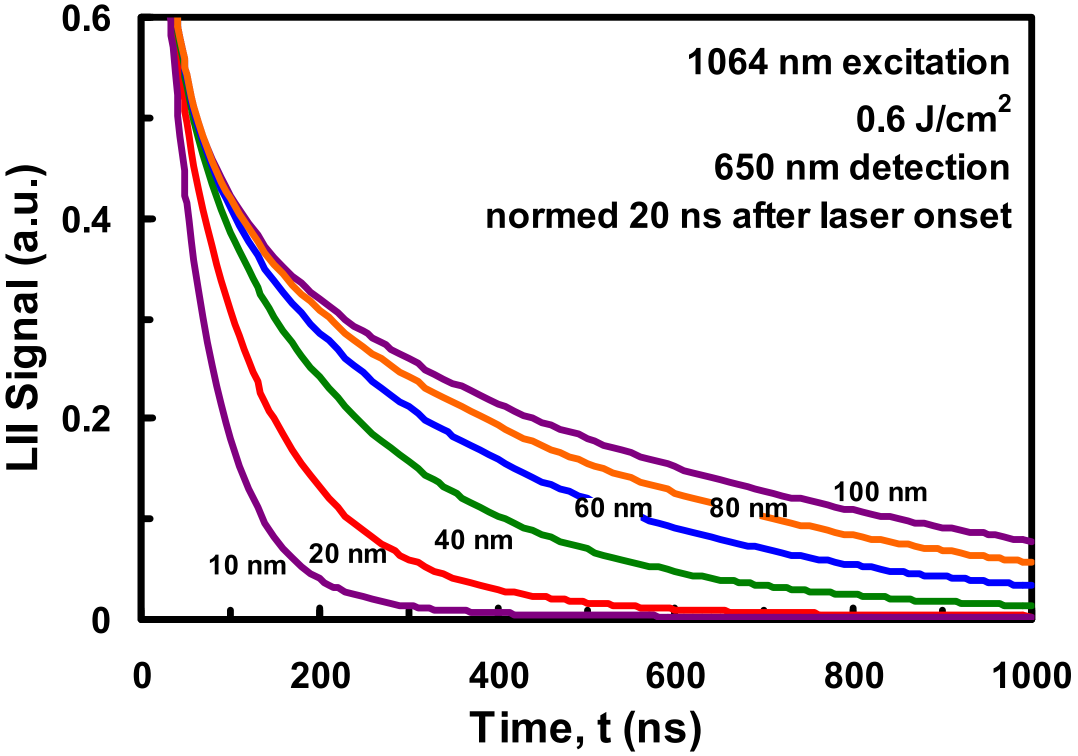

Figure 10. Model results for the signal decay from different sized particles illuminated by a 0.6 J/cm^2 laser pulse at 1064 nm. Detection is at 650 nm. Ambient temperature is 1700 K. Signals are normalized to each other at 20 ns after the start of the laser pulse.

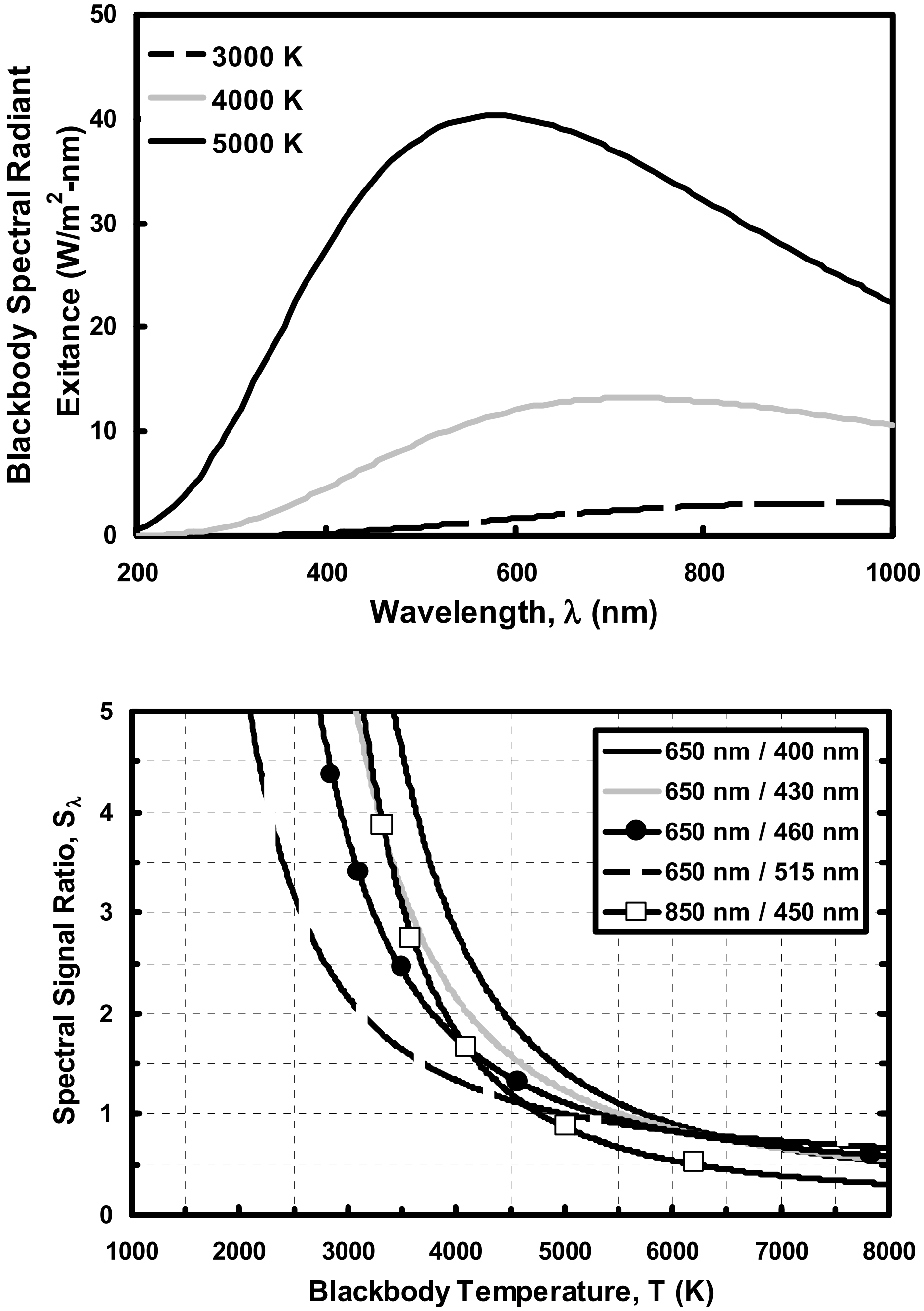

Figure 11. Blackbody behavior as a function of temperature. Above: Light intensity emitted by a blackbody at different temperatures, illustrating the spectral shift of the intensity peak. Below: Blackbody spectral signal ratios (S_λ) for several long/short wavelength pairs, plotted against temperature.

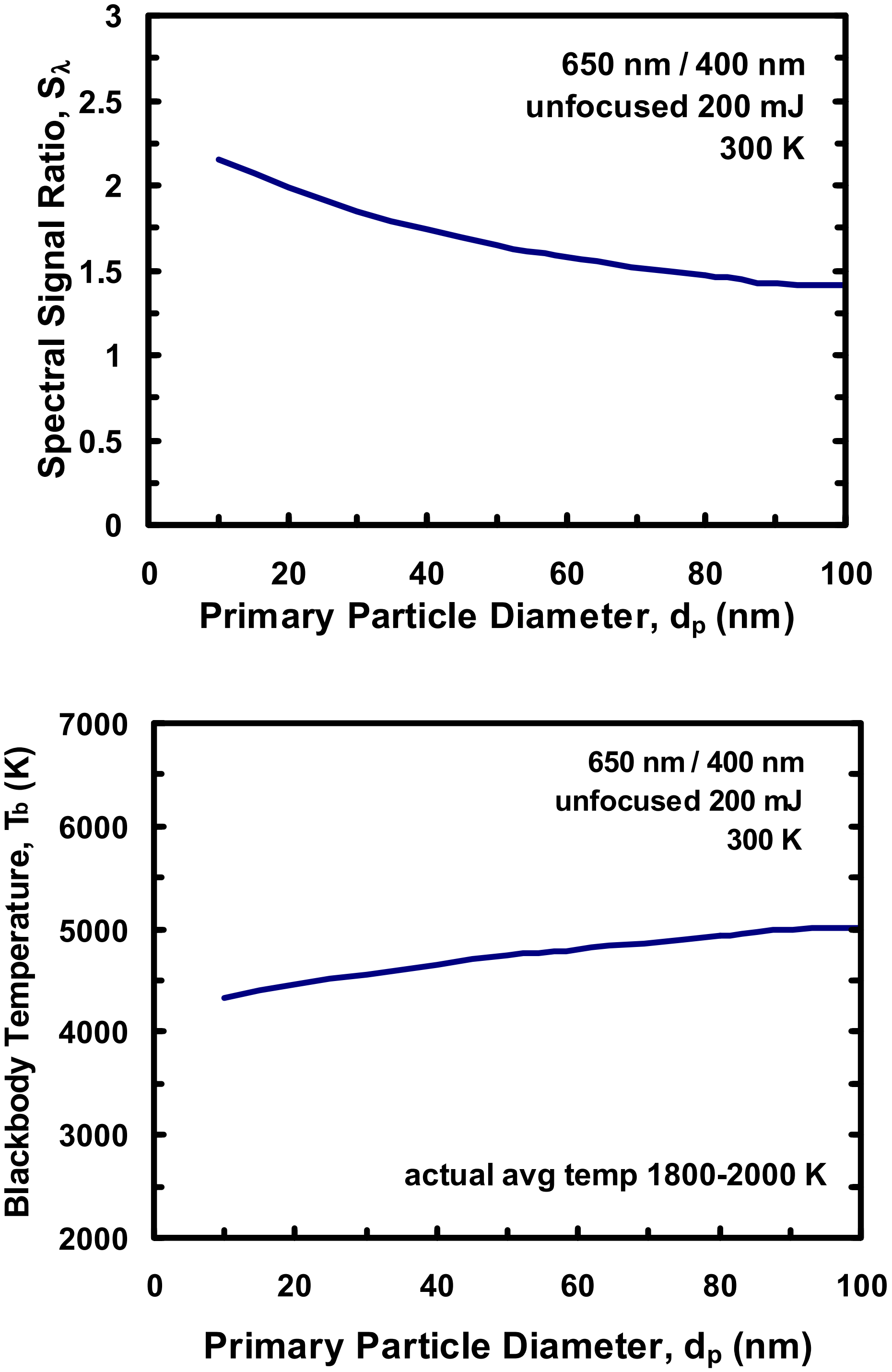

Figure 12. Spectral signal ratio ($S_{650/400}$) and particle temperature for different particle sizes illuminated by an unfocused 200 mJ (1.6 J/cm^2) IR laser pulse. Local gas temperature is 300 K.

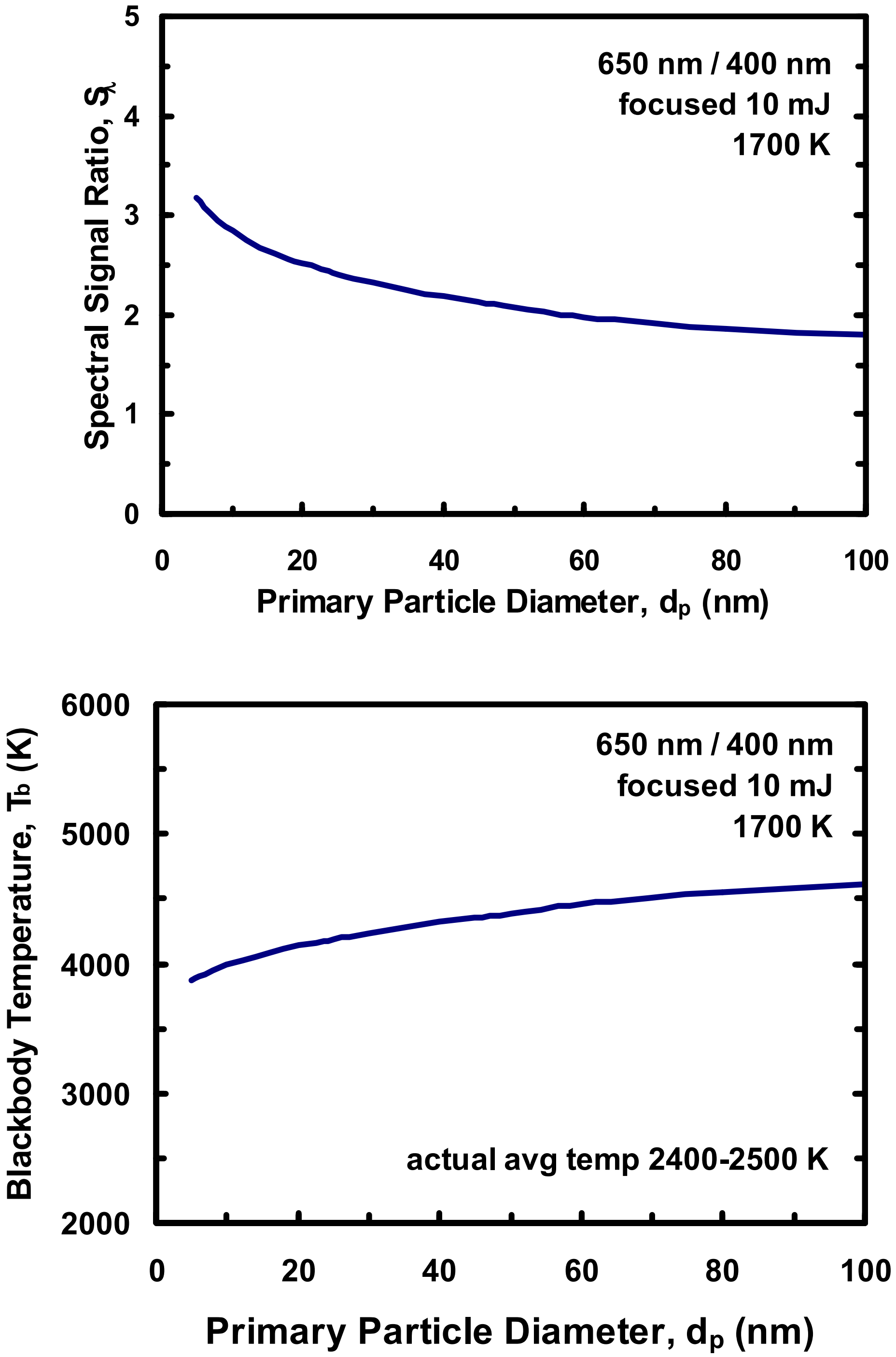

Figure 13. Spectral signal ratio ($S_{650/400}$) and particle temperature for different particle sizes illuminated by a focused 10 mJ (1.2 J/cm^2) IR laser pulse. Local gas temperature is 1700 K. Detection gate is 50 ns.

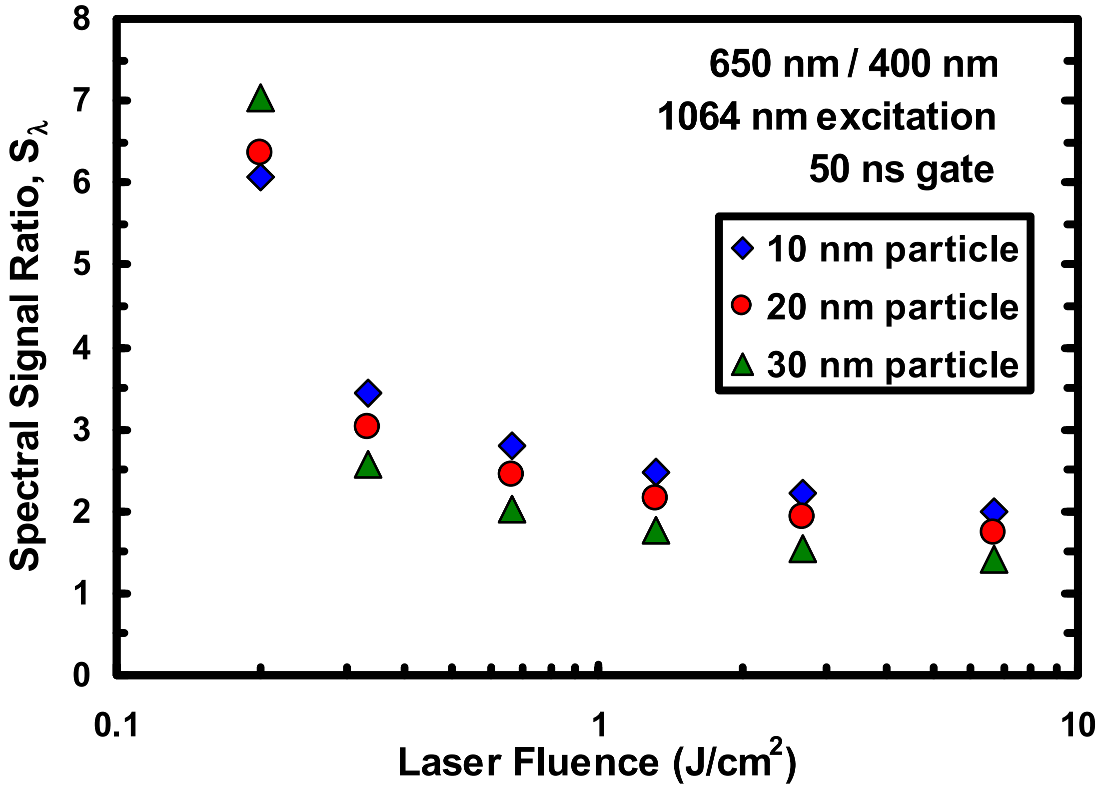

Figure 14. Spectral signal ratio ($S_{650/400}$) versus incident beam-integrated (FWHM) laser fluence for 1064 nm illumination. Local gas temperature is 1700 K. Detection gate is 50 ns.

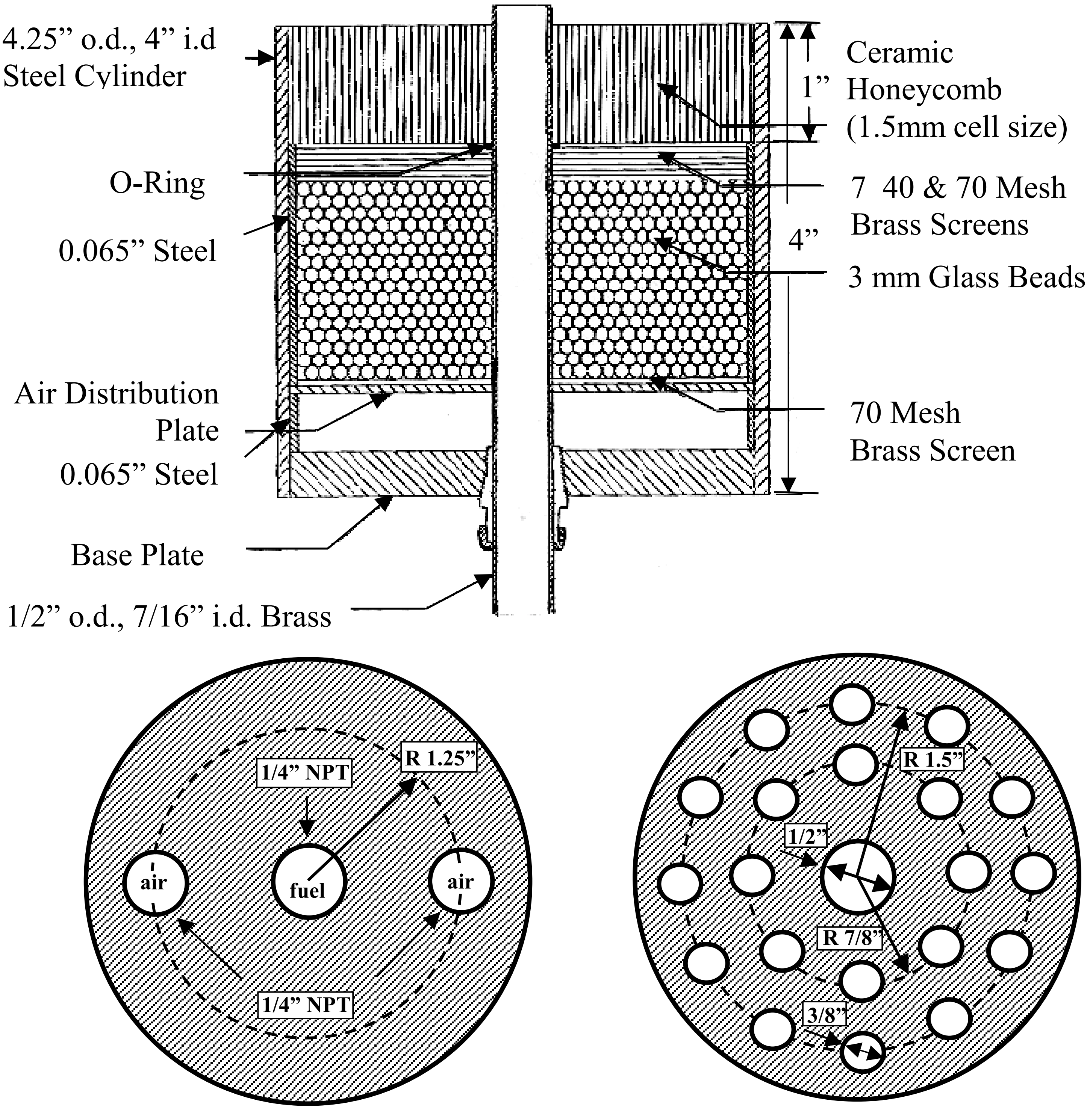

Base Plate

Air Distribution Plate

Figure 15. Schematic of the diffusion flame burner employed in this research. The flow rates employed are 3.85 cm^3/s for fuel (ethylene) in the central tube and 713 cm^3/s for air in the annular region. This design was originally presented in the work of Santoro *et al.*[49] in 1983. Note the ports for the air supply are not shown in the upper image.

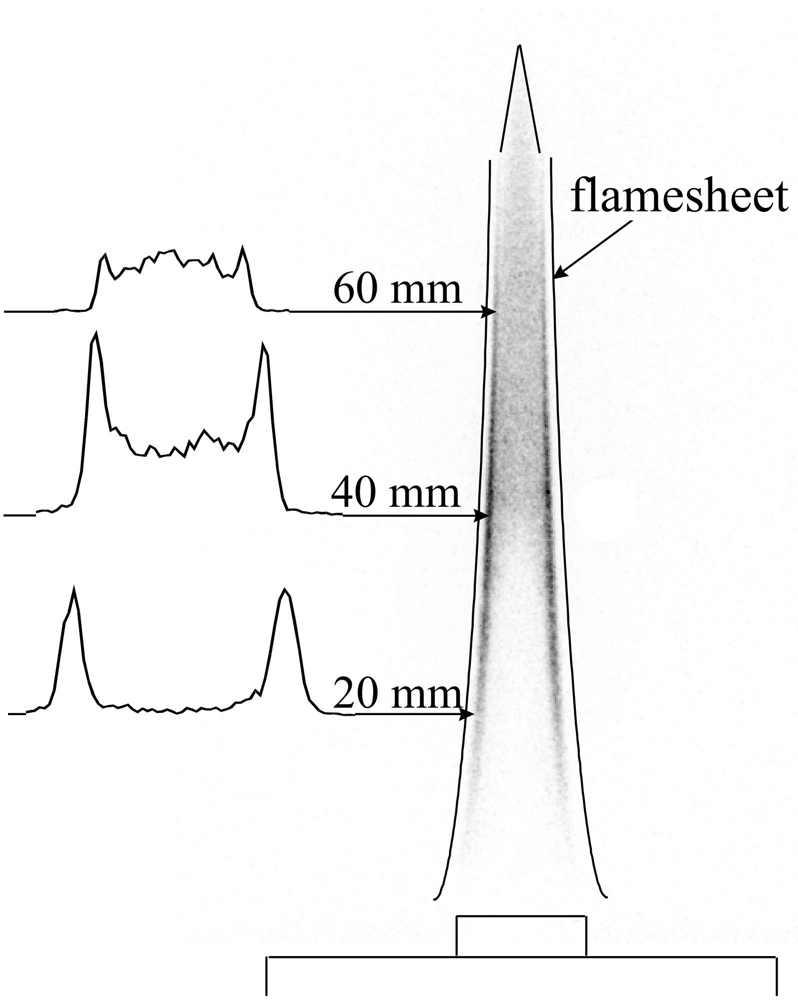

Figure 16. Instantaneous full flame LII image and cross-sectional cuts detected at 430 nm (10 nm bandwidth). The intensifier is gated for 30 ns from the beginning of the laser pulse. The cross-sections are averaged over 4 pixels (0.4 mm) in the vertical direction. The image is uncorrected for laser intensity profile (~0.7 J/cm^2, 532 nm).

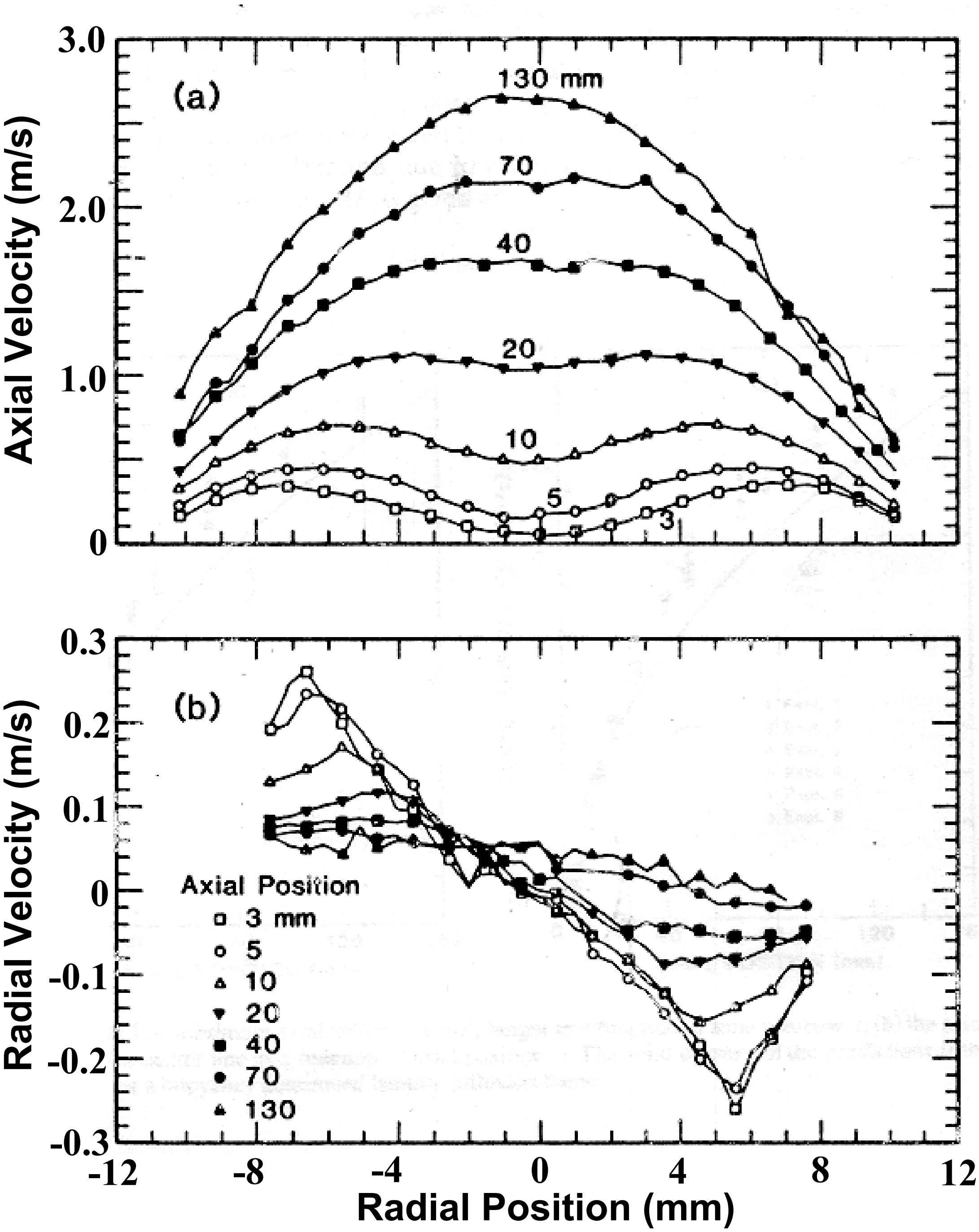

Figure 17. Plot of axial (a) and radial (b) velocity profiles for different heights above the burner fuel tube (HAB) from the laser velocimetry data of Santoro *et al.*[51] for the ethylene diffusion flame of 3.85 cm^3/s flowrate.

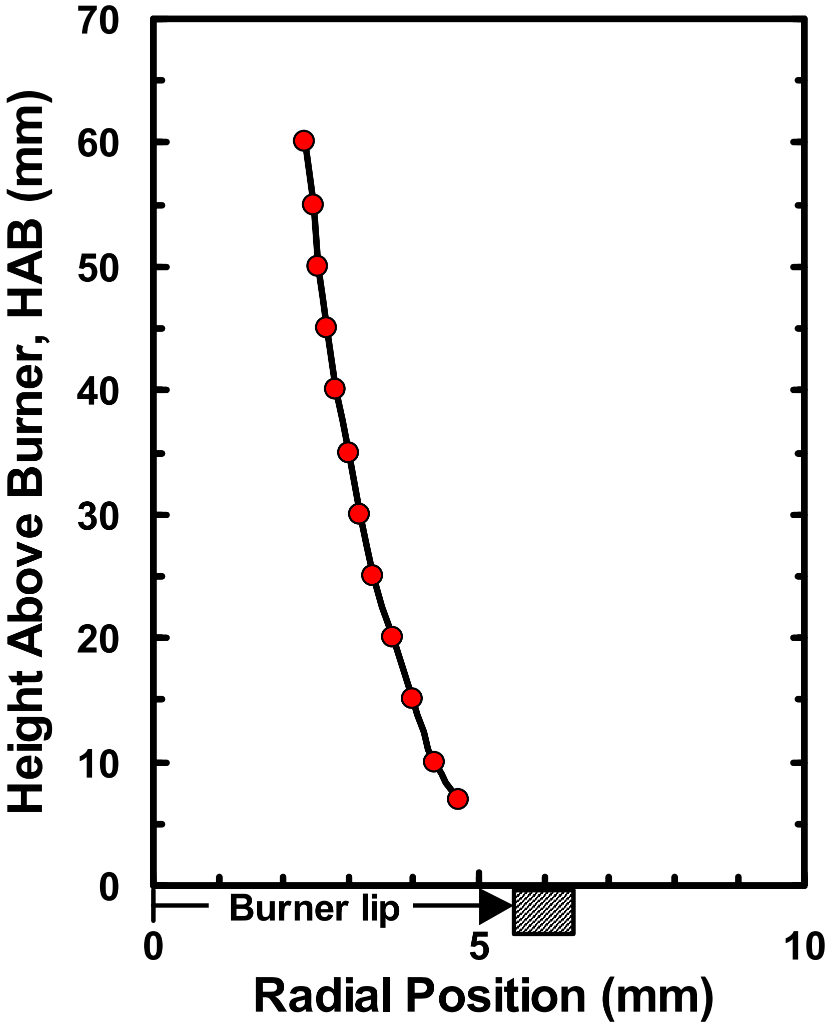

Figure 18. Measurement postitions for pointwise data acquisition against the height above the burner fuel tube (HAB). These are experimentally determined radial positions of maximum signal at each axial location.

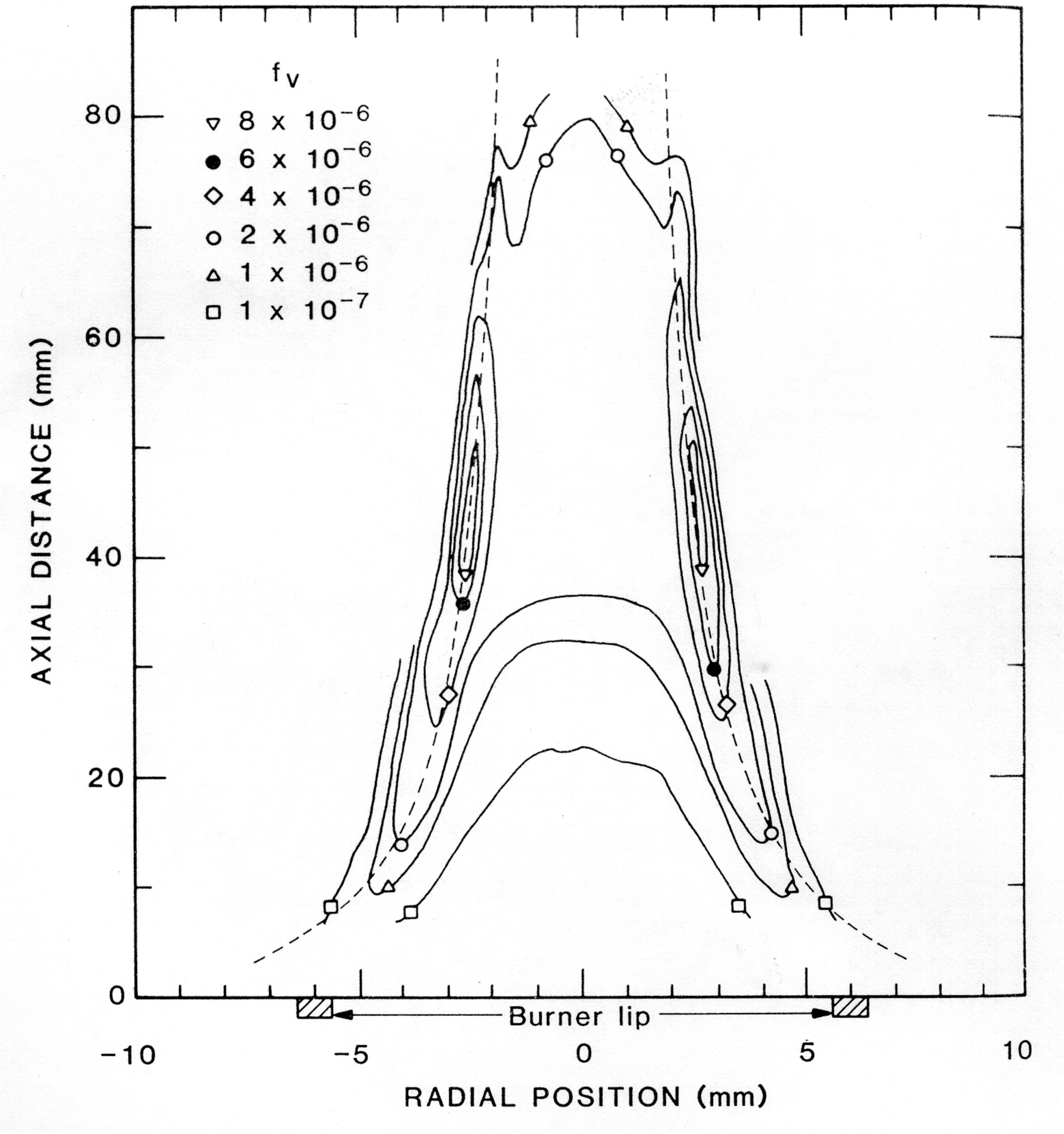

Figure 19. Soot volume fraction (f_v) contour plot for the ethylene diffusion flame. Data is from the extinction measurements of Santoro, *et al.*[51] Dashed line represents the path of maximum soot volume fraction.

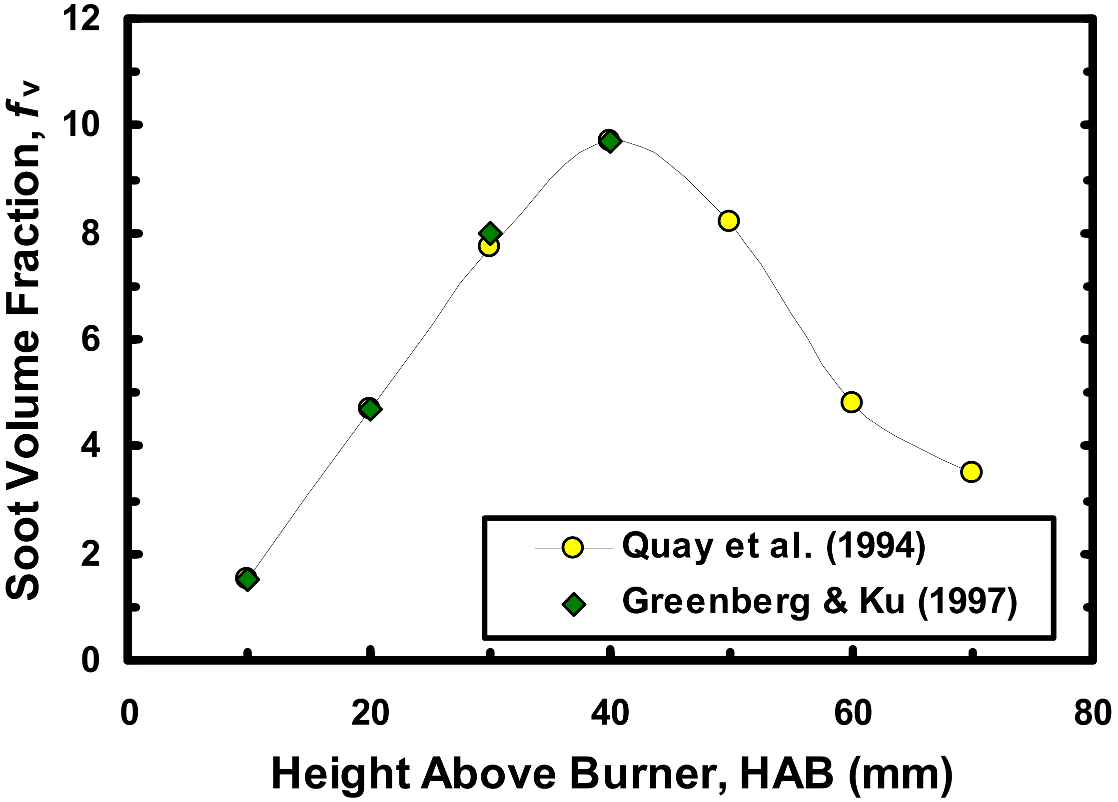

Figure 20. Soot volume fraction (f_v) against height above the burner fuel tube (HAB) along the path of maximum soot f_v in the ethylene diffusion flame. Data are from the extinction measurements of Quay, *et al.*[79] and Greenberg and Ku.[62]

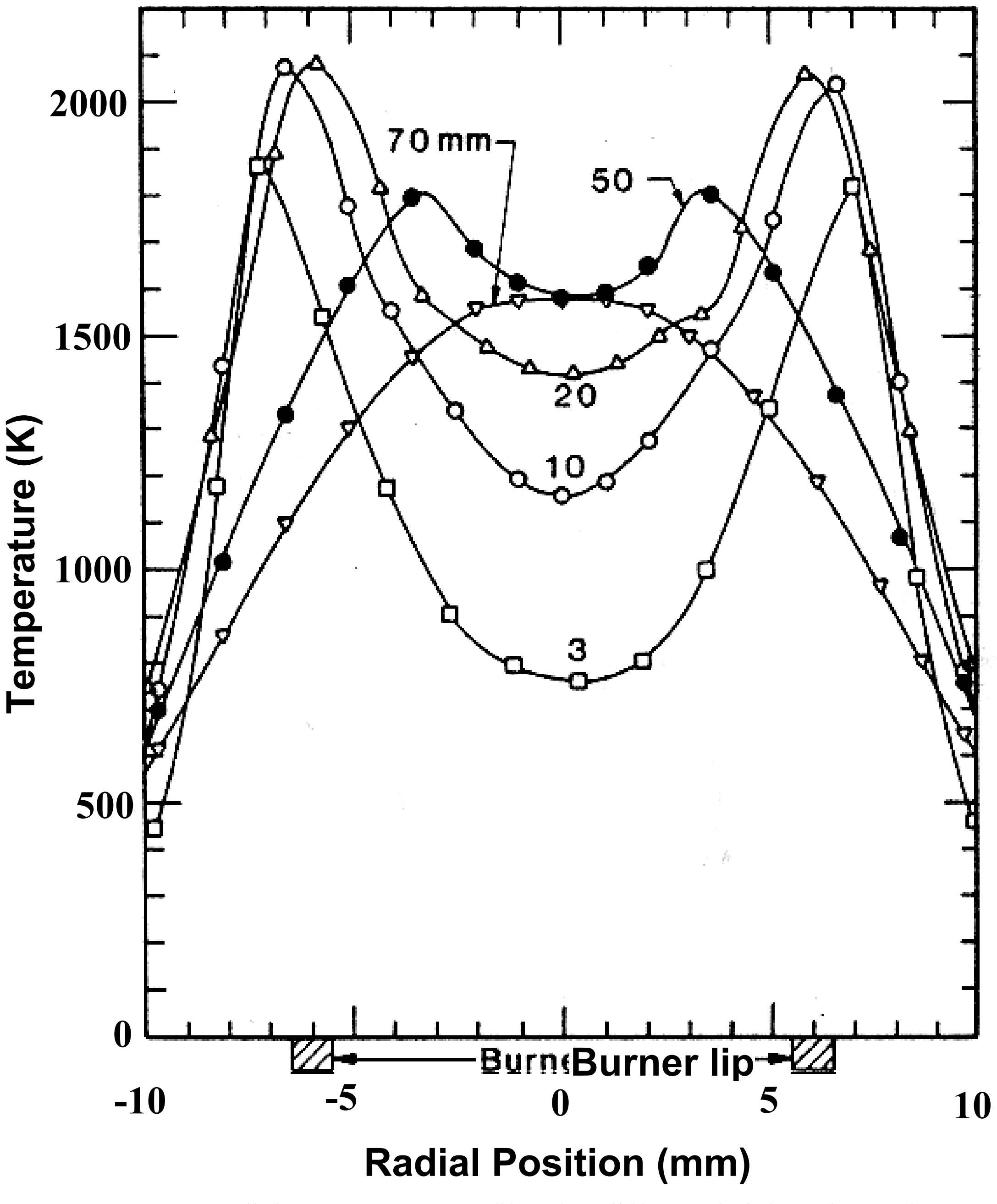

Figure 21. Radial temperature profiles for different heights above the burner fuel tube (HAB) from the thermocouple data of Santoro *et al.*[51] for the ethylene diffusion flame of 3.85 cm^3/s flowrate.

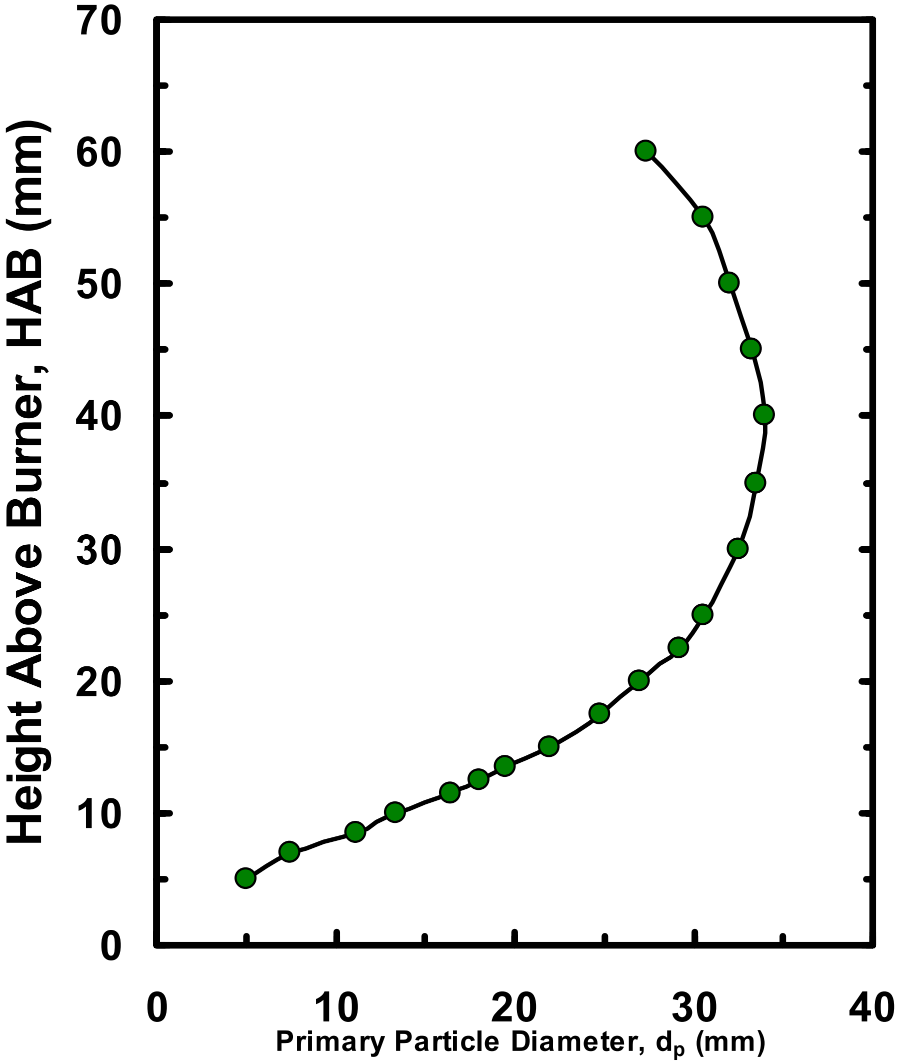

Figure 22. Plot of soot primary particle diameter against the height above the burner fuel tube (HAB) from the thermophoretic sampling/TEM data of Megaridis and Dobbins[39] Symbols represent experimental locations used in this research.

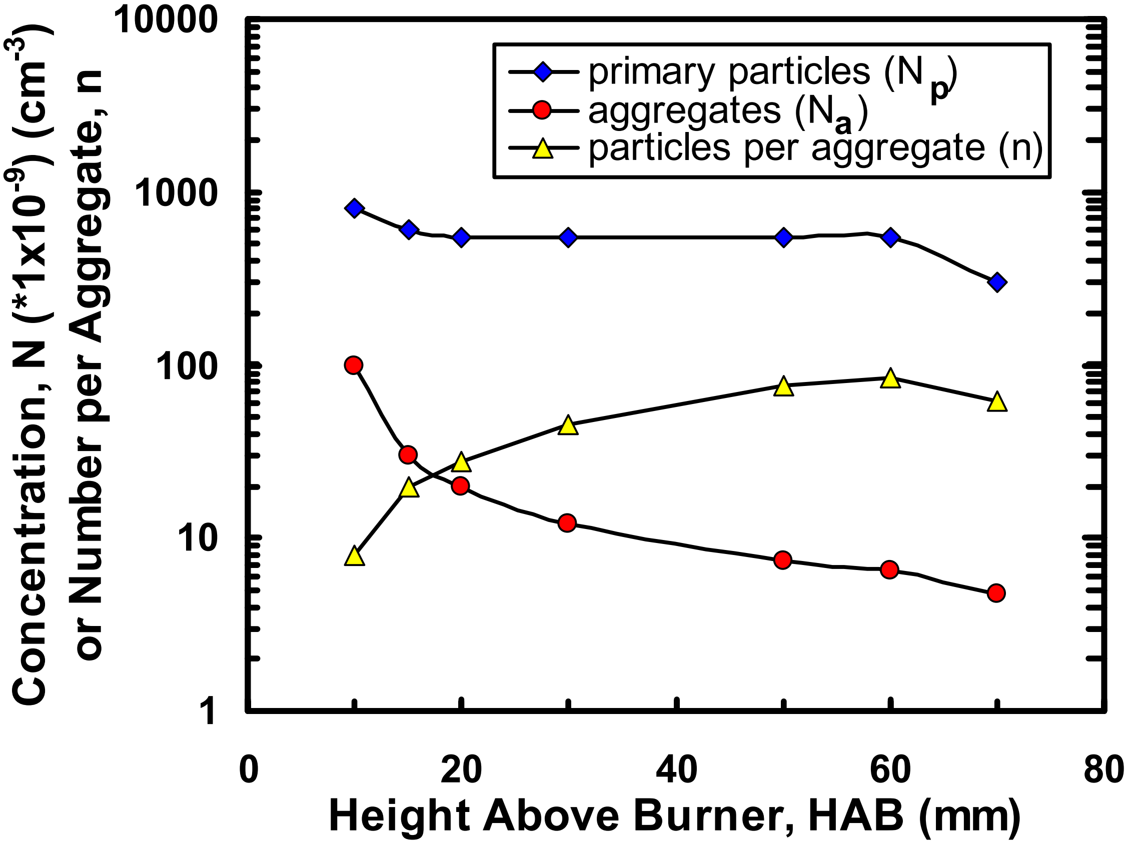

Figure 23. Number density of primary and aggregate particles and number of primary particles per aggregate versus height above the burner fuel tube (HAB) from the scattering and extinction measurements of Puri *et al.*[55] and supporting work.[39,51,52]

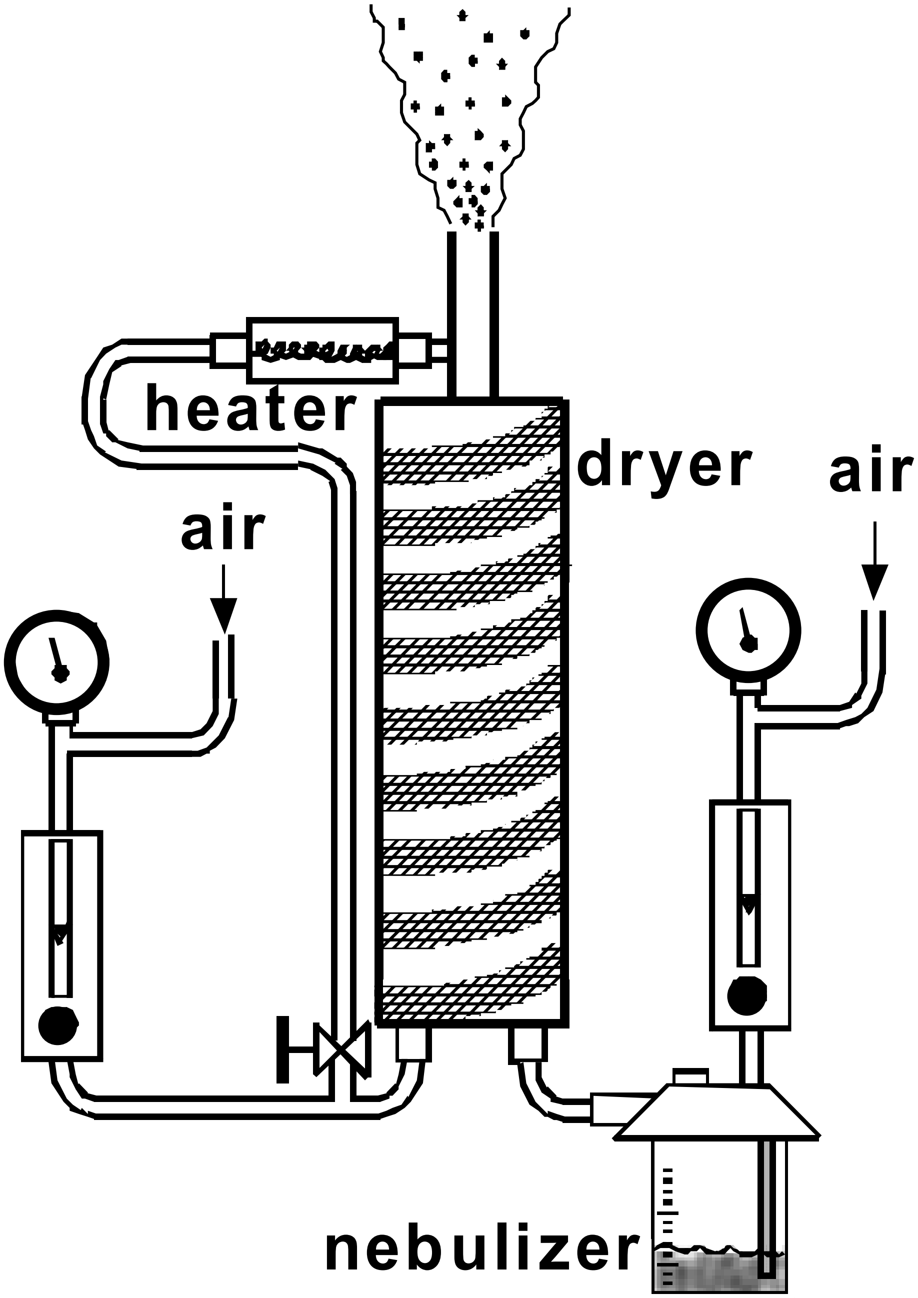

Figure 24. Soot generating experimental apparatus. Carbon/water solution is atomized in nebulizer and directed into dryer tube. Dryer tube is wrapped with heater tape to maintain approximately 100 ºC walls. Separate air flows are monitored with a rotameter and pressure gauge.

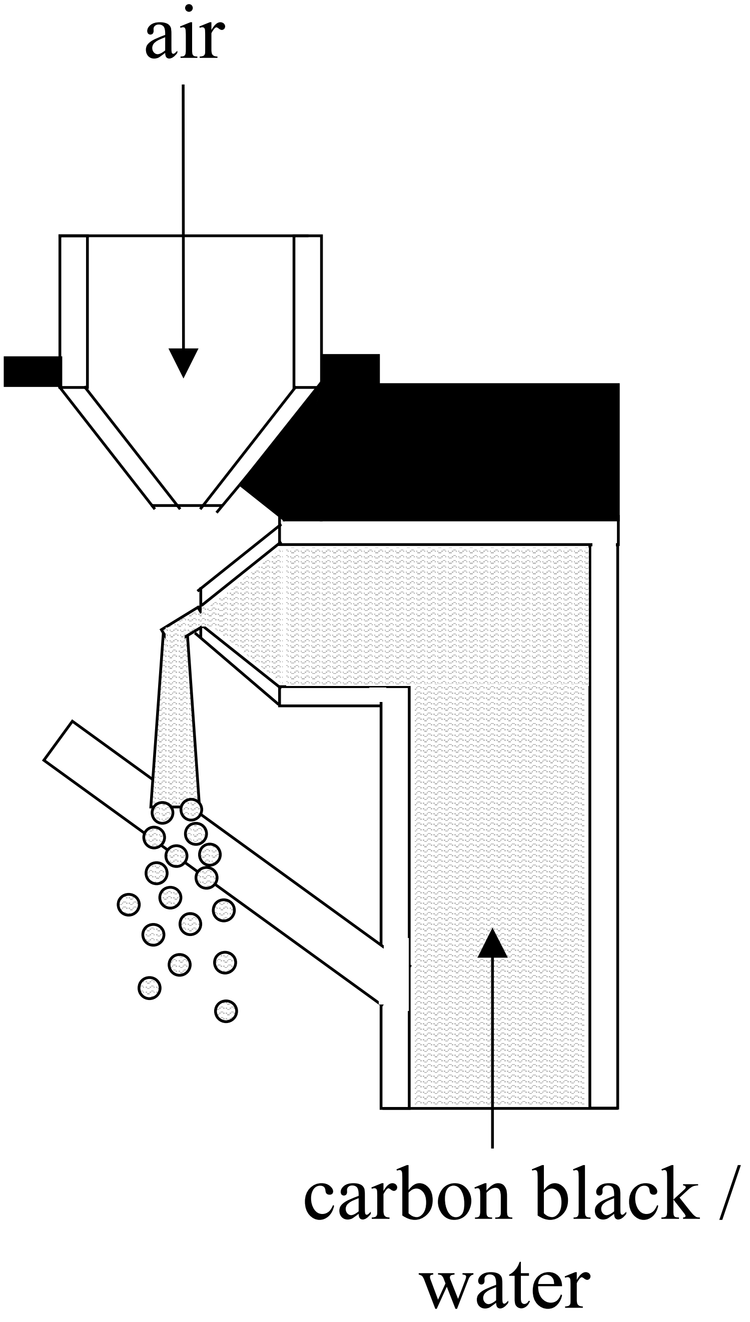

Figure 25. Illustration of the aspiration and impingement arrangement of the atomizer. This device is located inside the nebulizer at the top of the down tube to the carbon black/water solution.

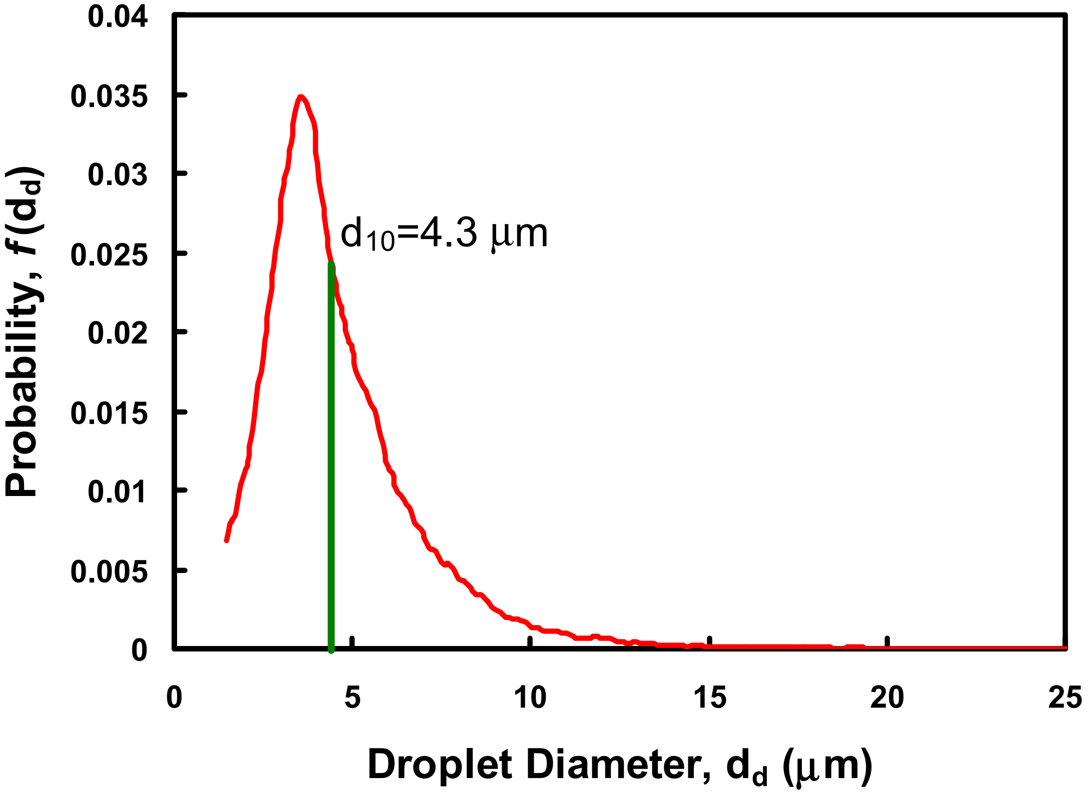

Figure 26. Phase Doppler particle analyzer (PDPA) measurements of the droplet (water only) size distribution at the outlet of the nebulizer. Air flow is 9.2 L/min.

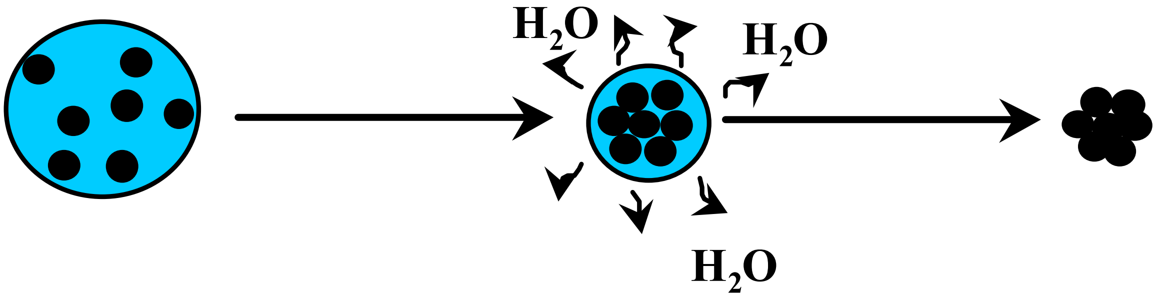

Figure 27. Illustration of soot generator aerosol particle formation from heated carbon black/water droplet. As water evaporates, surface tension and electrostatic forces pull and hold particles together in a spheroid agglomerate.

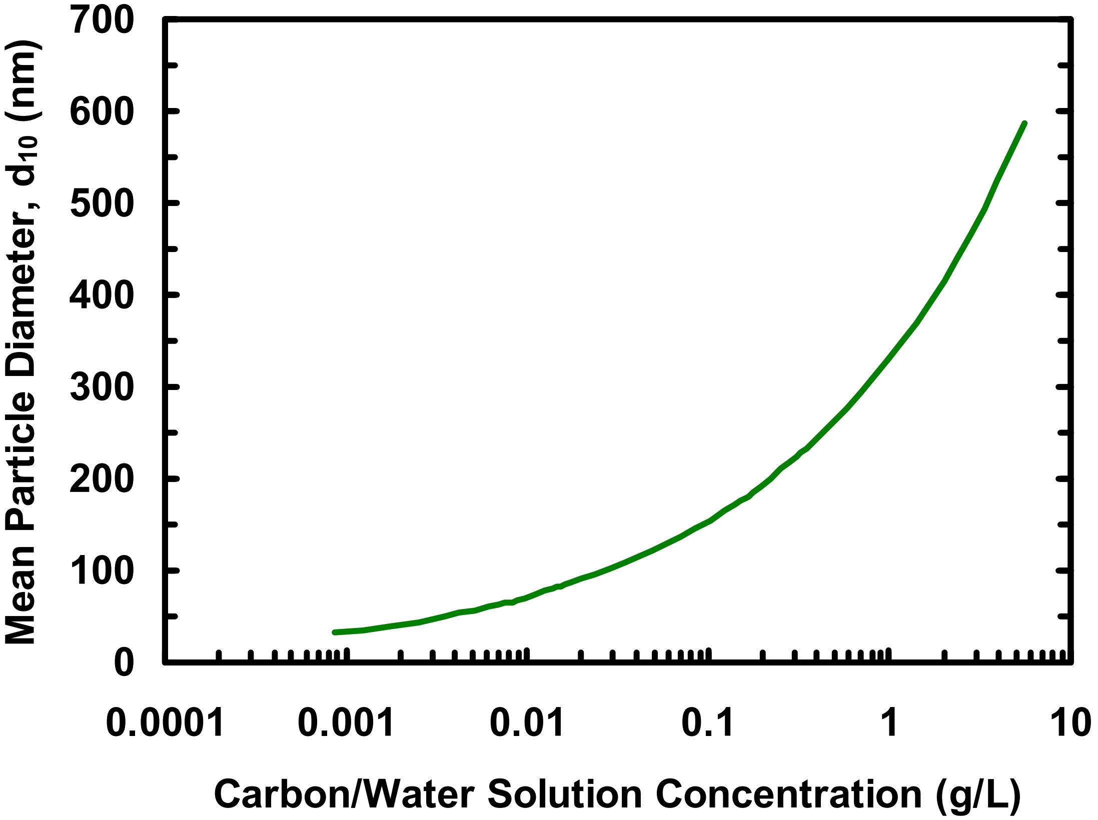

Figure 28. Calculated variation of mean particle size produced by the soot generator as a function of the mean nebulizer droplet size carbon black and water solution concentration. Note the log scaling.

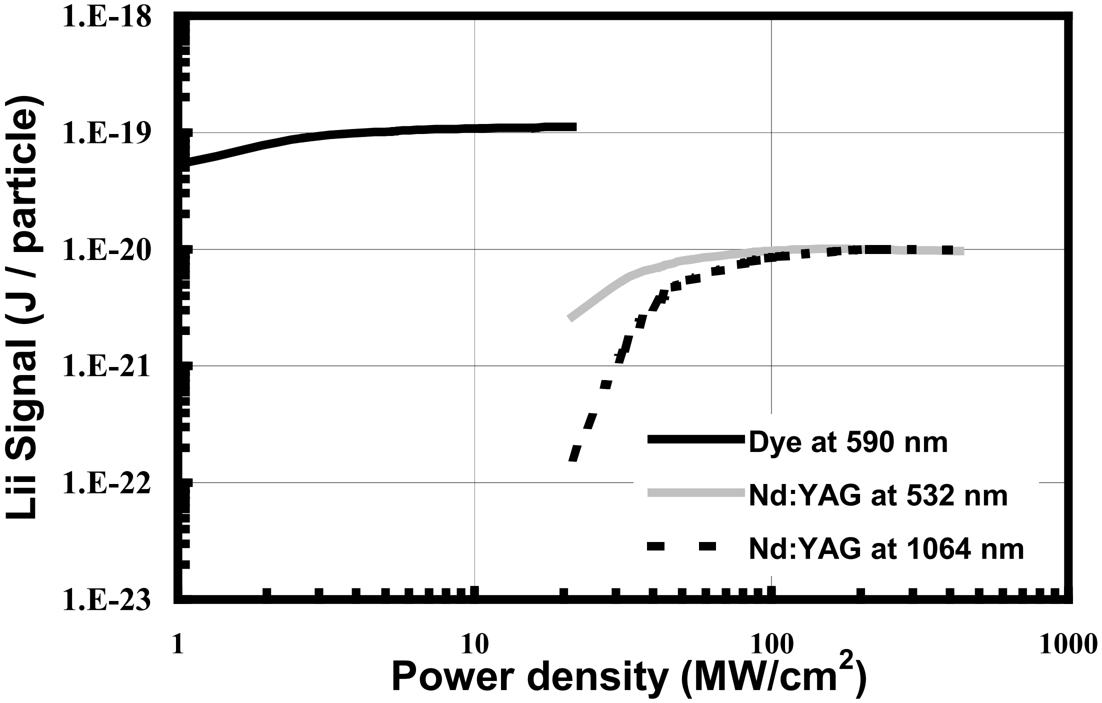

Figure 29. Model results of the temporally-integrated LII signal from a 20 nm particle versus laser intensity for the 1.6 μs dye laser (590 nm) and the fundamental (1064 nm) and frequency-doubled (532 nm) Nd:YAG laser. The signals are integrated over the full life of the signal, 3 μs for the dye laser and 500 ns for the YAG pulses. The local gas temperature is 1500 K. Detection is at 400nm.

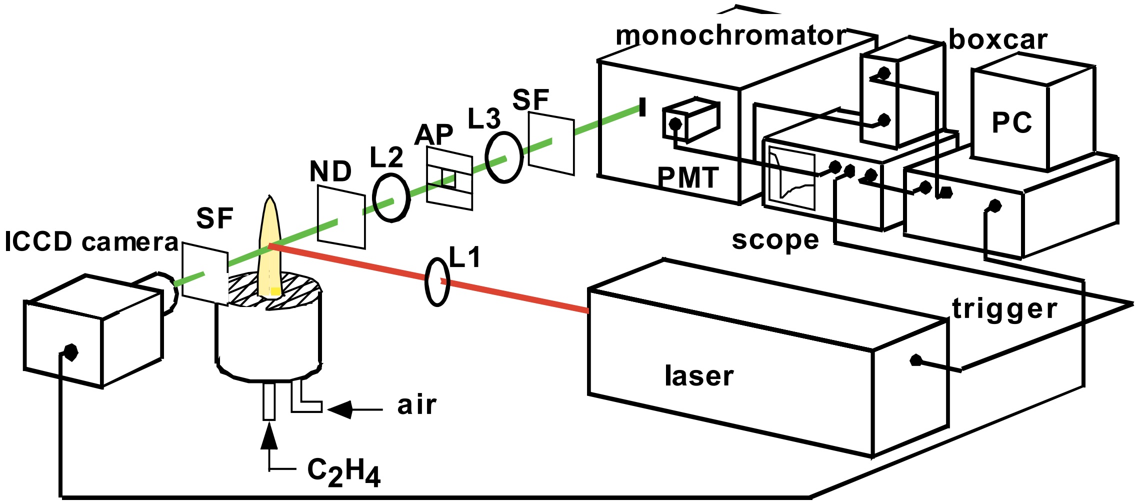

Figure 30. Laser-induced incandescence experimental setup. L1: *f* = 500 mm cylindrical lens, L2: *f* = 150 mm lens, L3: *f* = 100 mm lens, AP: height/width-adjustable rectangular aperture, SF: spectral filter, and ND: neutral density filter.

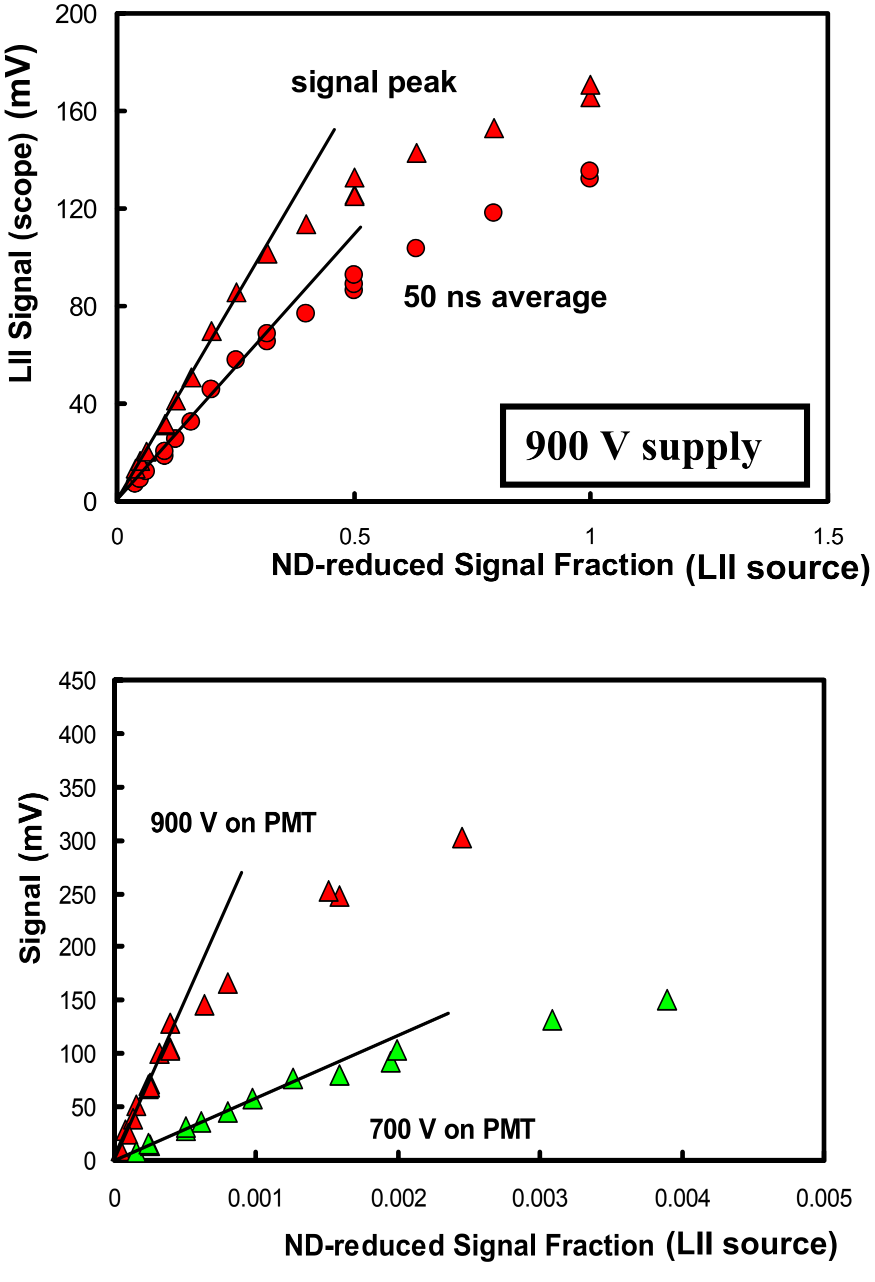

Figure 31. PMT output voltage (current, actually, through 50 Ω) versus ND-adjusted incident light. Top: Peak signal and signal averaged over first 50 ns at a supply voltage of 900 V. Bottom: Peak signal for supply voltages of 700 and 900 V. Input light intensity is varied with the use of combinations of neutral density (ND) filters. Note the difference in x-axis scale magnitudes represents a difference in input light reduction (ND value) due to different strengths of sources.

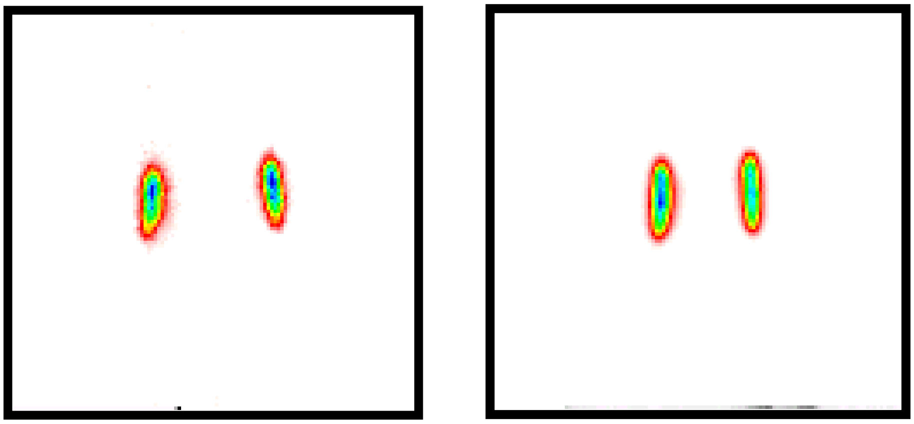

10 mm HAB **25 mm HAB**

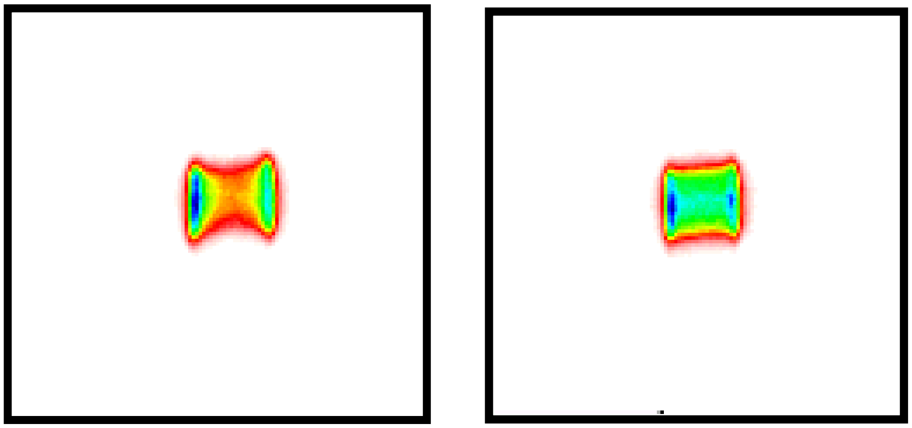

40 mm HAB **55 mm HAB**

Figure 32. Typical ICCD images acquired for pointwise measurements. Images are acquired with camera 2 at an angle of 50°. Signals are generated with a 10 mJ IR beam (1.2 J/cm^2). Detection is at 650 nm and signals are integrated over a 50 ns gate.

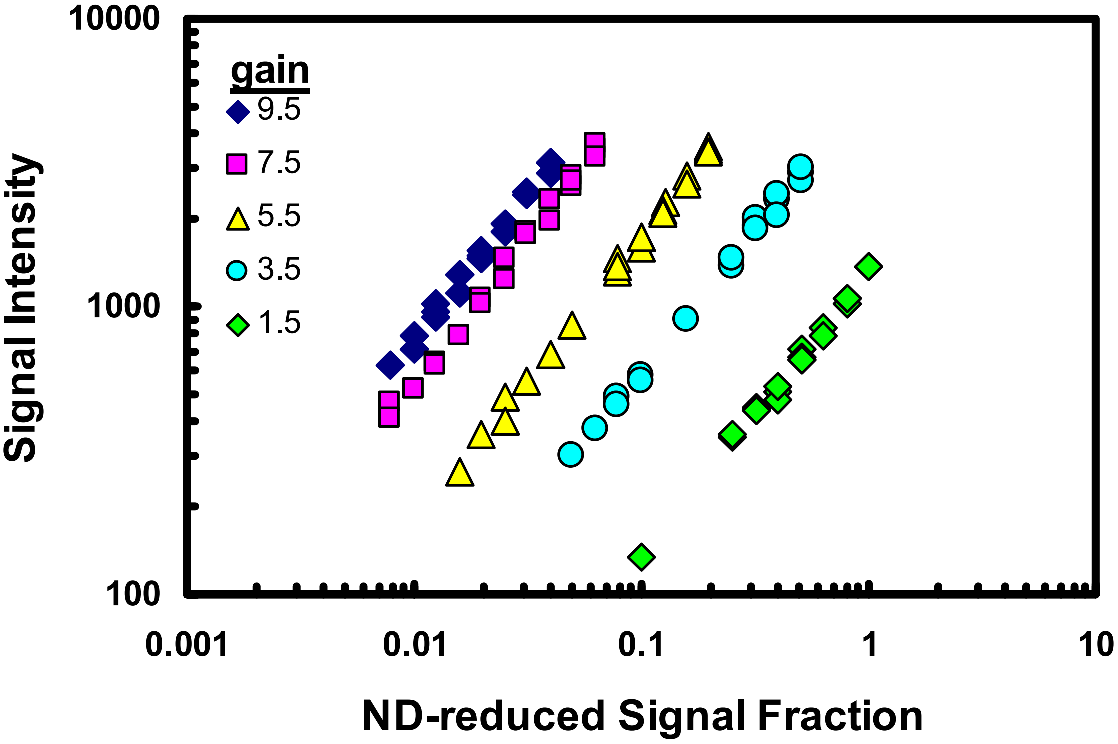

Figure 33. Average signal over a nominally uniform region of a laser sheet inducing fluorescence in acetone. Signals are integrated over 100 ns. Input light intensity is varied with the use of combinations of neutral density (ND) filters. Close to the whole 12-bit dynamic range is presented for each gain setting. The ifferent symbols represent the data acquired with different gain settings on the camera (which ranges from 1 to 10).

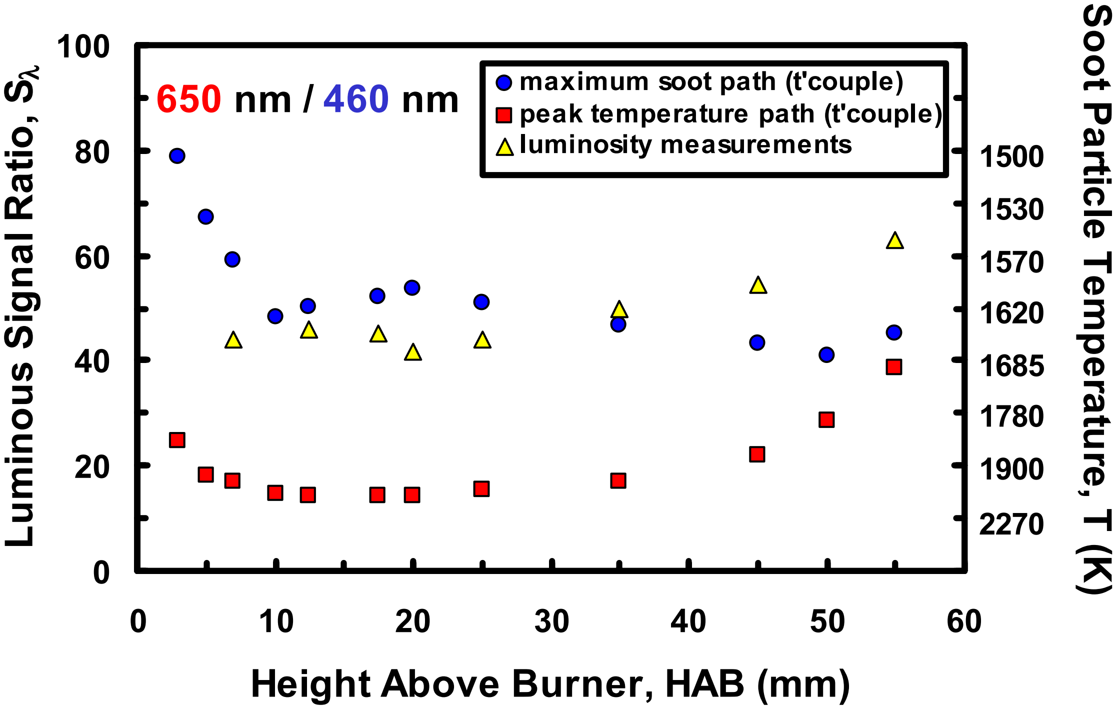

Figure 34. Ratio of blackbody signals (650nm/460nm) from emissivity-adjusted luminescent soot particles. Two data sets are thermocouple measurements[51] along the maximum soot and maximum temperature paths up the flame. These temperatures are converted to a ratio of signals by the blackbody function for each wavelength at the given temperature. The measured signal ratio is detected with the PMT/monochromator at the edge of the flame nearest the laser (not employed). Measurements are recorded with 1 MΩ impedance by the boxcar with 1 μs gating (arbitrary). Bandpass filters are employed, as well as 1.6 ND for the 650 nm signals.

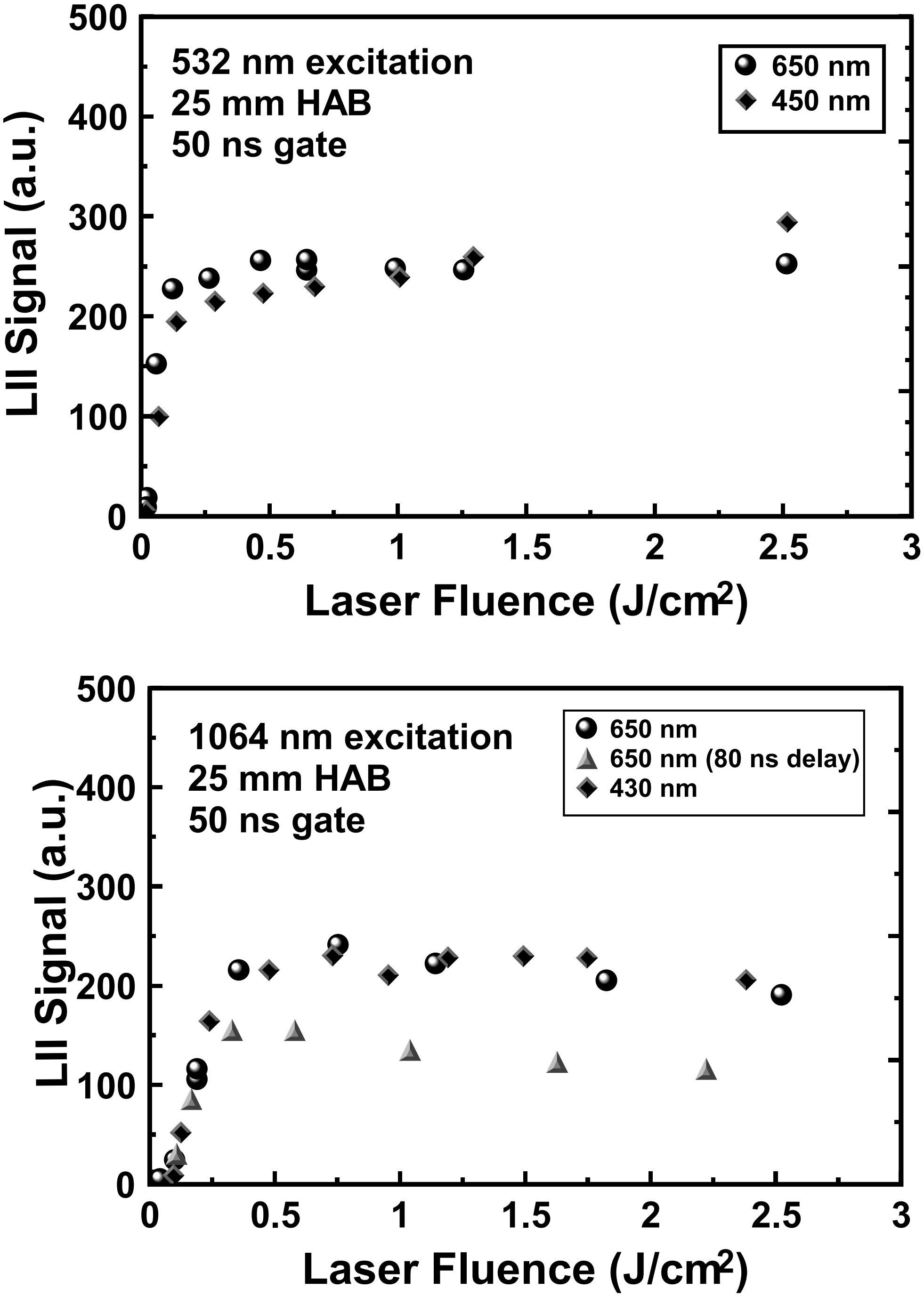

Figure 35. Prompt 50 ns integrated LII signals in the diffusion flame versus incident laser fluence at 1064 and 532 nm illumination. Signals are recorded at 650 and 430 nm. Holographic notch filter is employed for the case of 532 nm illumination. Arbitrary vertical scales of the two plots are correct relative to one another. Data are uncorrected for the spectral response of the detection system.

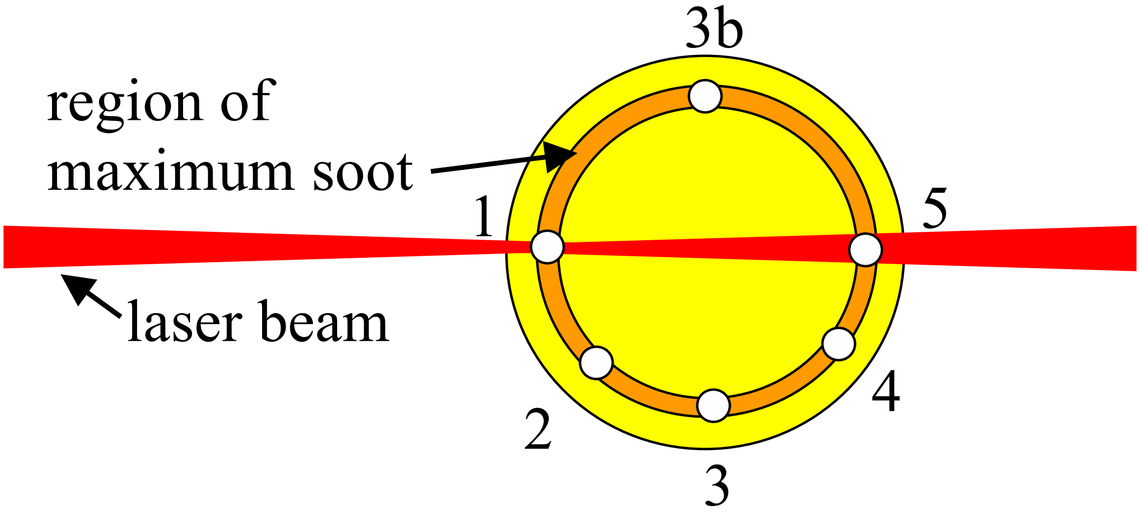

Figure 36. Cross-sectional schematic of the diffusion flame and location of all of the annular LII measurement points. For measurement, the point of interest is moved into the focus of the laser.

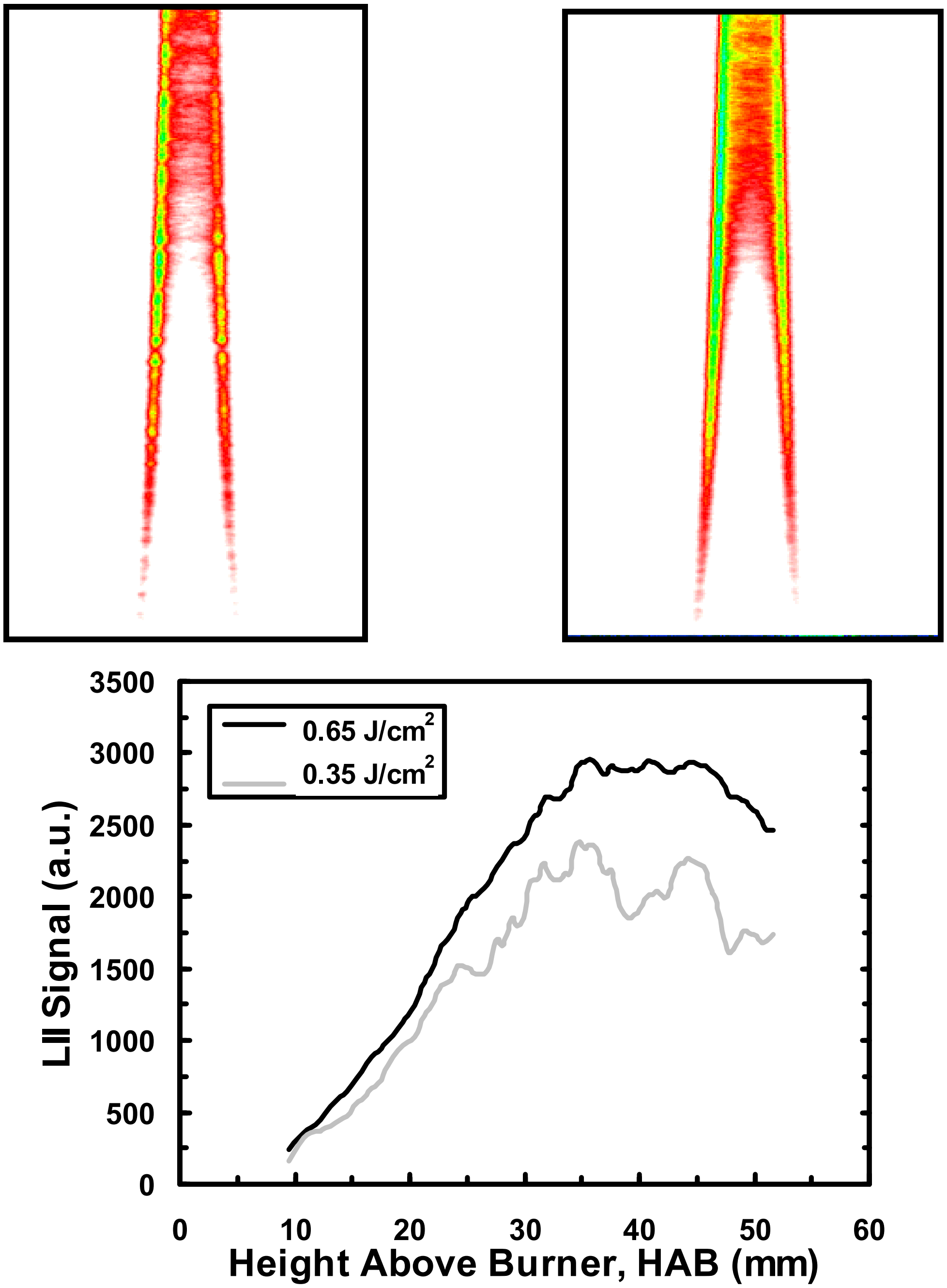

Figure 37. Imaging threshold effect. Above left: LII image generated by 0.35 J/cm^2 laser pulse (532 nm). Above right: LII image generated by 0.65 J/cm^2 laser pulse (532 nm). Below: Graph of maximum signal path up left side of images. Image sheet of 5 cm height is formed by a glass rod (*f*=5mm). Middle 4.2 cm of images are shown. Detection is at 650nm with a 100 ns gate and signals are averages over 10 images.

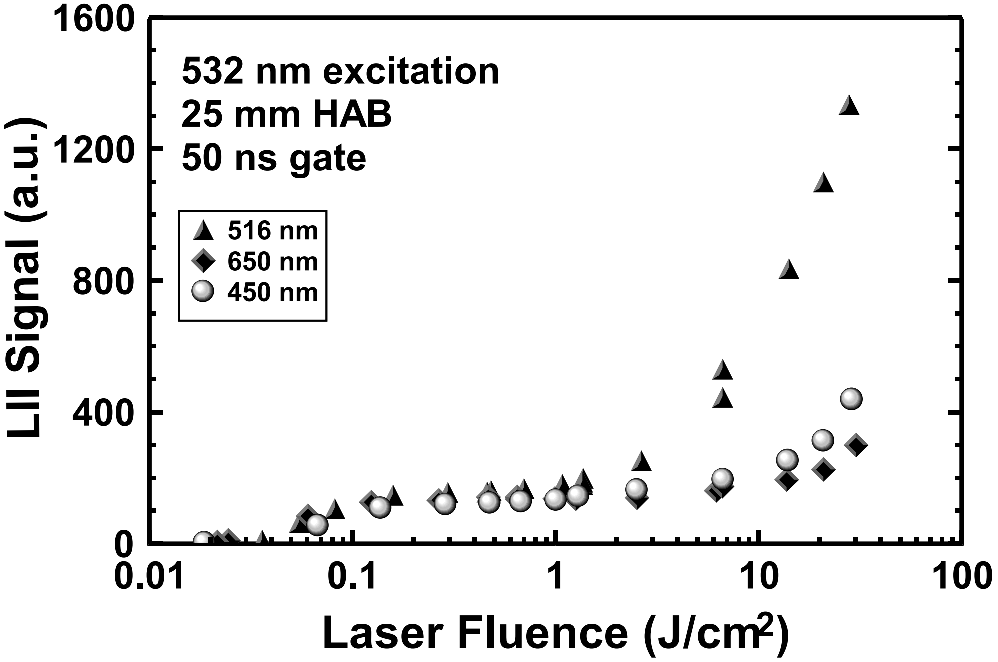

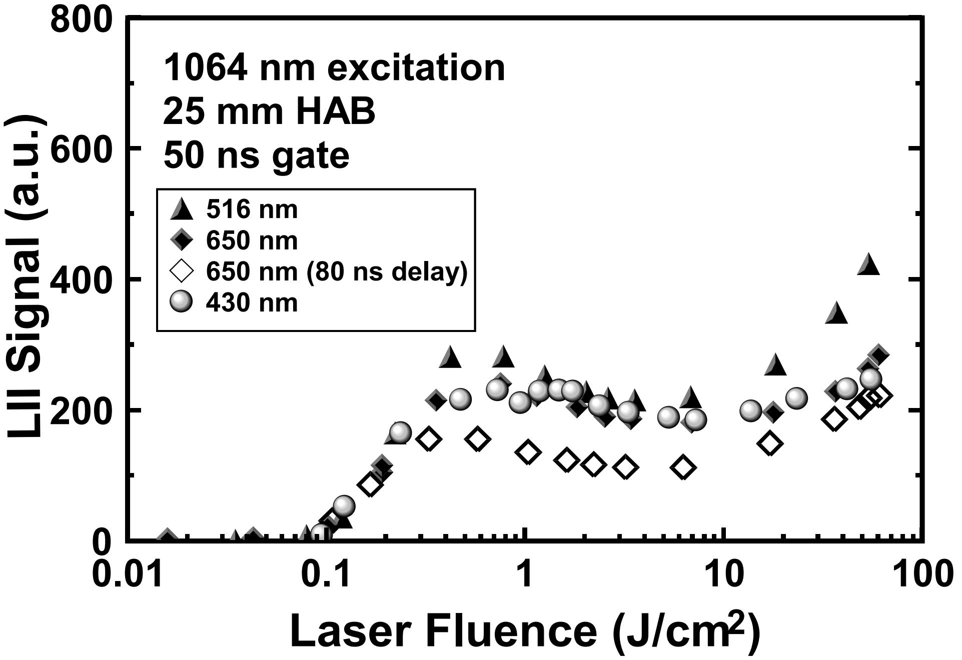

Figure 38. Prompt 50 ns integrated LII signals in the diffusion flame versus incident laser fluence at 1064 and 532 nm illumination. Signals are recorded at 650 nm, 430 nm and the Δν=0 Swan band head at 516 nm. Holographic notch filter is employed for the case of 532 nm illumination. Arbitrary vertical scales of the two plots are correct relative to one another. Data are uncorrected for the spectral response of the detection system.

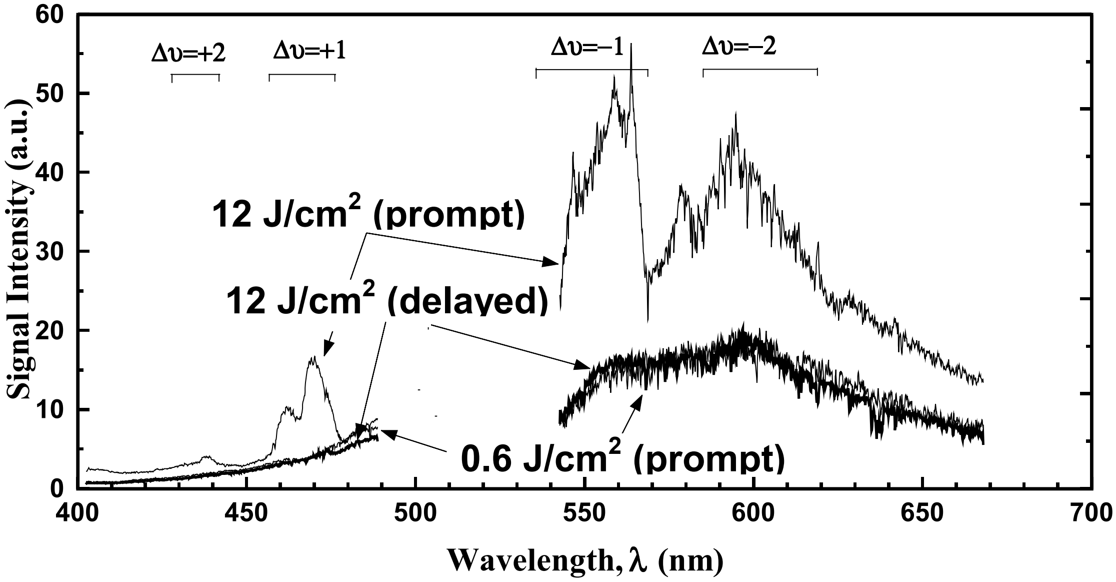

Figure 39. Laser-induced emission using a 532 nm Nd:YAG pulse of 0.6 J/cm^2 (prompt) and 12 J/cm^2 (both prompt (bold line), and at 30 ns delay (thin line)). All gates are 30 ns long. Scan is performed at 0.5 nm/min. and laser operating at 10 Hz. Blue region is detected through a 45° dichroic laser mirror (532 nm). Longer wavelengths were detected through 2 mm of OG550 Schott glass. Corrections for the spectral response of the monochromator and PMT are not included.

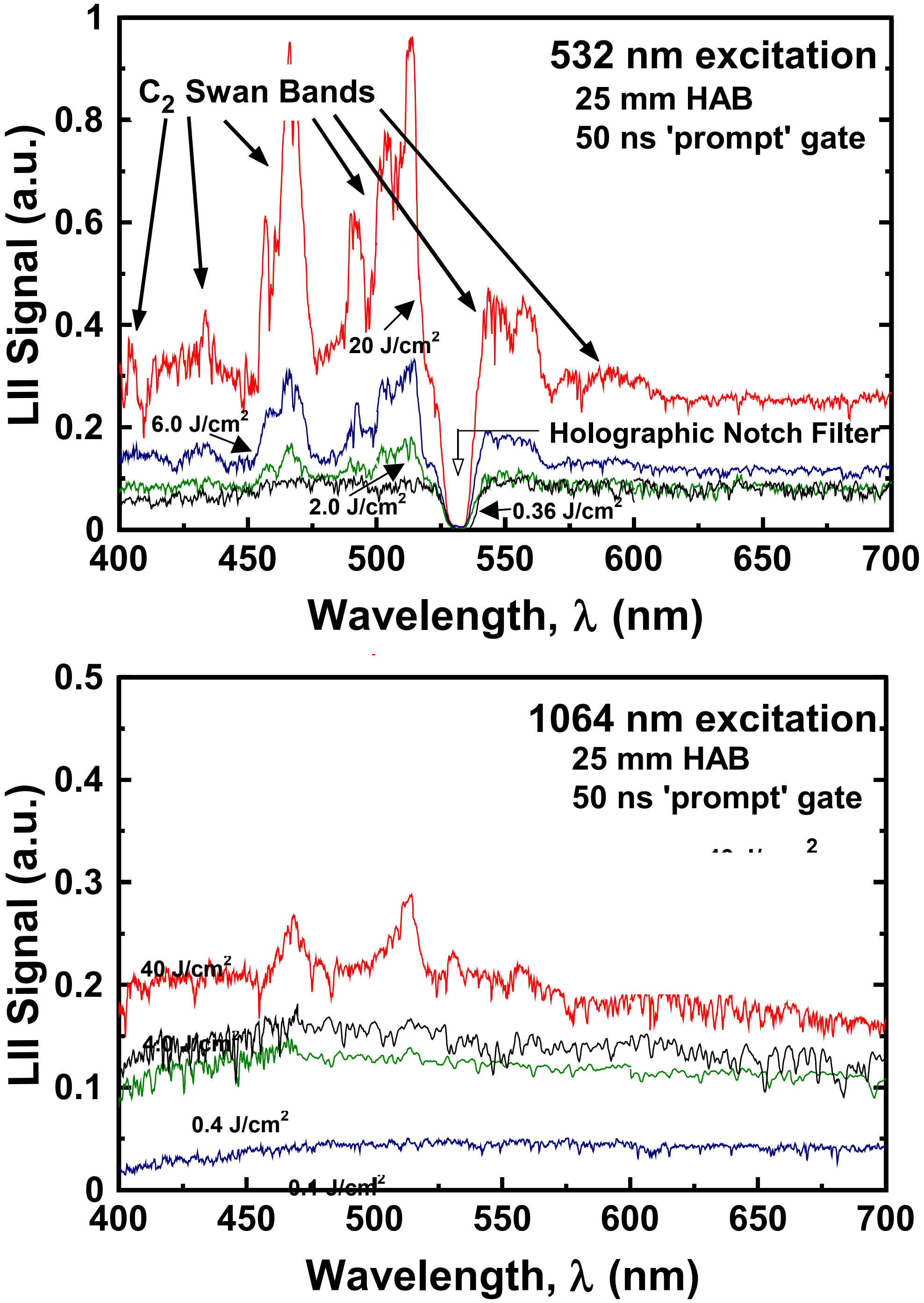

Figure 40. LII spectra recorded in the diffusion flame at a height of 25 mm. Visible wavelength spectra are shown for green and IR excitation and a wide range of excitation energies. The data are corrected for the response of the detection system and spectral emissivity of the soot particles. Arbitrary vertical scales of the two plots are correct relative to one another.

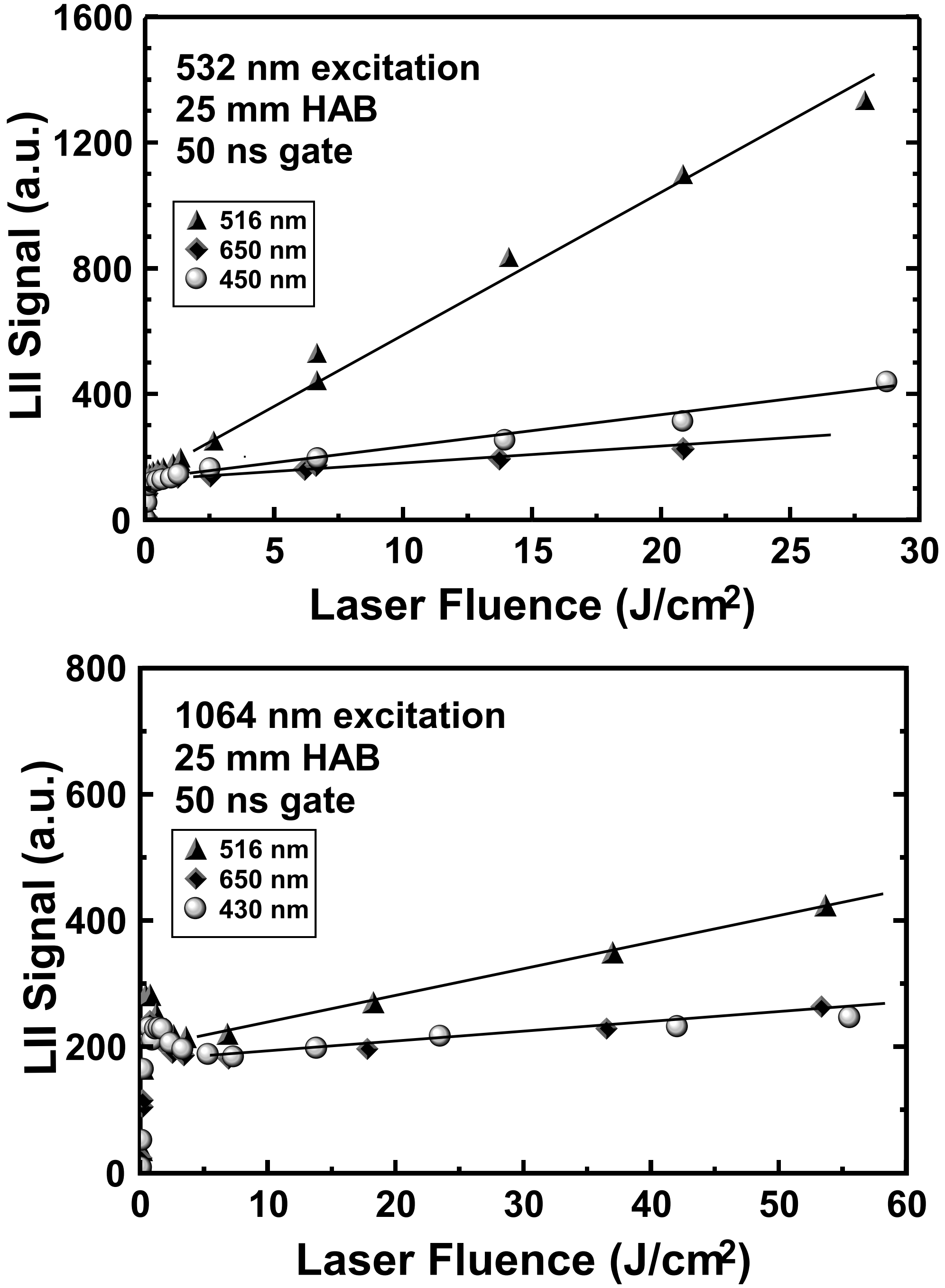

Figure 41. Replotting of data of Figure 38 on a linear scale. Prompt 50 ns integrated LII signals in the diffusion flame versus incident laser fluence at 1064 and 532 nm illumination. Signals are recorded at 650 nm, 430 nm and the Δν = 0 Swan band head at 516 nm. Holographic notch filter is employed for the case of 532 nm illumination. Arbitrary vertical scales of the two plots are correct relative to one another.

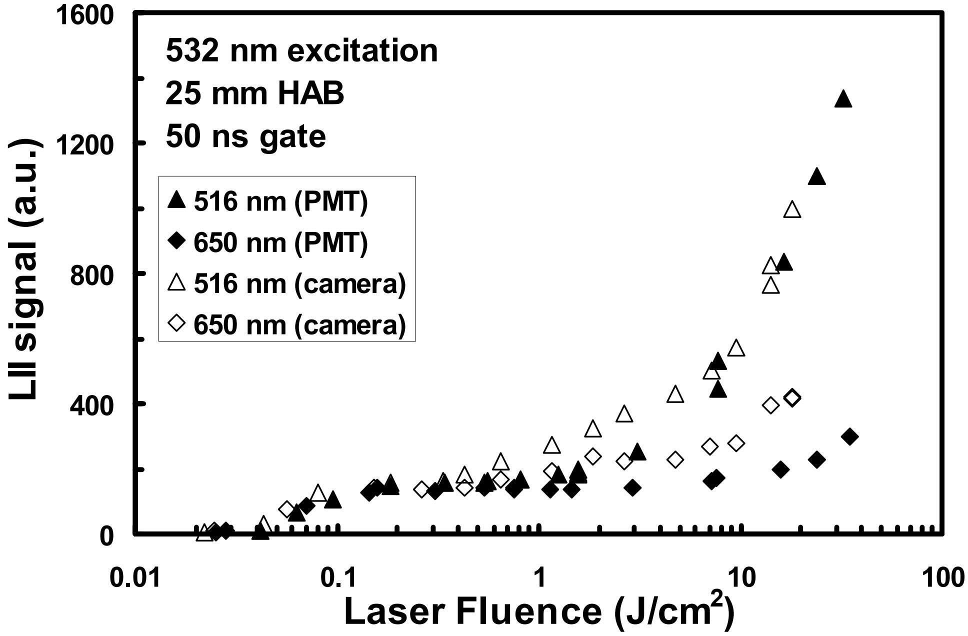

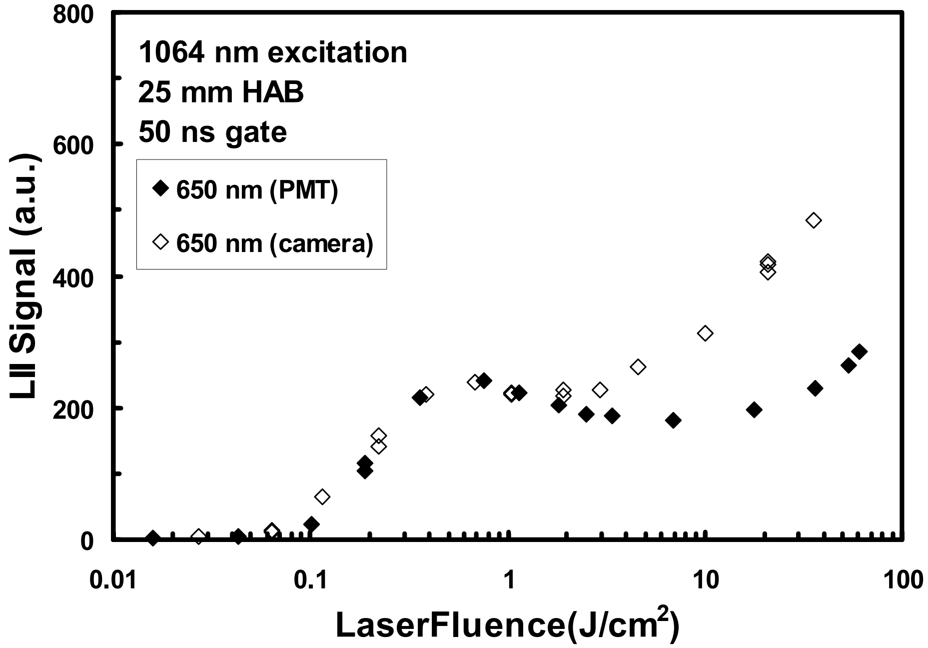

Figure 42. (green/infred.xls) Prompt 50 ns integrated LII signals in the diffusion flame versus incident laser fluence at 1064 and 532 nm illumination. Signals are recorded at 650 nm and at the $\Delta\nu = 0$ Swan band head at 516 nm by either the ICCD camera or the PMT/monochromator. The holographic notch filter is employed for the case of 532 nm illumination. Camera data employs bandpass filters at 514.5 nm and 650 nm. Arbitrary vertical scales of the two plots are correct relative to one another.

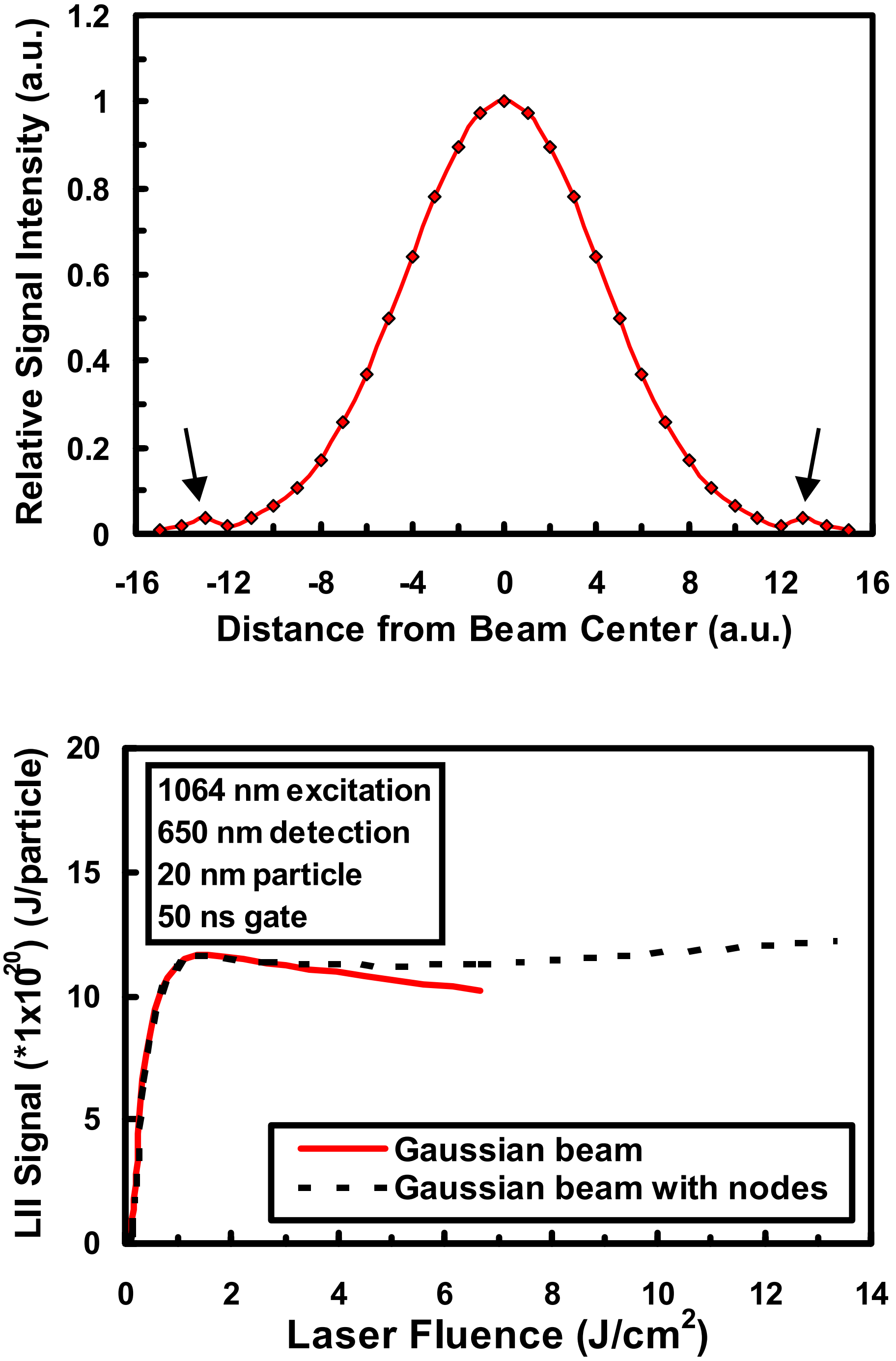

Figure 43. Sensitivity of signal at high fluence to bumps in wings of laser profile. Above: 1-D Gaussian laser intensity profile with small nonmonotonicities in the wings. Bottom: Comparison of spatially- and temporally-integrated signal behavior with laser fluence for Gaussian and Gaussian beam with 'nodes' in the wings.

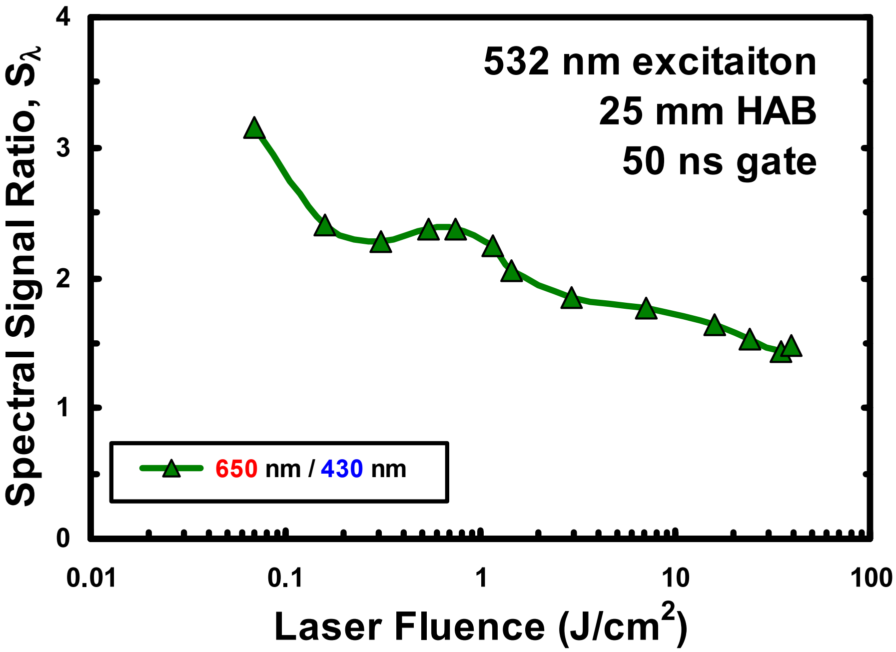

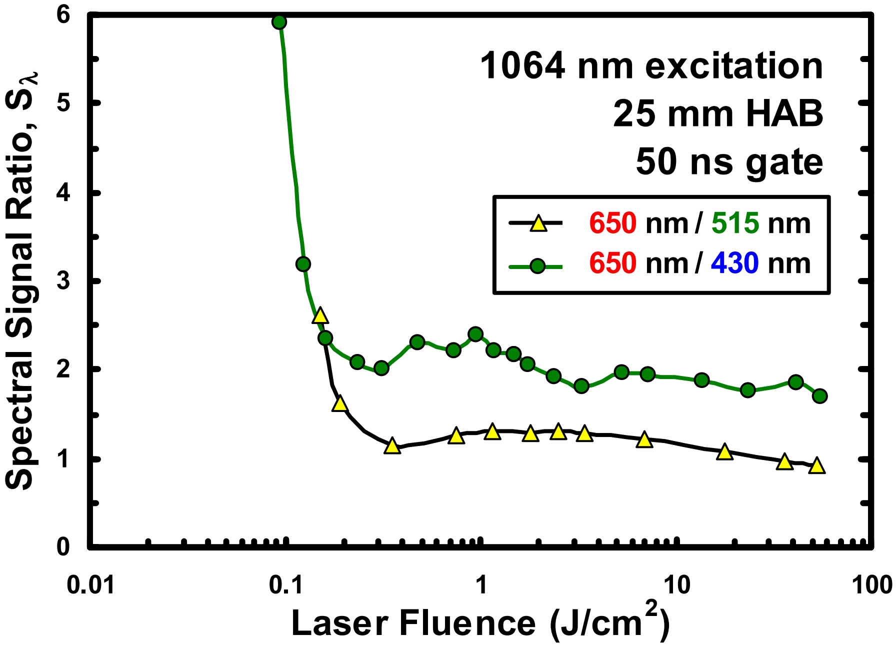

Figure 44. Prompt 50ns-integrated LII spectral signal ratios at 25 mm HAB in the diffusion flame versus incident laser fluence at 1064 and 532 nm illumination. Above: 650nm/430nm signal ratio for 532 nm illumination. Below: 650nm/430nm and 650nm/515nm signal ratio for 1064 nm illumination.

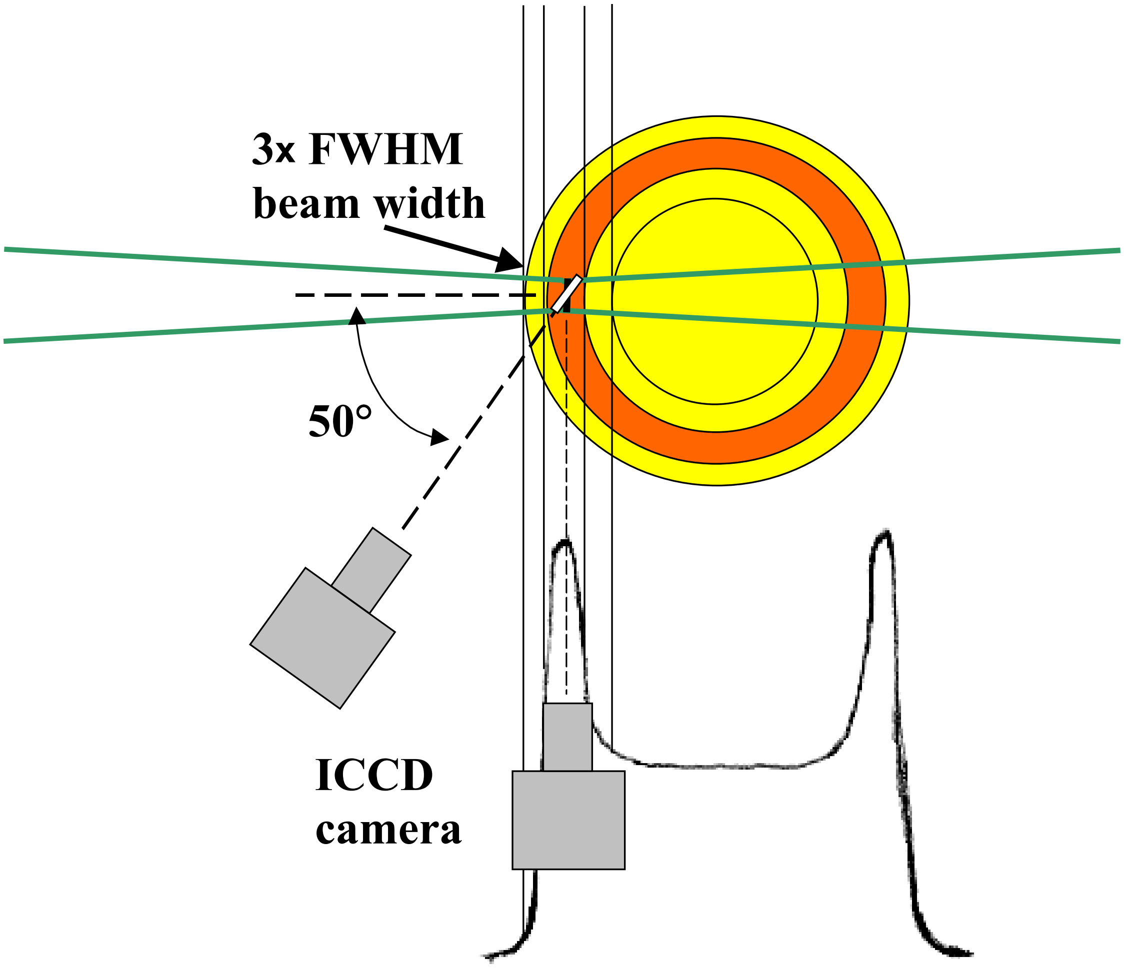

Figure 45. Illustration of the change in the measurement volume of a single pixel on the CCD and the change in the signal trapping path due to a change in detector angle. Soot profile is from 40 mm HAB in the flame. The 3xFWHM beamwidth is ~0.6 mm.

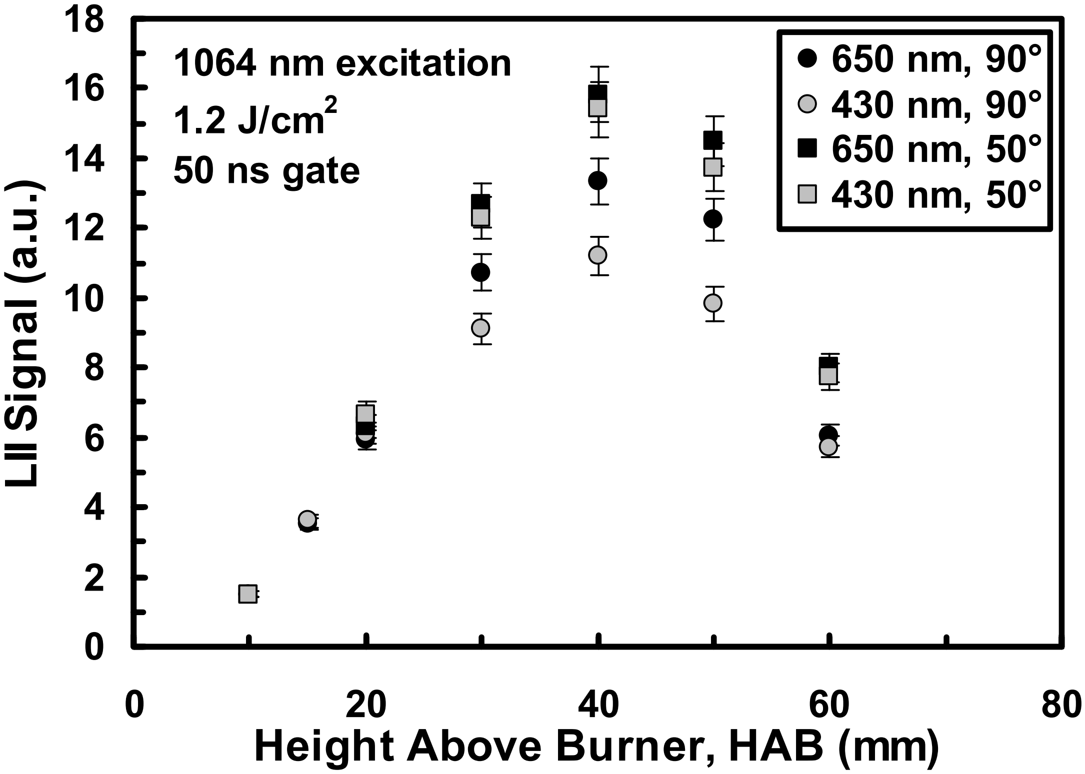

Figure 46. Comparison of 50ns-integrated LII signals acquired in the flame from a measurement angle of 50° and 90°. In both cases, a 10 mJ (1.2 J/cm^2) IR beam is employed. Detection is performed with the use of the 650 and 430 nm bandpass filters. Signals are normalized at 10 mm HAB.

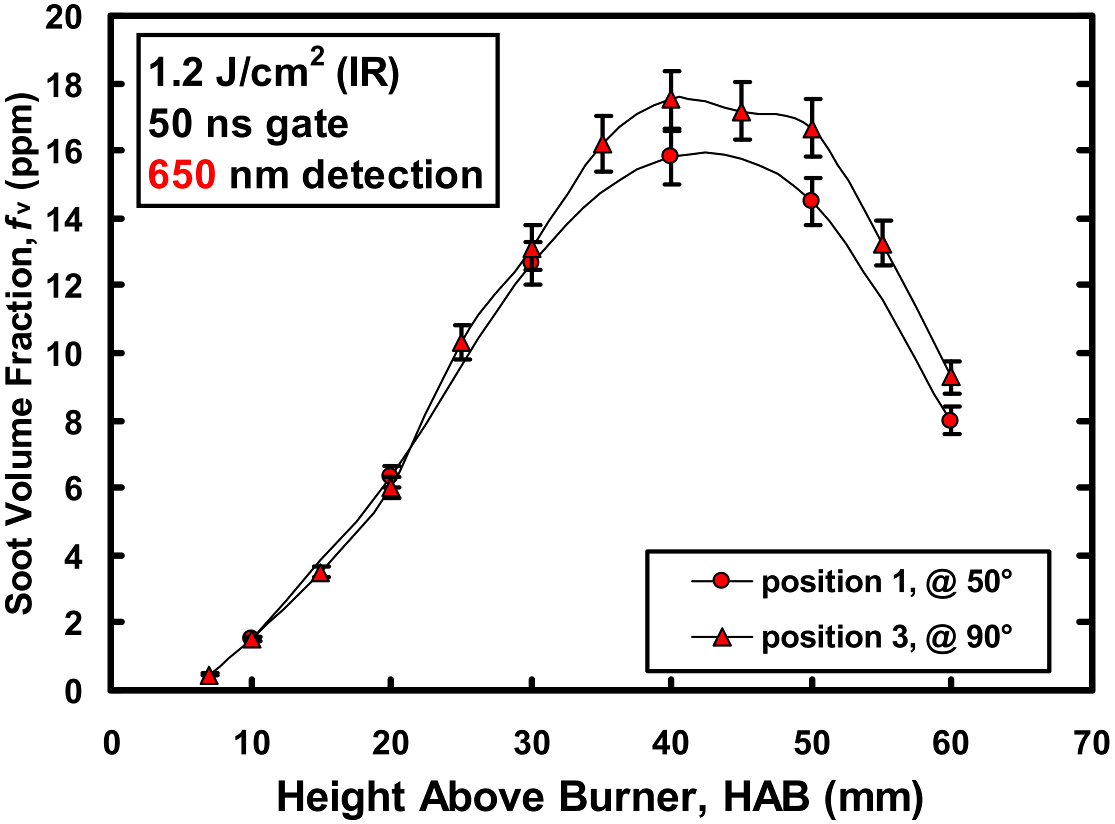

Figure 47. Comparison of 50ns-integrated LII signals acquired in the flame from a measurement angle of 50° at position 1 (see Figure 36) and 90° at position 3. In both cases, a 10 mJ (1.2 J/cm^2) IR beam is employed. Detection is at 650 nm for prompt 50 ns integration. Signals are normalized at 10 mm HAB.

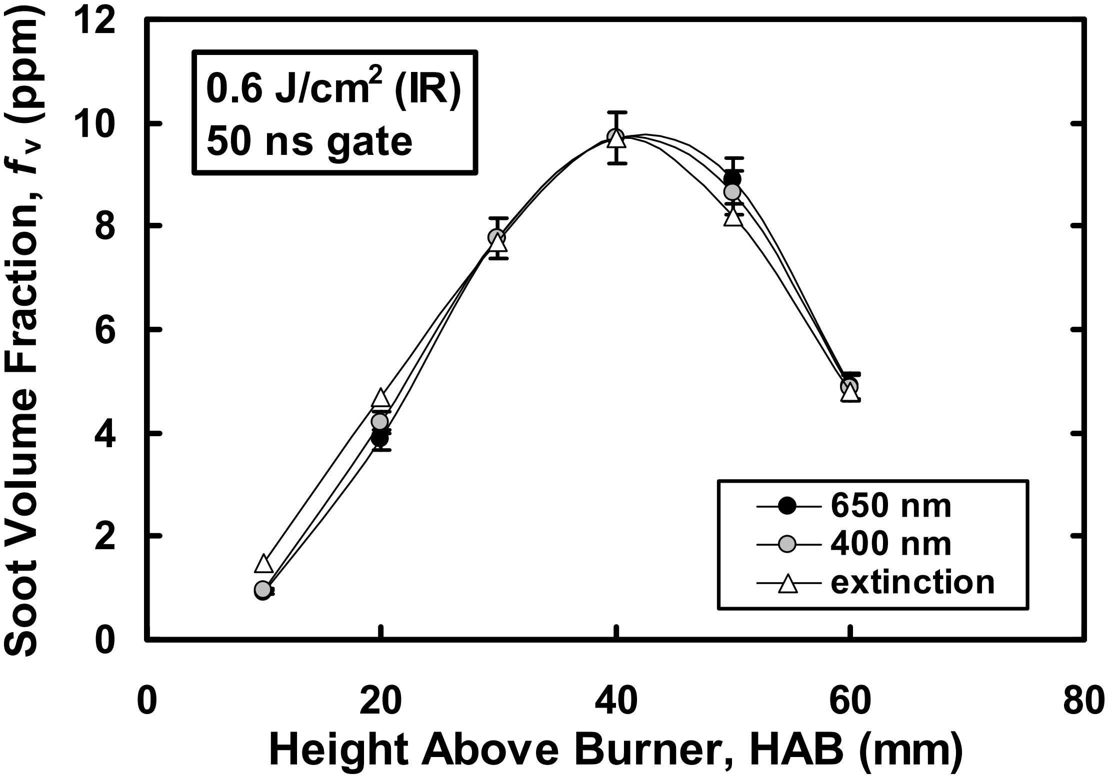

Figure 48. Comparison of LII signals acquired with the camera at 50° to the extinction measurements of Quay *et al.*[79] LII is generated with a 10 mJ (1.2 J/cm^2) IR pulse. Signals are integrated over a prompt 50 ns gate and averaged over 10 images. Broadband filters in the red (OG570) and blue (BG3&BG18) are employed. Signals are normalized at 40 mm HAB.

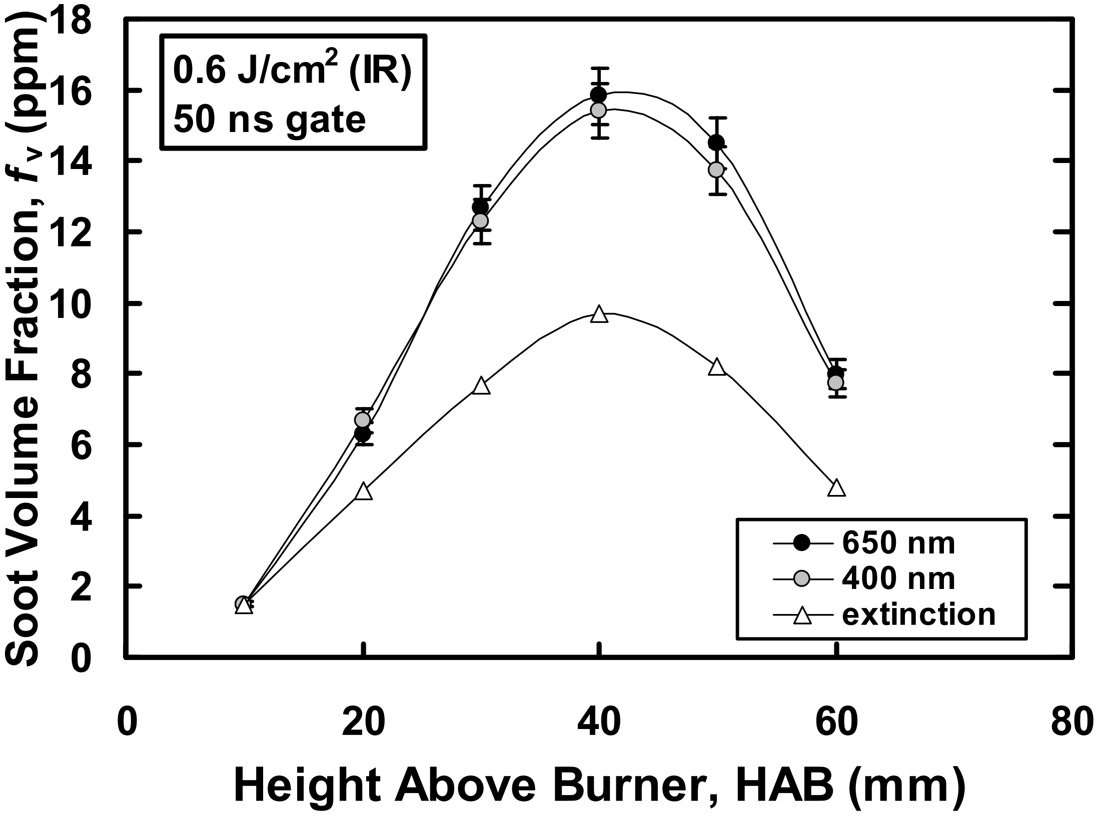

Figure 49. Replotting of the data of Figure 48, renormalized at 10 mm height in the flame. Signals are again compared to the extinction measurements of Quay *et al.*[79]

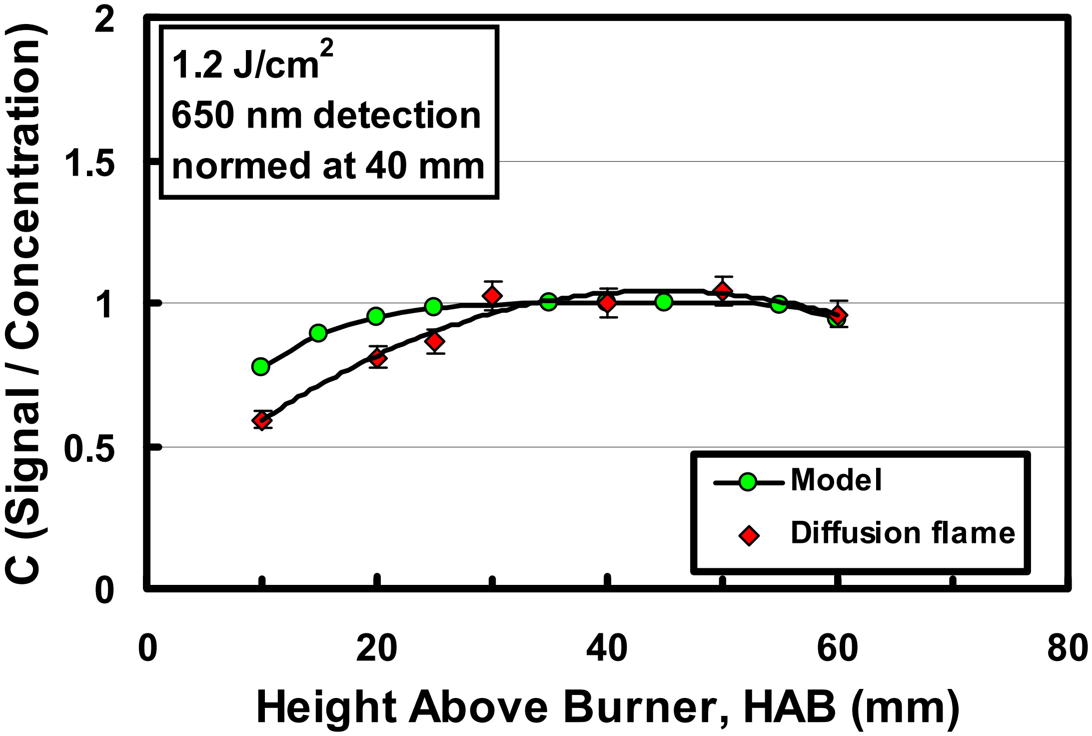

Figure 50. Comparison of the calibration constant, C, values in the flame to those predicted by the model for the same conditions as the experiment. Laser illumination is from a focused 10 mJ IR pulse (1.2 J/cm^2). Signals are detected with the broadband red filter (OG570), nominally 650 nm detection. ICCD peak signals are integrated over 50 ns and averaged over 10 images. Signals are normalized at 40 mm HAB.

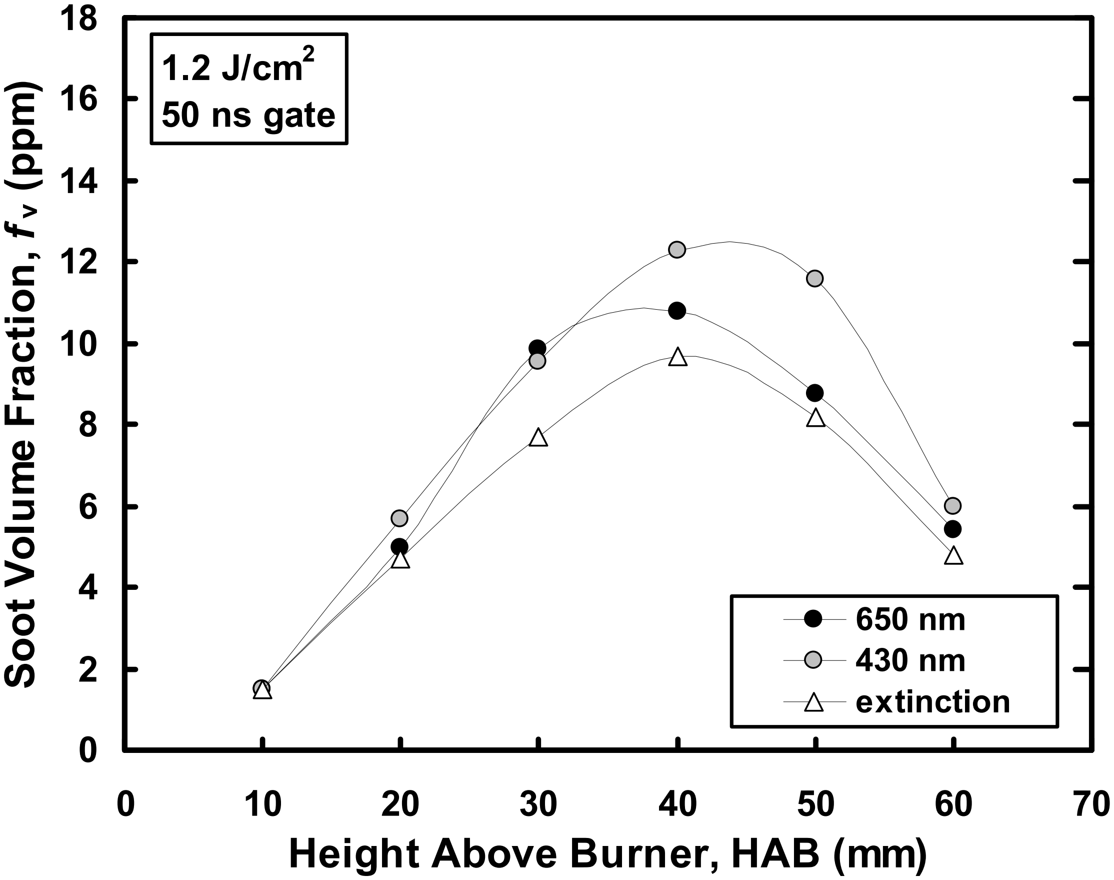

Figure 51. LII signals acquired with the camera for 100-shot accumulations on the CCD. Laser illumination is from a focused 10 mJ IR pulse (1.2 J/cm^2). Broadband filters in the red (OG570) and blue (BG3&BG18) are employed. Signals are normalized at 10 mm HAB.

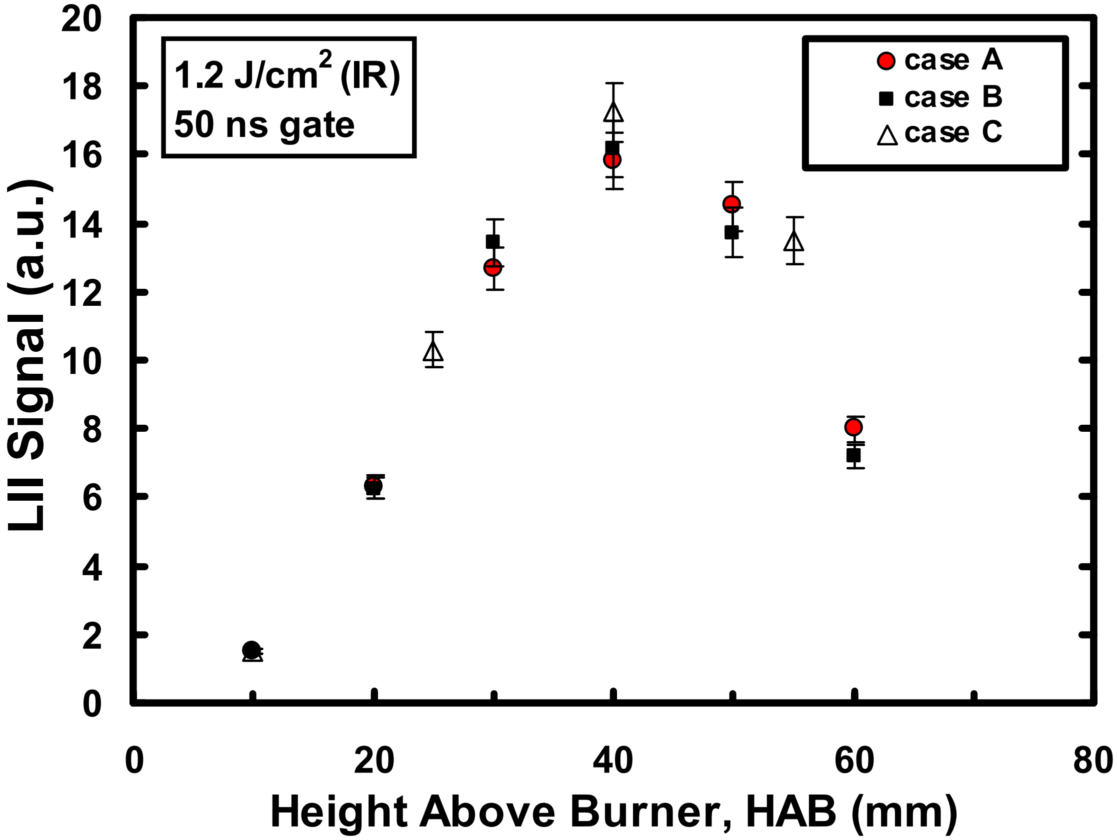

Figure 52. Repeatability of LII measurements. LII signals versus height in the flame are acquired on three different days with three different setups and compared to each other by normalizing at the 10 mm signals. In all cases the illuminating beam is 10 mJ at 1064 nm (1.2 J/cm^2), detection is at nominally 650 nm, signals are averages of 10 images, and the detection gate is 50 ns. Case A: camera 1, OG570 filter. Case B: camera 1, 650 nm bandpass filter. Case C: camera 2, 650 nm bandpass filter.

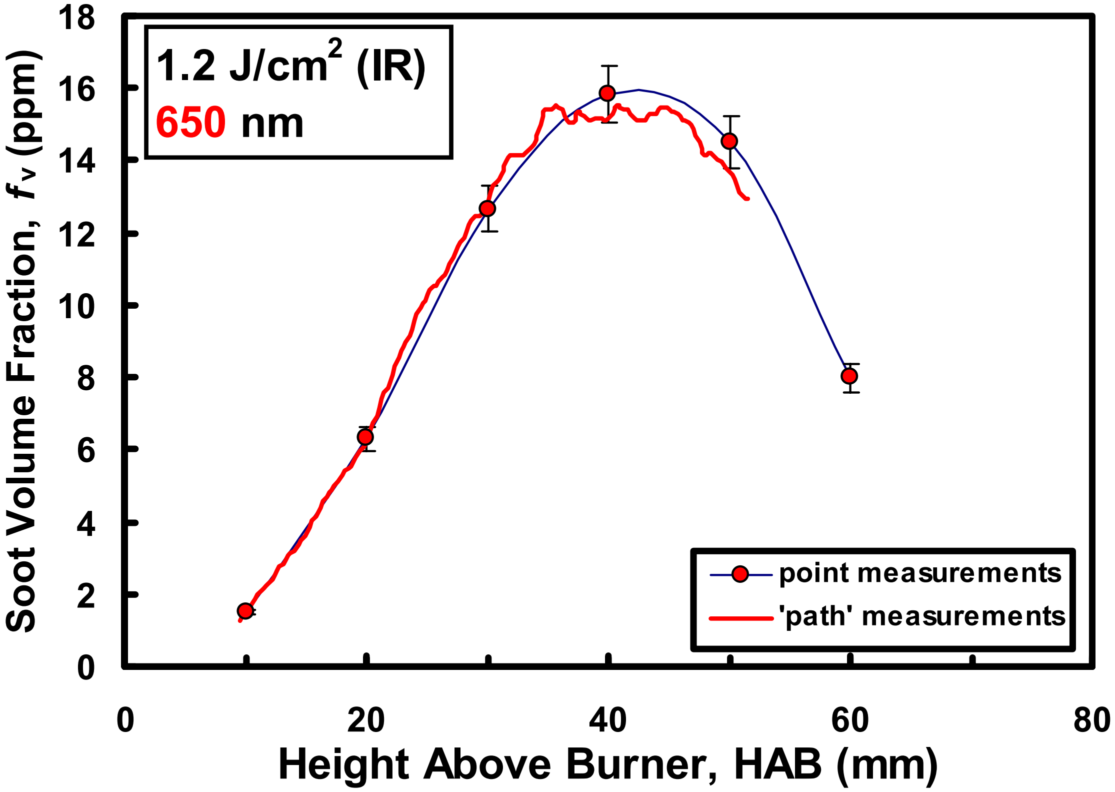

Figure 53. Comparison of pointwise signals from Figure 46 (50°, 1.2 J/cm^2 IR) to image sheet signals from Figure 37 (50°, 0.65 J/cm^2). Signals are detected at nominally 650 nm and are integrated over a prompt 50 ns gate. Signals are normalized at 10 mm HAB.

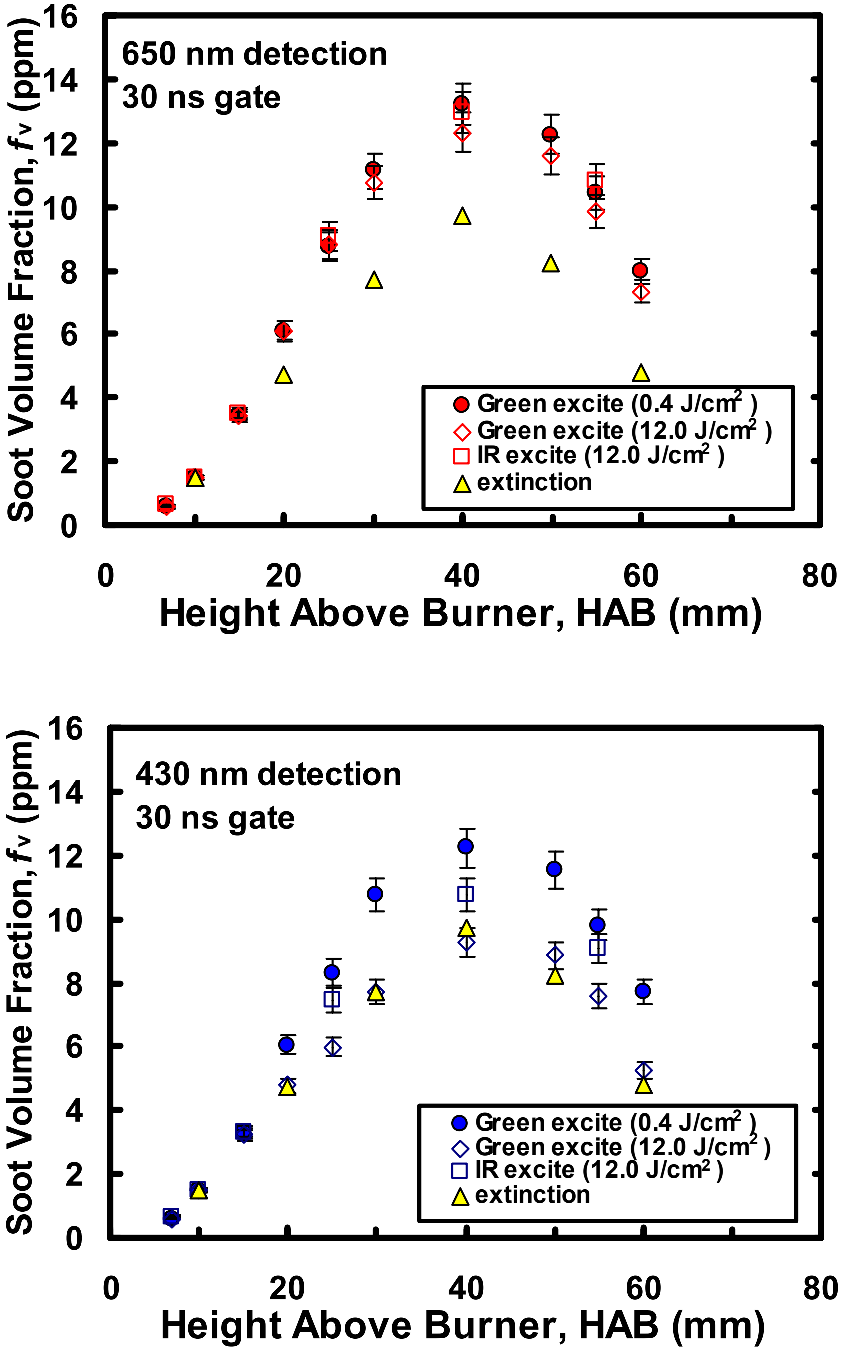

Figure 54. High intensity illumination (12 J/cm^2) results for both 1064 nm and 532 nm are compared to signals generated by green illumination a little over threshold (0.6 J/cm^2). Detection employs a 20 ns prompt gate and the data are averages of maxes from 10 images.

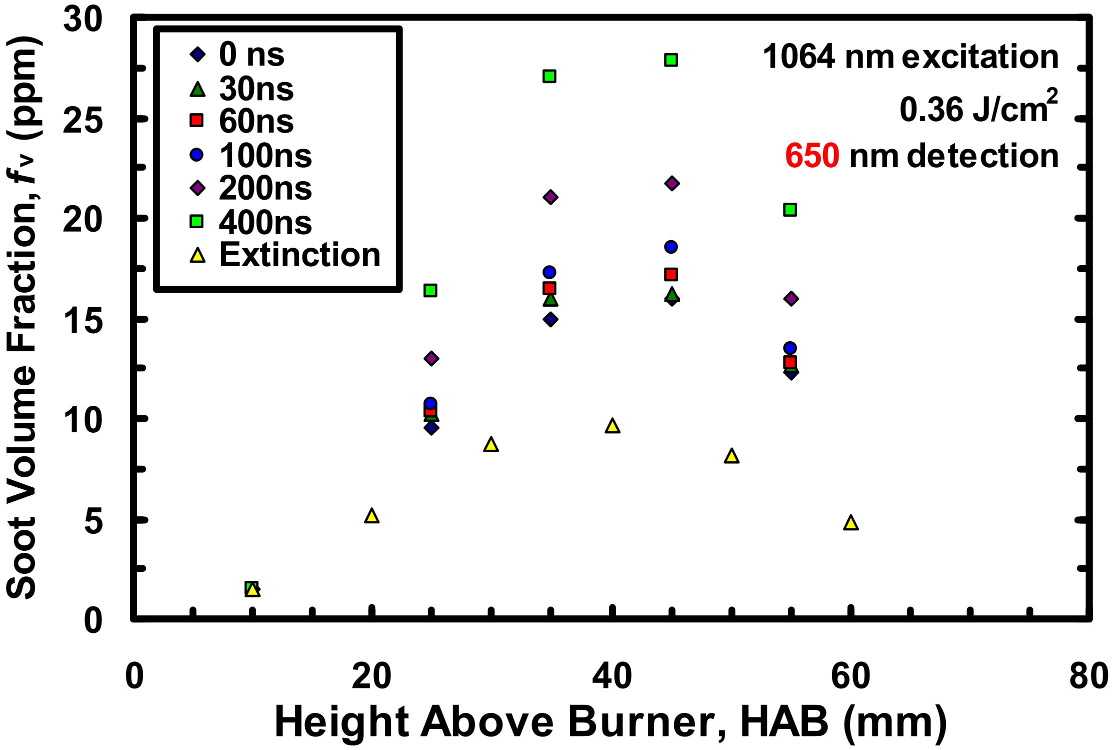

Figure 55. LII signals against height in the flame for various delays. Measurements are made up the front of the flame with 0.36 J/cm^2 IR illumination. Signals (650 nm) are recorded by the boxcar from the PMT/monochromator and gated for 20 ns. The data are again normalized at 10 mm HAB

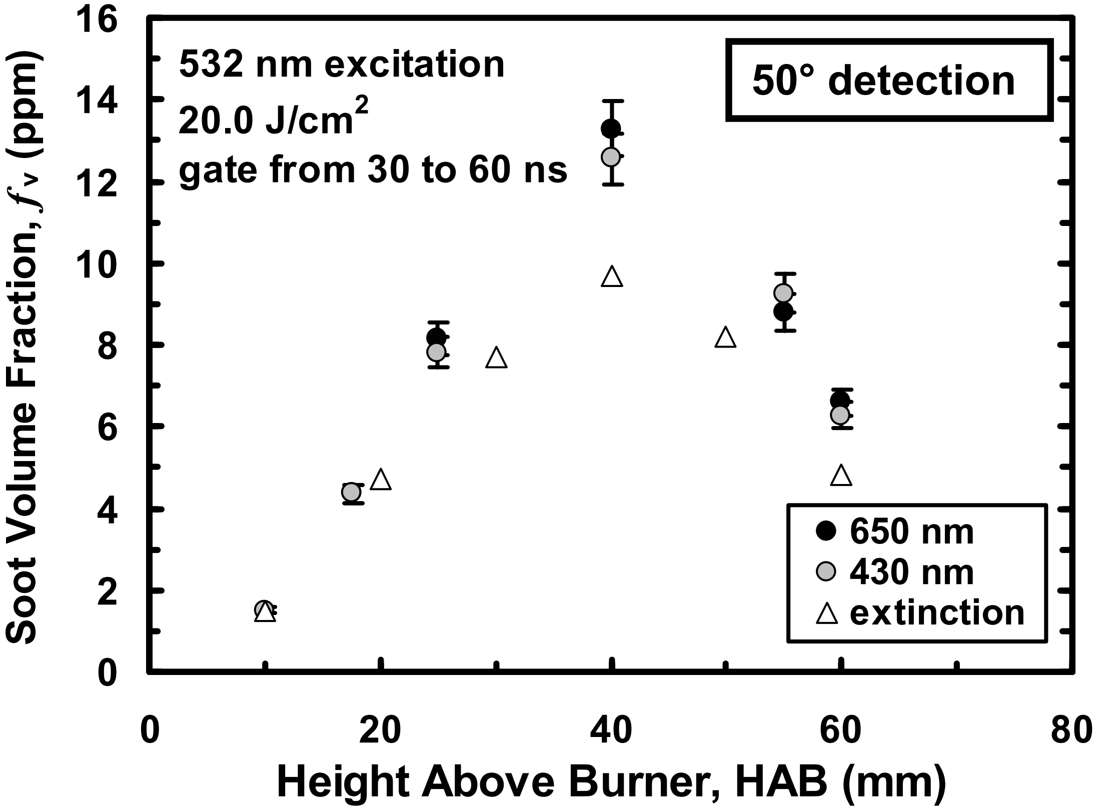

Figure 56. Delayed LII signals at very high intensity illumination. 650 and 430 nm camera signals are detected with 30 ns gates at 30 ns delay. The incident laser is at 532 nm and at a fluence of 20 J/cm^2. Data are averages of 10 maximum signals from the images. These are normalized at 10 mm HAB.

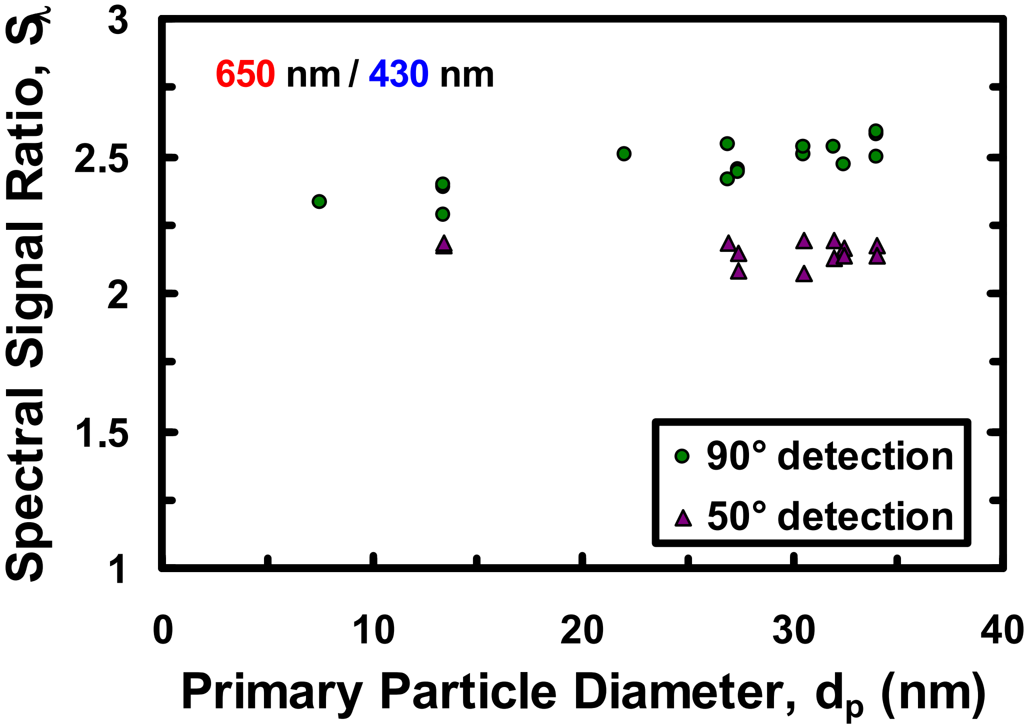

Figure 57. Spectral signal ratios for 650 and 430 nm detection from the two employed observation angles. Signals are acquired with prompt 50 ns gates. Illuminating intensities vary for the data but range near threshold.

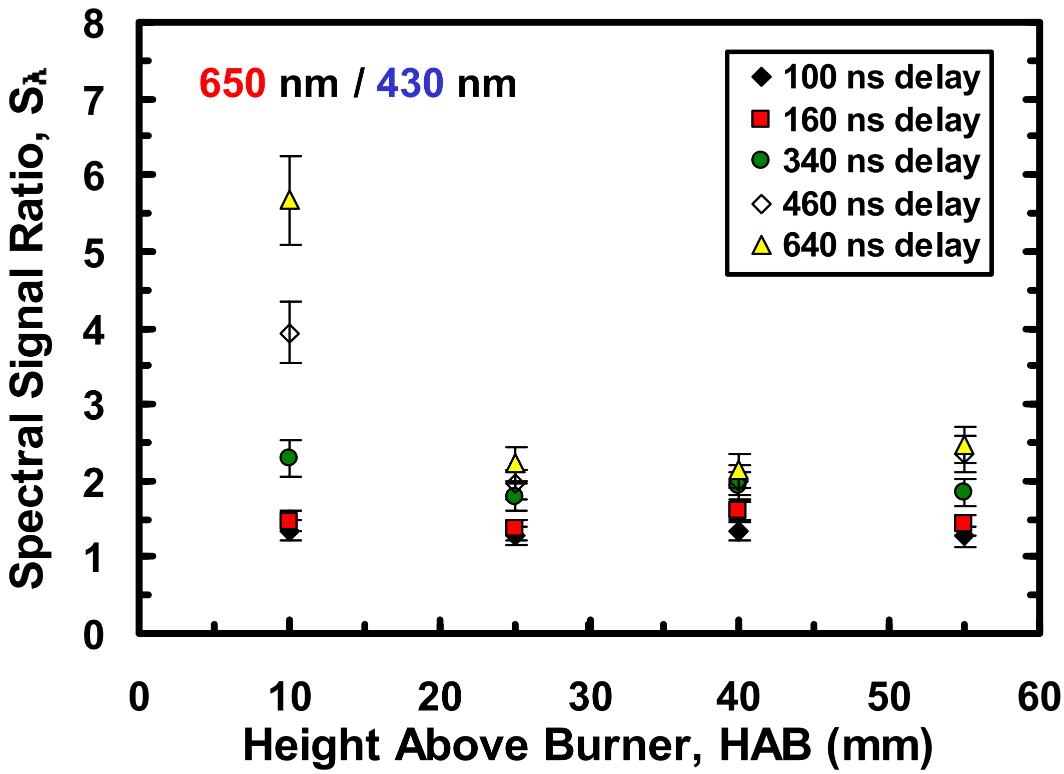

Figure 58. Spectral signal ratio for delayed detection. This ratio (650nm/430nm) is plotted against the height in the flame for different detection delays. Incident illumination is infrared at 1.2 J/cm$^{2.}$ Detection gates are 20 ns. The signals are uncorrected for the detector response.

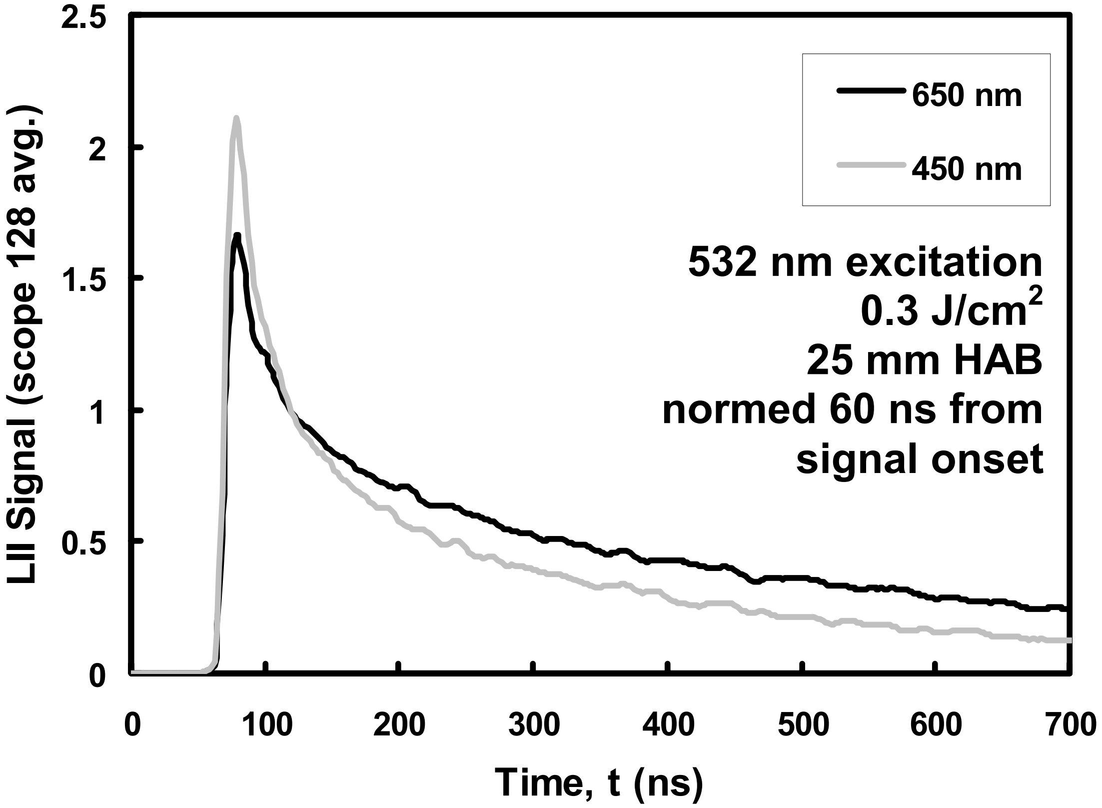

Figure 59. Red (650 nm)and blue (650 nm}time histories of the LII signal generated with ~2J of 532 nm (0.3 J/cm ^{2}). Signals are normalized at 60 ns from the onset of the signal. These are also strongly averaged, a running 128 average on the oscilloscope.

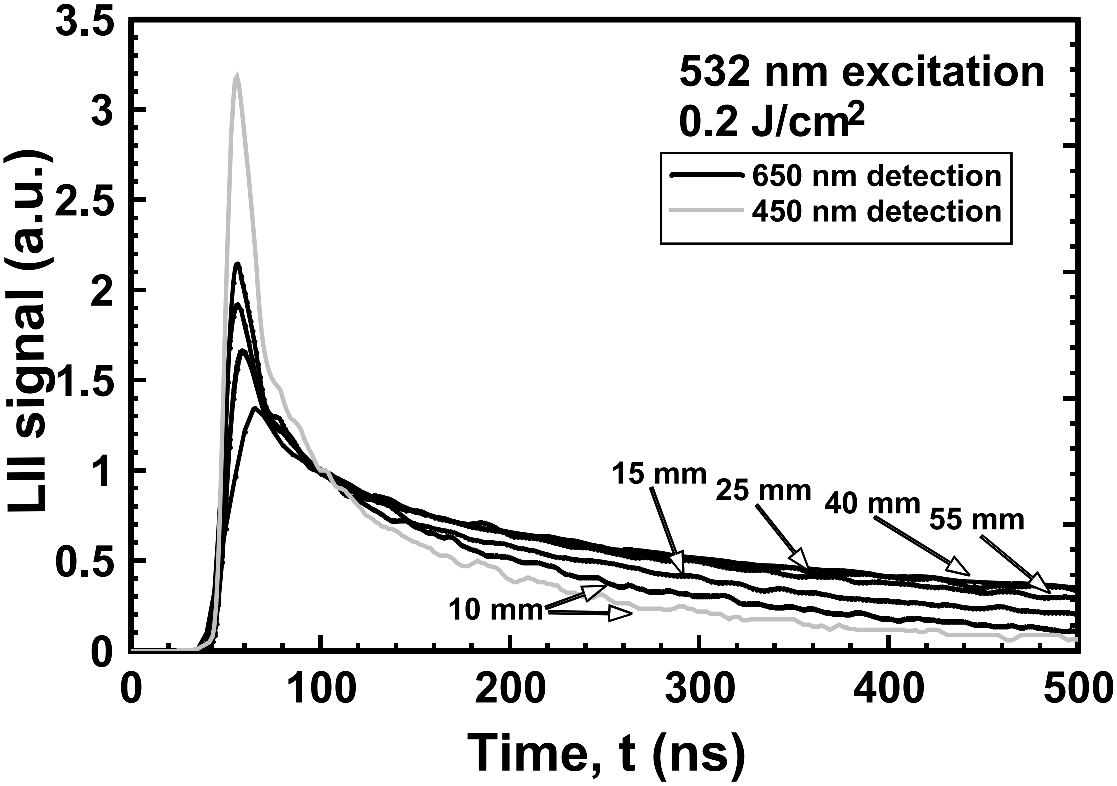

Figure 60. LII signal decay versus time for five heights in the ethylene flame and at two detection wavelengths. Primary particle diameters for these positions are 14, 22, 30, 33, and 31 from lowest to highest height.[55] Laser excitation is a Nd:YAG (532 nm) at 0.3 J/cm^2. Signals are normalized at 60 ns after signal onset.

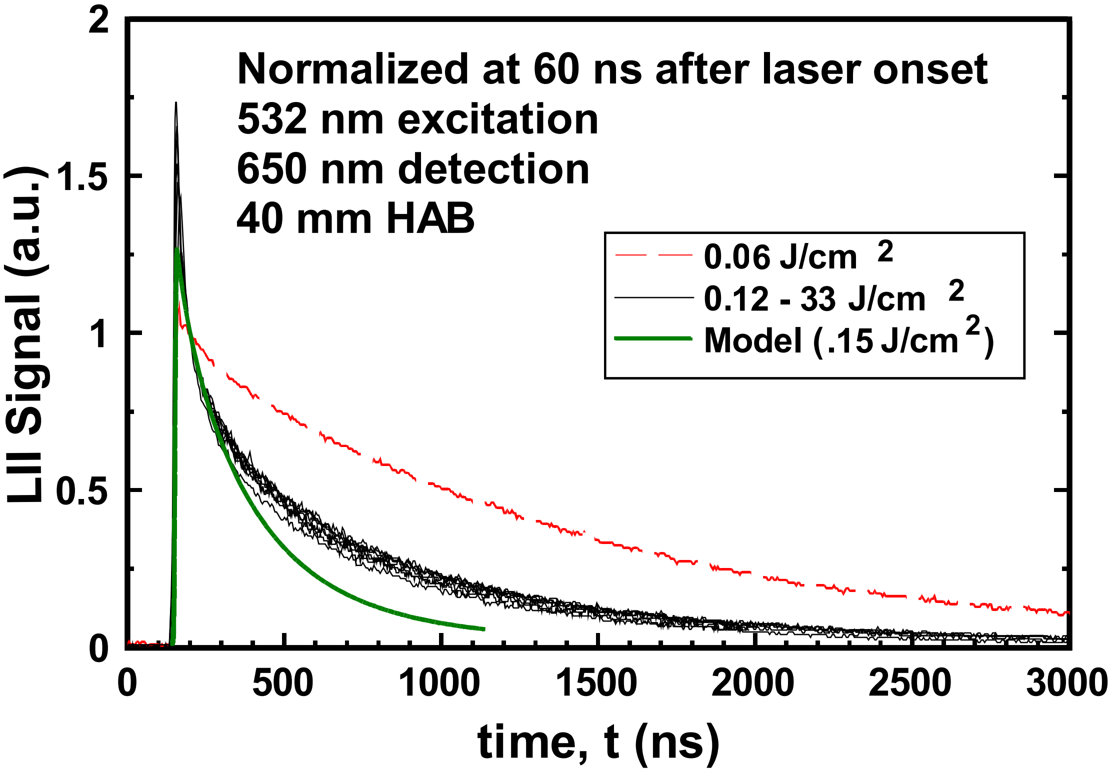

Figure 61. LII time traces for 40 mm HAB (33 nm particle) at various laser fluences. The red line represents a case below the threshold intensity, while the black curves range from threshold to over 200 times that fluence. The green line represents a numerical simulation of the experiment at threshold (0.15 J/cm^2).

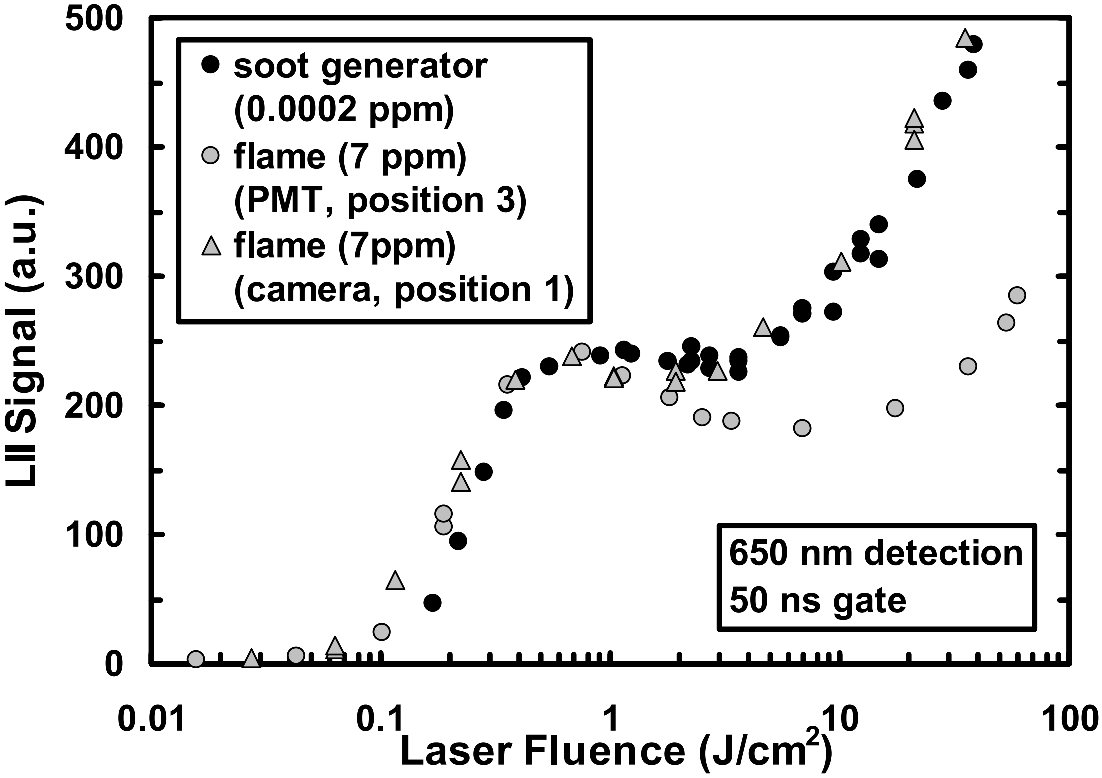

Figure 62. LII signal versus incident laser fluence in the soot generator aerosol. The aerosol concentration is 0.4 mg/m^3 (0.2 ppb) from a solution concentration of 0.035 g/L. The imaged area is 4 mm wide by 2 mm high and is imaged directly onto the PMT. Red detection (~650 nm) is through the OG570 longpass filter. The data from the soot generator are compared to the data recorded at the two measurement positions in the flame which were acquired with the camera and PMT, respectively. (see Figure 42).

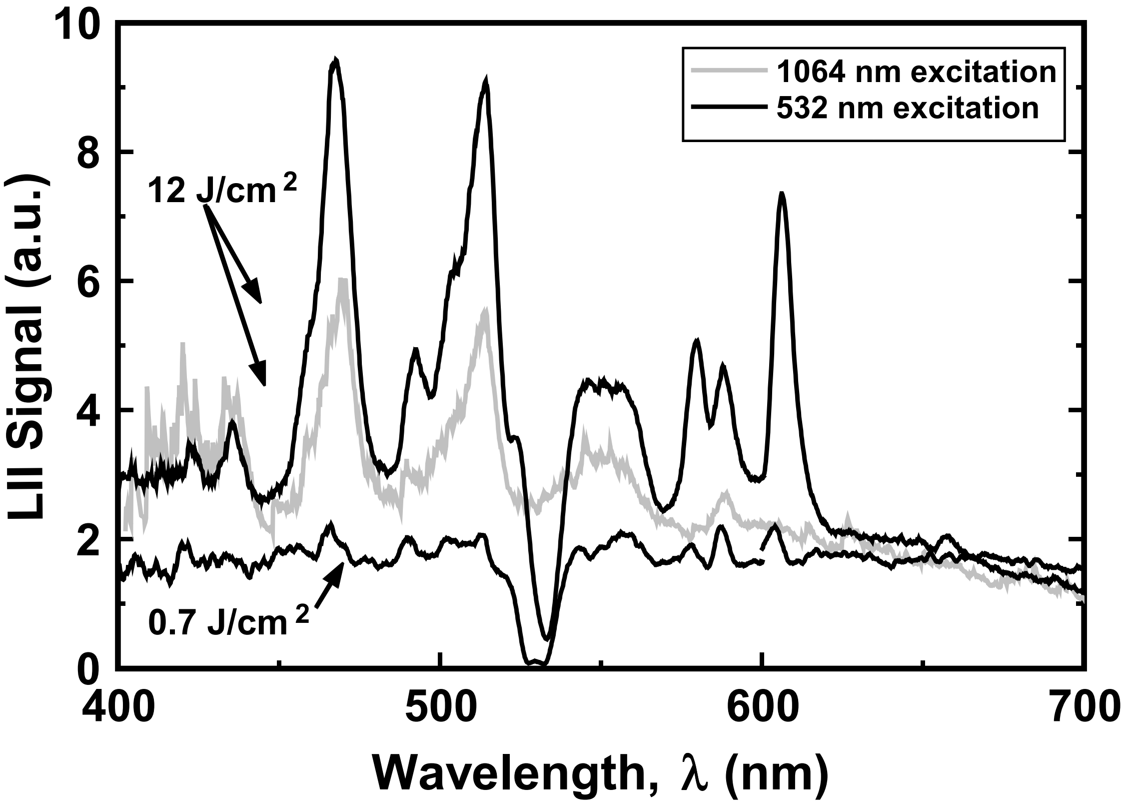

Figure 63. LII spectra recorded in the simulated exhaust flow. Visible wavelength spectra are shown for green excitation at high energy (12 J/cm^2) and IR excitation at the same high energy (no notch filter) and for green excitation at a 'plateau' value of 0.7 J/cm^2. The data are corrected for the response of the detection system and spectral emissivity of the soot particles. Scale of the two high fluence curves are correct relative to one another, while the lower fluence curve is simply scaled for presentation purposes.

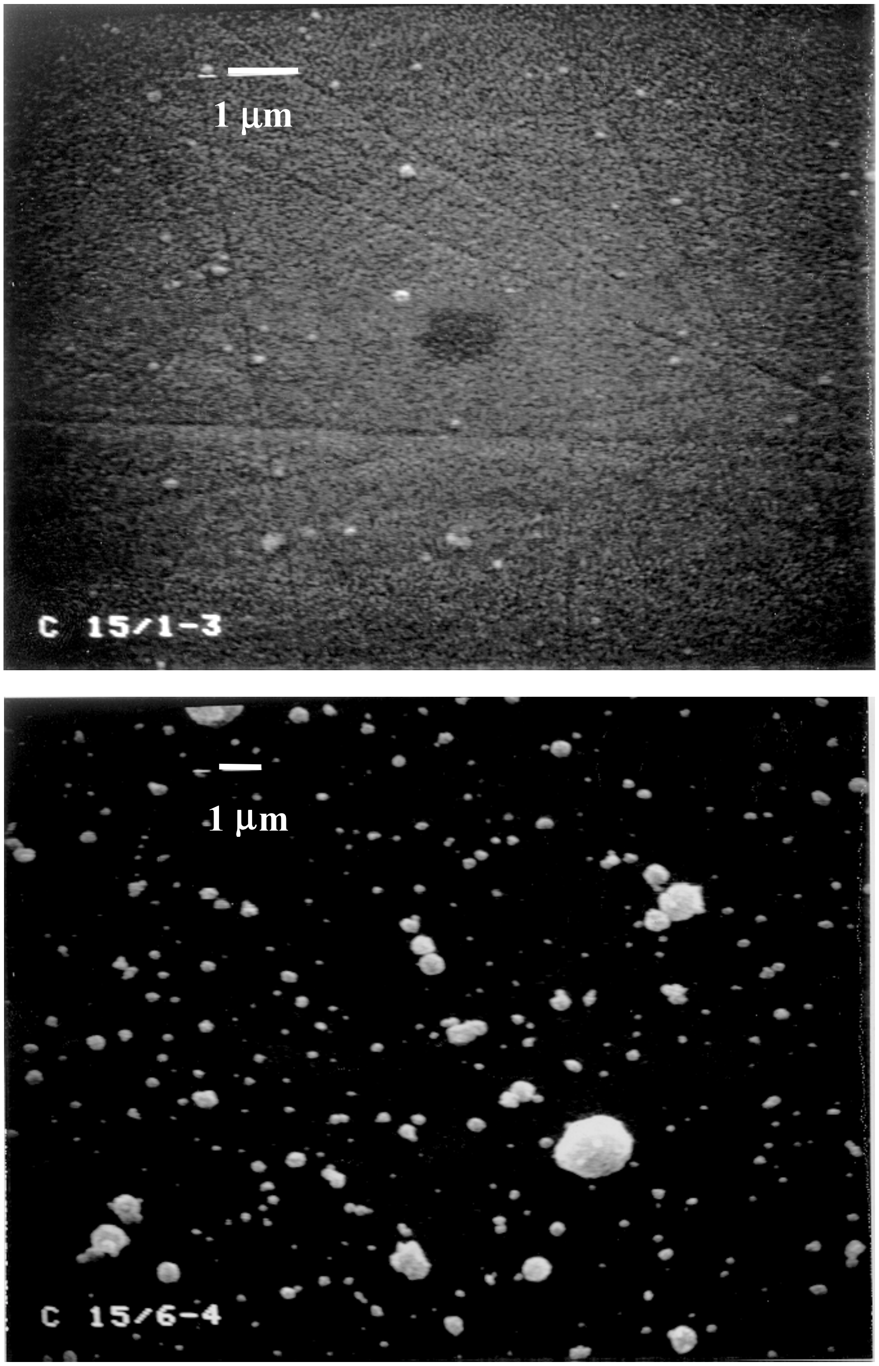

Figure 64. SEM images of sampled soot generator aerosol. Above: Aerosol concentration of 0.085 mg/m^3 (10,000× magnification). Below: Aerosol concentration of 34.0 mg/m^3 (5,000× magnification). Exposure time in both cases is 3 minutes

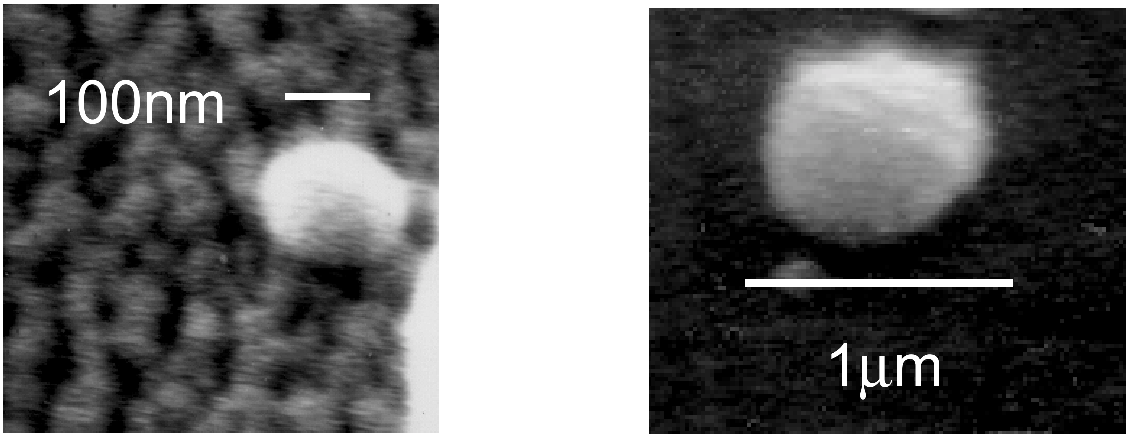

Figure 65. Spheroid carbon particles. SEM images of sampled soot generator aerosol. Aerosol concentrations are 0.085 mg/m^3 and 34.0 mg/m^3. Exposure time is 3 minutes.

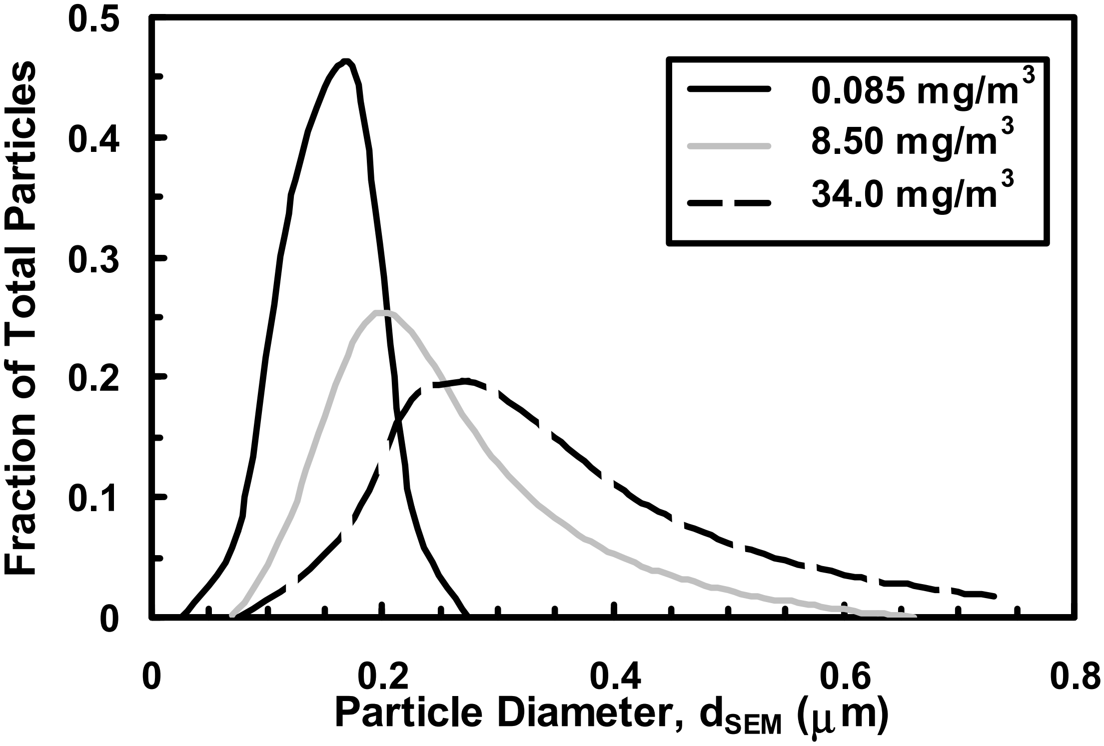

Figure 66. Measured particle size distributions from image analysis of samples from three of the carbon/water solution strengths. The mean particle sizes are 160, 270, 340 from the lowest to highest of the three.

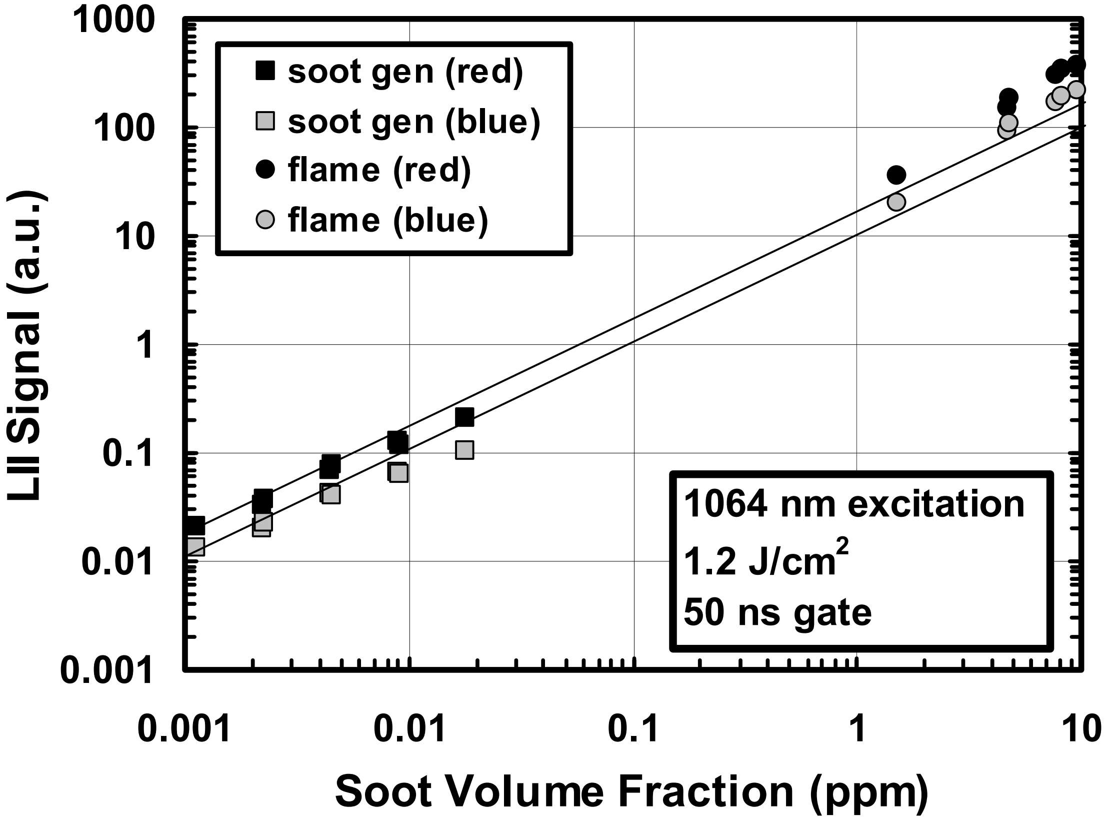

Figure 67. Flame / soot generator calibration. Signals are recorded in each environment with the exact same experimental setup. Signals were imaged directly onto the PMT through the OG570 or BG3/BG18 Schott glass. Incident laser fluence (IR) was 1.2 J/cm^2. Signals were integrated promptly over the first 50 ns.

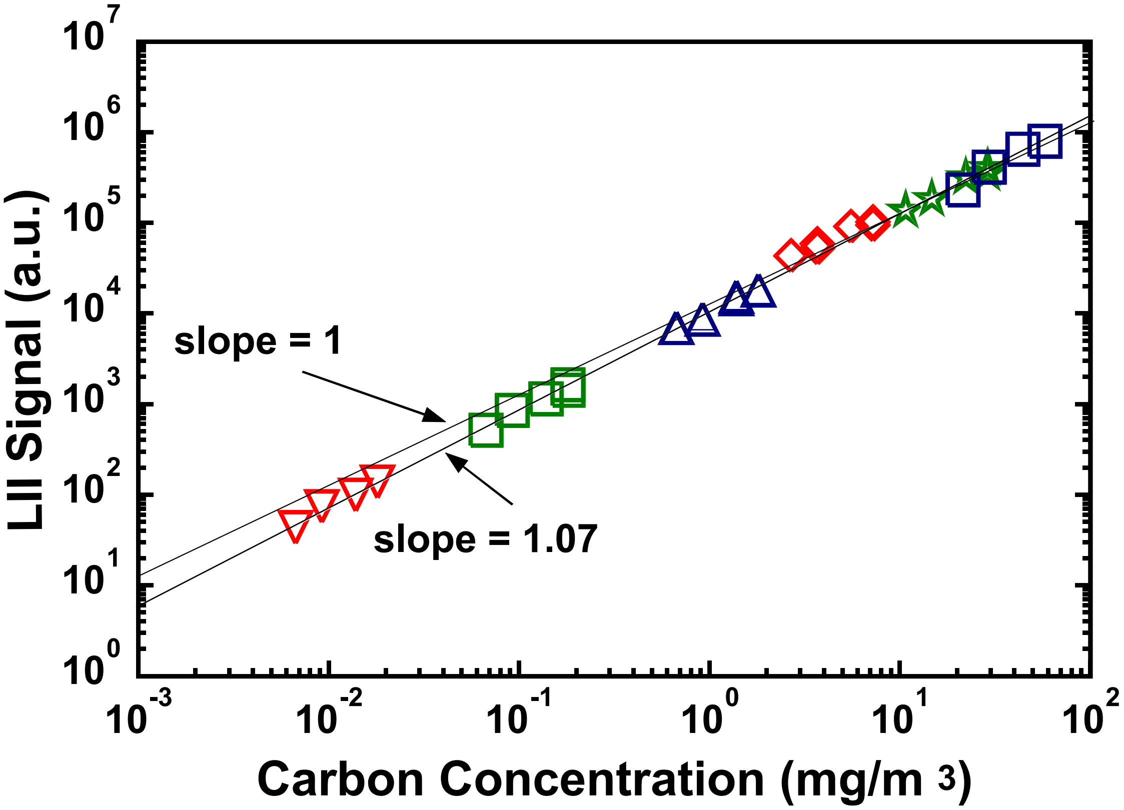

Figure 68. LII signals measured from the soot generator plotted against calculated carbon concentrations. Signals are detected over a range of approximately 570 to 850 nm (OG570). The signals are excited by a 250 mJ (0.5 J/cm^2) pulse at 1064 nm. Individual symbols represent a given concentration for the carbon/water solution. The lines represent a dependence of the signal on concentration only (slope=1) and a fit to the data with 315 cm^3/s air dilution. Note the log scaling.

Figure 69. Single-shot image of a 8 mg/m^3 (4 ppb) aerosol just at the exit of the soot generator. Laser intensity (IR) is 1.4 J/cm^2.

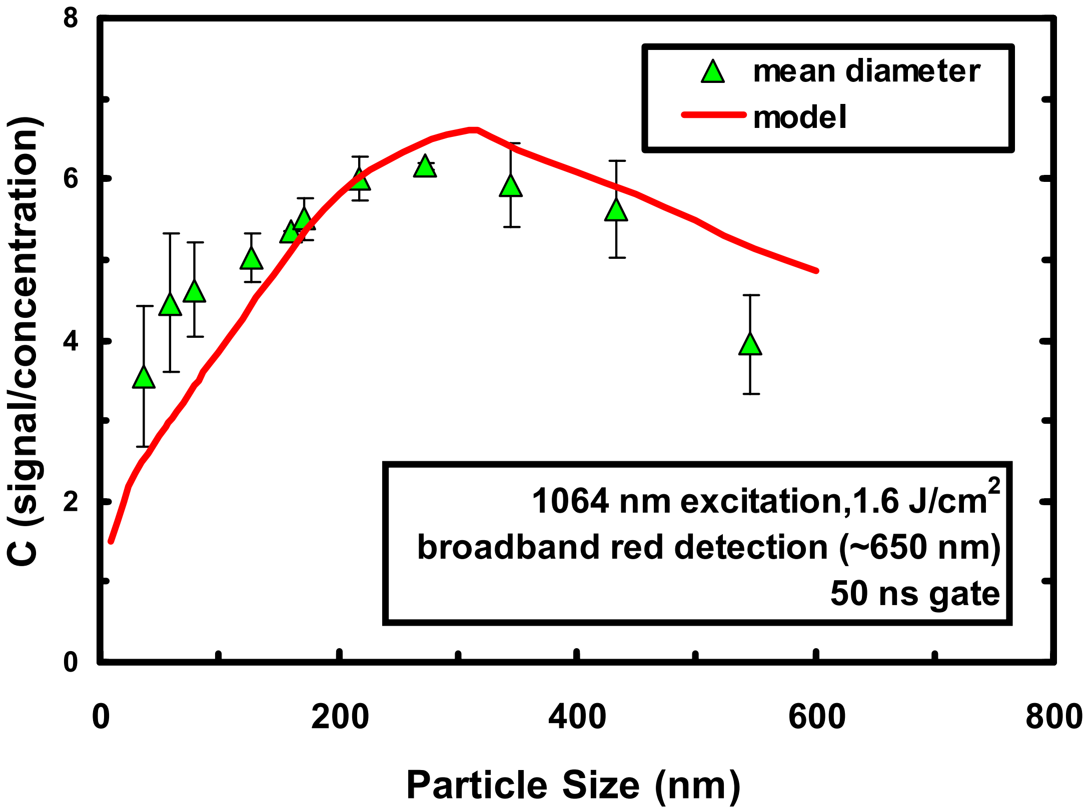

Figure 70. Calibration constant, C (signal / soot volume fraction) for LII signals from the soot generator aerosol with 315 cm^3/s air dilution and the model results for the same conditions plotted against soot particle diameter. Experimental data are plotted against calculated particle sizes from a 4.3 µm droplet (mean of the distribution). Signals are integrated over the first 50 ns. The model signal is calculated for 650 nm detection, while experiments are over the 570 to 850 nm range.

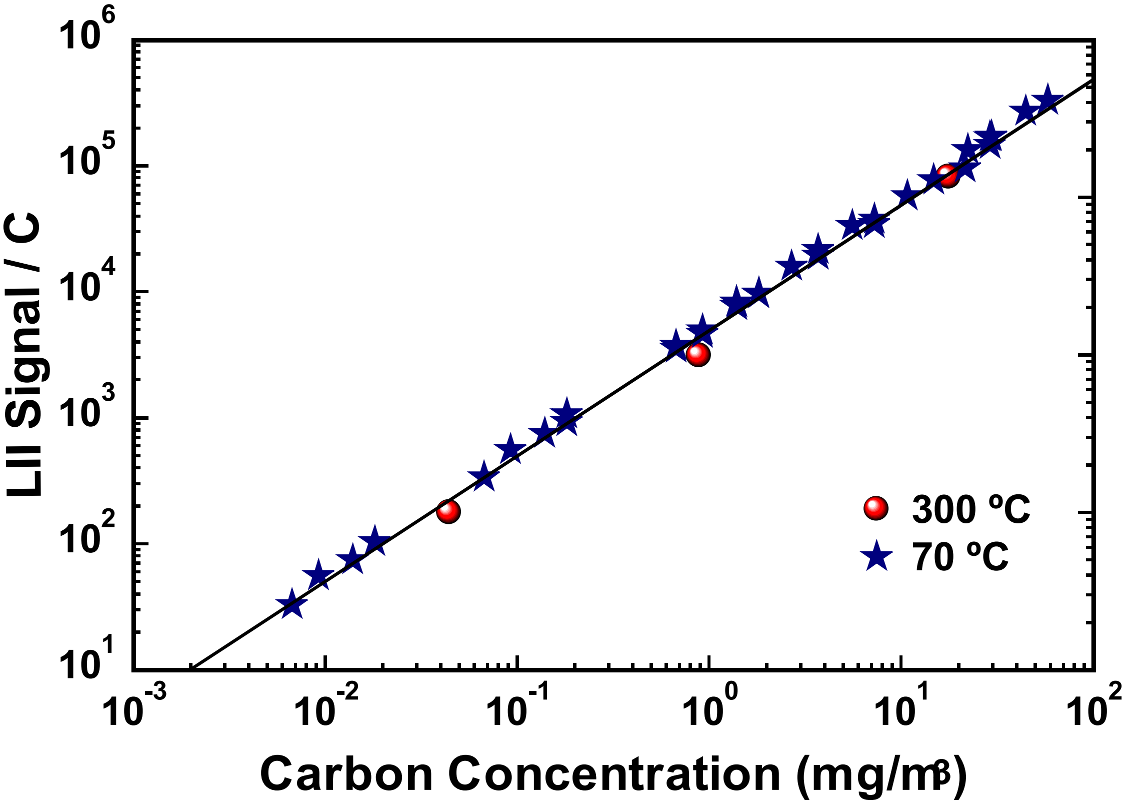

Figure 71. LII signals for three solution concentrations are plotted against calculated carbon concentrations for a preheated air flow rate of 770 cm^3/s. These three data points are compared to the data of Figure 68, which have been forced to linearity by dividing each group of data by its average C. Recorded temperatures are at the jet exit. Signals are excited and detected as in Figure 68. Note the log scaling. The data are corrected for the exit velocity variations from the elevated temperatures.

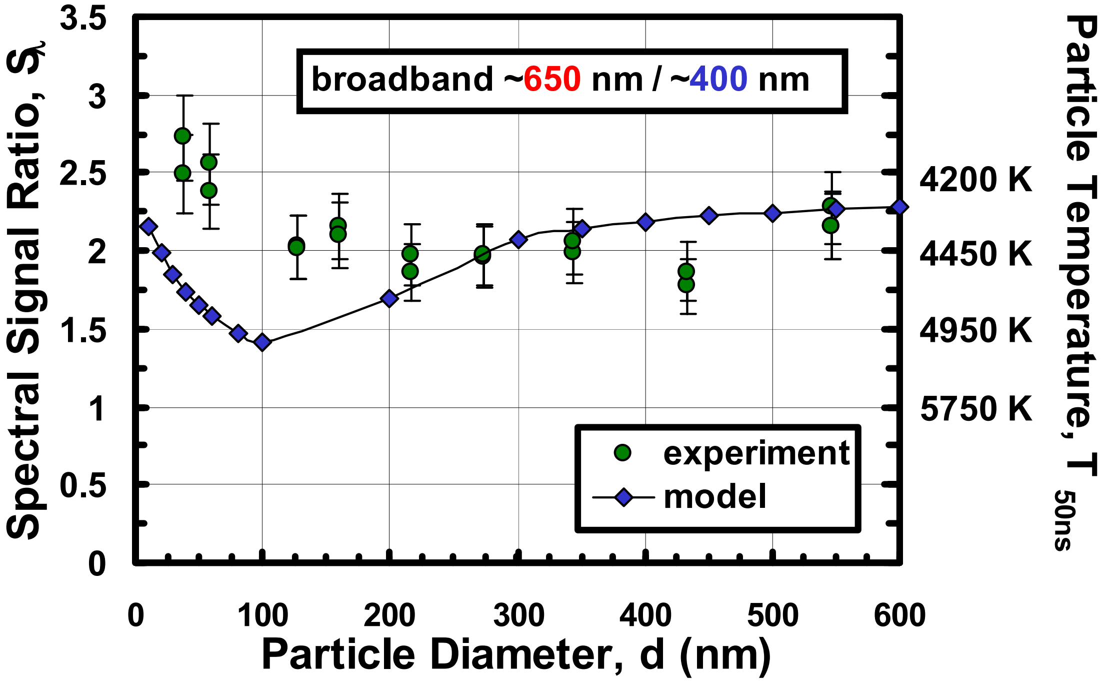

Figure 72. Ratio of broadband (~120 nm) red/blue signals from the soot generator aerosol for concentrations from 0.02 to 65 mg/m^3. These data are also plotted against the best estimate of the actual particle temperatures based on the reported camera responsivity and calculated response of the broadband filters. The predictions of the model for this range of particle sizes is also included. The unfocused IR laser is employed, with a fluence of 1.6 J/cm^2.

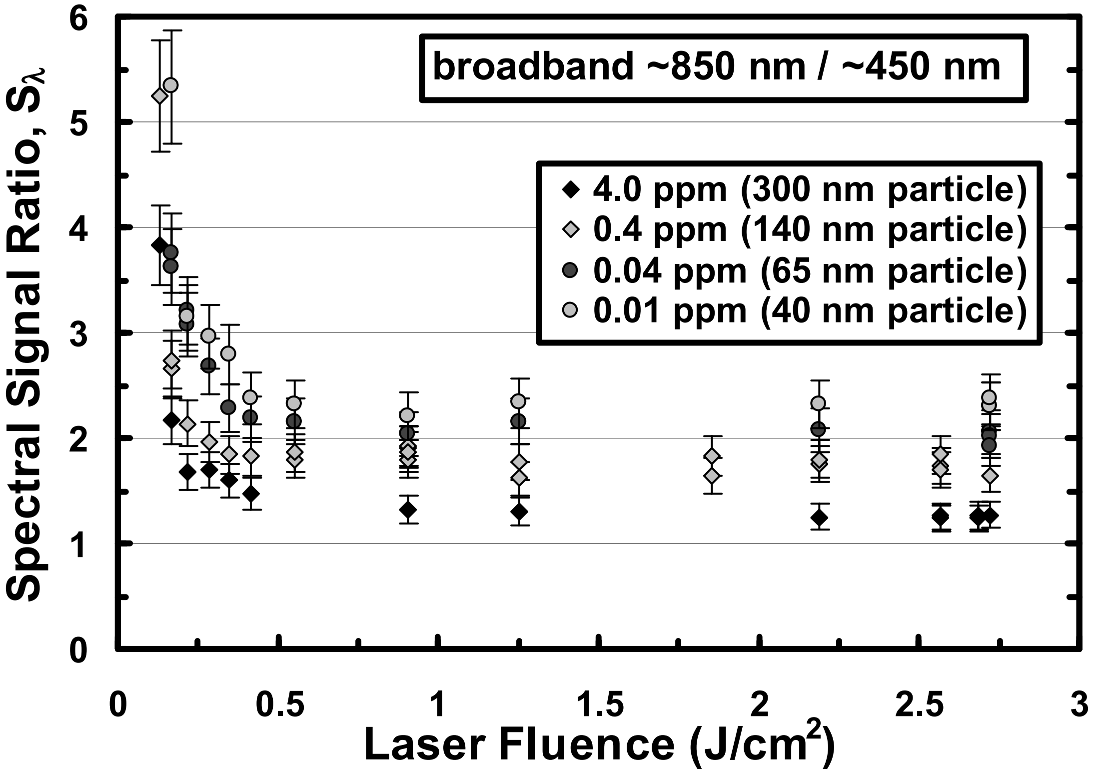

Figure 73. Signal ratios versus laser fluence are presented for a dynamic range in soot concentration of 400 and particle sizes ranging from 40 to 300 nm. The RG630 and BG3&BG18 filters were employed for red and blue detection, respectively. The Ir beam was unfocused and was essentially taken to its maximum intensity of near 3 J/cm^2.

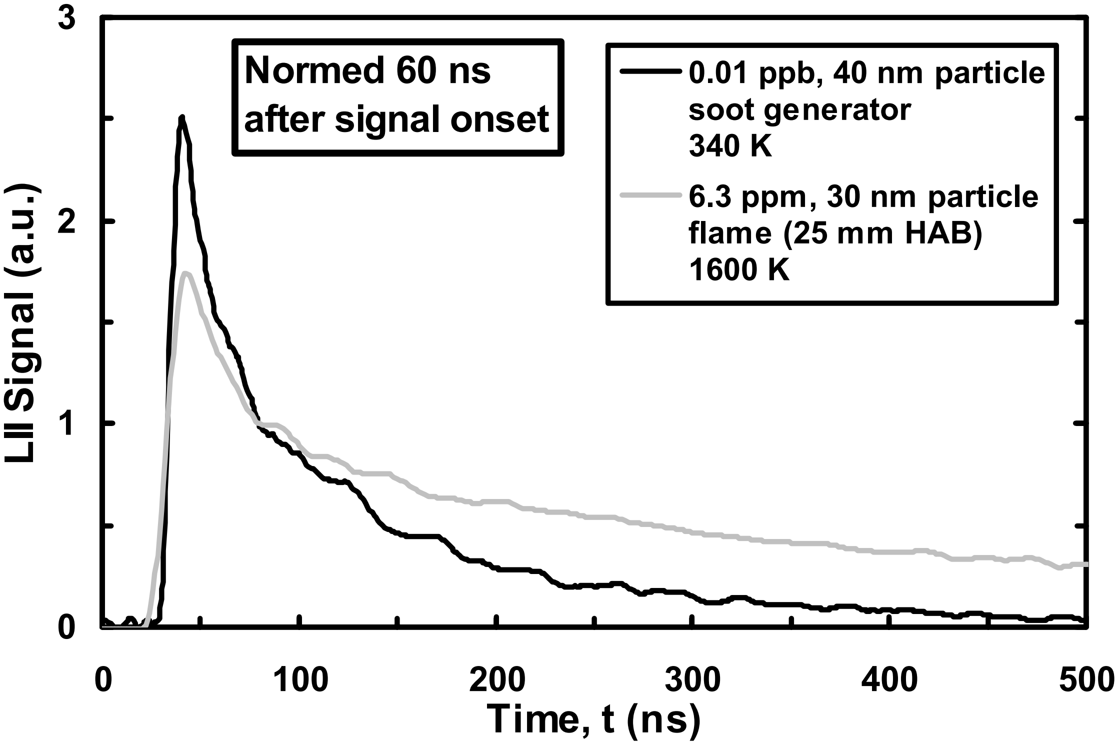

Figure 74. Comparison of the LII time histories for a 30 nm particle in the flame and a 40 nm particle in the soot generator aerosol. For the exhaust, the IR beam is unfocused at 120 mJ (1 J/cm^2) and the detection wavelength (~650 nm) is broadband. For the flame, a focused IR beam of 11.5 mJ was employed, yielding a 1.4 J/cm^2 fluence. The 650 nm bandpass filter was employed for signal detection.

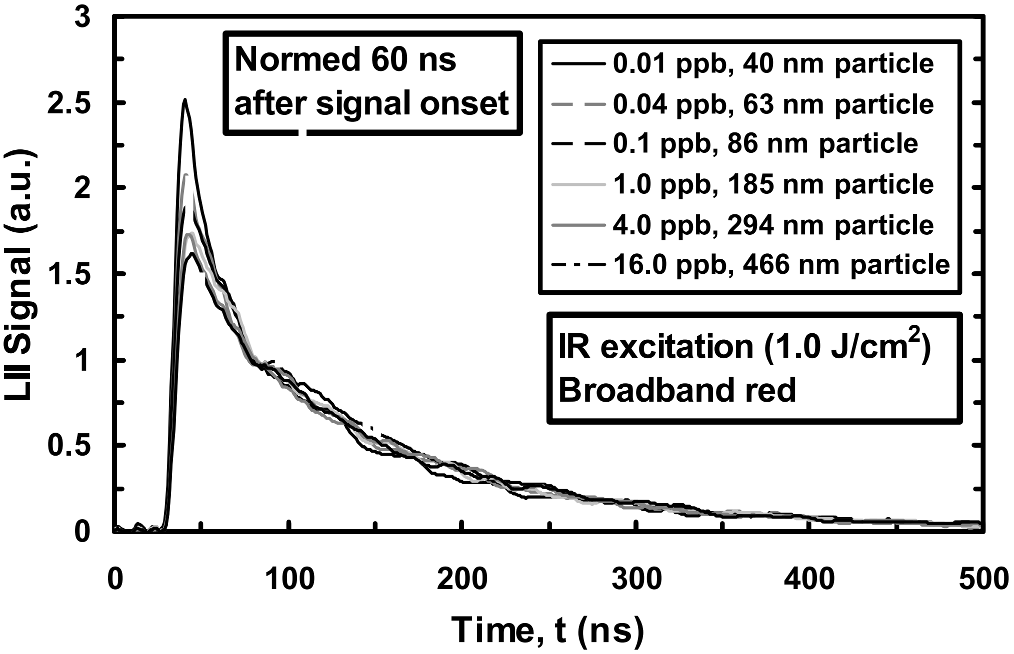

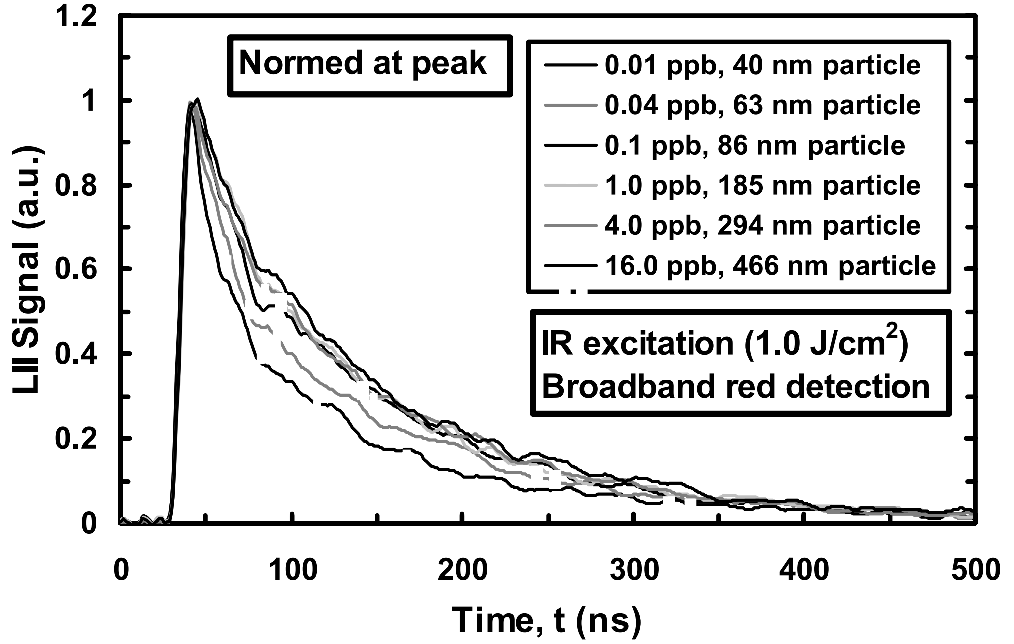

Figure 75. LII signal time histories for various particle sizes (distributions). The illuminating intensity is 1.0 J/cm^2. The signal trace is an instantaneous capture of a running average of 128 shots on the oscilloscope. Above: Data are normalized 60 ns after the signal onset. Below: The data are normalized at their peaks.

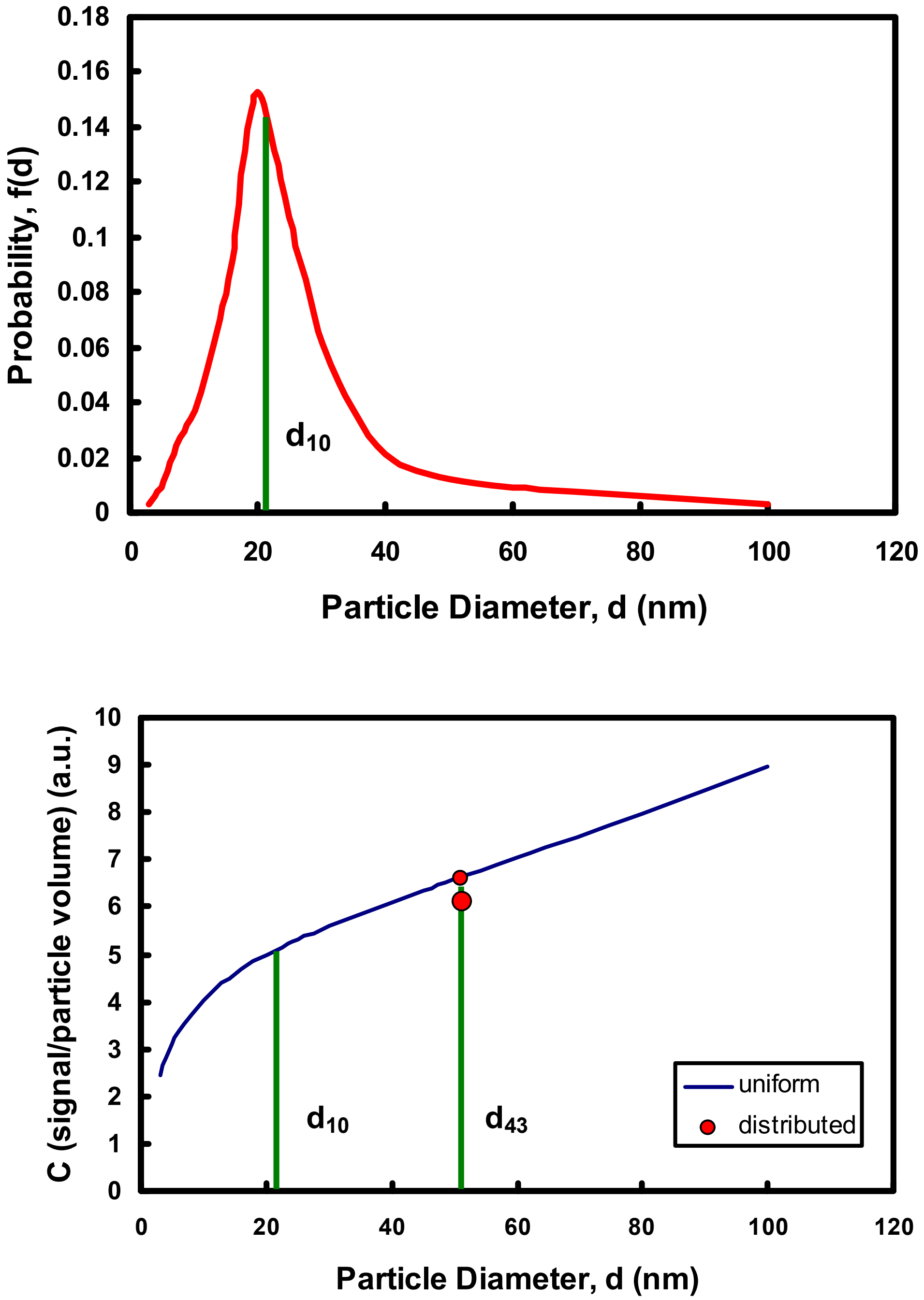

Figure 76. Modeled particle size distribution effect. Above: theoretical particle size distribution wit a mean near 21. Below: Calculated C for a range of discrete particle sizes illuminated by an IR pulse of 0.6 J/cm^2 and the resultant C (   ) obtained by integrating the signals produced by this distribution

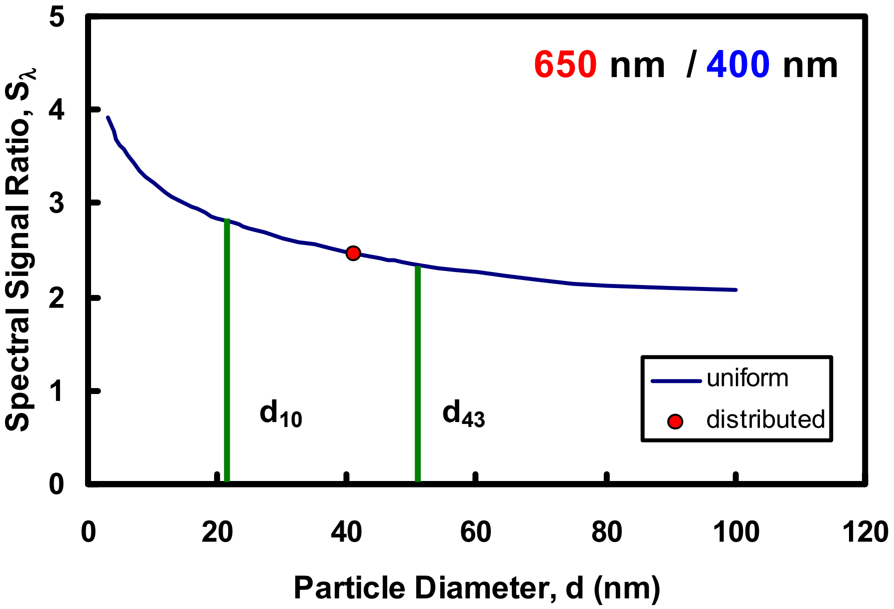

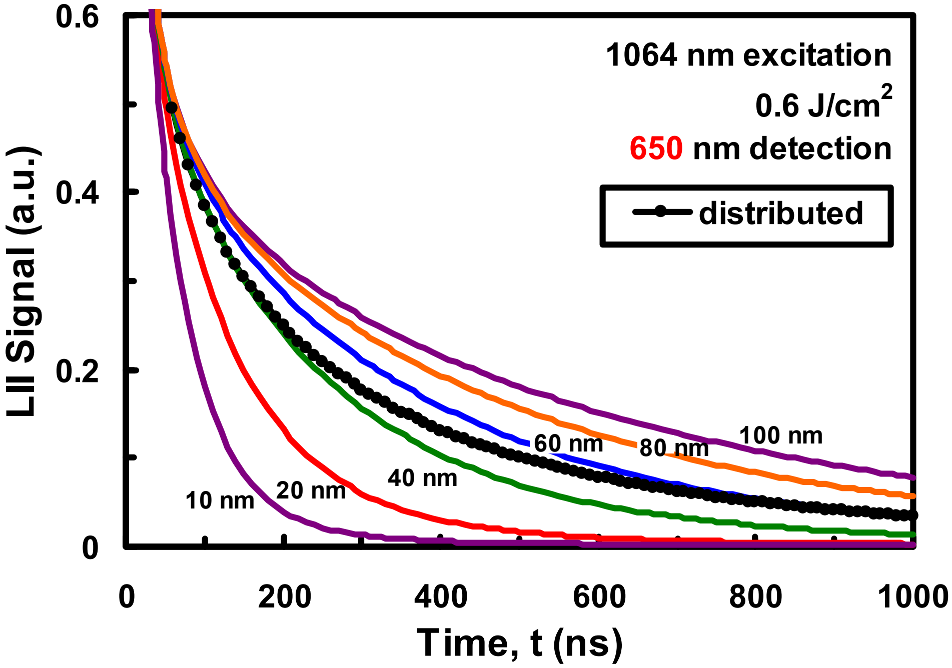

Figure 77. Above: Calculated spectral signal ratio (650nm/400nm, 50 ns) for a range of particle sizes and the resultant ratio produced by the distribution of particle sizes. Below: Calculated signal time histories for a range of discrete particle sizes and for the calculated behavior of the distribution above. The illuminating intensity is again 0.6 J/cm^2 The observed signal is at 650 nm.

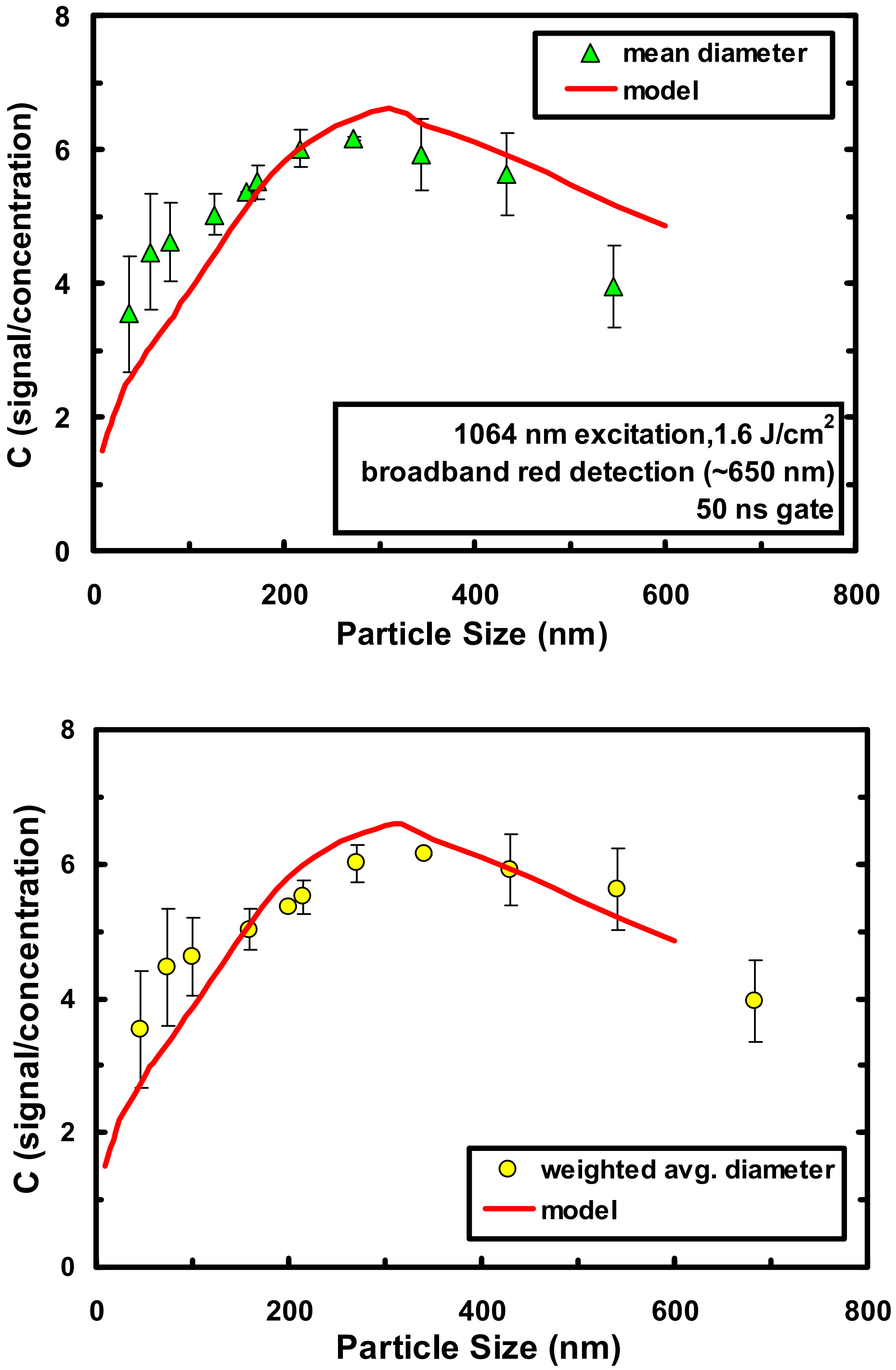

Figure 78. Above: Replotted graph of Figure 70, the measured C versus particle size in the soot generator. Below: Same C data as above, but scaled by a factor of 1.25.

APPENDICES

Appendix A – Rotameter Calibration

Three different rotameters were used in these experiments. Ethylene was metered to the diffusion flame by a Matheson E200 (601) series meter (model FM-1050) which had both glass and steel floats. Lower flow rates were employed and thus the glass float was most commonly monitored. This meter was calibrated with the soap bubble apparatus pictured in Figure A1. This setup measured the volumetric flow rate by moving a soap film up a volume-calibrated tube (in a piston manner, and in this case through a 50 mL volume) and measuring the elapsed time. The metering valve was located downstream of the meter and the pressure in the meter was maintained near 20 psig.

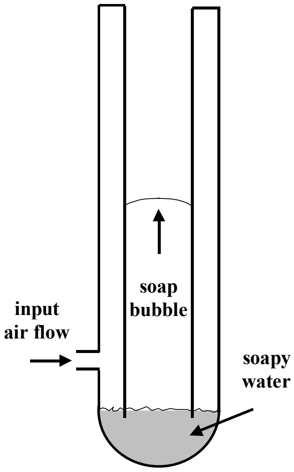

Figure A1. Soap-bubble flow rate measuring apparatus.

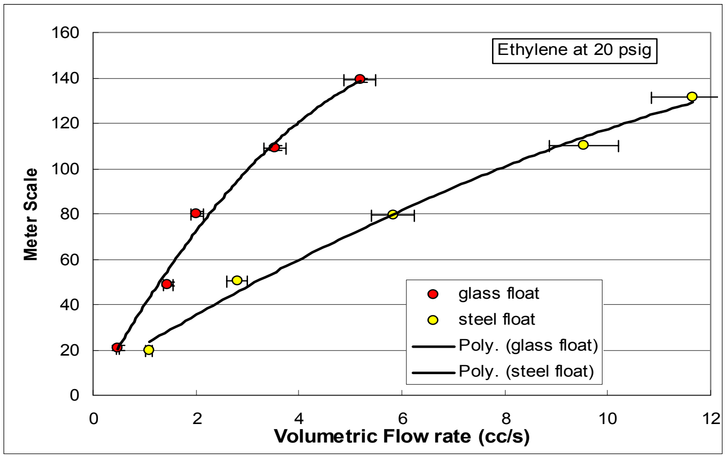

Figure A2. Rotameter calibration scale for fuel supply.

The experimental data and second order polynomial curve fit for the calibration of this meter are shown in Figure A2. A flow rate of 3.85 cc/s is represented by a scale reading of 118. A closer match to the 88 mm flame height was obtained with a setting of 116 (which the trendline would predict to be 3.77 cc/s, which is closer to 3.85 cc/s than the error bars of the experimental data) so this setting was used in the experiments.

The air supplied to the flame was metered by a Brooks meter (model R-7M-25-1F) which was calibrated by displacing water in a large inverted bottle in a water tank as depicted in Figure A3 (flow rates were too high for the soap bubble meter). The 10 L bottle was incrementally marked to every liter and 8 L was used as the displaced volume for each flow rate of the calibrat atmospheric pressure by raising the s water level in the bottle same h was loca downstream meter a Experimental data and a second order p

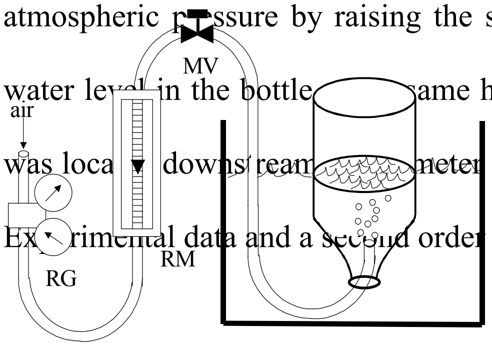

Figure A3. High volume flow rate measuring apparatus. PG: pressure guage, RM: rotameter, MV: metering valve.

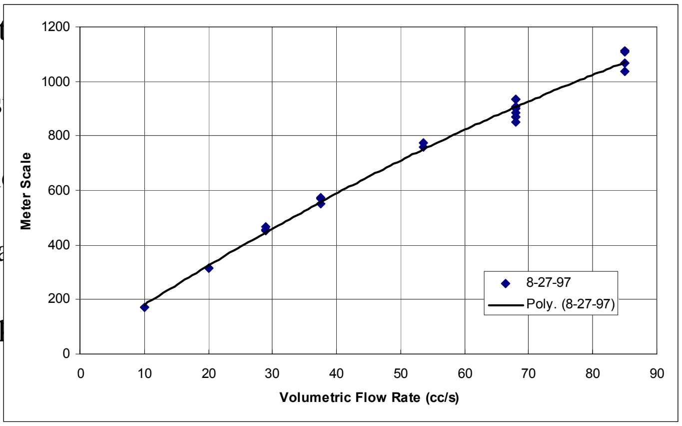

Figure A4. Rotameter calibration scale for air supply.

This rotameter was also used as the secondary air source for the soot generator. The primary air was supplied by a Dwyer meter (model RMB-52-SSV) at a fixed setting of 10.0 and a pressure of 36 psig which corresponded to 9.23 L/min as measured by the water displacing technique.

Appendix B – Laser Profile

The spatial distribution of the laser energy at the region of interest was determined by blocking various measured fractions of the beam area and measuring the transmitted energy. This was achieved by translating a razor blade across the beam in the direction in which the detector looks (Y-direction). This is done both left-to-right and right to left, with good agreement observed for the two traversing directions (e.g., see Figure B1). Prior to being cut horizontally, the beam is apertured vertically (cut at the top and bottom) to transmit just the center 1.5 mm (beam energy cut by 65%). This height represents the vertical dimension of the detected volume for most of the measurements in the flame. The beam is clipped so the measured energies will represent the energies present in the region being observed by the detector. These energies are measured in an averaged manner, i.e. at the 10 Hz rate, by a pyroelectric joulemeter (Scientech, model 380101). The measuring element is a volume-absorbing disc (with a high power density rating) coupled to a thermoelectric device that generates a calibrated voltage proportional to the energy contained in the laser-heated disc, i.e., the disc temperature (98 mV/W).

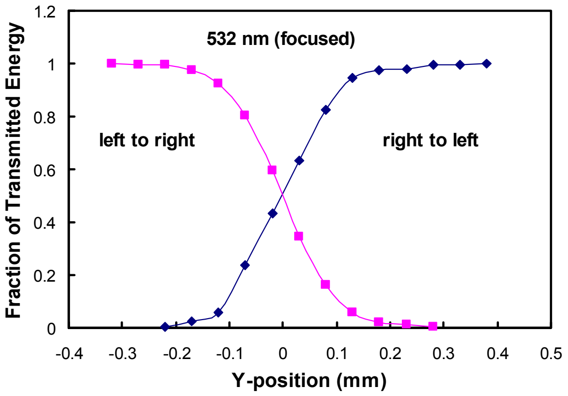

Figure B1. Beam profiling measurements for the focused 532 nm laser. Data are the transmitted energy of vertically clipped beam as a knife blade is moved across the beam.

The distribution is assumed to be Gaussian (Normal). The recorded energy fractions (energy / unblocked energy) are matched to normalized 1-D Gaussian distribution positions (z) yielding the same integral fraction (from z to ∞). The mean (μ) and standard deviation (σ) are determined (z = (y- μ) / σ) and the energy distribution (E(y)) obtained from the 1-D Gaussian function.

$$\mathrm{E(y)} = \frac{1}{\sigma\,(2\pi)^{2}}e^{(-\frac{z^2}{2})}$$

The resultant distributions for the fundamental and doubled Nd:YAG beams, both focused and unfocused are shown in Figure B2.

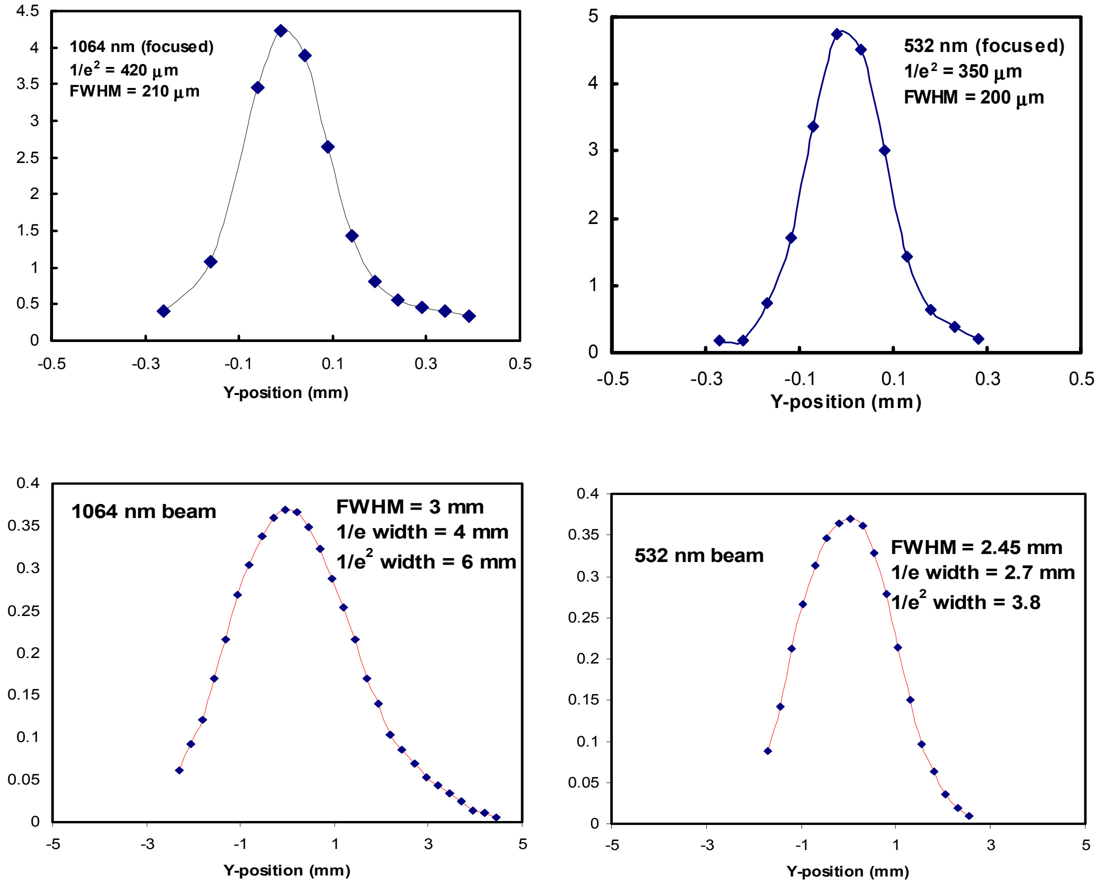

Figure B2. Measured beam profiles for the focused and unfocused 1064 and 532 nm beams.

The temporal distribution of the Nd:YAG pulse is displayed in Figure B3. This signal is generated by scattering a 532 nm pulse off a needle. The elastic scattering intensity is recorded by a fast photodiode (Thorlab DET2-SI) and recorded on an oscilloscope, which shows a pulse length of 8ns FWHM. A temporal profile for the dye laser was obtained in a similar fashion and is also displayed in Figure B3.

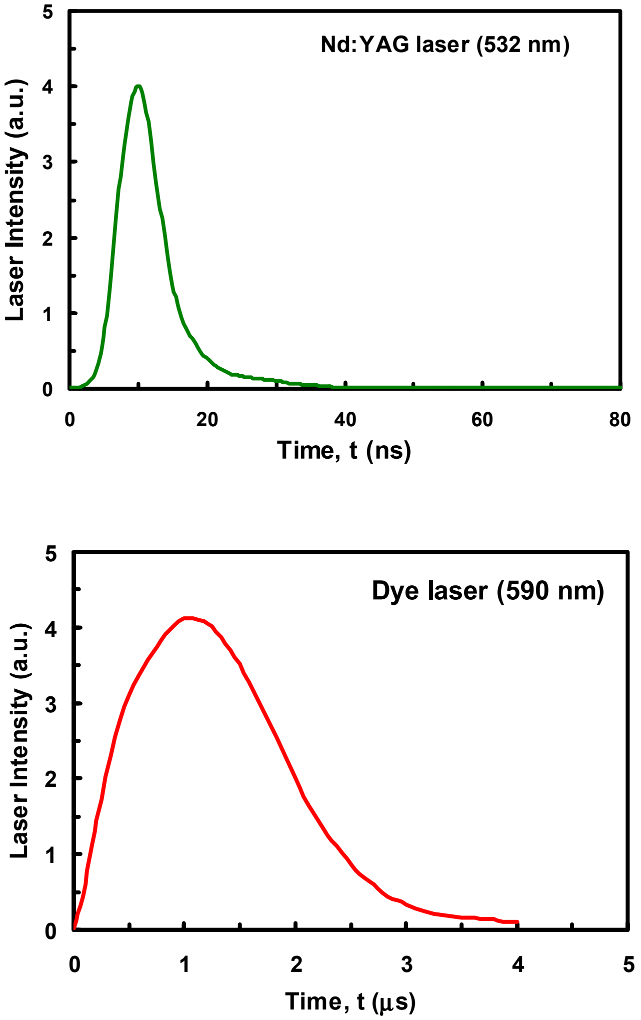

Figure B3. Temporal laser profiles acquired from scattering off a pin for the Nd:YAG laser (532 nm) and the dye laser. FWHM pulse durations are 8 ns and 1.6 μs, respectively.

Appendix C – Optical Filters

A number of optical filters were used in the experiments of this research. Several different spectral filters were employed for spectral selection and the rejection of interferences such as elastic scattering and neutral density (ND) filters were used to limit the light intensity reaching the detector to the detector’s linear (as well as nondestructive) range. The spectral filters included bandpass filters of 10 nm FWHM at 430, 550, and 650 nm, a 3 nm bandpass filter at 460 nm, Schott colored glass filters OG550 (2 mm), OG570 (3 mm), RG630 (3 mm), BG3 (1 mm), and BG18 (1 mm), a high-reflectivity Nd:YAG mirror (532 nm, 45 °), and a holographic notch filter (532 nm, 0°). All of these filters are 2 inch by 2 inch in size, except the mirror and notch filter which are 2 inch rounds and the 458 nm filter which is a 1 inch round.

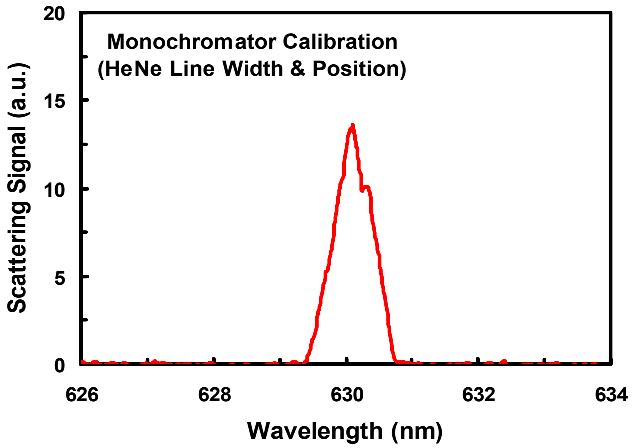

Figure C1. Linewidth and position for HeNe laser light filtered by the monochromator

Determining the spectral dependence of the transmissivity of the various filters required the use of the monochromator for scanning across the wavelength range of interest. The resolution of the monochromator was 0.7 nm FWHM and there is a –2.7 nm error in the monochromator wavelength scale. This shift must be accounted for when reporting spectral information. These monochromator characteristics were determined by measuring a scattering signal from a HeNe (632.8 nm) laser and scanning across the laserline region (see Figure C1).

The bandpass filters were calibrated using a 1000 Watt quartz-tungsten-halogen (QTH) lamp (Oriel 63351) running at 300 watts as a steady, broadband source. The wavelength region of interest was scanned with and without the appropriate filter and the ratio of signals yields the spectral transmissivities. The results are shown in Figure C2.

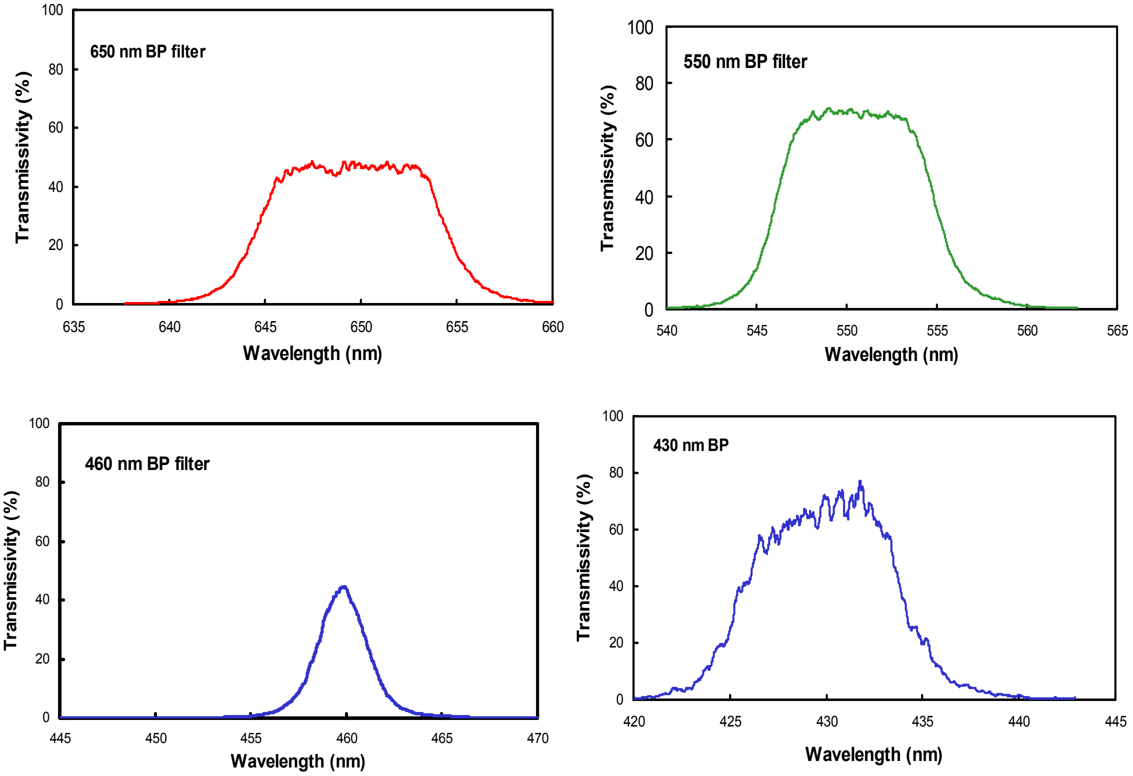

Figure C2. Transmission curves for the four employed bandpass filters. Calibration is performed with the monochromator (0.7 nm resolution) imaging the light from a quartz tungsten halogen lamp.

The OG550, OG570, and RG630 filters are longpass (short wavelength blocking) filters which 'cut on' very sharply, from <0.001% to 91% transmission in about 50 nm. The 50% transmission points are at 550, 570, and 630 nm, respectively. Calibration curves are available in the Schott glass catalog. Calibration with the QTH lamp showed good agreement with the catalog calibrations. The other two filters (BG3 and BG18) have more complicated spectral transmittance shapes. These two were used in combination to provide a 120 nm bandpass centered about 410 nm with a peak transmittance of 53%.

The spectral transmittance of the Nd:YAG mirror and holographic notch filter were acquired in the same fashion as the bandpass filters, except that the QTH lamp was running at 1000 W for the notch filter case. The spectral performance of these filters is shown in Figure C3.

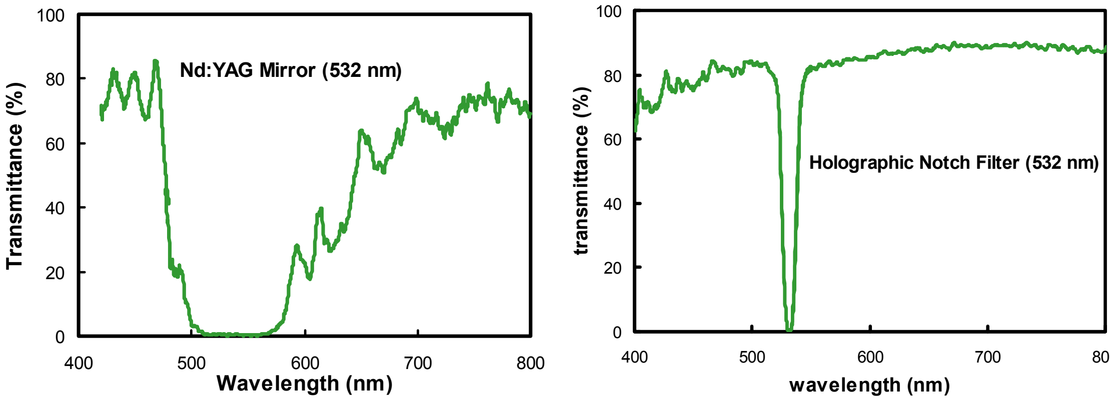

Figure C3. Spectral transmission curves for the 45° YAG mirror (532 nm) and the holographic notch filter. The QTH lamp is again employed with the monochromator for the calibration.

The spectral response of the monochromator and PMT combination was itself also calibrated with the QTH lamp (at 1000 W) by comparing the spectral signal generated across the visible wavelengths with the expected distribution of the lamp irradiance. The lamp itself was not factory-calibrated. Rather, the expected distribution that was assumed was the nominal performance characteristics for the lamp as reported by the manufacturer (see Figure C4). Dividing the detector-generated signal by the lamp profile yields the PMT / monochromator spectral response curve. This data is also shown in Figure C4.

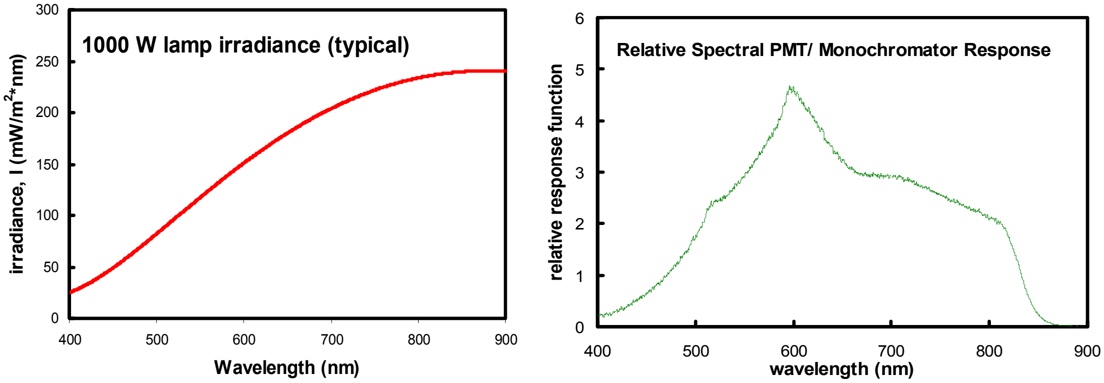

Figure C4. Monochromator/PMT calibration. Left: Manufacturer's catalog report of nominal spectral irradiance of the QTH lamp. Right: Response of the monochromator and PMT combination to the lamp source (i.e., spectral signal/lamp spectral irradiance).

It is important to note also that the monochromator is susceptible to picking up significant 2nd order reflections from the grating (Bausch & Lomb 35-53-06-36, 1200 grooves/mm), e.g., 400 nm light at a setting of 800 nm. This occurred for wavelengths greater than 750 nm. Therefore, a long-pass filter (e.g., OG550) is used when scanning the longer wavelengths.

The ND filters varied in the above experiments had expected values of 0.1, 0.2, 0.3, 0.4, 0.5, 0.6, and 1.0. The good linearity for the lower signals of the detectors above suggests these values are at least fairly accurate relative to one another. Further analysis, using the linear ranges of both detectors, shows the filters are more accurately represented by 0.095, 0.195, 0.28, 0.4, 0.48, 0.6, and 1.0 at red wavelengths and 0.115, 0.21, 0.3, 0.41, 0.49, 0.6, and 1.035 at blue wavelengths. The other ND filters used in this research had the stronger expected values of 2.0, 3.0, and 4.0. The detectors do not have sufficient dynamic range to calibrate these filters absolutely, so these were quantified by comparing to combinations of filters of lower value, but similar total magnitude. Again, the filters were not fully spectrally analyzed, but measurements were made for red (RG630) and blue (BG3 and BG18). This showed a significant dependence of the stronger filters on incident wavelength. In the red, the three strongest filters had measured values of 1.98, 2.82, and 3.95. In the blue, these values were 2.25, 3.05, and 4.25. The weaker filters showed no such spectral dependence.

Appendix D – Quantitative LII Measurement Issues

Many factors can influence the LII signal. If care is not taken, some of these influences may be user-imposed. For example, imperfections in the detection setup can be the root of an unrealistic result. A few instances of just such experimental error were observed on the road to acquiring a meaningful LII signal. Among the more important points detailed below are: (1) that the monochromator is, by itself, not a strong enough filter to sufficiently reject elastic laser scattering, (2) that positions in the signal path inside the 'light-tight' box which houses the detection optics are not good places to put strong filters due to the reflections not being able to escape and thus, interfering with the signal of interest, (3) that the transmissivity of the ND filters employed are sensitive to the incident wavelength (see Appendix C), (4) that the monochromator is subject to 2nd order reflections above 750 nm (see Appendix C), and (5) that signal trapping is significant in the flame, at least 20% and 30% signal blockage occurs for red and blue detection wavelengths, respectively, at the maximum soot location, when observing the side of the flame nearest the laser.

D.1 Laser Scattering Interference

The first experimental LII signals were obtained using the dye laser and the monochromator as the sole spectral filter. Example signals recorded at 700, 500, and 400 nm are plotted in Figure D1 against the height in the flame and matched to concentration data as measured by extinction at 10 mm HAB. Normalization at this height makes the difference in the data sets most obvious. The 400 nm signal is scaling much differently than the signals of the other two detection bands.

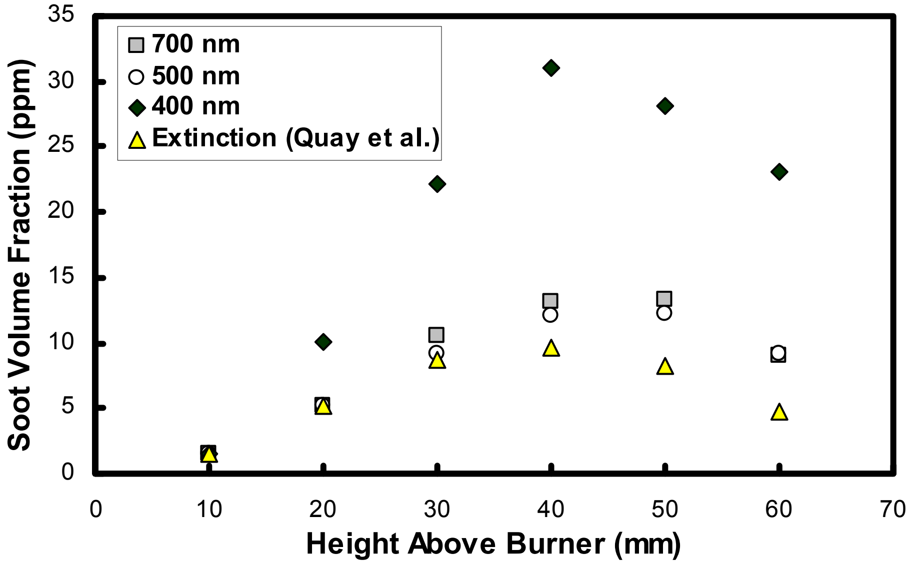

Figure D1. LII signals acquired in the diffusion flame using the dye laser (590 nm, 3.5 J/cm^2). Spectral filtering is achieved with the monochromator only. Detection gate is over the first 2.5 μs of the signal.

The cause becomes apparent after comparing the spectral distribution of the LII signal and that of the laser light elastically scattered from the soot particles. This comparison is shown in Figure D2. Detector gating during the laser pulse (as cannot be avoided when using the long-pulse dye laser) of the LII signal provides both a contribution from soot incandescence and soot-scattered laser light. The elastic scattering contribution (at 590 nm) to the LII signal (at other wavelengths) is isolated by measuring the scattered light (unsaturated) off a reflective surface (in this case, a needle) and scaling this signal down by a factor proportional to the relative scattering intensity of the observed volume of soot to that of the needle, each at the laser wavelength (590 nm). The

LII signal was from a 20 mJ pulse (18 J/cm^2), was recorded at the maximum soot location at 25 mm HAB, and has had the elastic scattering contribution subtracted.

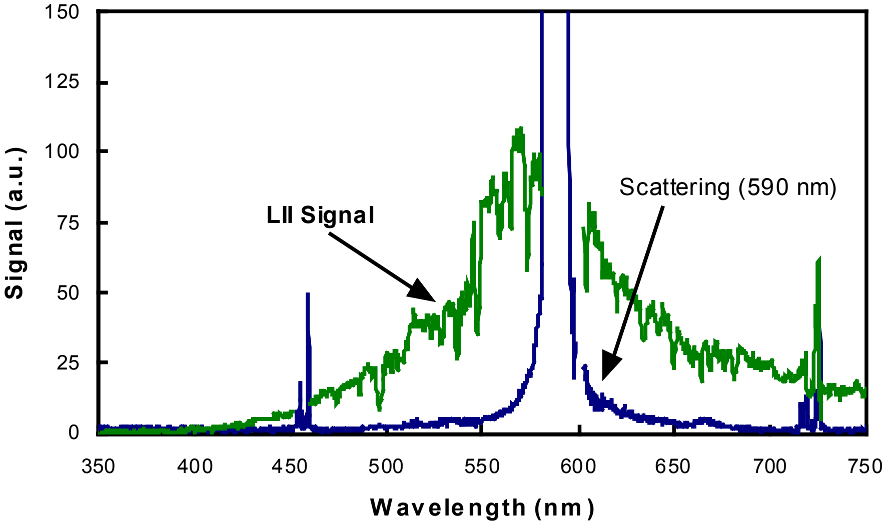

Figure D2. Comparative spectral scan of the dye laser-induced LII emission and the elastic scattering of the laser. LII signal has had the scattering contribution subtracted from it. Spectra are not corrected for the response of the detection system.

Though the laser linewidth is actually less than 5 nm, as is the resolution of the monochromator (0.7nm), the linewidth appears greater because there is a significant amount of diffuse scattering inside the monochromator and two more direct reflections at two monochromator grating positions which correspond to 460 and 725 nm. It is apparent that the monochromator alone does not offer enough rejection of the elastically scattered laser light. For example, at the 400 and 700 nm detection wavelengths, the monochromator's transmission of the 590 nm scattering was determined to be ~10$^{-5.0}$ (relative to its transmission at 590 nm). Though this is a significant intensity reduction, all detection wavelengths have some measurable scattering contribution and the smaller

LII signals at the short wavelengths (e.g., 400 nm) are most susceptible. Further filtering of the scattered light is required. It was also found that the scattering interference was almost negligible low in the flame, but significant higher in the flame. The scattering interference increases downstream because the effective soot scattering diameter grows significantly and the scattering has a strong dependence on size, e.g., d^6.

D.2 Reflections in Detection Setup

The signals recorded in many of these experiments employed ND filters of large magnitudes (> 1). The ND filters of ND value ≥ 1 are reflectively coated on both sides and are strongly reflecting. It was discovered some time after the fact that the detection setup as it was arranged for a long time (see Figure D3) was highly susceptible to interference from reflected light, and more so when combinations of strong filters were used. The spectral filters are also quite strong reflectors and can thus contribute to reflections reaching the detector as well. The magnitude of the interference is also dependent upon the angle at which the filters sit and their proximity to one another. Both the trend in the signal magnitude and S_λ are possibly affected by changing ND filter values as the signal level changes. On realizing this effect of reflection interference, when strong ND filters were required in future measurements, they were applied outside the light-tight box. Filters of lower reflectivity can be employed in the front compartment without interfering with the signal.

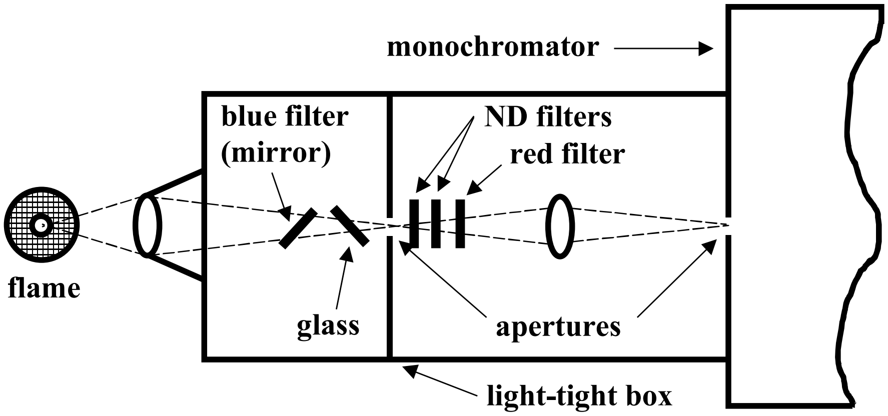

Figure D3. Detection optics arrangement for early Nd:YAG pointwise LII measurements (view from above).

Also, for the majority of the duration of the research, it was assumed that the actual effective value for the ND filters at 430 nm was the same as it was for 650 nm. This is not the case (see Appendix C). The strong ND filters actually reflect better at the shorter wavelengths. not correcting for this leads to an observed increase in the red/blue ratio with increasing signal (increasing ND value).

D.3 Signal Trapping

Signal trapping is known to be problematic for thick regions of dense soot. A set of experiments were devised to test this source of possible LII signal interference. Figure D4 denotes the various locations where signals were observed in these experiments. As with all previous measurements, the position in space imaged by the detector remains fixed, as does the focal point of the laser. The traverse connected to the burner moves the region of interest into the detected volume. Most measurements in this research were made along the line of maximum soot closest to the laser (position 1 in Figure D4). Observing this region ensured minimal attenuation of the laser beam (as compared to position 5 which could possibly see a reduced laser intensity due to the soot between it and the laser) and a more uniform soot density through the laser beam in the direction of the detector’s depth of field than position 3, for example.

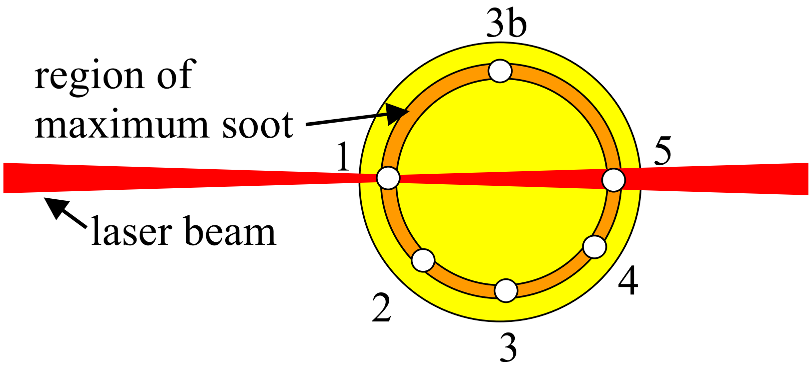

Figure D4. Cross-sectional schematic of the diffusion flame and location of the measurement points for the signal trapping experiments.

First, the attenuating capability of a pathlength through the center of the flame is examined by comparing signals generated at points 3 and 3b. Measurements made at 650 nm and 430 nm and at the heights of 15 and 40 mm HAB are shown in Figure D5 with all four signals from point 3 normalized to 1. This shows the relative trapping effect of a full flame width at the two heights and wavelengths. The signals are generated by a 100 mJ (12 J/cm^2) infrared pulse, are integrated over the first 30 ns of the signal, and are the average of the ten peak signals in a 2000 shot record. Spectral discrimination is achieved with the monochromator only. A noticeable amount of signal trapping does exist. As would be expected, there is more trapping for the higher soot loading at 40 mm HAB than 15 mm HAB and these magnitudes are somewhat stronger for the shorter wavelength light.

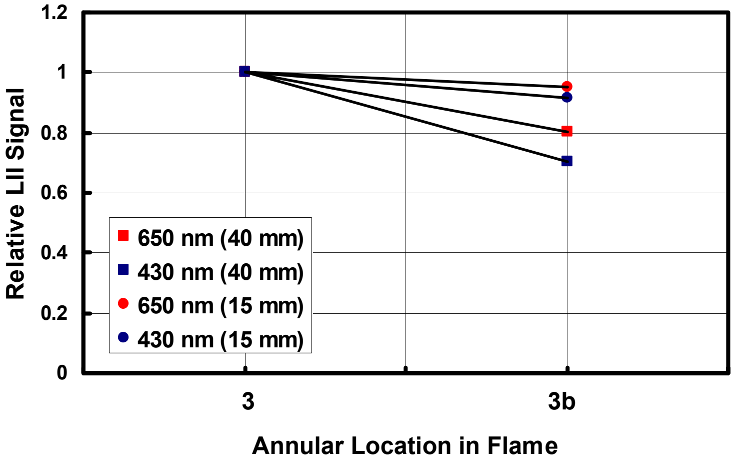

Figure D5. Relative signal trapping through the thickness of the flame. Signals are generated by a 12 J/cm^2 pulse at 1064 nm and are promptly integrated for 30 ns. All four signal pairs are normalized to 1 at position 3, nearest the detector.

The effect this has on the spectral signal ratio, S_λ is shown in Figure D6. Measurements made at two heights at the side of the flame nearest to the detector (position 3, which should have minimal problems with signal trapping) indicate a nearly constant signal ratio, which also implies that the attained temperatures are equal. Due to the variation in signal trapping at different wavelengths and different amounts of interfering soot, the values for S_λ at the back of the flame (imaged through the flame) are larger and increase with increasing amounts of trapping. In fact, the ratio changes by 10 % from 15 to 40 mm HAB. The 20-30 % reduced signals at 40 mm across this 1 cm flame (Figure D5) may discourage attempts to employ LII for concentration measurements in more sizeable sooty flames.

The data of Figure D6 at the position closest to the detector suggest that different-sized primary particles are averaging very similar temperatures, at least for a prompt detection gate. Further measurements were made at various heights up this side of the flame. Results indicate a nominally flat signal ratio (S_λ), though the sensitivity of the detection setup to ND reflections was still undiscovered at this time. Thus, while S_λ is essentially flat with changing particle diameter, the magnitude of the ratio is no indicator of the temperature of the particle.

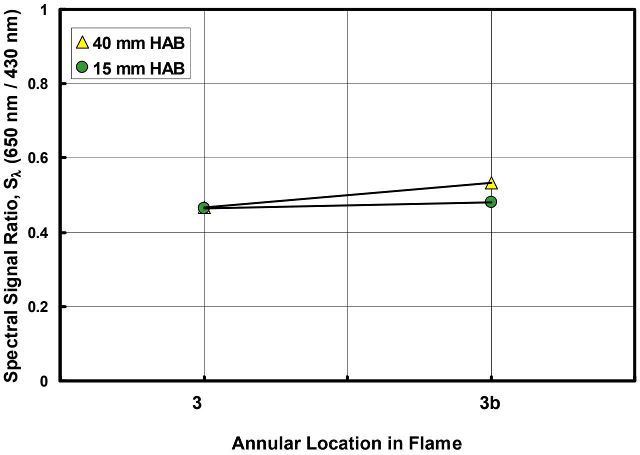

Figure D6. Spectral ratio (S_λ) at the front and back of the flame for two heights above the burner. Signals are detected at 650 and 430 nm. Due to reflection issues, magnitudes do not reflect particle temperature via a blackbody fit.

As S_λ changed by 10% due to signal trapping when comparing signals from the maximum soot region at the back and front of the flame, we may suspect an error of this magnitude to exist on all the signal ratios measured in this investigation. This is essentially true. However, one might think that the amount of trapping at position 1 would lie somewhere between the measures at 3 and 3b. The data presented in Figure D7 show that there is, in fact, more signal trapping for measurements at this location. This is due to the fact that the optical path runs along the zone of maximum soot for a greater distance than at positions 3 or 3b. Figure D7 shows the signal ratio obtained at 6 positions around the flame at 40 mm HAB. Little trapping occurs at 15 mm HAB. It was not possible to measure the amount of trapping at position 1 (40 mm) absolutely as the signal magnitude also changes due to the angle between the thin maximum soot zone and the laser sheet. Position 3 yields an averaged signal *across* this zone, while position 1 yields an averaged signal *along* this zone. Given the known differences in signal and thus S_λ at positions 3 and 3b, a linear calculation indicates that the signal ratio at position 1 would equate to signal reductions of up to 30% in the red and 55% in the blue. The fact that S_λ is larger than that of position 3b indicates that these respective values are at least 20 and 30%.

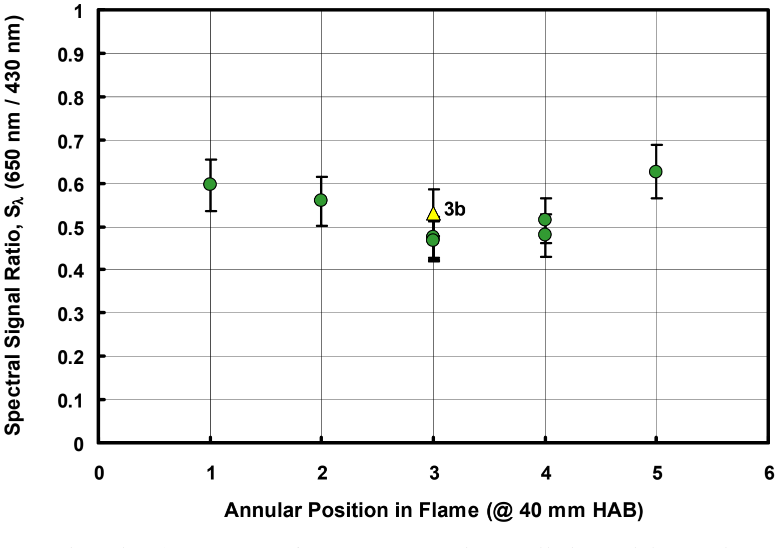

Figure D7. Spectral ratio ($S_{\lambda,}$650nm/430 nm) at the radial position of maximum soot at 40 mm HAB. Signals are measured at 5 locations along the side of the flame nearest the detector and also at the middle position on the opposite side.

Shaddix and Smyth[63] also noted this effect, though they indicated only 25% trapping at 40 mm in this same flame for blue detection. They obtained their signal trapping information by imaging a one-dimensional LII signal line generated by the intersection of a spherically focused beam and the flame, as the laser is scanned across the flame normal to the detector line of sight. Deduction of the true signals is possible for an axisymmetric geometry such as this by performing a tomographic inversion of the data with a technique such as the 3-point Abel technique.[63]

Another point should be noted in regard to the signal trapping experiments. Though the reflection problem with the detection setup was also present in these experiments, the results from those experiments are mostly unaffected. At a fixed height, the employed filters did not vary, though the observed radial location in the flame changes. A certain percent reflection interference, say R%, yields a reflection coefficient of 1.R. The absolute values of signals and signal ratios at a given height will not be correct, but the relative differences at the various radial positions will be (e.g. signal$_1$*(1.R) / signal$_3$*(1.R) = signal$_1$/signal$_3$). The measured relative change in signal and signal ratio will also not necessarily have been correct from 15 mm to 40 mm HAB. Correction for the trapping of the signals should yield dependencies on soot concentration for both channels which scale greater than the extinction data, with the blue channel perhaps responding even more strongly than the red. This is what we would have expected the effect of a changing primary particle diameter to be.

Appendix E – 1-D Gaussian LII Signal Calculation

```
%
% Subprogram 1D Gaussian Spatial Signal Calculation
%
% (see Advanced Engineering Math (Kreyszig), Sect 23.7)
%
% ENTER VARIABLES:

global power_total ext;

% Emitting soot volume parameters
height=2e-3; % (m)
width=4e-4; % (m)
area=height*width; % (m^2)
sootfraction=1e-6;
fwhm_detector=10e-9; % (m)

% -----------------------------------------------------
% Example Case:
% focused 10 mJ (532 nm)(in flame)

t_flame=1700; %[K]
single_soot_rad=[5e-9 10e-9 15e-9 20e-9 30e-9 50e-9 100e-9];
power_total=0.625e6; %[W] (10 mJ beam ~50% in aperture (8ns))
focus_width=210e-6; %[m]
focus_area=focus_width*height; %[m^2] (2mm (aperture) x 210 micron
...(fwhm))
power_dens_avg=power_total/focus_area; %[W/m^2]

a_focus=focus_area;
% -------------------------------------------------------
% Energy distribution

sigma=focus_width./(2.*sqrt(2.*log(2)));
x_step=focus_width./10;
x_pos_val=[0:x_step:focus_width.*1.5];
phi_function=normal(x_pos_val,0,focus_width,1);
power_dens=power_total*(1/height)*(1/(sigma*sqrt(2.*pi)))*phi_function;
check=2*height*trapz(x_pos_val,power_dens);
size_x_array=length(x_pos_val);

for i=1:1:size_x_array
      ext=i;
      power_density=power_dens(i);
      liivsflu;   % single-particle T, d history and LII signal
...calculation
```

```
end

sizesootarray=length(single_soot_rad);
time_end=1000.e-9;
t_sol=[0:0.2e-10:15.8e-9 16e-9:5e-10:19.5e-9 20.e-9:2.e-9:48e-9 50e-
...9:10e-9:time_end];
sizet=length(t_sol);

% ----------------------------------------------------
% Particle temperature and size


for j=1:1:sizesootarray
for k=1:1:sizet
gausst(k,j)=0;
gaussr(k,j)=0;
end
end

for j=1:1:sizesootarray
for i=1:1:size_x_array
ext=i;
power_density=power_dens(i);
savename1=['t' int2str(power_total*1e-4) int2str(ext)];
eval(['load ' savename1]);
for k=1:1:sizet
gausst(k,j)=gausst(k,j)+soltemp(k,j)./size_x_array;
gaussr(k,j)=gaussr(k,j)+solrad(k,j)./size_x_array;

end
end
end


%-------------------------------------
% Red signal (instantaneous and 50ns integration)

ldet=650e-9;

for j=1:1:sizesootarray
sumsigred(j)=0;
for k=1:1:sizet
gausigr(k,j)=0;
end
end

for j=1:1:sizesootarray
for i=1:1:size_x_array
ext=i;
power_density=power_dens(i);
```

```
savename2=[int2str(ldet.*1e8) int2str(power_total*1e-4) int2str(ext)];
eval(['load ' savename2]);
sigred(i,j)=trapz(t_sol(1:815),solsig(1:815,j));
sumsigred(j)=sumsigred(j)+sigred(i,j)/size_x_array;
for k=1:1:sizet
gausigr(k,j)=gausigr(k,j)+solsig(k,j)./size_x_array;
end
end
cred(j)=sumsigred(j)./(single_soot_rad(j)^3);
end



% ---------------------------------------------------------
% Blue signal (instantaneous and 50ns integration)

ldet=400e-9;

for j=1:1:sizesootarray
sumsigblue(j)=0;
for k=1:1:sizet
gausigb(k,j)=0;
end
end

for j=1:1:sizesootarray
for i=1:1:size_x_array
ext=i;
power_density=power_dens(i);
savename2=[int2str(ldet.*1e8) int2str(power_total*1e-4) int2str(ext)];
eval(['load ' savename2]);
sigblue(i,j)=trapz(t_sol(1:815),solsig(1:815,j));
sumsigblue(j)=sumsigblue(j)+sigblue(i,j)/size_x_array;
for k=1:1:sizet
gausigb(k,j)=gausigb(k,j)+solsig(k,j)./size_x_array;
end
end
cblue(j)=sumsigblue(j)./(single_soot_rad(j)^3);
end


% ----------------------------------------------------------

savename3=['x' int2str(t_flame./100) int2str(power_total*1e-4)];
eval(['save ' savename3 '.dat single_soot_rad power_total
...power_dens_avg power_dens sumsigred cred sumsigblue cblue -double -
...ascii -tabs']);

savename4=['y' int2str(t_flame./100) int2str(power_total*1e-4)];
```

```
eval(['save ' savename4 '.dat single_soot_rad power_total
...power_dens_avg power_dens gausst gaussr gausigr gausigb -double -
...ascii -tabs']);
```

REFERENCES

1. McCoy, B. J., and Cha, C. Y., "Transport Phenomena in the Rarefied Gas Transition Regime," *Chemical Engineering Science*, Vol. 29, 1983, p.381-388.

2. Vincenti, W. G. and Kruger, Jr., C. H., Introduction to Physical Gas Dynamics, Krieger Publishing, Malabar, FL, 1965, p. 1-26, 77-85, 524.

3. Leider, H. R., Krikorian, O. H., and Young, D.A., "Thermodynamic Properties of Carbon up to the Critical Point," *Carbon*, Vol. 11, 1973, p.555-563.

4. White, F. A., Viscous Fluid Flow, McGraw-Hill, New York, 1991, p. 28-32.

5. Klingenberg, H., Automobile Exhaust Emission Testing, Springer-Verlag, Berlin, 1996.

6. Rickeard, D., Bateman, J., Kwon, Y., McAughey, J., and Dickens, C., "Exhaust Particulate Size Distribution: Vehicle and Fuel Influences in Light Duty Vehicles," SAE Special Publications, Diesel Engine Combustion and Emission Control, Vol. 1206, October 1996, p. 97-111.

7. Miguel, A., Kirschstetter, T., and Harley, R., "On-Road Emissions of Particulate Polycyclic Aromatic Hydrocarbons and Black Carbon from Gasoline and Diesel Vehicles," *Environmental Science and Technology*, Vol. 32, No. 4, 1998, p. 450-455.

8. Kleeman, M. and Cass, G., "Source Contributions to the Size and Composition Distribution of Urban Particulate Air Pollution," *Atmospheric Environment*, Vol. 32, No. 16, 1998, p. 2803-2816.

9. Morawska, L., Thomas, S., Bofinger, N., Wainwright, D., and Neale, D., "Comprehensive Characterization of Aerosols in a Subtropical Urban Atmosphere: Particle Size Distribution and Correlation with Gaseous Pollutants," *Atmospheric Environment*, Vol. 32, No. 14/15, 1998, p. 2467-2478.

10. Kasparian, J., Frejafon, E., Rambaldi, P., Yu, J., Vezin, B., Wolf, J. P., Ritter, P., and Viscardi, P., " Characterization of Urban Aerosols Using SEM Microscopy, X-Ray Analysis, and LIDAR Measurements," *Atmospheric Environment*, Vol. 32, No. 17, 1998, p. 2957-2967.

11. Dickerson, R. R., Kondragunta, S., Stenchikov, G. L., Civerolo, K. L., Doddridge, B. G., and Holben, B. N., "The Impact of Aerosols on Solar UV Radiation and Photochemical Smog," World Wide Web article, http://metosrv2.umd.edu/~russ/aerosol.d/aerosol.html, 1997.

12. Puri, I. K., Environmental Implications of Combustion Processes," CRC Press, Boca Raton, FL, 1993, p. 71-95.

13. Wilson, R., and Spengler, J. D., Particles in Our Air: Concentrations and Health Effects, Harvard University Press, 1996.

14. Barnum, A., "Microscopic Soot Shortens Many Lives," *San Francisco Chronicle* (web available: http://www.electrocorp.nu/partharm.html), May 9, 1996.

15. International Technology Roadmap for Semiconductors, SEMATECH (web available: http://notes.sematech.org/ntrs/PublNTRS.nsf), Austin, TX, 1997.

16. Greaves, K., "Practical On-Line Solution to Control Ash Deposition and Improve Boiler Efficiency," Proceedings of the Engineering Foundation Conference on Coal-Blending and Switching of Low-Sulfur Western Coals, ASME, New York, 1994, p. 243-256.

17. Brouwer, J., Ault, B. A., Bobrow, J. E., and Samuelsen, G. S., "Active Control Application to a Model Gas Turbine Combustor," ASME Conference Paper 90-GT-326, Gas Turbine and Aeroengine Congress and Exposition, Brussels, Belgium, 1990.

18. Burtscher, H., Schmidt-Ott, A., and Siegmann, H. C., "Monitoring Particulate Emissions from Combustions by Photoemissions", *Aerosol Sci. and Tech.*, Vol. 8, 1988, p. 125-132.

19. Cadle, R. D., The Mesurement of Airborne Particles, Wiley and Sons, New York, 1975.

20. Harrison, R. M., Shi, J. P., and Jones, M. R., "Continuous Measurements of Aerosol Physical Properties in the Urban Atmosphere," *Atmospheric Environment*, Vol. 33, No. 7, March, 1999, p. 1037-1047.

21. Cofer, W. R., Anderson, B. E., Winstead, E. L., and Bagwell, D. R., "Calibration and Demonstration of a Condensation Nuclei Counting System for Airborne Measurements of Aircraft Exhausted Particles," *Atmospheric Environment*, Vol. 32, No. 2, January, 1998, p. 169-177.

22. Abdul-Khalek, I. S., Kittelson, D. B., Graskow, B. R., Wei, Q., and Brear, F., "Diesel Exhaust Particle Size: Measurement Issues and Trends," *SAE Special Publications*

(In-Cylinder Diesel Particulate and NO_x Control), Vol. 1326, February, 1998, p. 133-145.

23. Graskow, B. R., Kittelson, D. B., Abdul-Khalek, I. S., Ahmadi, M. R., and Morris, J. E., "Characterization of Exhaust Particulate Emissions from a Spark Ignition Engine," *SAE Special Publications (In-Cylinder Diesel Particulate and NO_x Control)*, Vol. 1326, February, 1998, p. 155-165

24. Chen, D. R., Pui, D. Y. H., Hummes, D., Fissan, H., Quant, F. R., and Sem, G. J., "Design and Evaluation of a Nanometer Aerosol Differential Mobility Analyzer (Nano-DMA)," *Journal of Aerosol Science*, Vol. 29, No. 5-6, June-July, 1998, p. 497-509.

25. Ahlvik, P., Ntziachristos, L., Keskinen, J., and Virtanen, A., "Real Time Measurements of Diesel Particle Size Distribution with an Electrical Low Pressure Impactor," *SAE Special Publications (General Emissions)*, Vol. 1335, February, 1998, p. 215-234

26. Chippett, S., and Gray, A., "The Size and Optical Properties of Soot Particles," *Combustion and Flame*, Vol. 31, 1978, p. 149-159.

27. Lahaye, J., and Prado, G., "Morphology and Internal Structure of Soot and Carbon Blacks," in Particulate Carbon, ed. Siegla, D. and Smith, G., Plenum Press, New York, 1981, p. 33-55.

28. Rivin, D. and Medalia, A. I., "A Comparative Study of Soot and Carbon Black," in Soot in Combustion Systems and its Toxic Properties, ed. Lahaye, J. and Prado, G., Plenum Press, New York, 1983, p.25-40.

29. Dobbins, R. A., Fletcher, R. A., and Lu, W., "Laser Microprobe Analysis of Soot Precursor Particles and Carbonaceous Soot", *Combustion and Flame*, Vol. 100, 1995, p. 301-309.

30. Vander Wal, R. L., Choi, M. Y., and Lee, K.-O., "The Effects of Rapid Heating of Soot: Implications When Using Laser-Induced Incandescence for Soot Diagnostics," AIAA Conference Paper 96-0538, 34th AIAA Aerospace Science Meeting and Exhibit, Reno, NV, 1996.

31. Vander Wal, R. L., "Soot Precursor Material: Visualization via Simultaneous LIF-LII and Characterization via TEM," *26th Symposium (International) on Combustion*, The Combusiton Institute, 1996, p. 2269-2275.

32. Vander Wal, R. L., Jensen, K. A., and Choi, M. Y., "Simultaneous Laser-Induced Emission of Soot and Polycyclic Aromatic Hydrocarbons Within a Gas-Jet Diffusion Flame," *Combustion and Flame*, Vol. 109, 1997, p. 399-414.

33. Köylü, Ü. Ö., McEnally, C. S., Rosner, D.E., and Pfefferle, L. D., "Simultaneous Measurements of Soot Volume Fraction and Particle Size / Microstructure in Flames Using a Thermophoretic Sampling Technique," *Combustion and Flame*, Vol. 110, 1997, p. 494-507.

34. Zhang, J., and Megaridis, C. M., "Soot Microstructure in Steady and Flickering Laminar Methane/Air Diffusion Flames." *Combustion and Flame*, Vol. 112, 1998, p. 473-484.

35. Vander Wal, R. L., Ticich, T. M., and Stephens, A. B., "Optical and Microscopy Investigations of Soot Structure Alterations by Laser-Induced Incandescence," *Applied Physics B,* Vol. 67, No. 1, 1998, p. 115-123.

36. Vander Wal, R. L., "Soot Precursor Carbonization: Visualization Using LIF and LII and Comparison Using Bright and Dark Field TEM," *Combustion and Flame*, Vol. 112, 1998, p. 607-616.

37. Vander Wal, R. L. and Jensen, K. A., "Laser-Induced Incandescence: Excitation Intensity," *Applied Optics*, Vol. 37, No. 9, March, 1998, p. 1607-1616.

38. Vander Wal, R. L., Ticich, T. M., and Stephens, A. B., "Can Soot Primary Particle Size be Determined Using Laser-Induced Incandescence?," *Combustion and Flame*, Vol. 116, 1999, p. 291-296.

39. Megaridis, C. M. and Dobbins, R. A., "Comparison of Soot Growth and Oxidation in Smoking and Non-Smoking Ethylene Diffusion Flames," *Combustion Science and Technology*, Vol. 66, 1989, p. 1-16.

40. Köylü, Ü. Ö. and Faeth, G. M., "Structure of Overfire Soot in Buoyant Turbulent Diffusion Flames at Long Residence Times," *Combustion and Flame*, Vol. 89, 1992, p. 140-156.

41. Sunderland, P. B. and Faeth, G. M., "Soot Formation in Hydrocarbon / Air Laminar Jet Diffusion Flames," *Combustion and Flame*, 1996, p. 132-146.

42. Binder, E., and Wurster, R., "Detection of Microparticles by Laser-Induced Vaporization and Ionization," *Journal of Aerosol Science*, Vol. 27, Suppl. 1, 1996, p. s291-s292.

43. Kawai, T., Iuchi, Y., Nakamura, S., and Ishida, K., "Real Time Analysis of Particulate Matter by Flame Ionization Detection," *SAE Special Publications (General Emissions)*, Vol. 1335, February, 1998, p. 73-79.

44. Smyth, K. C., Miller, J. H., Dorfman, R. C., Mallard, W. G., and Santoro, R. J., "Soot Inception in a Methane/Air Diffusion Flame as Characterized by Detailed Species Profiles," *Combusiton and Flame*, Vol. 62, 1985, p. 157-181.

45. Prado, G., Jagoda, J., Neoh, K., and Lahaye, J., "A Study of Soot Formation in Premixed Propane/Oxygen Flames by In-Situ Optical Techniques and Sampling Probes," *18th Symposium (International) on Combustion,* The Combustion Institute, 1981, p. 1127-1135.

46. Bockhorn, H., Fetting, F., Meyer, U., Reck, R., and Wannemacher, G., "Measurement of the Soot Concentration and Soot Particle Sizes in Propane Oxygen Flames," *18th Symposium (International) on Combustion,* The Combustion Institute, 1981, p. 1137-1147.

47. Dasch, C., "Continuous-Wave Probe Laser Investigation of Laser Vaporization of Small Soot Particles in a Flame," *Applied Optics*, Vol. 23, No. 13, July, 1984, p. 2209-2215.

48. Flower, W. L., "Optical Measurements of Soot Formation in Premixed Flames," *Combustion Science and Technology*, Vol. 33, 1983, p. 17-33.

49. Santoro, R.J., Semerjian, H. G., and Dobbins, R. A., "Soot Particle Measurements in Diffusion Flames," *Combustion and Flame*, Vol. 51, 1983, p. 203-218.

50. Kadota, T., and Hiroyasu, H., "Soot Concentration Measurement in a Fuel Droplet Flame via Laser Light Scattering," *Combustion and Flame*, Vol. 55, 1984, p. 195-201.

51. Santoro, R. J., Yeh, T. T., Horvath, J. J., and Semerjian, H. G., "The Transport and Growth of Soot Particles in Laminar Diffusion Flames," *Combustion Science and Technology*, Vol. 53, 1987, p. 89-115.

52. Dobbins, R. A., Santoro, R. J., and Semerjian, H. G., "Analysis of Light Scattering from Soot Using Optical Cross Sections for Aggregates," *23rd Symposium (International) on Combustion,* The Combustion Institute, 1990, p. 1525-1532.

53. Klingen, H. J. and Roth, P., "Time-Resolved and Time-Averaged Diesel Particle Measurement at the Exhaust Valve and in the Exhaust Pipe," *Journal of Aerosol Science*, Vol. 21, Suppl. 1, 1990, p. s745-s750.

54. Sorensen, C. M., Cai, J., and Lu, N., "Light-Scattering Measurements of Monomer Size, Monomers per Aggregate, and Fractal Dimension for Soot Aggregates in Flames," *Applied Optics,* Vol. 31, No. 30, October, 1992, p. 6547-6557.

55. Puri, R., Richardson, T. F., Santoro, R. J., and Dobbins, R. A., "Aerosol Dynamic Processes of Soot Aggregates in a Laminar Ethene Diffusion Flame," *Combustion and Flame*, Vol. 92, 1993, p. 320-333.

56. Bockhorn, H. (Ed.), Soot Formation in Combustion (Mechanisms and Models), Springer Series in Chemical Physics 59, Springer-Verlag, New York, 1994.

57. Megaridis, C. M., Griffin, D. W., and Konsur, B., "Soot-field Structure in Laminar Soot-Emitting Microgravity Nonpremixed Flames," *26th Symposium (International) on Combustion,* The Combustion Institute, 1996, p. 1291-1299.

58. Guoguang, C., Prochnau, T. J., and Hofeldt, D. L., "Feasibility of Remote Sensing of Particulate Emissions from Heavy-Duty Vehicles," in Engine Emissions and Emissions Measurement (SP-1161), SAE, Warrendale, PA, 1996.

59. Köylü, Ü. Ö., "Quantitative Analysis of In-Situ Optical Diagnostics for Inferring Particle/Aggregate Parameters in Flames: Implications for Soot Surface Growth and Total Emissivity," *Combustion and Flame*, Vol. 109, 1997, p. 488-500.

60. Bengtsson, P.-E., Aldén, M., "Application of a Pulsed Laser for Soot Measurements in Premixed Flames," *Applied Physics B*, Vol. 48, 1989, 155-164.

61. Dasch, C. J. and Heffelfinger, D. M., "Planar Imaging of Soot Formation in Turbulent Ethylene Diffusion Flames: Fluctuations and Integral Scales," *Combustion and Flame*, Vol. 85, 1991, p. 389-402.

62. Greenberg, P. S. and Ku, J. C., "Soot Volume Fraction Imaging," *Applied Optics*, Vol. 36, No. 22, August, 1997, p. 5514-5522.

63. Shaddix, C., and Smyth, K., "Laser-Induced Incandescence Measurements of Soot Production in Steady and Flickering Methane, Propane, and Ethylene Diffusion Flames," *Combustion and Flame,* Vol. 107, 1996, p. 418-452.

64. Vander Wal, R. L., Zhou, Z., and Choi, M. Y., "Laser-Induced Incandescence Calibration via Gravimetric Sampling," *Combustion and Flame,* Vol. 105, 1996, p. 462-470.

65. Choi, M. Y. and Jensen, K. A., "Calibration and Correction of Laser-Induced Incandescence for Soot Volume Fraction Measurements," *Combustion and Flame,* Vol. 112, 1998, p. 485-491.

66. Brookes, S. J. and Moss, J. B., "Measurements of Soot Production and Thermal Radiation from Confined Turbulent Jet Diffusion Flames of Methane," *Combustion and Flame,* Vol. 116, 1999, p. 49-61.

67. Weeks, R. W., and Duley, W. W., “Aerosol-Particle Sizes From Light Emission During Excitation by TEA CO_2 Laser Pulses,” *Journal of Applied Physics,* Vol. 45, 1974, p. 4661-4662.

68. Eckbreth, A. C., “Effects of Laser-Modulated Particle Incandescence on Raman Scattering Diagnostics,” *Journal of Applied Physics,* Vol. 48, 1977, p. 4473-4479.

69. Melton, L. A., “Soot Diagnostics Based on Laser Heating,” *Applied Optics,* Vol. 23, 1984, p. 2201-2208.

70. Greenhalgh, D. A., “RECLAS: Resonant-Enhanced CARS from C_2 Produced by Laser Ablation of Soot Particles,” *Applied Optics*, Vol. 22, No. 8, 1983, p. 1128-1130.

71. Zur Loye, A. O., Siebers, D. L., and Dec, J. E., “2-D Soot Imaging in a Direct Injection Diesel Engine Using Laser-Induced Incandescence,” COMMODIA 90, Proceedings of the International Symposium on Diagnostics and Modeling of Combustion in Internal Combustion Engines, Kyoto, Japan, September 3-5, 1990, p. 523-528.

72. Dec, J. E., zur Loye, A. O., and Siebers, D. L., “Soot Distribution in a D.I. Diesel Engine Using 2-D Laser-Induced Incandescence,” SAE Transactions, Vol. 100, Sect. 3, paper 910224, 1991, p. 277-288.

73. Pinson, J. A., Mitchell, D. L., Santoro, R. J., Litzinger, T. A., “Quantitative, Planar Soot Measurements in a D.I. Diesel Engine Using Laser-Induced Incandescence and Light Scattering,” SAE Paper 932650, 1993.

74. Hofeldt, D. L., “Real-Time Soot Concentration Measurement Technique for Engine Exhaust Streams” SAE Paper 930079, 1993.

75. Cignoli, F., Benecchi, S., and Zizak, G., “Time-Delayed Detection of Laser-Induced Incandescence for the Two-Dimensional Visualization of Soot in Flames,” *Applied Optics*, Vol. 33, No. 24, 1994, p. 5778-5782.

76. Bengtsson, P.-E. and Alden, M., “Optical Investigation of Laser-Produced C_2 from Laser-Vaporized Soot,” *Combustion and Flame,* Vol. 80, 1990, p. 322-328.

77. D’Alessio, A., Gambi, G., Minutolo, P., Russo, S., and D’Anna, A., “Optical Characterization of Rich Premixed CH_4/O_2 Flames Across the Soot Formation Threshold,” *25th Symposium (International) on Combustion,* The Combustion Institute, 1994, p. 645-651.

78. Bengtsson, P.-E. and Alden, M., “Soot Visualization Strategies Using Laser Techniques,” *Applied Physics B,* Vol. 60, 1995, p. 51-59.

79. Quay, B., Lee, T. W., Ni, T., and Santoro, R. J., “Spatially Resolved Measurements of Soot Volume Fraction Using Laser-Induced Incandescence,” *Combust. and Flame,* Vol. 97, 1994, p. 384-392.

80. Ni, T., Pinson, J. A., Gupta, S., and Santoro, R. J., “Two-Dimensional Imaging of Soot Volume Fraction by the Use of Laser-Induced Incandescence,” *Applied Optics*, Vol. 34, No. 30, October, 1995, p. 7083-7091.

81. Vander Wal, R. L., “Laser-Induced Incandescence: Detection Issues,” *Applied Optics*, Vol. 35, No. 33, 1996, p.6548-6559.

82. Vander Wal, R. L. and Weiland, K. J., “Laser-Induced Incandescence: Development and Characterization Towards a Measurement of Soot Volume Fraction,” *Applied Physics B,* Vol. 59, 1994, p. 445-452.

83. Vander Wal, R. L. and Dietrich, D. L., “Laser-Induced Incandescence Applied to Droplet Combustion,” *Applied Optics*, Vol. 34, No. 6, 1995, p. 1103-1107.

84. Choi, M. Y., Mulholland, G. W., Hamins, A., Kashiwagi, T., “Comparisons of the Soot Volume Fraction Using Gravimetric and Light Extinction Techniques,” *Combust. and Flame,* Vol. 102, No 1, 1995, p. 161-169.

85. Will, S., Schraml, S., and Leipertz, A., “Two-dimensional Soot Particle Sizing by Time-resolved Laser-induced Incandescence,” *Optics Letters*, Vol. 20, No. 22, 1995, p. 2342-2344.

86. Mewes, B., and Seitzman, J. M., “Soot Volume Fraction and Particle Size Measurements with Laser-Induced Incandescence,” *Applied Optics,* Vol. 36, No. 3, 1997, p. 709-717.

87. Will, S., Schraml. S., and Leipertz, A., “Comprehensive Two-Dimensional Soot Diagnostics Based on Laser-Induced Incandescence (LII).” *26th Symposium (International) on Combustion,* The Combustion Institute, 1996, p. 2277-2284.

88. Case, M. and Hofeldt, D. L., “Soot Mass Concentration Measurements in Diesel Engine Exhaust Using Laser-Induced Incandescence,” *Aerosol Science and Technology*, Vol. 25, 1996, p. 46-60.

89. Snelling, D. R., Smallwood, G. J., Campbell, I. G., Medlock, J. E., Gülder, Ö. L., “Development and Application of Laser-Induced Inceandescence (LII) as a Diagnostic for Soot Particulate Measurements,” *AGARD 90th Symposium of the Propulsion and Energetics Panel on Advanced Non-Intrusive Instrumentation for Propulsion Engines.*, Brussels, Belgium, Oct. 1997.

90. Appel, J., Jungfleisch, B., Marquardt, M., Suntz, R., and Bockhorn, H., "Assessment of Soot Volume Fractions from Laser-Induced Incandescence by Comparison with Extinction Measurements in Laminar, Premixed, Flat Flames," *26th Symposium (International) on Combustion.*, The Combustion Institute, Pittsburgh, 1996, p. 2387-2395.

91. Will, S., Schraml. S., Bader, K., and Leipertz, A., "Performance Characteristics of Soot Primary Particle Size Measurements by Time-Resolved Laser-Induced Incandescence," *Applied Optics,* Vol. 37, No. 24, 1997, p. 5647-5658.

92. McManus, K. R., Frank, J. H., Allen, M. G., and Rawlins, W. T., "Characterization of Laser-Heated Soot Particles Using Optical Pyrometry," conference paper #98-0159, AIAA, 36th Aerospace Sciences Meeting and Exhibit, January 12-15, 1998, Reno, NV.

93. Wainner, R. T., Seitzman, J. M., and Martin, S. R., "Soot Measurements in a Simulated Engine Exhaust Using Laser-Induced Incandescence," *AIAA Journal*, Vol. 37, No. 36, June, 1999, p. 738-743.

94. Wainner, R. T. and Seitzman, J. M., "Soot Diagnostics Using Laser-Induced Incandescence in Flames and Exhaust Flows," conference paper #99-0640, AIAA, 37th Aerospace Sciences Meeting and Exhibit, January 11-14, 1999, Reno, NV.

95. Van de Hulst, H. C., Light Scattering by Small Particles, Dover Publications, New York, 1981, p. 172-199, 267-296.

96. Dalzell, W. H., and Sarofim, A. F., "Optical Constants of Soot and Their Application to Heat Flux Calculations," *Transactions of the ASME (Journal of Heat Transfer)*, February, 1969, p. 100-104.

97. Habib, Z. G., and Vervisch, P., "On the Refractive Index of Soot at Flame Temperature," *Combustion Science and Technology*, Vol. 59, 1988, p. 261-274.

98. D'alessio, A., Minutolo, P., Gambi, G., and D'Anna, A., "Optical Characterization of Soot," *Ber. Bunsenges. Phys. Chem.*, Vol. 97, No. 12, 1993, p. 1574-1582.

99. Vaglieco, B. M., Beretta, F., and D'Alessio, A., "In Situ Evaluation of the Soot Refractive Index in the UV-Visible from the Measurement of the Scattering and Extinction Coefficients in Rich Flames," *Combustion and Flame*, Vol. 79, 1990, p. 259-271.

100. Chang, H., and Charlampopoulos, T. T., "Determination of the Wavelength Dependence of Refractive Indices fo Flame Soot," *Proceedings of the Royal Society of London A*, Vol. 430, 1990, p. 577-591.

101. Lee, S. C. and Tien, C. L., “Optical Constants of Soot in Hydrocarbon Flames,” *18th Symposium (International) on Combustion*, The Combustion Institute, Pittsburgh, 1981, p. 1159-1166.

102. Smyth, K. and Shaddix, C., “The Elusive History of $m = 1.57 - 0.56i$ for the Refractive Index of Soot,” *Combustion and Flame*, Vol. 107, 1996, p. 314-320.

103. Siegel, R. and Howell, J. R., Thermal Radiation Heat Transfer, Hemisphere Publishing Corp., Washington, D.C., 1992, p.1-86.

104. Tait, N. P., and Greenhalgh, D. A., “PLIF Imaging of Fuel Fraction in Practical Devices and LII Imaging of Soot,” *Ber. Bunsenges. Phys. Chem.*, Vol. 97, No. 12, 1993, p. 1619-1625.

105. Brockhinke, A., Hartlieb, A. T., Kohse-Höinghaus, and Crosley, D. R., “Tunable KrF Laser-Induced Fluorescence of C_2 in a Sooting Flame,” *Applied Physics B*, Vol. 67, 1998, p. 659-665.

106. Rohlfing, E. A., “Optical Emission Studies of Atomic, Molecular, and Particulate Carbon Produced from a Laser Vaporization Cluster Source,” *Journal of Chemical Physics*, Vol. 89, No. 10, November, 1988, p. 6103-6112.

107. Mewes, B. “Modeling of Laser-Induced Incandescence,” final report for Aerospace Engineering Masters Degree Special Problem (course #8500), Georgia Institute of Technology, Summer 1995.

108. Bohren, C. F. and Huffman, D. R., Absorption and Scattering of Light by Small Particles, Wiley and Sons, New York, 1983.

109. Condon, E. U. and Odishaw, H., Handbook of Physics, McGraw-Hill, New York, 1967.

110. Köylü, Ü. Ö. and Faeth, G. M., “Radiative Properties of Flame-Generated Soot,” *Journal of Heat Transfer*, Vol. 115, 1993, p. 409-417.

111. Gray, C. A., personal communication, Vice President of Technology, Cabot Corporation, October 16, 1998.

112. Pedrotti, F. and Pedrotti, L., Introduction to Optics, Prentice-Hall, Englewood Cliffs, 1993, p.109-145.

113. Herzberg, G., Molecular Spectra and Molecular Structure: 1. Spectra of Diatomic Molecules, D. Van Nostrand Company, New York, 1950, p. 31, 560.

114. Choi, M. Y., Hamins, A., Mulholland, G. W., Kashiwagi, T., "Simultaneous Optical Measurement of Soot Volume Fraction and Temperature in Premixed Flames," *Combust. and Flame,* Vol. 99, 1994, p. 174-186.

115. Panagiotou, T., Levendis, Y., and Delichatsios, M., "Measurements of Particle Flame Temperatures Using Three-Color Optical Pyrometry," *Combust. And Flame*, Vol. 104, 1996, p. 272-287.

116. Hampson, G. J. and Reitz, R. D., "Two-Color Imaging of In-Cylinder Soot Concentration and Temperature in a Heavy-Duty DI Diesel Engine with Comparison to Multidimensional Modeling for Single and Split injections," *SAE Paper* #980524, 1998, 111-132.

117. Seitzman, J. M., Wainner, R. T., and Yang, P., "Soot Velocity Measurements by Particle Vaporization Velocimetry," submitted to *Optics Letters*, July, 1999.

VITA

Richard Trent Wainner was born in Oklahoma City, Oklahoma on March 17, 1970. He is the first of three children and only son of Kenneth F. Wainner, an Air Force medical doctor, and Bobbie J. Wainner (McMahan), an elementary school teacher. He was raised and educated in Oklahoma, Texas, Arizona, Germany, England, and then longest and most impressionably in Niceville, Florida where he graduated Niceville High School in 1988. He attended the University of Florida the next four years on scholarship, earning a Bachelor of Science in Mechanical Engineering, with High Honors, in June of 1992. Continuing his education at the Aerospace Engineering department of the Georgia Institute of Technology, he earned a Master of Science degree in August of 1993.

In the midst of a busy season of thesis writing, Richard married Kellee Anne Middlebrooks on May 1, 1993.